AAAS

Science

18 SEPTEMBER 2025

ADAPTING TO PASTORALISM

The genetic basis of dehydration resilience in the Turkana **pp. 1191 & 1246**

AAAS CARIBBEAN DIVISION 40TH ANNUAL MEETING 2025

SCIENCE IN THE CARIBBEAN:

PAST, PRESENT & FUTURE

REGISTRATION OPEN NOW!

ABSTRACT APPLICATION DEADLINE: OCTOBER 1, 2025

REGISTER TODAY: AAAS.org/CaribbeanMeeting

OCTOBER 24-25, 2025

CENTRO DE BELLAS ARTES EN HUMACAO, PUERTO RICO

AAAS | Caribbean Division

CONTENTS

18 SEPTEMBER 2025 | VOLUME 389 | ISSUE 6766

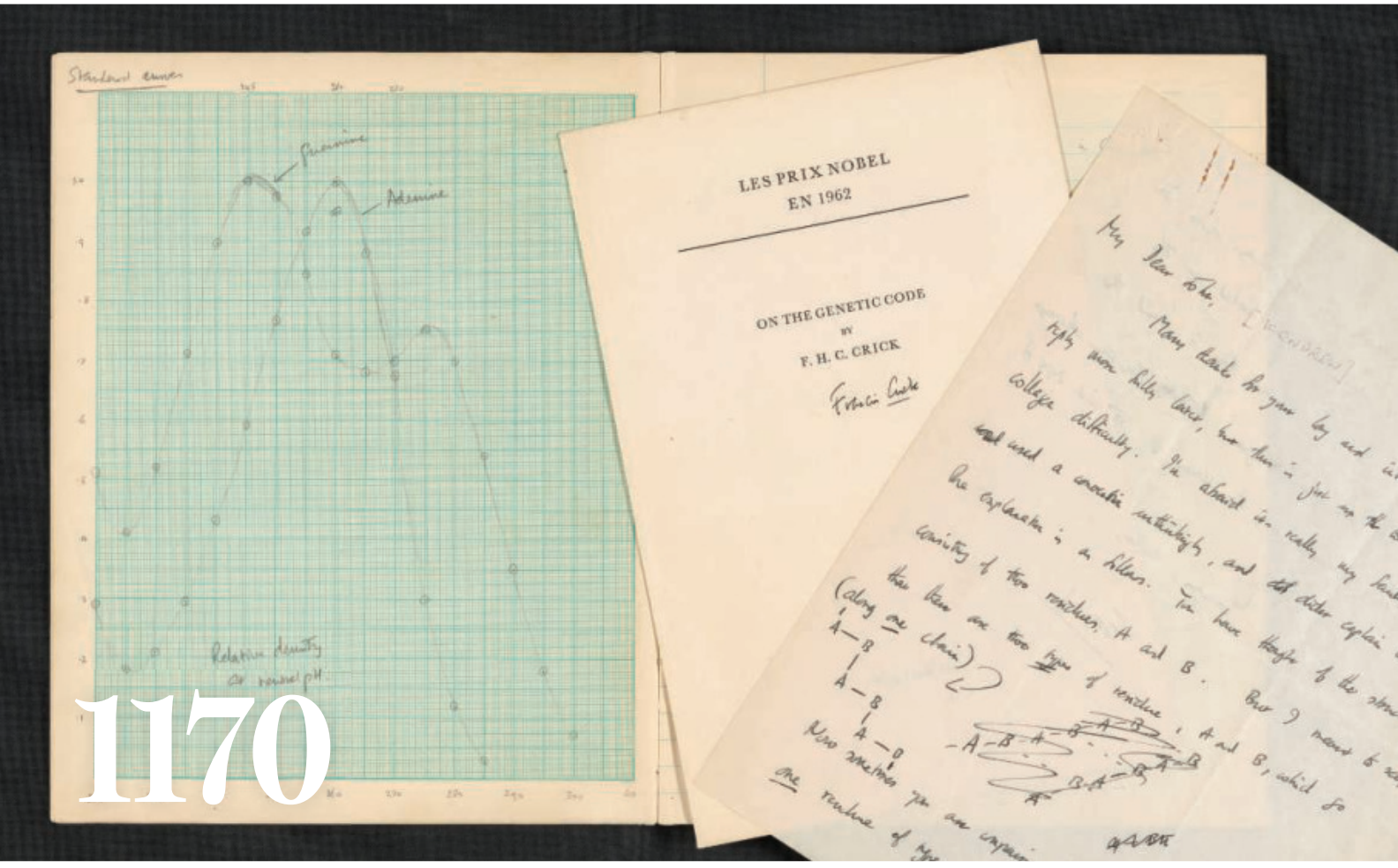

1170

EDITORIAL

NEWS

FEATURES

COMMENTARY

BOOKS ET AL.

PERSPECTIVES

PHOTO: SCIENCE HISTORY INSTITUTE

CONTENTS

ON THE COVER

Young Turkana herders guide camels across Kenya's arid landscape near Lake Turkana at sunset. Pastoralism remains central to survival in this region, where heat and water scarcity pose constant challenges. New research uncovers the genetic signatures that underlie adaptation to arid living in this pastoralist community. See pages 1191 and 1246. Photo: Kirsten Frost/FROST Photo Tours

ON THE PODCAST

Protecting newborns from an invisible killer, the rise of drones for farming, and a Druid mystery

Science **serves as a forum for discussion of important issues related to the advancement of science by publishing material on which a consensus has been reached as well as including the presentation of minority or conflicting points of view. Accordingly, all articles published in *Science*—including editorials, news, commentary, and book reviews—are signed and reflect the individual views of the authors and not official points of view adopted by AAAS or the institutions with which the authors are affiliated.** *Science* (ISSN 0036-8075) is published weekly on Thursday, except last week in December, by the American Association for the Advancement of Science, 1200 New York Avenue, NW, Washington, DC 20005. Periodicals mail postage (publication No. 484460) paid at Washington, DC, and additional mailing offices.

The title *Science* is a registered trademark of the AAAS. Domestic individual membership, including subscription (12 months): $165 ($74 allocated to subscription). Domestic institutional subscription (51 issues): $2865; Foreign postage extra: Air assist delivery: $135. First class, airmail, student, and emeritus rates on request. Canadian rates with GST available upon request, GST #125488122. Publications Mail Agreement Number 1069624. **Printed in the U.S.A. Change of address:** Allow 4 weeks, giving old and new addresses and 8-digit account number. **Postmaster:** Send change of address to AAAS, P.O. Box 96178, Washington, DC 20090–6178. **Single-copy sales:** $15 each plus shipping and handling available from backissues.science.org; bulk rate on request.

The identification code for *Science* is 0036-8075. *Science* is indexed in the *Reader's Guide to Periodical Literature* and in several specialized indexes.

Gold standard science requires gold standard scholarship

H. Holden Thorp

Scientists often casually refer to research and "library work" as separate endeavors. Research involves the execution of experiments in the laboratory whereas library work means finding references to relevant studies in the literature and analyzing them—often as a precursor to writing a paper. Treating careful scholarship as somehow less important than the acquisition of data can adversely affect the reliability of the scientific record and consequently, the course of science. In today's tense environment around science and politics, meticulous scholarship has never been more important.

Less than a month after his inauguration this year, US president Trump issued an executive order to establish the "Make America Healthy Again" (MAHA) Commission tasked with addressing the health of Americans, particularly children. When the MAHA report was released in May—which the Trump administration hailed as a landmark study—it contained fake citations that had been apparently hallucinated by a large language model. Rather than admitting that they hadn't taken the time to check that their references existed, the authors and the administration dismissed the episode as arising from "formatting errors." Perhaps even more concerning, though, was the existence of at least one citation in which the paper was real but its content was misrepresented.

...checking citations is just as important as carrying out experiments...

In its new effort to investigate the origins of autism, the Trump administration has enlisted the frequently criticized researcher David Geier. In a recent piece in the *New York Times*, Jessica Steier, a public health expert specializing in science communication, showed how Geier manipulated citations to make unsubstantiated claims. In one of his published studies that seeks to connect the vaccine additive thimerosal to autism, Geier dismisses factors that could confound his assertion by referring to published studies all written by himself. In other words, there is no independent evidence from any other laboratory or researcher to support his claims, a fact that a reader would know by digging into the citations and not assuming them to be true.

Sad to say, citation manipulation is not limited to agenda-driven research that deliberately obfuscates the science. A recent study shows that 17% of citations do not support the statement to which they are applied. Authors who were surveyed suggested that for the most part, these errors are the unfortunate by-product of the pressure for quantity over quality in a scientific enterprise driven by the ever-increasing glut of papers and journals. At the same time, published summaries of research papers make it easier to grab on to what seems like an appropriate citation without reading and understanding the entire paper.

Although this kind of poor scholarship is likely to be less consequential than those that distort the use of science in public health, it weakens the ability of the scientific community to call out the misrepresentations by politicians. In a political world driven by anecdote and "whataboutism"—where the answer to all criticisms is pointing out a similar error by the critics—all politicians need do to dismiss these concerns is to point out similar errors in the mainstream literature and then let social media and ideologically driven podcasters do the rest.

Robert F. Kennedy Jr., the secretary of Health and Human Services and chair of the MAHA report, has promised to reveal new findings this month regarding the origins of autism that implicate what he vaguely called an "intervention" and that President Trump referred to as "a drug or something." Recent news suggests that this revelation will be a proposed link between autism and acetaminophen use in pregnancy.

When the official autism report is issued, scientists should calmly and methodically evaluate whether it contains any new and convincing evidence. If there is none, then the best defense is to carefully document the ways in which the report is unpersuasive, just as Steier did in her essay. A logical place to start will be with the citations. If there is manipulation of the references to make points that the cited papers do not support, there are probably problems with the evidence as well. If more studies are needed, that should be explained, too.

The success of this pushback will depend on redoubled efforts by scientists and journals to promote outstanding scholarship in which the "library work" of checking citations is just as important as carrying out experiments and interpreting their results, and where misrepresentation of references is treated as seriously as research misconduct. □

H. Holden Thorp is Editor-in-Chief of the *Science* journals. hthorp@aaas.org

10.1126/science.aec2360

NEWS

ENVIRONMENTAL REMEDIATION

Hanford set to finally lock up nuclear waste in glass

But some officials fear Trump administration may be aiming for an alternative solution **WARREN CORNWALL**

Waste from plutonium production is stored in 177 tanks that have corroded.

After decades of delays, one of the world's most polluted places is finally set to get a little cleaner. Next month, workers at the U.S. Department of Energy's (DOE's) Hanford site are scheduled to open a multibillion-dollar facility that would begin to entomb radioactive waste in thousands of glass logs, which would then be buried elsewhere. It would be a major milestone in the cleanup of nuclear weapons waste currently held in corroding tanks. But amid signs of upheaval at DOE's cleanup office, state and local officials are worried the White House may be delaying the project at the eleventh hour and trying to shift to an approach that is faster and cheaper but perhaps not as foolproof: locking up waste in cement-like grout.

"We're concerned about the rumors because we are so very close to, for the first time ever, meaningfully reducing the volume of waste at Hanford's tanks," says David Reeploeg, vice president for federal programs at the Tri-City Development Council, an economic development nonprofit representing towns flanking the federal site in Washington state.

From World War II through the Cold War, Hanford engineers made the plutonium for thousands of nuclear bombs, including the one dropped on Nagasaki, Japan. Some 325 million liters of liquid waste from this process—enough to fill 85 Olympic swimming pools—was funneled into 177 buried carbon steel tanks. Some tanks have corroded, and an estimated 3.7 million liters of toxic, radioactive waste have leaked into the ground, threatening to contaminate groundwater that flows into the nearby Columbia River.

In 1989, DOE reached a deal with the U.S. Environmental Protection Agency and the state of Washington to clean up the mess. Amended over time, the agreement now specifies that much of the waste will be entombed in glass, a process known

PHOTO: DEPARTMENT OF ENERGY

as vitrification. But for DOE and Bechtel National, the project's lead contractor, making good on this promise has proved tricky. Initially, the vitrification plant was supposed to cost $4.3 billion and open by 2007. Today, more than $10 billion has been spent on the plant alone, and the entire cleanup is estimated to cost $200 billion to $350 billion and stretch into the 2070s.

Workers recently tested furnaces and emission controls at the newly completed facility, which is slated to handle much of the low-level waste that comprises 90% of the total volume. For the past 3 years some of the waste has been siphoned from the storage tanks and pumped to a facility that removes traces of highly radioactive cesium, one of the most dangerous radioisotopes. Some 3 million liters of this partially treated waste is now waiting to be encased in glass. A second facility, which isn't scheduled for completion until the 2030s, will treat the high-level waste that has accumulated at the bottom of the tanks as a thick, radioactive sludge.

On 8 September, however, DOE fired Roger Jarrell, who had been named in April to head the agency's Office of Environmental Management, which oversees the Hanford cleanup. That prompted speculation the agency was changing course. Last week, U.S. Senator Patty Murray (D–WA) issued a press release stating that in a phone call on 10 September, DOE Secretary Chris Wright said the department was planning to "curb" the start of vitrification because of safety concerns. The move would be "an astonishingly senseless and destructive move and a threat to the entire nuclear cleanup mission at Hanford," Murray said.

The day after the call, Wright issued a statement that DOE "has made no changes to our plans or strategy for the [low-level] waste treatment facility. Although there are challenges, we are committed to beginning operations by October 15, 2025."

Nevertheless, some wonder whether President Donald Trump's administration wants to treat more of the waste by mixing it with grout, which could be cheaper and faster than vitrification. Such a move was touted in Project 2025, a 900-page plan by the conservative Heritage Foundation that has foretold many actions by the new Trump administration. That report calls for adopting policies that would allow much of the waste at Hanford "to be grouted rather than vitrified."

Jim Conca, a geochemist who worked for decades on nuclear waste research for both DOE and private companies, agrees. "It should be grouted," says Conca, who lives on the outskirts of Hanford in the city of Richland. "Vitrification is a stupid thing to do with this waste."

Vitrification, Conca says, became the default because Washington state officials saw it being used to entomb highly radioactive waste from nuclear power plants in other countries. But because the waste at Hanford is a heterogeneous brew of highly radioactive, short-lived waste and low-level, long-lived waste, he says, it would be better off mixed with grout and stored either in place or at a special facility. Grout is already used to treat low-level radioactive waste left from bombmaking at another federal nuclear site in South Carolina. And an expert National Academies of Sciences, Engineering, and Medicine panel on which Conca served recommended grout as a cheaper way to effectively handle some high-level waste as well.

But in Washington state, officials and environmental groups have long resisted the idea. Cement breaks down more quickly than glass and is more porous, allowing water to infiltrate, notes Ian Pegg, a physical chemist at the Catholic University of America who conducts vitrification research. "You look at concrete roads and bridges, yeah they last for many years, but do they last for hundreds of years, or thousands of years, or hundreds of thousands of years?" he says. "It's widely accepted that glass is the better waste form."

Earlier this year, Washington state did agree to having some of the waste encased in grout as long as it's stored outside the state. But officials say they will challenge any move by the federal government to break the 1989 agreement. As amended early this year, it calls for vitrifying most of the waste, and to begin doing it next month.

DOE should not renege on those promises, Washington Governor Bob Ferguson (D) said at a press conference last week. If the agency does, he said, "there will be a legal challenge to them, and they will lose." □

TRUMP TRACKER

EPA NIXES CARBON TRACKING The U.S. Environmental Protection Agency (EPA) moved ahead last week with a proposal to effectively end its 15-year-old program tracking the greenhouse gas emissions from more than 8000 industrial facilities, including coal-fired power plants, refineries, and steel mills. EPA contends the change would save "up to $2.4 billion" in regulatory costs because companies would no longer be required to track their emissions. The move, which could take effect early next year, would force estimates of U.S. carbon emissions to rely on other data, such as energy consumption and electricity production statistics. —Paul Voosen

CONTROVERSIAL CLIMATE PANEL DISBANDED The U.S. Department of Energy (DOE) has dissolved the five-person panel of scientific contrarians behind a draft report this summer that purported to provide a "critical review" of climate science. The report was widely cited in EPA's effort to overturn its own ability to regulate greenhouse gases as a pollutant. But in the month since its release, climate scientists have pointed out mistakes and misinformation made in the report. Environmental groups also brought a suit arguing that DOE did not follow federal law in how it established the group, whose members were handpicked by DOE Secretary Chris Wright. —Paul Voosen

NIH TURNS AWAY FROM FETAL TISSUE, AGAIN The U.S. National Institutes of Health (NIH) says it will not renew a handful of research grants that an advocacy group identified as involving human fetal tissue—a decision that is setting off alarm bells for some in the scientific community. The White Coat Waste Project, a self-described "taxpayer watchdog" that campaigns to eliminate animal research across the U.S. federal government, last week publicized a list of 17 grants categorized in NIH's grants database as active and listed under the spending category "human fetal tissue." But it's not clear whether all of the studies actually involved the controversial material—or whether NIH's pledge not to renew them signals the revival of restrictive policies on fetal tissue studies that President Donald Trump imposed during his first term in office. —Phie Jacobs

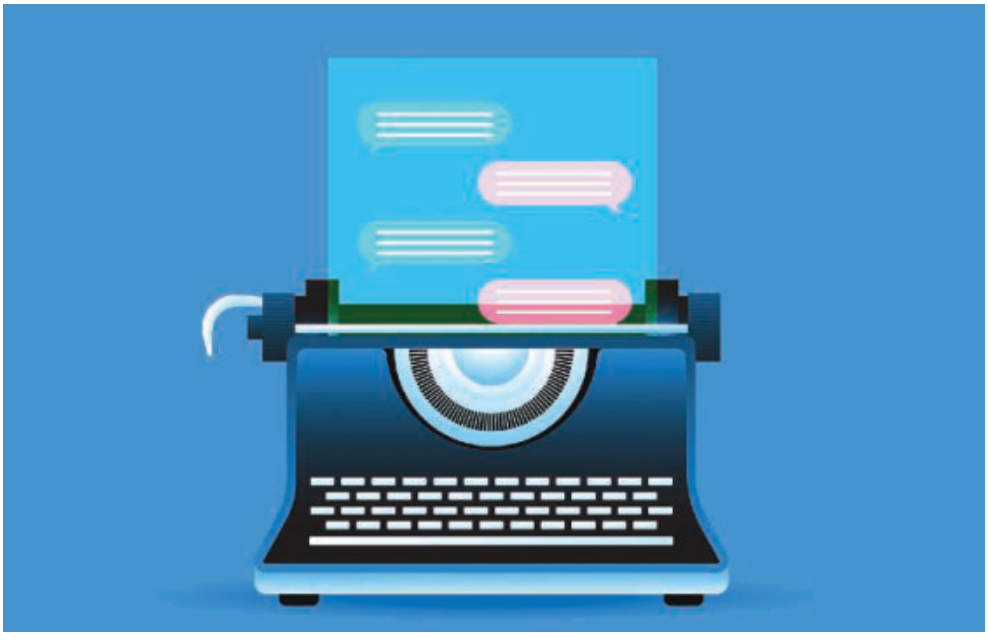

PUBLISHING

Far more authors use AI than admit it

Study by cancer publisher highlights promise of AI detectors and the challenges they pose

JEFFREY BRAINARD

After ChatGPT debuted in late 2022 and wowed users with its humanlike fluency, many academic journals rolled out policies requiring authors to disclose whether they had employed artificial intelligence (AI) to help write their papers. But new evidence from one publisher suggests four times as many authors use AI as admit to it—and that peer reviewers are turning to it, too, even though they are asked not to.

The new study, run by the American Association for Cancer Research (AACR), investigated the 10 journals the society publishes. AACR launched it after some authors wondered whether the peer-review reports on papers they had submitted were AI-generated, says Daniel Evanko, who oversees AACR's editorial systems. It made use of a recently developed AI detector the AACR team and others say appears to be highly accurate.

From 1 January to 30 June, the team found, 36% of the abstracts in 7177 manuscripts submitted to AACR contained at least some AI-generated text. But when asked in an automatic step in the submission process to disclose any use of AI to prepare the manuscript, authors only did so for 9% of the papers studied.

Earlier studies tried to quantify the use of AI in papers and peer reviews. But the new study, presented at the International Congress on Peer Review and Scientific Publication earlier this month, is one of the first to assess the reliability of author disclosures. "Disclosures on their own have virtually no value without some means of determining their accuracy," Evanko says.

The work is "a good place to start" to address the problem, says Roy Perlis, editor-in-chief of the JAMA Network's content channel JAMA+AI and a psychiatrist at Massachusetts General Hospital. But AI detectors produce false positives, and human editors must use judgment in interpreting their readings, he says. "There is a real risk that we plug these things into our [editorial] pipelines and treat their outputs as if they are infallible."

Evanko says he was initially "extremely skeptical" about the high accuracy claims from the new detector his team ultimately used in its study, the AI Detection Dashboard from Pangram Labs. Pangram's detector, unveiled in 2024, relies on a form of AI called deep learning, a computational method also used in large language models (LLMs) such as ChatGPT. In a preprint that year, its creators described the detector's text classifier as more accurate than others because they trained it using an unusual method and data set.

They started with a large body of human-written texts. They then prompted LLMs to produce a similar version of each text that matched its style, tone, and semantic content. They trained their text classifier to spot telltale differences between the two, progressively modifying the prompts so the LLMs generated text increasingly difficult for their classifier to distinguish from human-written text. The tool produces scores on a 10-point scale reflecting the likelihood of AI use.

Despite Evanko's initial misgivings, he was reassured that the tool is unusually good at avoiding false positives when he ran it on AACR's submissions from 2020 and 2021, before ChatGPT. It flagged well under 1% of those manuscripts as possibly AI-generated.

After ChatGPT arrived, the detector showed, AI-generated text steadily became more common in AACR papers' abstracts, methods sections, and peer-review reports. (Evanko's study only covered those kinds of texts because AACR's database includes them in a format that is readily analyzable.) In addition to the high proportion of abstracts with AI-generated text, Evanko's team found it in nearly 15% of the methods sections and 7% of reviewer reports in the last quarter of 2024.

He speculates authors are not disclosing AI use because they fear journals will reject their manuscript, even if AI was used only for editing the manuscript and not generating text. Some evidence supports that reviewers penalize this use. But how authors perceive that risk varies by field, according to a 2024 survey of more than 800 researchers, co-authored by Amy Zhang of the University of Washington, who studies human-computer interaction. Respondents in computer science were more likely than those in biology and medicine to say they were comfortable with disclosure. In computer science, "it just has become so common and normal to use," she says. But norms about AI use "are unsettled in these other fields." The International Association of Scientific, Technical & Medical Publishers

ILLUSTRATION: MOOR STUDIO/GETTY IMAGES

reported in April that many authors are confused about when they should report AI use; the group, known as STM, expects to finalize updated guidelines this week.

Using AI for editing manuscripts and other purposes can be legitimate, Evanko and Perlis say, especially when authors are not native speakers of English. In fact, Evanko found that manuscripts from countries where English is not an official language were flagged for AI-generated text twice as often as those from English-speaking countries, perhaps because authors turned to AI to improve their writing. But AI-generated text can also be one of many markers of submissions that might have come from paper mills, Evanko adds. A spate of letters to the editor recently submitted to an AACR journal was all generated by the DeepSeek LLM, Pangram's tool indicated.

AACR is considering next steps in response to Evanko's findings, including using the new tool to screen all submissions. But with more than 2500 AACR submissions flagged for AI-generated abstracts from January to June alone, "It's too many to put a human in the loop" to follow up on each undisclosed instance, he says. The publisher might start by sending automated emails to authors asking for an explanation, as it does about other deficiencies in manuscripts.

But Perlis says he's not persuaded that AI-text detectors are accurate enough to help publishers and editors deal with the machine-generated text appropriately. He wants common performance benchmarks and more data about how the detectors perform on manuscripts from different fields of science before they are used routinely. "We want to encourage people to continue to develop these kinds of tools," he says. "We also want to acknowledge that there will absolutely be an arms race—the better the tools get, the harder people will work to circumvent them." □

IN FOCUS

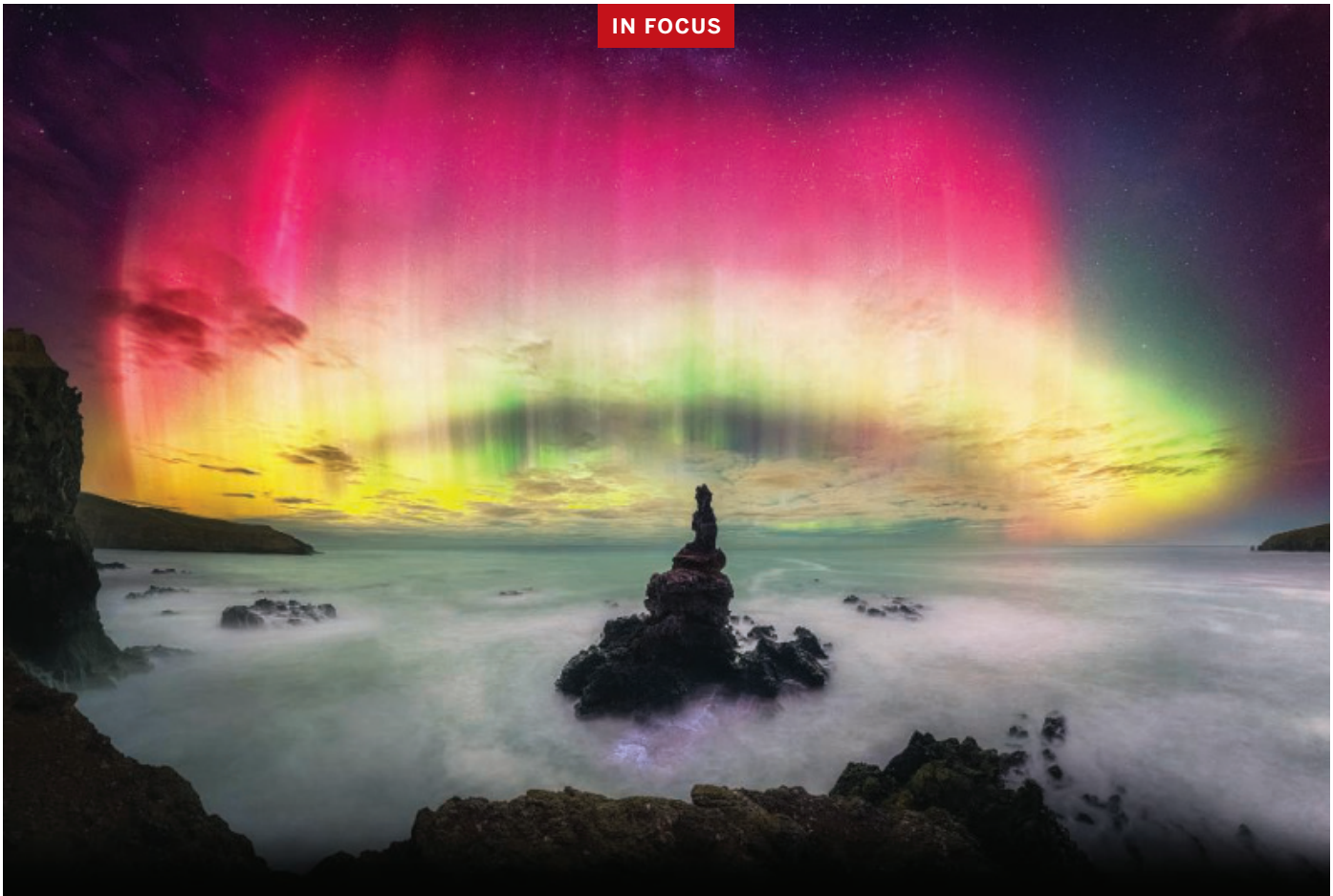

A prize-winning light show

This image of the southern lights, or the aurora australis, captured in Tumbledown Bay, New Zealand, in May 2024, was among the winners of this year's Astronomy Photographer of the Year competition, run by the Royal Observatory Greenwich. That month, scientists recorded the strongest geomagnetic storm in more than 2 decades, brought on as blobs of plasma ejected from the Sun slammed into Earth's magnetic field. The huge amounts of energy released led to aurorae that lit up night skies around the globe at lower latitudes than usual. Of the New Zealand display, photographer Kavan Chay noted, "The reds were a level of intensity I had never experienced." —Katie Langin

PHOTO: KAVAN CHAY

GENETICS

After bizarre journey, precious archive of molecular biology history finds new home

Science History Institute makes public multimillion-dollar collection, including Rosalind Franklin's famous DNA image, assembled by fake scientist

JON COHEN

A storied trove of documents, photos, and lab tools from the race to decipher DNA's structure and function is finally being made public. The Science History Institute (SHI) in Philadelphia recently purchased the collection for an undisclosed amount from a research institute founded by noted human genome scientist J. Craig Venter and on 8 September began making it available to visitors. It's also putting digital versions of many of the letters, lab notebooks, book drafts, and images online. "It's wonderful that this collection is going to be readily accessible to scholars and other researchers," says Nathaniel Comfort, a science historian of this era at Johns Hopkins University.

Science historian Michelle DiMeo, a vice president at SHI, says the collection illuminates "the foundations of molecular biology" with many firsthand perspectives from pioneering DNA researchers as well as key artifacts. The "jewel of the collection," according to SHI, is the original Photo 51, an x-ray diffraction image of DNA made in 1952 by Rosalind Franklin and her student Raymond Gosling, which Maurice Wilkins shared with James Watson. In his classic book *The Double Helix*, Watson credits the image with helping him and Francis Crick deduce DNA's structure—for which they and Wilkins won the Nobel Prize in Physiology or Medicine in 1962, after Franklin had died.

For scholars and the public, it is a happy end to a decadeslong saga that began when an amateur rare book seller with faked scientific credentials and a knack for befriending the rich and famous—including disgraced financier Jeffrey Epstein—began buying up the artifacts from prominent scientists, planning to profit by reselling them. Its subsequent journey involved lawsuits, multiple parties willing to pay millions for the material, a contentious sale at Christie's auction house, and 2 decades largely out of sight at the J. Craig Venter Institute (JCVI). In the end, DiMeo says, the collection "in some ways fell into our hands."

Now, researchers will be able to easily access key documents from this period to help resolve contentious debates about everything from Photo 51's relevance to the scientific community's treatment of Franklin. Although the collection contains copies of documents available in other archives—including an early draft of *The Double Helix* called *Honest Jim*—there's also unique material: an important "missing" 1952 notebook of Crick's, revealing letters between several of these scientists, and a second historic x-ray of DNA from Franklin and Gosling, made under different conditions. Historians say the image led Franklin to dismiss the idea of a helical structure, allowing Watson and Crick to have the key insight.

The collection contains material from other, now-deceased Nobel Prize–winning scientists: Barbara McClintock, Max Perutz, Aaron Klug, Sydney Brenner, Linus Pauling, and Max Delbrück. "Historians studying the lives and works of Perutz and Klug in particular will be overjoyed at this news," says Matthew Cobb, a zoologist at the University of Manchester who has authored a forthcoming biography of Crick. He posted on social media that the SHI acquisition is "a tremendous contribution to scholarship and public understanding."

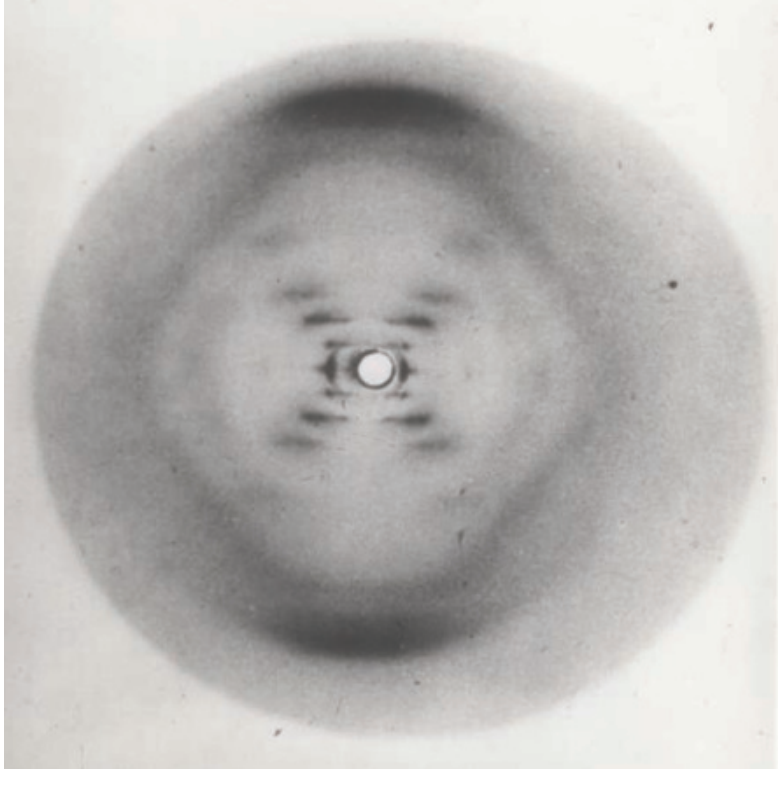

Photo 51, an early x-ray diffraction image of DNA, helped reveal the molecule's helical structure.

PHOTO: SCIENCE HISTORY INSTITUTE

"I'M NOT SO NAÏVE NOW."

The collection had unsavory beginnings. "It's not complimentary to me to really talk about this stuff," says Jeremy Norman, a seller of rare books and manuscripts who assembled almost all of it in partnership with Al Seckel, who presented himself as a neuroscientist from the California Institute of Technology (Caltech). Norman, 80, who lives in

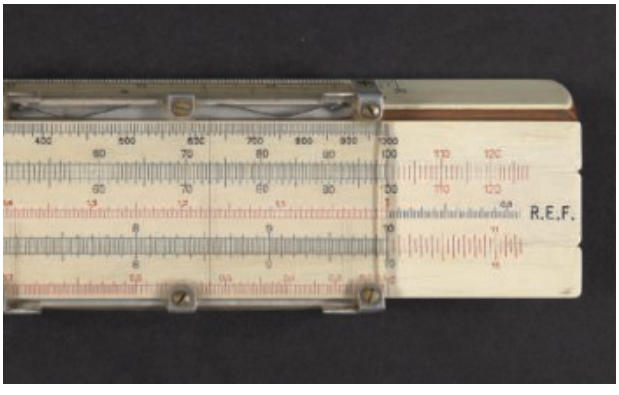

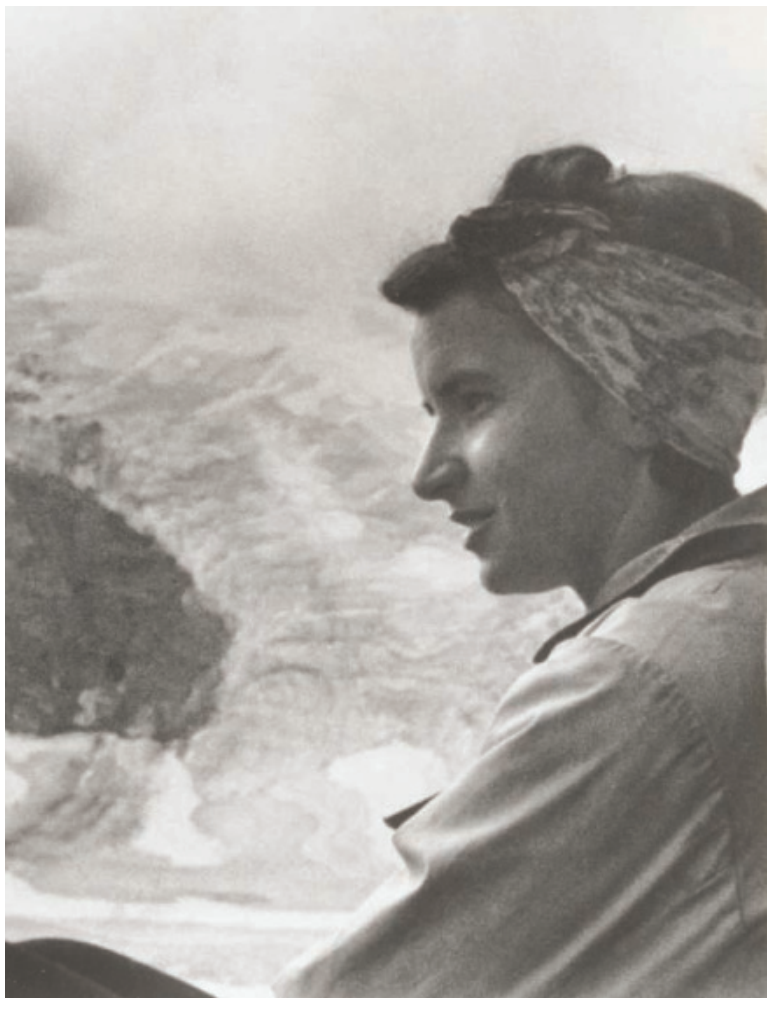

PHOTOS: (CLOCKWISE FROM TOP LEFT) SCIENCE HISTORY INSTITUTE; VITTORI LUZZATI/SCIENCE HISTORY INSTITUTE; SCIENCE HISTORY INSTITUTE CC BY

Photos of Rosalind Franklin on an Italian vacation, her slide rule, and her office after her death join other items in the collection that could shed light on her pioneering DNA research.

Novato, California, agreed to speak publicly about the backstory in detail for the first time to *Science*. "I was naïve. I'm not so naïve now."

Norman, who has a website called the HistoryofScience.com, says he had done business for several years with Seckel. "I didn't realize he was a con man," Norman says. "A number of the scientists who had basically either given him or sold him their papers rather cheaply didn't realize that I was going to turn around and resell it," Norman says. "He told them that I was a philanthropist acquiring material."

Seckel, born in New York City, briefly attended Cornell University and then moved to Los Angeles around 1980, where he founded the Southern California Skeptics society. He traveled among high rollers like Epstein, rock stars, and celebrity scientists, including Crick and physicist Richard Feynman, says Tom McIver, an anthropologist–turned–research librarian who joined the skeptics society and then investigated and clashed with Seckel for decades. Seckel also became a well-known collector of optical illusions, publishing a half-dozen books about them and giving a popular TED talk on the subject.

McIver, who jokes he has become a "Seckelologist," has documented the many lawsuits in which Seckel was involved, his falling out with Feynman, troubled marriages (including to Isabel Maxwell, whose sister Ghislaine was convicted of sex trafficking on Epstein's behalf), and his false claims that he had a Cornell degree and a Ph.D. from Caltech. Many of Seckel's deceptions were detailed in a 2015 exposé by *Tablet* magazine called "The Illusionist."

According to Norman, the molecular biology collection began when Seckel sold him an archive he had bought from Klug, who was a Franklin collaborator and possessed some of her papers. It built from there, with Norman ultimately paying Seckel $1.5 million between 1998 and 2001, according to court filings. "It was very hard for me to resist this material," Norman says. Seckel and Norman also worked together to try to convince Crick to sell them his papers, although the deal fell through and Crick sold them in 2001 to the Wellcome Trust for $2.4 million.

Acrimony between Seckel and Norman exploded in 2003, when Christie's agreed to individually sell the items from what had become known as the Norman Collection. In a *Nature* news story, Seckel, the supposed Caltech neuroscientist, decried the move, insisting the agreements he signed with scientists assured them that their items would be part of a large molecular biology archive and available to scholars. "This impacts on my reputation," Seckel said. The possibility that the collection might fall into private hands or be split up also upset many biologists and historians. Klug at the time decried it as "an outrage."

A month before the auction was to take place, Christie's canceled it after Seckel showed the company

documentation he had from the scientists that required keeping the collection intact. Lawsuits erupted. Norman claimed Seckel had no right to sell him the papers in the first place because he didn't have clear title. Seckel claimed his "lucrative business" in rare scientific works had been "completely destroyed" by Norman. The suits were ultimately dismissed.

Christie's kept trying to negotiate the sale for Norman. In January 2005, *Science* published a letter by Nobel laureate Richard Roberts and geneticist Norton Zinder that appealed to scientists to collectively raise at least $2 million to purchase the archive so it could go to Cold Spring Harbor Laboratory (CSHL), where Watson would build a new wing of its library to house the papers and those from many other molecular biologists. "We had some offers from people, but it was small change," Roberts says.

In the end, JCVI was the sole bidder, purchasing the collection for $2 million and building a climate-controlled room to house the 100 boxes of material. "Christie's was happy to be rid of the problem," Venter says, noting that the purchase also resolved legal issues about ownership. After curating the archive, JCVI made it available to researchers, but Venter says fewer than 100 have viewed it over the past 2 decades. "My dream was to take 2 years and rewrite the history of molecular biology from the collection," Venter says. "I couldn't find the 2-year horizon."

By this year, JCVI was planning to move across town, from its longtime home in La Jolla to downtown San Diego, and was reluctant to invest in a similar storage space at its new facility. But in February, Venter met DiMeo by chance in Pacific Grove, California, at the Asilomar meeting she co-organized on regulating risky scientific research. "It's been on our mind for some time to find the right home for it, and we didn't want it to end up in somebody's private collection," Venter says.

Norman is relieved at where the historic collection has ended up. "I'm happy that the Science History Institute has it," he says. "It's now going to an appropriate home." Roberts still contends CSHL, which already has a large molecular biology collection, would have been a better home. "We're disappointed," he says.

For SHI, which until 2018 focused on chemistry, the collection marks the beginning of a new era, DiMeo says. "It's our seed collection in the history of the life sciences," she says. "We're hoping that it might spark future donations from life scientists to preserve their archives."

As for Seckel, the tarnished co-creator of the collection, *The Daily Mail*, a U.K. tabloid, reported he died in 2015 by jumping off a cliff near his French home around the time the *Tablet* exposé appeared. McIver says the circumstances of Seckel's death remain "very mysterious" but doubts he's alive. "It just doesn't seem like him to remain silent." □

Samples of DNA collected from thousands of Ukrainians are part of a study probing the genetics of type 1 diabetes.

PHOTO: YAROSLAVA HASYNETS

GENOMICS

Amid war, a genomics research program blooms in Ukraine

Inaugural project for new center searches for genes involved in diabetes **RICHARD STONE**, in Uzhhorod, Ukraine

In the basement of a building that decades ago was a Hebrew trade school for boys, Yaroslava Hasynets opens a freezer packed with some 12,000 plastic vials. "Part of our genetic heritage," says Hasynets, dean of biology at Uzhhorod National University (UzhNU). The vials contain DNA from an ongoing study of Ukrainians with type 1 diabetes (T1D) that UzhNU's new genomics facility, to be inaugurated on 22 September, will mine for genetic insights.

Russian attacks, power outages, and parlous budgets have posed severe challenges to Ukrainian science. But a surprising hot spot for frontier genomics is emerging here in the foothills of the Carpathian Mountains near Slovakia and Hungary, taking advantage of Ukraine's distinctive population—and scientists seeking refuge here from elsewhere in the war-torn country. Uzhhorod, named after the Uzh River snaking through it, has not been attacked and is widely considered "the safest place in Ukraine," says Fyodor Kondrashov, an evolutionary genomics expert at the Okinawa Institute of Science and Technology who runs a bioinformatics and data science summer school here that draws participants from across Ukraine.

Still, on most scientific radars this tranquil haven is at best a faint blip. "A colleague joked Uzhhorod is a great place for a witness protection program for scientists, because nobody will ever look for you there," says geneticist Taras Oleksyk of Oakland University, who was born in this city.

He is one of the movers behind the new genomics facility. As a faculty member of the University of Puerto Rico in the late 2000s, Oleksyk watched with envy as many European countries established national genetic databases, while his homeland largely remained a genomic black hole. "I thought, 'What about Ukrainians? Who's going to do this kind of effort for my country, if not me?'"

He got his chance in 2018, just before moving to Rochester, Michigan, when he initiated the first study on genomewide diversity in Ukraine, arranging for labs in China and the

United States to sequence 97 Ukrainian genomes. In the journal *GigaScience* in 2021, Oleksyk and colleagues described 189 medically relevant alleles implicated in conditions such as autism and breast cancer, as well as 20 potentially protective mutations. He and Oakland biologist Khrystyna Shchubelka—also from Uzhhorod—then teamed up with Romanian scientists to sequence 150 genomes from each country as part of Genome of Europe, a continentwide genomic survey.

"All of a sudden, we had a system that works. Collecting samples, extracting DNA. We had an ethics committee," Oleksyk says. That infrastructure attracted Regeneron, which in 2021 dangled support for a T1D study in Ukraine. Genomewide association studies elsewhere had implicated several dozen alleles in the disorder. But studies of variants found only in specific populations are scarce, Oleksyk says. After months of negotiations, the Leona M. and Harry B. Helmsley Charitable Trust came aboard to fund a $5 million Ukraine project—and ensure that the sequencing data would be publicly available.

Oleksyk had another asset: his sister. Endocrinologist Olga Oleksyk's clinic in Uzhhorod has become a sanctuary for top specialists on metabolic diseases who fled occupied or embattled Ukrainian cities. To recruit T1D patients, she and Shchubelka linked up with 85 other endocrinologists and molecular biologists across Ukraine, gathering blood samples from more than 12,000 patients and healthy age-matched controls. The result, Taras Oleksyk says, is the largest T1D genetics study in the world. In some regions, Shchubelka says, "We don't have any more patients with type 1 diabetes left to enroll. We got nearly everybody."

"We need more data sets relevant to Ukraine, which is exactly what Taras and his team are doing," says Serghei Mangul, a computational biologist at the University of Southern California. "And studying the population like this will be a great resource as Ukraine develops precision medicine."

The UzhNU consortium has joined forces with colleagues in Poland to expand the study to include 20,000 patients and controls by mid-2027. So far, Regeneron has sequenced DNA from 10,000 samples. A key target is the human leukocyte antigen (HLA) system—a complex of genes that encode immune-regulating proteins and is known to be involved in T1D. The project hopes to zero in on alleles that elevate T1D risk and are more prevalent in Eastern Europeans.

The project is already paying a diagnostic dividend: A few dozen subjects appear to have maturity-onset diabetes of the young (MODY), a rare genetic form of the disorder that masquerades as T1D. Whereas T1D patients need daily insulin shots, MODY patients can be treated with oral drugs. The five MODY cases confirmed so far "got their true diagnosis and could start a new life, without insulin injections," Olga Oleksyk says.

The new genomics facility intends to build on these findings by taking the sequencing in-house, using Oxford Nanopore Technologies's PromethION 2 Solo, a DNA and RNA sequencer the size of a thick paperback novel. The company is sending a team to Uzhhorod next week for the lab's inauguration and training. The device, more capable and versatile than earlier sequencers, will enable the team to find rare HLA variants in their T1D study participants, sequence RNA from stool samples to study their microbiomes, and sequence RNA from blood to examine gene expression patterns associated with T1D and inflammation.

The UzhNU facility is also launching a new study that will probe the microbiomes of about a dozen scientists who winter at Ukraine's Vernadsky Research Base on the western Antarctic Peninsula. Because they eat the same food and don't meet other people for months, "Our hypothesis is that their microbiomes gradually become more similar" during the yearlong deployment, says Mariia Pavlovska, a marine microbiologist with the National Antarctic Scientific Center of Ukraine. Another Oleksyk recruit—UzhNU's Walter Wolfsberger—has formed a bioinformatics group to help make sense of the expected data windfall.

"In genomics, you can't do anything alone, right?" Taras Oleksyk says. "My goal in whatever time I have left is to bring as much expertise to Uzhhorod as I can—and turn it into the Cambridge of Ukraine." □

TRUMP ADMINISTRATION

Funding delays frustrate agricultural researchers

Grants awarded by the U.S. Department of Agriculture have dropped sharply **ERIK STOKSTAD**

Georg Jander was delighted in May when a grant he'd submitted last year to the U.S. Department of Agriculture (USDA) to study how maize responds to attacking insects received favorable reviews. But now, 4 months later, he still doesn't know whether it will be funded. The same cloud of uncertainty hangs over the heads of many agricultural scientists, as USDA continues to postpone grant decisions and fails to announce many new funding opportunities. Jander, a Boyce Thompson Institute plant biologist, says he and "a lot of other people are just frustrated because we don't know what to do next."

USDA typically awards more than $1.7 billion in funding each year for a wide range of research on food, nutrition, and agriculture. But by the end of this fiscal year it will have awarded just over $1 billion, according to its public database. Some approved grants have yet to receive a single dollar for work that was expected to begin earlier this year. "We've missed an entire field season," one agricultural researcher says.

It's not unusual for new administrations to review funding programs. But after President Donald Trump took office in January, his administration went further. It ordered USDA to freeze funding of all awarded grants, a stoppage that lasted for much of the first half of the year. The aim was to identify grants that included work related to diversity, equity, and inclusion, which were canceled wholesale. The agency also canceled grants to universities for research related to climate-smart agriculture. And it stopped awarding new grants.

Other funding agencies took similar steps. But USDA remains behind even as other agencies, such as the National Institutes of Health, have ramped up grant funding in recent months. "It's been very, very delayed," says Julie McClure of the Torrey Advisory Group, which lobbies on behalf of the American Society of Agronomy, Crop Science Society of America, and Soil Science Society of America. (USDA did not respond to a request for comment.)

Competitive grants, which fund research at universities and other organizations, have fared the worst. As of 16 September, with 2 weeks

left before the end of this fiscal year, USDA's center for extramural research funding, the National Institute of Food and Agriculture (NIFA), had awarded just 558 competitive grants, according to its public database. That's 68% fewer than during the prior fiscal year—and $741 million less in competitively awarded research funds. In contrast, the $800 million of so-called capacity funds, which are largely distributed by formulas to certain universities, has all been committed.

One reason for the shortfall in competitive funding is that NIFA simply did not invite new grant applications for much of the year. The first funding opportunities were only posted in July—and with tight deadlines of just a few weeks. The long-standing Foundational and Applied Science Program, which awards $300 million per year, was posted on 1 August with deadlines as soon as 2 October. "A ridiculously short turnaround time," says Crispin Taylor, executive director of the American Society of Plant Biology. The agency also appears to have a backlog of applications submitted last year that remain in limbo. The number could be in the thousands, a former USDA staff member says.

Morgan Carter, who studies plant pathogens at the University of North Carolina at Charlotte, had hoped a graduate student in her lab could win a USDA fellowship to study new biocontrol approaches for fungi. But the agency has not posted a request for applications. "We don't know the status of this program."

Even for scientists who were awarded grants, the path hasn't been smooth. According to USASpending.gov, a federal database, USDA turned the spigot back on for many suspended grants in August. But the delays complicated research plans. Many labs have delayed hiring postdocs or project managers or have had to scramble to find other support.

What's causing the delays is unclear. Some observers suspect the White House Office of Management and Budget or the Department of Government Efficiency, formerly run by Elon Musk, have taken charge of funding and are responsible for the holdup. "The real question is who's making the decisions?" says Elizabeth Stulberg, a lobbyist with Lewis-Burke Associates.

Stulberg adds that because the Senate has only confirmed some of the Trump administration's nominees for USDA posts (four of 12), the agency also may not have the bandwidth to make swift funding decisions. Staffing has also dropped at NIFA. By March, 11% of its 488 employees had taken the Trump administration's offer of deferred retirement and another 8% had left for other reasons.

Senate confirmation of entomologist Scott Hutchins as USDA's undersecretary for research, education, and economics, which could happen as early as this month, could help break the logjam, McClure says. Observers say Hutchins knows agricultural research and USDA. New money Congress has put into agricultural research could also help. The One Big Beautiful Bill Act includes $1.25 billion over 9 years for agricultural research facilities, beginning with the next fiscal year.

But until the delays subside, many researchers remain on tenterhooks. For now, says one pretenure faculty member who has waited more than a year to learn whether a grant submitted to USDA will be funded, "We are all juggling." □

IN FOCUS

Realistic minikidneys take shape in the lab

Using mouse kidney stem cells, scientists have produced the most realistic lab-grown replicas of the vital organ so far. For more than a decade, researchers have been rearing so-called kidney organoids in lab dishes to study kidney function and development—and in hopes of someday making new kidneys for patients who need transplants. This week in *Cell Stem Cell*, a team reports fine-tuning the medium in which mouse kidney stem cells grow, allowing the organoids to develop for a longer period of time. The resulting collections of cells showed a complex internal structure that more closely resembled the structure of a real kidney than in previous attempts. Implanted into mice, the structures connected to the circulatory system, producing a dilute urine from filtered blood. The scientists then grew similar organoids from human stem cells (below, revealed by fluorescent staining). The 1-millimeter-long organoids are still far from replacement organs that could be transplanted into a patient. —Mitch Leslie

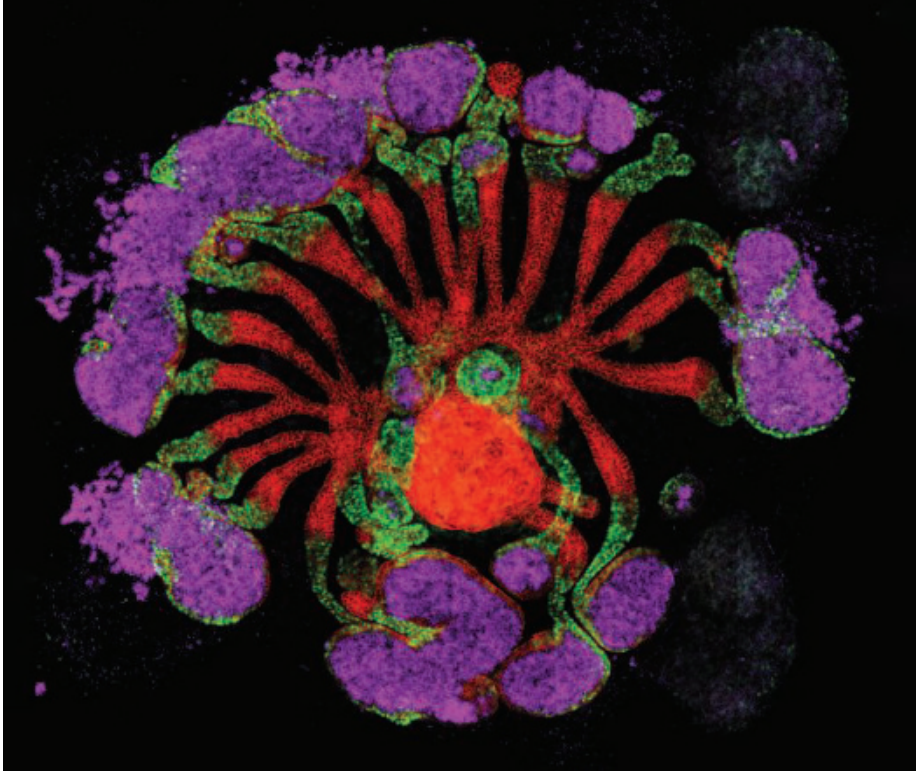

PHOTO: ZHONGWEI LI

Jennifer Mankae (right) with her son Kananelo, who survived a severe group B streptococcus infection after his birth in 2023.

PHOTO: OUPA NKOSI

A SHOT AT SURVIVAL

Fifty years ago, Carol Baker proposed vaccinating pregnant women to save babies from a deadly microbe. Now, the idea is nearing fruition

LESLIE ROBERTS, in Johannesburg

When Carol Baker proposed in the early 1970s that a little-known pathogen was killing newborns at an alarming rate, she was roundly dismissed. After all, she was just a pediatric resident at Baylor College of Medicine, fresh out of medical school, where she was one of two women in a class of 84. Besides, the bacterium she fingered, group B streptococcus (GBS), was not known to be a human pathogen—it caused udder infections in cows. How could it be killing babies? "The microbiologists who knew more said I was mad," she recalls.

Even more preposterous, her colleagues said, was her 1976 proposal that vaccinating women late in pregnancy against GBS might save newborns from the deadly disease. The thalidomide tragedy of the early 1960s was still fresh in people's minds. What if a vaccine harmed the mother or the baby?

But Baker, now 84 years old and retired in Texas, is nothing if not persistent. "No one would listen to me," she says. "It inspired me."

Today, there is no question that GBS is a leading cause of disease and death in infants up to 3 months old. Worldwide, it sickens about 400,000 babies a year and kills at least 91,000, mostly from sepsis, an infection of the bloodstream, and meningitis, an infection of the membranes that protect the brain. Those who survive sometimes suffer lifelong neurodevelopmental impairments. GBS also causes tens of thousands of stillbirths and is implicated in many preterm births.

Baker's ideas about vaccinating pregnant women may soon be vindicated as well. On 25 August, a woman in the United States in her third trimester was the first to receive a shot of Pfizer's candidate GBS vaccine as part of a long-awaited phase 3 trial. A small Danish company called MinervaX is close behind. The World Health Organization (WHO) has called these maternal vaccines an "urgent need."

"A vaccine could have a major, major public

This story was supported by the Pulitzer Center.

health impact"—especially in sub-Saharan Africa, which accounts for more than half of all fetal and infant deaths from GBS, says Shabir Madhi, a vaccinologist at the University of the Witwatersrand (Wits) here. Madhi has conducted pivotal phase 1 and 2 trials for both GBS vaccine candidates.

There are many reasons why it has taken half a century to get to this point, in addition to sexism and fears about vaccinating pregnant women. Vaccine companies initially didn't see a lucrative market, and they have long tussled with regulators about how best to show the vaccine works.

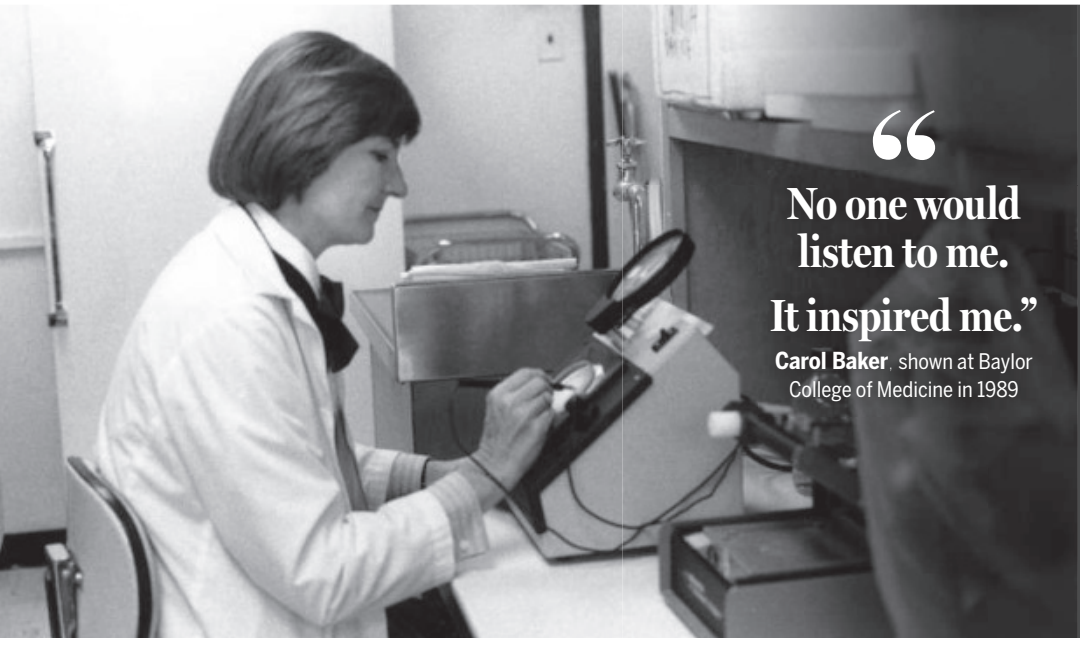

But perhaps the biggest challenge has been that GBS, and its burden, have long remained invisible. Newborns are rarely tested for the bacterium, and stillbirths are often attributed to congenital defects. "People construe an absence of data as an absence of disease," says Madhi, who believes the true toll of GBS is still vastly underestimated.

Colleagues hope a maternal GBS vaccine will become available in Baker's lifetime. Baker, who has been showered with awards and honors, takes an "I'll believe it when I see it" attitude, because lots of things could still go wrong. The saddest part of this journey, she says, is how long it has taken and how many babies could have been saved.

BAKER WAS 6 YEARS OLD when she declared she wanted to be a doctor, after briefly flirting with becoming a firefighter. "You can't be a doctor," her teachers said. "But you can be a nurse."

She entered Baylor at age 22. In an early rotation at a Houston hospital nursery, she saw "beautiful, term babies who within a day or two struggled for breath, turned blue, and died of sepsis or pneumonia," she says. Dogma at the time said the common bacterium *Escherichia coli* was responsible, but when Baker cultured and stained the microbes, a dark blue color revealed they were Gram-positive, ruling out *E. coli*. But "I wasn't allowed to investigate," she says. So she worked nights and weekends, culturing samples from infants and storing the plates in her apartment closet.

The bacterium looked like *Streptococcus*, Baker recalls, but not the familiar group A type that causes strep throat. She suspected group B, a bovine pathogen that had been implicated in disease in a few women in the 1930s. In 1971 she sent 13 cultures to *Streptococcus* expert Rebecca Lancefield, an emeritus professor at Rockefeller University. Twelve turned out to be type III GBS, now known to be the most virulent of the 10 GBS serotypes. Thrilled, Lancefield invited Baker to Rockefeller for a 6-week visit in 1972. It changed Baker's career. "She was my only mentor," she says. Once back in Houston, with a letter from Lancefield, Baker was finally allowed to study GBS: "I was no longer officially blown off."

Soon, GBS was recognized as the single most frequent cause of sepsis and meningitis in U.S. neonates and young infants. It turned out to be a remarkably versatile pathogen, able to attach to the vaginal tract, enter epithelial cells, and invade the placenta and the brain. It can also slip into an infant's bloodstream after it's inhaled or swallowed during delivery.

Globally, about 15% of women carry GBS in their genital tract and rectum, without experiencing symptoms. Babies typically encounter the bacterium during delivery, but a fetus can also become infected in the womb. Baker and two other groups identified two forms of GBS disease in babies: early onset, which occurs in the first 6 days of life and usually manifests as sepsis; and late onset, which strikes between days 7 and 90 after birth and typically results in meningitis, which can lead to severe neurodevelopmental damage. GBS can also cause disease in pregnant women.

Yet only 1% to 2% of children born to women who carry GBS become sick. Baker, working as a postdoc with Dennis Kasper of Boston City Hospital and Harvard University, learned why: Women who had relatively high levels of naturally acquired antibodies against the microbe gave birth to healthy babies. When maternal levels were low, newborns were at risk of disease, their immature immune systems unable to muster protective antibodies for the first few months of life.

The finding suggested a vaccine given late in pregnancy might elicit high levels of maternal antibodies that would protect the baby, Baker and Kasper argued in a now-classic 1976 paper in *The New England Journal of Medicine*. Baker's early work "was the basis of all maternal vaccination," says Kirsty Le Doare, a vaccinologist at St. George's, University of London and a technical adviser to WHO on maternal immunization.

IT TOOK 2 DECADES for Baker and Kasper to devise a workable vaccine. They initially hoped to base it on the capsule encasing the bacterium, composed of repeating sugars, or polysaccharides. The capsule contains a sialic acid, they discovered, a sugar that is recognized by the human immune system and stimulates the production of antibodies. Still, candidate vaccines

PHOTO: BAYLOR COLLEGE OF MEDICINE ARCHIVES

based on the capsule didn't consistently elicit high enough antibody levels in healthy adults.

But they were inspired by the success of a vaccine against another pathogen, *Haemophilus influenzae* type b, which linked its polysaccharide capsule to a protein carrier, resulting in a big immunologic boost. In 1996, Baker, Kasper, and colleagues made a similar "conjugate" vaccine for GBS, coupling the polysaccharide to an inactivated version of the tetanus toxin. It generated an immune response that appeared powerful enough to protect newborns.

But Big Pharma wasn't interested. The market for a one-dose vaccine given only to pregnant women was too small, companies said. And they were worried about liability issues if the vaccine caused complications. "Science did not hold back a vaccine. … We had all the scientific data we needed," Baker says.

Even without a vaccine, the toll of early onset disease began to fall in the 1990s in the U.S., where an increasing number of pregnant women were screened for GBS during the third trimester using vaginal and rectal swabs. Women who were positive received intravenous antibiotics during labor to prevent transmission to the baby (see graphic, right). In 2002, the Centers for Disease Control and Prevention (CDC) called for screening all pregnant women this way.

"The uptake was gratifyingly rapid," says epidemiologist Stephanie Schrag, who led CDC's GBS program for 20 years before retiring in April. Cases of early onset GBS in the U.S. have fallen by more than 80% since the early '90s. "I'm proud of that," says Baker, who was closely involved. Many wealthy countries have adopted the approach.

But it wasn't enough. Protection from antibiotics is short-lived, so the incidence of late onset disease didn't budge. Nor does the screen-and-treat approach prevent stillbirths and preterm births. Perhaps most important, low- and middle-income countries can't afford to test all pregnant women, and many don't have access to neonatal intensive care to keep sick babies alive. All of that means a maternal vaccine—at an affordable price—is urgently needed, Madhi says.

MADHI HAD ALREADY SEEN the power of maternal vaccination against another disease, neonatal tetanus. While training as a pediatrician in the 1980s, he saw many babies dying from the infection, typically acquired from unsanitary delivery instruments. "It was heartbreaking," says Madhi, who directs the Wits Vaccines & Infectious Diseases Analytics Research Unit (Wits VIDA). A global campaign to give pregnant women two doses of a tetanus vaccine in the third trimester caused neonatal tetanus deaths to plummet from about 750,000 in the 1980s to fewer than 50,000 today.

A decade later, Madhi found GBS was stalking South Africa's maternity wards, too. In the first GBS epidemiology study in South Africa, he and colleagues showed it caused three cases of disease per 1000 live births. But journal reviewers were skeptical. "Most scientists are from high-income countries," he says, and thanks to screening, "they weren't seeing the same incidence." The paper finally appeared in 2003.

As Madhi's team and other researchers have shown, rates of GBS

An uneven burden

Group B streptococcus (GBS) sickens about 400,000 babies a year and kills at least 91,000, more than half of them in Africa. South Central and South Asia are hard hit as well. Africa also has the highest burden of stillbirths, premature births, and neurological impairment caused by GBS.

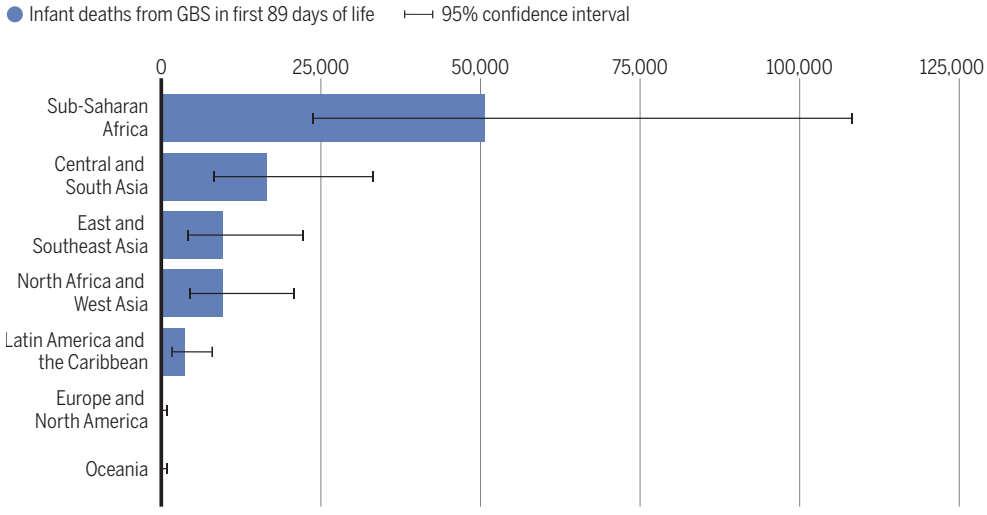

Partial victory

U.S. cases of early onset GBS disease plummeted after the introduction of antibiotic treatment during labor. In 1992, this was recommended for women with risk factors such as preterm labor or membrane rupture. New guidelines in 1996 recommended using this risk-based approach or testing for GBS late in pregnancy and treating women who test positive. In 2002, the latter strategy became standard. Cases of late onset GBS disease have not budged because antibiotics only give short-term protection.

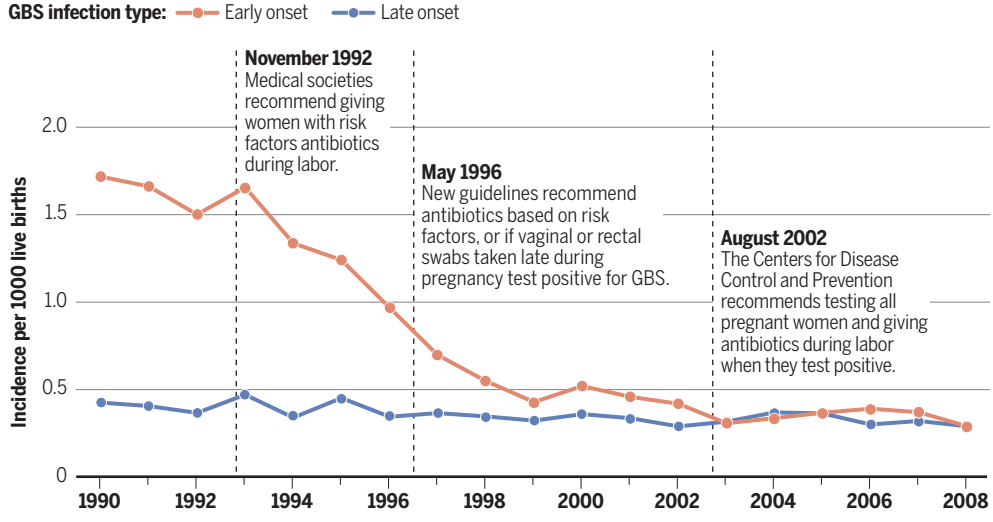

CREDITS: (GRAPHICS) V. PENNEY/*SCIENCE*; (DATA, TOP TO BOTTOM) B. GONÇALVES *ET AL.*, *THE LANCET GLOBAL HEALTH*, 10, 6, E776 (2022); PREVENTION OF PERINATAL GROUP B STREPTOCOCCAL DISEASE REVISED GUIDELINES, CENTERS FOR DISEASE CONTROL AND PREVENTION (2010)

Vaccinologist Shabir Madhi (left) of the University of the Witwatersrand has long studied the toll of group B streptococcus and conducted phase 1 and 2 vaccine trials.

PHOTO: GULSHAN KHAN/*THE NEW YORK TIMES* VIA REDUX

carriage in women and disease in newborns vary widely from country to country, with the highest numbers in sub-Saharan Africa and Central and South Asia. They also vary by region and population group. In the U.S. and other high-income countries, Black women have a higher carriage rate than white women, and their babies have a higher incidence of the disease. What accounts for the variability remains unclear. Meanwhile, the full extent of the damage done by GBS disease is still coming into focus.

ON A MORNING IN LATE MAY in the morgue at the Chris Hani Baragwanath Hospital in Soweto, two members of the Wits VIDA team gown up and lay out their instruments. Then they gently unwrap a baby with a full head of hair who was delivered stillborn the day before. To find out what killed their baby, the parents have consented to a type of autopsy known as minimally invasive tissue sampling.

Palesa Makekeng, a clinical associate, and Keitumetse Sethabela, a research assistant, first measure the body and sterilize it, so as not to introduce any pathogens. Then, with great precision, they insert needles to extract cerebrospinal fluid and blood. Next, they take multiple tissue samples from the liver, the lungs, and the brain. Then they carefully wrap the body and return it to the mortuary refrigerator. The samples will be tested for about 120 pathogens, including GBS, after which an expert panel will determine the cause of death. Just because GBS was present, for instance, does not mean it was the causative agent, Makekeng says.

The work is part of the Child Health and Mortality Prevention Surveillance (CHAMPS) study, funded by the Gates Foundation, which aims to determine the causes of stillbirths and deaths among infants and children under age 5 in nine low- and middle-income countries. It is one of several studies shedding more light on GBS's toll. Earlier studies looked only at wealthy countries, and most mortality estimates ignored stillbirths. "But why should a baby who dies a few days before birth count less than a baby that dies a few days after birth?" asks Joy Lawn, a pediatrician and epidemiologist at the London School of Hygiene & Tropical Medicine (LSHTM).

Lawn and her LSHTM colleague Anna Seale led a study involving some 100 researchers worldwide that provided the first global estimates of GBS's burden. Published in 2017 in a series of papers in *Clinical Infectious Diseases*, the research showed the toll was shockingly high, especially in Africa and South Asia. An update of their analysis, published in *The Lancet Global Health* in 2022, estimated that in addition to 91,000 infant deaths, GBS causes some 46,000 stillbirths a year.

CHAMPS has sharpened that picture. In a study published in 2023, researchers found that overall, 2.3% of stillbirths in the nine study countries were caused by GBS, although the proportion varied from 1.6% in Bangladesh to 8% in South Africa. When they factored in live births as well, the CHAMPS collaborators found that GBS caused one in every 37 deaths of infants less than 90 days old.

The 2022 analysis also suggested GBS is involved in half a million of the roughly 15 million preterm births worldwide—although the authors acknowledged their estimate came "with wide uncertainty," because GBS's exact role in preterm births has been especially hard to untangle. Complications from prematurity are the biggest cause of death for children under age 5, and preterm births can lead to developmental disorders, hearing and vision impairment, underdeveloped lungs, and a higher risk of chronic diseases.

Studies examining GBS's effects on neurodevelopment are ongoing. Kananelo, an impish 1.5-year-old boy, is part of one such study at Wits VIDA. His 20-year-old mother, Jennifer Mankae, says she was terrified when Kananelo was born prematurely in 2023, struggling for breath. He was treated in intensive care for more than 3 weeks. Tests showed he was infected with GBS, which she had never heard of. "I was afraid he was going to die," Mankae says.

Now, Kananelo is playfully dropping his toys on the hospital floor for his mother to pick up. "He is naughty," Mankae says—a troublemaker who causes chaos in the house he shares with his mother and her sister. Mankae is no longer worried about her son's health.

But a recent multicountry study found that children who recovered from GBS disease have a 70% increased risk of some form of neurodevelopmental impairment. Worldwide, an estimated 40,000 survivors develop moderate or severe forms of impairment each year, according to the 2022 analysis, including cerebral palsy and deficits in vision, motor skills, speech, and cognitive function. What was "surprising and unexpected," says co-author Ziyaad Dangor, clinical research director at Wits VIDA, is that these lasting effects, previously thought to be caused exclusively by GBS meningitis, also occur in survivors of GBS sepsis, which is far more common. That means the extent of neurodevelopmental problems has likely been underestimated.

A FAIRLY PRICED MATERNAL vaccine could avert much of this toll, WHO has concluded. Gavi, the Vaccine Alliance, which makes vaccines available to low-income countries, has expressed interest. And anxieties about maternal vaccination have faded. Pregnant women are now routinely vaccinated not just against tetanus (sometimes in combination with pertussis and diphtheria), but also against influenza and, in some places, COVID-19. In May, WHO recommended maternal vaccination against respiratory syncytial virus, which can kill newborns. Still, a GBS vaccine would break new ground. Most of the vaccines now given in pregnancy were already widely used and had established safety records. None was developed specifically to protect the infant.

The Pfizer shot that just entered a phase 3 study is a polysaccharide conjugate vaccine, similar to the one codeveloped by Baker, designed to protect against the six GBS serotypes that cause 98% of cases. The Gates Foundation is supporting the work in exchange for Pfizer's commitment to make an affordable version available to poor countries, Keith Klugman of the Gates Foundation says.

MinervaX, which is developing the other leading contender, decided to bet on a vaccine based on the surface proteins sticking out through the bacterial capsule. CEO Per Fischer says it should be effective against all GBS serotypes, and that the company will offer its vaccine at a price acceptable to Gavi.

Both vaccines have proved safe and able to elicit a strong immune response in phase 1 and 2 trials in healthy adults and pregnant women. But because the incidence of GBS is low, a conventional phase 3 efficacy trial to demonstrate that the vaccine reduces death and disease would need to enroll about 100,000 pregnant women, take a decade, and cost about $1 billion, Klugman estimates. That would be "untenable," says vaccinologist Annaliesa Anderson, who is leading Pfizer's effort.

Instead, the companies and GBS researchers have been pushing for a newer approach to licensure that would use "serological endpoints"—essentially showing the vaccine elicits high enough levels of anti-GBS antibodies to protect infants throughout the first 3 months of life. Such trials require far fewer participants. But regulators at the U.S. Food and Drug Administration and the European Medicines Agency have spent years forging agreement on the exact serological endpoints. "This is a vaccine given during pregnancy using a serological marker" for licensure, Lawn says. "If you're looking for a combination of things that regulators will feel nervous about, this is it." "People want everything to be 100% risk free," Baker says. "They may as well go in a closet."

Last month, regulators finally gave Pfizer the go-ahead for its trial, which will enroll about 6000 healthy, pregnant women between 24 and 36 weeks of gestation and their infants, first in the U.S. and then in South Africa and other countries. The expected completion date is 2029. MinervaX expects to start trials in 2026, Fischer says.

IF A VACCINE is ultimately licensed, Madhi expects many wealthy countries to quickly adopt it. But it will face growing vaccine hesitancy, especially in the U.S. In low- and middle-income countries, where the need is greatest, lack of awareness about GBS may be the key problem. "The case for vaccines for pneumonia and diarrhea was clear. The symptoms are visible," says Wits VIDA epidemiologist Michelle Groome, technical lead for a consortium of African and Southeast Asian countries laying the groundwork for new maternal vaccines. "But GBS is invisible. Babies are stillborn or they die shortly after birth."

Madhi thinks South Africa may be an exception, as studies there have left little doubt about the need: "We have the epidemiology." In other countries, where data are lacking, widespread adoption may depend on the large postlicensure, or phase 4, studies that regulators will require the vaccinemakers to conduct. Those studies will show how much the vaccine truly reduces death and disease, Madhi says.

Obstetricians, midwives, and community health workers will also have to be receptive to a maternal GBS vaccine, and antenatal visits will be critical. Many women in sub-Saharan Africa have only four visits—WHO recommends eight—and go too late in pregnancy for a vaccine to prevent stillbirths and preterm births. Families will have to agree as well. "Moms want to protect their babies," Groome says. "In low-income countries, it's more about community acceptance, what the husband and the mother-in-law think."

GIVEN THE REMAINING challenges, "we have miles to go," Schrag says. But, Le Doare adds, "We have to get a vaccine over the line in Carol's lifetime." Baker is delighted that a younger generation of scientists—many of them women she inspired—have taken on her cause. "I had to crash through a lot of barriers," she says. She still attends meetings, gives talks, and writes papers and editorials. "This is what retirement looks like for Carol," Le Doare says.

On some days, Baker fears her dream will never reach fruition. On others, she is more optimistic. "There has been incredible progress. But it has taken so long." □

Leslie Roberts is a science journalist in Washington, D.C.

Editor's note: *Science* understands some people who become pregnant and give birth do not identify as women. This story uses maternal, mother, and women throughout because those are the terms scientists have used when describing GBS and affected people, and in vaccine studies—including Pfizer's recently launched phase 3 trial.

COMMENTARY

BOOKS ET AL.

REVIEW ROUNDUP

Fall Books 2025

Does humanizing researchers help to combat distrust in science? What factors fuel innovation, and can nations avoid technological stagnation? How should we prepare for smarter-than-human artificial intelligence? From sensible, science-backed advice about nutrition and immune health to thought-provoking lessons from mycology and geology to fictional forays into the near future and the ancient past, the titles on this year's fall reading list investigate questions of survival, community, and connection as pathways to human flourishing. Read on to learn what our reviewers thought of these nine new books publishing this fall. **—Valerie Thompson**

How Progress Ends

Reviewed by **Margaret Linak**[1]

Throughout history, competition—between ideas, individuals, companies, and nations—has fueled innovation and technological advancement. Yet progress is not inevitable, nor is it guaranteed. It ebbs and flows, shaped by the choices that governments and societies make and the systems they build.

In *How Progress Ends: Technology, Innovation, and the Fate of Nations*, economist and historian Carl Benedikt Frey unpacks the complex forces that drive, sustain, or stall innovation. Drawing from a rich historical record, he explores key technological breakthroughs and the enabling environments behind them, deftly contrasting flourishing periods of innovation with stretches of stagnation in order to extract vital lessons from the past that resonate powerfully today. Rather than advocating a single path for progress, he establishes common themes, choices, and their consequences in various regions, from dynastic China to the Prussian Empire, Tsarist Russia, Meiji Japan, and the USSR, applying lessons learned from each time and place to today's global landscape.

Frey begins by illustrating how centralized state power in ancient China catalyzed innovation before eventually stifling it. He then moves through Europe's scientific awakening, the transformative decades of industrialization, and the contrasting paths taken by nations in the 20th century as they navigated the Second Industrial Revolution and the rise of computing. He closes with an exploration of artificial intelligence and the pivotal decisions facing governments today—decisions that will shape whether this new era accelerates global progress or leads to its decline.

What makes *How Progress Ends* especially compelling is Frey's central thesis: The real threat to innovation is not rivalry but rather

ILLUSTRATION: WENJING YANG

inertia. He shows how the very technologies that initially empower states and institutions can later entrench power, discourage competition, and ultimately sow the seeds of stagnation. In this, Frey echoes T. S. Eliot's haunting lines from "The Hollow Men": "This is the way the world ends / Not with a bang but a whimper."

A thoughtful, deeply informed study, *How Progress Ends* is both a historical journey and a warning. It challenges readers to recognize that progress is not self-sustaining and that the choices we make now will determine whether innovation continues or quietly fades away.

How Progress Ends: Technology, Innovation, and the Fate of Nations, *Carl Benedikt Frey*, Princeton University Press, 2025, 552 pp.

The Shape of Wonder

Reviewed by **Adam Shapiro**[2]

Most people do not really know what scientists do, argue Alan Lightman and Martin Rees in their new book, *The Shape of Wonder*. The authors posit that showing that scientists are emotional, curious, awe-inspired human beings just like everyone else will counteract common populist tropes that reject scientific knowledge and foment distrust in science.

The book features biographical vignettes aimed at showing scientists' humanity, ranging from the historical to the present day. For example, an account of the contemporary Polish American CERN physicist Dorota Grabowska hints at the challenges of making a career in the crowded, competitive profession of theoretical physics and the complexity of doing so in a field where women and LGBTQ+ individuals remain severely underrepresented. In this and other modern examples, there are tantalizing glimpses of the humanity of the people who make science happen.

But if the authors' goal is to humanize scientists, one might question their choice to devote so much of the book to Nobel laureates and other famous scientific "heroes" who seem less relatable than more quotidian scientists who make a living without receiving global acclaim. Little new insight is gleaned from these well-studied historical examples, and the authors eschew detailed secondary scholarship that has revealed complexity and nuance to our understanding of these famous figures' lives.

Surprisingly, Werner Heisenberg is used to illustrate the moral complexities of being a scientist. Yet the authors' reflection on his life as the lead scientist for the Nazi atomic bomb project puzzlingly leads them to conclude that science is itself inherently "apolitical" and that "neither science nor technology have moral or ethical values." Furthermore, the authors assert that a rigid compartmentalization between science/technology and ethics/politics accurately describes the scientific enterprise, yet in the space of mere paragraphs, the book shifts to a robust defense of science as a practice that has hastened progress and human flourishing. If this does not represent a form of politics, what does?

Awe evoked by the natural world inspires many researchers, a fact the authors of *The Shape of Wonder* believe can help humanize scientists and restore trust.

In recent years, a growing number of scientists have spoken out against the trope of science's supposed apolitical nature, pointing out that their own career paths, the opportunities and obstacles they have faced, and the way that they understand and interpret their work cannot be separated from the science that they do. Indeed, it seems that acknowledging the personal and the political aspects of the scientific enterprise has helped scientists better connect with wider audiences and foster trust in their work. In this context, *The Shape of Wonder* reads less like a humanization of science and more like an uneasy retrenchment that clings to apolitical platitudes in the face of its own counterexamples.

The Shape of Wonder: How Scientists Think, Work, and Live, *Alan Lightman* and *Martin Rees*, Pantheon, 2025, 224 pp.

All That We See or Seem

Reviewed by **Meryleen Mena**[3]

Ken Liu's *All That We See or Seem* is a timely science fiction thriller that introduces readers to Julia Z, a brilliant and reclusive hacktivist who reluctantly agrees to help a desperate lawyer named Piers track down his missing wife, Elli, a New Age guru with a large following. Elli's work as a "dream artist"—a performer who weaves together audiences' memories into a shared virtual tapestry—has earned her many fans but has also attracted the attention of an international criminal and his minions, who the pair believe are responsible for Elli's disappearance. Along for the ride and, at times, providing comic relief are Julia's personal AI-assistant Talos, her shape-shifting drone Puck, and other futuristic gadgets.

Loss and reconnection are prominent themes in this work, which are compellingly explored as Julia attempts to make sense of the digital traces Elli left behind. It is in seemingly mundane scenarios—when Piers prepares food and coffee for Julia while she works, for example—that Liu demonstrates how we can show up for each other through simple acts of care. The absurd and treacherous situations the pair find themselves in do not drive them apart but rather allow Julia, in particular, to find safety in community. Although Julia's identity as a Chinese American is not central to the plot of this book—the first in a planned series—Liu takes the time to contextualize how xenophobia and anti-Asian bias and discrimination have affected her and her "restless and fearless" mother, a Chinese immigrant.

This is the sort of book a reader can get lost in—not to escape the world but rather to meditate on questions of deep moral significance. As new technologies emerge, Liu invites readers to consider how we might tap into our collective subconscious, meeting ourselves in the places that scare us in order to transform how we show up in the world and relate to each other. Despite her reluctance to interact with others, Julia helps Piers and Elli and other vulnerable people she encounters, making the case that we should fight hard for a human-centered society. Meanwhile, the sadistic, narcissistic despot Liu imagines and the fictional world he envisions, in which atrocities are being televised, live streamed, and posted on social media, may feel uncomfortably familiar. In short, this is a work of speculative fiction with a healthy dose of realism warning us that we must work together to disable possible dystopian futures.

All That We See or Seem, *Ken Liu*, S&S/Saga Press, 2025, 416 pp.

What to Eat Now

Reviewed by **Carolyn Wong Simpkins**[4]

Even with my training as an internal medicine physician and a strong health and science background, I find the messaging and ever-shifting vocabulary surrounding food choices challenging to interpret. In her new book, *What to Eat Now*, Marion Nestle offers expert advice on this topic, presented in such an engaging, lively

PHOTO: DESIGN PICS EDITORIAL/GETTY IMAGES

Food scholar Marion Nestle combines solid science with a deeply informed understanding of public policy to offer readers dietary advice in *What to Eat Now*.

PHOTO: LECHATNOIR/ISTOCK PHOTO

voice that readers will quickly get past any initial trepidation that might have arisen as a result of the book's considerable heft. Nestle has a clear point of view and the expertise to back it up, and she presents the relevant science and public policy history with objectivity, leaving readers to determine which choices fit their values and preferences without judgment.

The book begins with a section called "The Basics," which lays the groundwork and establishes some core vocabulary and concepts useful to subsequent deeper dives. As someone with serious food allergies who has been reading food labels carefully most of my life, this section helped me understand why some categories of foods do not display nutrition facts and the political nuances behind seemingly synonymous terms such as "organic" and "natural," and it provided an objective review of the various types of certifications offered by different organizations.

The core of the book is helpfully organized by food category, explicitly mirroring how foods are organized in the grocery store ("Beverages," "Produce," "Dairy," etc.). In each section, readers will find clear explanations of what all types of food labels mean, how trustworthy they are and why, and what to do about them. Nestle also incorporates the environmental impact of the choices presented, leaving to readers the decision of how heavily to weight this factor.

I found most helpful the sections where Nestle summarized her own approach to selecting among the available options. In the "Meat" section, for example, she lists her personal hierarchy of priorities, with "Certified Organic," "Animal Welfare Approved," and "Natural" topping the list, offering a brief recap on why she chooses this ranking system. Meanwhile, in the "Produce" section, I found her bullet points on product safety clear, reliable, and particularly timely, given recent cuts to so many US regulatory agencies.

Expect a generous dose of food policy discussion sprinkled throughout the book, which is presented in the context of how seriously it affects the information and messaging made available to consumers. Ultimately, readers will leave better equipped not only to interpret the food messaging of today but to look out for the forces that will shape it over time.

What to Eat Now: The Indispensable Guide to Good Food, How to Find It, and Why It Matters, *Marion Nestle,* North Point Press, 2025, 720 pp.

Self-Defense

Reviewed by **Amit Chandra**[5]

In *Self-Defense*, immunologist Daniel Davis frames the human immune system as a linchpin of our health, serving as both the cure and cause—in disorders of autoimmunity—of many diseases. The book treads familiar questions with exceptional sharpness. Do vitamins work? What is the role of the microbiome? What is the impact of weight, exercise, stress, and sleep on human health? How does our immune system change as we age? Each of the book's chapters is prefaced with a widely held health myth or preconception. Davis then explores the relevant immunological pathways, diving into the research, confounding variables, and methodological biases that underlie it.

Take, for example, the chapter on stress. It begins with both the commonsense and scientific basis for the belief that stress weakens your immune system, making various infections more likely and

more severe. Beyond simple advice such as "avoid stress," Davis explores other factors that might help lower circulating levels of the cortisol stress hormone, such as mindfulness exercises, nature walks, and positive psychology interventions.

For each topic, Davis presents a story of twisting lanes driving readers toward actionable ways to optimize immune health. Where the research is limited, he speculates on mechanisms that could underpin or refute common beliefs. In the chapter on longevity, for example, he hypothesizes that chronically elevated cytokine levels are behind the increased incidence of autoimmune diseases and severe infections as we age. Ultimately, each chapter reveals that the human body defies quick fixes. Yes, minimize stress whenever possible, but also exercise, eat a balanced diet, and get eight hours of sleep.

What is missing is a wider focus on the policy and media landscape in which health myths exist. Davis is an ardent believer in the power of vaccines and shares the incredible story of the development of the COVID-19 vaccine and others in the works for cancers, malaria, and HIV. But he fails to address growing vaccine hesitancy and mistrust in science among segments of our society.

Despite this gap, the book succeeds in inoculating the reader against easy health answers, headlines, and platitudes. When it comes to our immune system, as Davis writes, "there's always more to the story."

Self-Defense: A Myth-Busting Guide to Immune Health, *Daniel M. Davis*, University of Chicago Press, 2025, 296 pp.

If Anyone Builds It, Everyone Dies

Reviewed by **Lisa Poggiali**[6]

If Anyone Builds It, Everyone Dies by Eliezer Yudkowsky and Nate Soares is a stark warning and a call to action: Stop building ever-more-complex forms of artificial intelligence (AI) before it is too late. Yudkowsky spent years studying how machines smarter than humans might think and behave, contributing to an area of research known as "AI alignment." The results were sobering, and, together with Soares, he abandoned his work helping to build the first "superintelligent" AI, instead dedicating his efforts to stopping its creation entirely. This book is a contribution to that new direction. Unfortunately, its major conclusions fall far afield of the evidence offered by empirically grounded scientific analysis.

Yudkowsky and Soares's bold plea is rooted in the assertion that engineers will eventually lose control of the AIs that they are training. This is because engineers cannot "create" intelligence, they can only "grow" it through a mathematically guided progression of trial and error. While there is broad agreement that AIs "grown" in this way will behave unpredictably, Yudkowsky and Soares take their argument a step further: The AIs will eventually behave nefariously, and once they surpass human intelligence, human extinction is inevitable.

Foundational to their alarmist idea is a simplistic understanding of intelligence as analytical and disembodied. "Intelligence," for Yudkowsky and Soares, is purely about cognitive horsepower; it relies on the speed and efficiency of data processing. Other critical elements—for example, embodied cognition, the empathy and self-awareness crucial for social skills, cultural embeddedness—are disregarded.

The authors also espouse a functionalist view of human progress, implying that because "superhuman" AIs will not find humans "useful," they will eliminate them. They reference moments in history when one group introduced a new technology to another group, leading to the latter group's elimination—for example, when the Spanish, armed with guns, defeated the Aztecs, equipped with bows and arrows. But history resists their techno-determinist reading; the rise and fall of civilizations has always been shaped by complex systems, not merely by tools or technologies.

The surprisingly banal solution the authors suggest for the problem of superhuman AI is an international treaty and monitoring structure that would regulate all countries' AI development trajectories and limit AI models' efficiency and power. Such a framework could be useful if it were scoped to focus on concrete threats, such as lethal autonomous weapons systems or the climate impacts of energy-intensive data centers. With these parameters in place, it could indeed help curtail the expansion of AI-generated harms in a world increasingly shaped not by rogue AIs with superhuman powers but by all-too-human hubris.

If Anyone Builds It, Everyone Dies: Why Superhuman AI Would Kill Us All, *Eliezer Yudkowsky* and *Nate Soares*, Little, Brown, 2025, 272 pp.

Human hubris often underlies AI-generated harms.

ILLUSTRATION: MOOR STUDIO/ISTOCK PHOTO

Fearless, Sleepless, Deathless

Reviewed by **Bradley G. Lusk**[7]

In *Fearless, Sleepless, Deathless: What Fungi Taught Me about Nourishment, Poison, Ecology, Hidden Histories, Zombies, and Black Survival*, Maria Pinto tells a story that is as much an exploration of mycology as it is an interrogation of Indigenous traditions in the West and a tale of the author's spiritual journey. To accomplish this, Pinto employs a kind of "Gonzo mycology," placing herself at the center of a metaphor that explores how society's loss and subsequent rediscovery of fungus as a force that connects all life is akin to the loss and subsequent rediscovery of Indigenous understandings of the harmony and interconnectedness of life.

In the wake of the 2016 US presidential election, Pinto and most of her friends were descending into existential dread and hopelessness. Rather than lose herself in politics, she made her way into the woods to discover the wonders of nature. It was here that she embarked on her mycological journey and ultimately reconnected with her Jamaican roots.

Fearless, Sleepless, Deathless delivers a well-sourced account of the ways mushrooms and other fungi provide essential nutrients within Earth's root systems that enable much of life to exist as a symbiosis of "messy, communally wired opportunists." Fungi draw nutrients and water from the soil and pass those to trees, protect the roots from pathogens, and use and store carbon produced by trees to enhance the health of the forest. Fungi also parasitize ants, using their bodies to propagate themselves.

Despite their critical role in nature, as with many other Indigenous traditions, mushrooms were denigrated by imperialists, reveals Pinto—frequently feared for their poisoning potential and referred to as "poor man's meat." Here, she draws parallels between mushrooms and her cultural heritage, observing how—in the absence of European judgments—mushrooms and Indigenous traditions are both beautiful and valuable.

Fearless, Sleepless, Deathless challenges the reader to see mushrooms as more than merely an organism to be eaten, seen, or feared. Mushrooms, Pinto argues, are the ever-present ghosts that have borne witness to the past. They are the gateway to understanding the story of civilization, and they are the Gaia that binds us all.

Fearless, Sleepless, Deathless: What Fungi Taught Me about Nourishment, Poison, Ecology, Hidden Histories, Zombies, and Black Survival, *Maria Pinto*, University of North Carolina Press, 2025, 240 pp.

The Whispers of Rock

Reviewed by **Josh Trapani**[8]

In an age dominated by chatbots and dysfunctional politics, we could all benefit from more connection with Earth. In *The Whispers of Rock*, geologist Anjana Khatwa describes how such connections undergird Indigenous societies across the globe and how she has incorporated them into her own life.

The Whispers of Rock includes an impressive range of Indigenous origin stories, beliefs, and cultural practices tied to geological features in Japan, New Zealand, the Black Hills, and other places. At its best, the book recalls Adrienne Mayor's *The First Fossil Hunters* and *Fossil Legends of the First Americans*. But it is hardly revelatory that environment shapes culture. And, unlike Mayor, Khatwa frequently veers toward moralizing. The narrative, with its broad survey of cultures, risks presenting an oversimplified binary: Indigenous populations as sustainably in harmony with Earth, and others as disconnected and exploitative. Khatwa worries, for example, that scientists will resist anything besides a Western scientific view, but I think this underestimates the sense of wonder that animates many researchers.

On the personal side, Khatwa bravely reveals events from her own life—some joyous, others devastating—and how geology provided perspective or solace. I was especially moved by her visit to the Shetani lava flows in Kenya, where—years earlier, as a teenager—her love of geology was kindled as "the barren terrain was transformed by my imagination into churning rivers of lava that flowed over the landscape."

Rocks speak to Khatwa, telling their stories. And in them she sees reflections of humanity's story and her own. Metamorphic rocks, for example, are exposed to intense conditions before emerging transformed and sometimes stronger. Glacial erratics are uprooted and displaced from their places of origin and later deposited as strangers in distant lands.

Reading *The Whispers of Rock* led me to reflect on my own fascination with geology. I first encountered deep time in an undergraduate class in upstate New York. Outside, I saw it reflected in the 400-million-year-old rocks, deposited in a tropical sea, that made up the forested hills around campus. But I did not want or need rocks to reflect my own life. On the contrary, what drew me to geology was how Earth's history transcended human foibles and struggles.

We all see things differently, and I wish *The Whispers of Rock* had been more encouraging and less didactic about how and why to embrace alternative ways of knowing. Surely, reconnecting with Earth and embracing other perspectives can only help us better care for our planet and for ourselves.

The Whispers of Rock: The Stories That Stone Tells About Our World and Our Lives, *Anjana Khatwa*, Basic Books, 2025, 336 pp.

The Indigenous Paiute people believe that the sandstone hoodoos of Bryce Canyon are petrified "Legend People" who were turned into stone for their bad deeds.

PHOTO: INGO ARNDT/MINDEN PICTURES

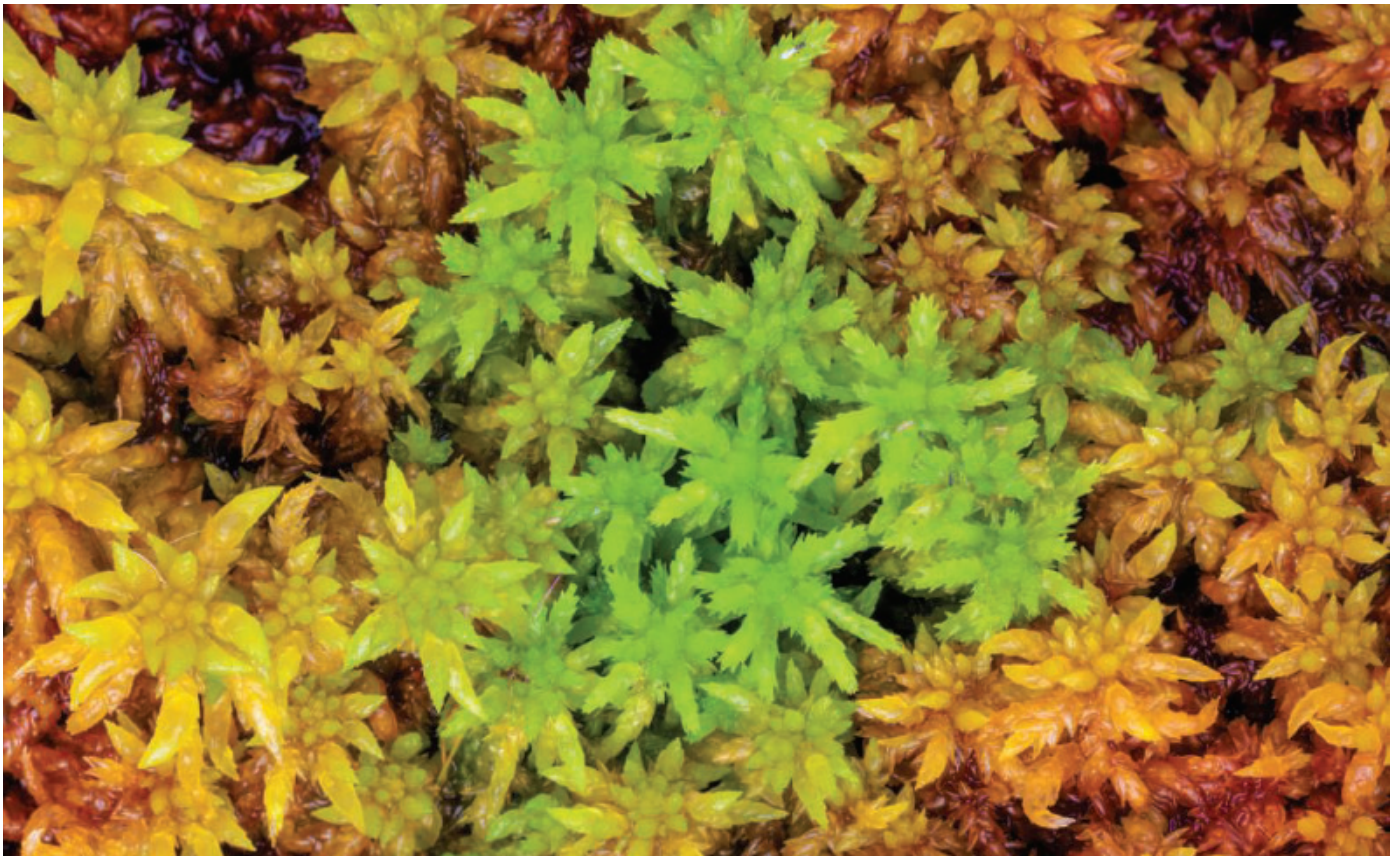

In *Bog Queen*, peat moss helps narrate a fictional mystery featuring a modern-day anthropologist and an Iron Age druid.

Bog Queen

Reviewed by **Rosemarie Szostak**[9]

Bog Queen is a tale of two young women—Agnes, a forensic anthropologist in the 21st century, and an unnamed Iron Age druid—whose paths of personal discovery converge in a mossy English bog. The narrative transitions back and forth in time while alternating between the two main characters' points of view, maintaining momentum throughout. Interspersed are short interludes from the perspective of the bog moss itself, which brings a deep-time perspective to the two humans' stories.

It is 2018, and Agnes has been assigned to identify a body unearthed in the bog during a search for the victim of a 1961 murder. The body is female, but the remains are much older than expected. Intrigued and driven by a deep desire to understand this well-preserved woman's story, Agnes soon becomes invested in identifying her and determining what caused her death. Complicating matters, peat harvesters are suing to continue fuel collection in the bog, which the investigation has temporarily halted, while an environmental group seeks to preserve it and a developer aims to reclaim the land for low- to middle-income housing.

In 50 BCE, the druid—newly anointed and trained in the healing arts by her mother—grapples with her role as a community spiritual leader. She embarks on a journey to Camulodunon, near modern-day Colchester, UK, facing perils along the way. Her greatest challenge, however, comes when she brings back to her people the insights she learned during her trip.

Author Anna North spins a compelling tale of two strong young women as each seeks to carve her niche in worlds 20 centuries apart. Dedicated to their chosen professions, both of the book's protagonists must deal with political turmoil, greed, and conflicting ideologies. Their stories diverge as one ends up dead in an English bog and the other searches to understand why. However, the book's ending—which is both satisfying and memorable, albeit somewhat rushed—entwines the two women forever.

Bog Queen combines the genres of forensic anthropology with historical fiction and a touch of eco-fiction—a challenge that the author handles admirably. Missing are rich details about the characters and their habits, making it difficult, at times, for the reader to relate to them. The bog moss, however, is lovingly described and adds a unique perspective to the story.

Bog Queen, *Anna North*, Bloomsbury, 2025, 288 pp.

10.1126/science.aeb4192

[1]The reviewer is a science policy adviser based in Washington, DC, USA. Contact: www.linkedin.com/in/maggie-linak [2]The reviewer is an independent scholar based in Lancaster, PA, USA. Email: adam256@gmail.com [3]The reviewer is at the Department of Latin American and Latino Studies, The City College of New York, New York, NY, USA. Email: drmm2037@gmail.com [4]The reviewer is a physician and molecular biologist based in Washington, DC, USA. Email: carolyndca@gmail.com [5]The reviewer is an emergency physician and global public health specialist based in Washington, DC, USA. Email: amit.chandra@georgetown.edu [6]The reviewer is at the International Foundation for Electoral Systems, Arlington, VA, USA. Email: lpoggiali@ifes.org [7]The reviewer is at Science The Earth, Phoenix, AZ, USA. Email: sciencetheearth@gmail.com [8]The reviewer is a writer based in Silver Spring, MD, USA. Email: jtrapani@hushmail.com [9]The reviewer is at the Innovation and IP Management Group, Nerac Inc., Tolland, CT, USA. Email: rszostak@nerac.com

ELECTROCHEMISTRY

Solid-state hydrogen storage goes electric

Electrochemistry enables reversible storage and release of hydrogen gas in a metal hydride

Ryan O'Hayre[1] and **Sossina M. Haile**[2]

Broad adoption of hydrogen as a versatile energy carrier is primarily hampered by a lack of safe and compact hydrogen storage. Hydrogen is often stored as compressed gas or cryogenic liquid, which requires high pressures or extremely low temperatures. Metal hydrides—compounds in which hydrogen is chemically bonded to solid metallic or intermetallic hosts—can store hydrogen with a high volumetric density (*1*). The inherent thermodynamic stability of these solid-state storage compounds provides safety but also requires impractically high temperatures for hydrogen release. On page 1252 of this issue, Hirose *et al.* (*2*) report an approach that electrochemically "pumps" hydrogen in the form of hydride ions (H^-) through a solid electrolyte into or out of a metal hydride. This elegantly circumvents the requirement of high temperature to free hydrogen from the metal hydride, offering a pathway to harness high-capacity hydrogen storage under practical release conditions.

Using electricity rather than temperature or pressure to drive hydrogen exchange between electrodes was first practically demonstrated in 1985 to investigate metal hydride thermodynamics (*3*). The Nernst equation—a central formula for calculating electrochemical cell potential under a given condition—also illustrates how a small voltage equates to many orders of magnitude change in hydrogen gas pressure, generating a large driving force for hydrogen exchange. For example, a small cell potential of 0.3 V is equivalent to a pressure of 1.4×10^{10} atm. However, using this thermodynamic driving force requires an ion-conducting electrolyte that is electronically insulating. Decades of work on hydride-ion conductors have underscored the difficulty in achieving this goal (*4*).

Hirose *et al.* developed a solid electrolyte by compositional tuning of a pseudo-ternary system in which barium, calcium, and sodium atoms form a compound with hydrogen atoms. This electrolyte exhibited good hydride ion conductivity (~2×10^{-5} S/cm) at room temperature, low electronic conductivity (1.3×10^{-9} S/cm), and stability over a suitably wide voltage range. The hydride-conducting electrolyte was sandwiched between a hydrogen-storage electrode and a counter electrode that delivered hydrogen gas to a reservoir (see the figure). This solid-state electrolyte could reversibly insert and extract hydride ions into and out of a diverse array of metal hydrides (such as TiH_2, MgH_2, $NaAlH_4$, $LiAlH_4$, $NaBH_4$, and NaH) at moderate temperatures (60° to 100°C). Notably, magnesium hydride and sodium aluminum hydride electrodes achieved reversible hydrogen adsorption capacities that are close to their theoretical values, maximizing the full storage potential offered by these materials. At 90°C, the electrochemical cell with a magnesium hydride electrode achieved reversible hydrogen storage over 10 cycles (charge and discharge) at >99% of theoretical capacity (~2020 mA·hour/g), although at rather low charge and discharge rates. This achievement demonstrates the feasibility of the electrochemical approach to metal hydride hydrogen storage.

The study of Hirose *et al.* opens new directions to overcome the impractically high temperature requirements imposed by high-capacity metal hydride–based hydrogen-storage systems. Magnesium hydride has a theoretical gravimetric hydrogen-storage capacity (the amount of hydrogen that can be held per total mass) of 7.6 wt %, and much of this capacity was successfully accessed. However, the overall electrochemical cell configuration achieved a capacity of only 0.11 wt %. This is due, in part, to the thick, heavy solid-electrolyte layer (~450 μm) and a low active material ratio (20 wt % metal hydride) in the electrode. Furthermore, Hirose *et al.* acknowledged that voids in the cold-pressed solid electrolyte permit hydrogen-gas crossover. This leakage leads to a mixed storage mechanism in which the desired electrochemical hydride-ion insertion occurs simultaneously with an uncontrolled thermochemical reaction between the permeated hydrogen gas and the magnesium hydride electrode. The energy efficiency of the electrochemical system is also presently lower than that of thermal methods. The device of Hirose *et al.* required an energy input of ~81 kJ/mol, which is higher than that for optimized thermal desorption of hydro-

Electrochemical delivery of hydrogen

Metal hydrides can store hydrogen safely with a large volumetric density, but their inherent stability requires impractically high temperatures to release the stored hydrogen for use. A solid-state electrolyte can reversibly insert or extract hydrogen from the hydride at moderate temperatures (60° to 100°C) under an electric potential.

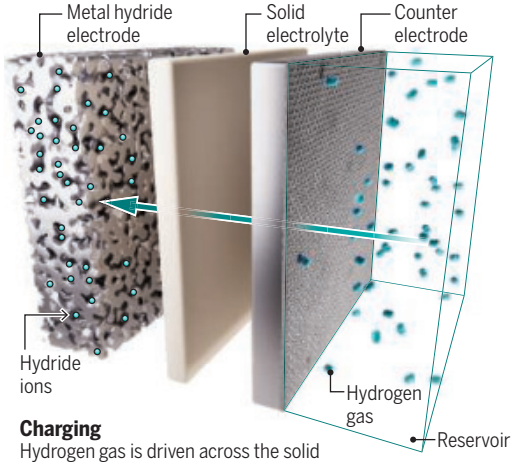

Charging
Hydrogen gas is driven across the solid electrolyte as hydride ions, which are inserted into the metal hydride electrode for storage.

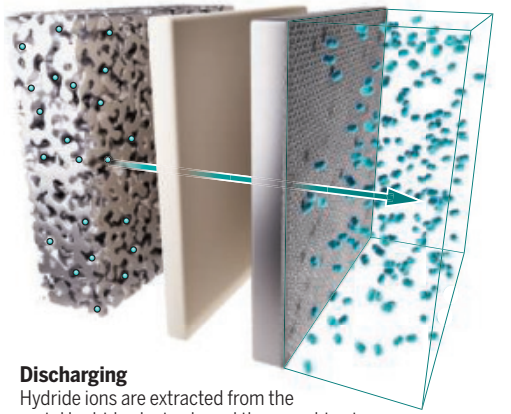

Discharging
Hydride ions are extracted from the metal hydride electrode and then combine to form hydrogen gas at the counter electrode.

GRAPHIC: N. BURGESS/*SCIENCE*

gen (~72 kJ/mol). The authors note that further engineering of the constituent materials and the electrochemical device (such as by decreasing the electrolyte thickness) could substantially reduce the voltage needed for charging, potentially decreasing the energy requirement down to ~45 kJ/mol, which is considerably lower than that for thermal-based metal hydride storage.

Practical deployment of hydrogen storage systems will require durability for >1000 cycles. Electrodes change their volumes as hydrogen atoms move in and out. At present, maintaining the chemical and mechanical stabilities of electrodes and their interfaces with electrolytes under the practical number of cycles remains unproven and is a crucial area for future research. In addition, thermal management, which is also problematic for conventional temperature- and pressure-based metal hydride storage, is an essential aspect that needs to be considered for a large-scale electrochemical system (*5*). Hydrogen absorption is strongly exothermic (heat releasing), whereas desorption is endothermic (heat absorbing). For fast fueling of hydrogen gas, heat must be ejected at tens of kilowatts per kilogram of hydrogen gas during charge and supplied at a similar rate during discharge. Complex device-level heat management strategies such as fin and foam structures integrated into the metal hydride electrode, embedded heat-exchange tubes, and heat-pipe and phase-change augmentation have been reported (*6*). However, these additions increase the weight of the device and reduce gravimetric and volumetric hydrogen-storage densities.

Beyond the electrochemical approach of Hirose *et al.*, other promising directions to improve metal hydride–based hydrogen storage are under active exploration. These include nanostructuring the metal hydride particles to enhance the kinetics of hydrogen adsorption and desorption (*7*) and engineering the composition of the metal hydride to address the trade-off between capacity and stability (*8*). Although many hurdles need to be overcome, ongoing studies offer a credible and exciting proposition: By taming hydrogen in a solid state, a critical component to a future sustainable energy source could be unlocked. □

REFERENCES AND NOTES

1. E. Nemukula, C. B. Mtshali, F. Nemangwele, *Int. J. Energy Res.* **2025**, 6300225 (2025).
2. T. Hirose *et al.*, *Science* **389**, 1252 (2025).
3. C. M. Luedecke, G. Deublein, R. A. Huggins, *J. Electrochem. Soc.* **132**, 52 (1985).
4. S. Sun *et al.*, *Mater. Adv.* **4**, 389 (2023).
5. J. B. Hardy, S. N. Gamble, *Int. J. Hydrogen Energy* **62**, 148 (2024).
6. V. K. Kukkapalli, S. Kim, S. A. Thomas, *Energies* **16**, 3444 (2023).
7. V. Bérubé, G. Radtke, M. Dresselhaus, G. Chen, *Int. J. Energy Res.* **31**, 637 (2007).
8. J. J. Vajo, T. T. Salguero, A. F. Gross, S. L. Skeith, G. L. Olson, *J. Alloys Compd.* **446**, 409 (2007).

ACKNOWLEDGMENTS

R.O. and S.M.H. acknowledge support through the Hydrogen in Energy and Information Sciences (HEISs) EFRC, an Energy Frontier Research Center funded by the US Department of Energy, Office of Science, Basic Energy Sciences, under award no. DE-SC0023450

10.1126/science.aeb3327

[1]Department of Metallurgical and Materials Engineering, Colorado School of Mines, Golden, CO, USA. [2]Department of Materials Science and Engineering, Northwestern University, Evanston, IL, USA. Email: rohayre@mines.edu; sossina.haile@northwestern.edu

GENOMICS

Genomic clues into the spread of deadly mosquitoes

Ancient and more recent human interactions shape mosquito vector evolution

Tamar E. Carter

Vector-borne diseases threaten 80% of the world's population (*1*). At the top of the list is malaria, of which there are roughly 260 million cases each year (*2*), and dengue, which is present in 132 countries (*3*). As the world becomes more connected, populations of mosquitoes that were once geographically confined are now being transported long distances and adapting to new environments. Genomic data from present populations can be used to reconstruct the evolutionary and demographic history of lineages of mosquito vectors. These reconstructions can facilitate prediction of the movement and adaptation of modern mosquito populations and the development of interventions to prevent the spread of disease. On pages 1209 and 1208 of this issue, Boddé *et al.* (*4*) and Crawford *et al.* (*5*), respectively, report findings on the evolution of two mosquito vectors. Their results highlight the population health consequences of ancient and contemporary interactions between humans and deadly mosquitoes.

The *Anopheles funestus* species of mosquito is a major malaria vector across sub-Saharan Africa. Most studies on the evolution of malaria-transmitting *Anopheles* species have centered on the *Anopheles gambiae* species group, and important gaps in knowledge remain for *An. funestus*, a dominant vector in parts of east and southern Africa. Previous investigations have sought out the molecular basis of adaptations to environmental factors and vector control measures such as insecticides using targeted sequencing of limited regions of the genome, karyotyping (which detects chromosomal abnormalities), or whole-genome sequencing of limited geographic scope. High frequencies of insecticide-resistance mutations have been reported in this species (*6*), and structural variants such as chromosomal inversions have been linked to variable ecological conditions and adaptation (*7*), as observed in other malaria vectors.

To examine the molecular basis for adaptation in *An. funestus* at high genomic, spatial, and temporal resolutions, Boddé *et al.* analyzed mosquito genomes from 13 African countries to determine the level of connectivity across *An. funestus* populations and identify genomic loci affected by selective pressure. They found that the genetic diversity of many populations was structured by geography, whereas others appeared to be genetically connected across wide geographic distances. Notably, populations in the North Ghana and South Benin cohorts were more genetically distinct from neighboring populations than expected. Boddé *et al.* argue that these findings suggest the existence of distinct ecotypes (i.e., highly divergent lineages) within *An. funestus*. Such complex patterns of diversity mean that a universal strategy for vector control of this species would likely be ineffective and that such efforts should include locally tailored surveillance and intervention.

Boddé *et al.* also sequenced samples from museum specimens of *An. funestus* collected in 1927, before heavy insecticide use. Using these older specimens as a baseline, the authors found that insecticide resistance had emerged through the independent evolution of resistance mutations in some populations and importation in others.

The *Aedes aegypti* mosquito, a vector for dengue and chikungunya, has spread to new geographical regions over the past several decades.

PHOTO: EDOM BERHANE SEYOUM

These findings are critically important for identifying populations to prioritize for vector control efforts and solidify the need for targeted vector control approaches. One such approach is a vector gene drive, which uses gene editing to rapidly introduce traits such as pathogen incompatibility and/or infertility into mosquito populations, with the goal of reducing disease transmission. Boddé *et al*. were able to identify gene-drive target sites within the *An. funestus* genome.

Over the past several decades, there has been a geographic expansion of arboviral diseases such as dengue and chikungunya within the Americas, Africa, Europe, and Asia. The mosquito vector for these diseases, *Aedes aegypti*, has also emerged in new areas and reemerged in previously eradicated areas during the same time frame, but the role that the *Ae. aegypti* invasion has had in the spread of dengue and chikungunya is not yet clear. Two *Ae. aegypti* subspecies exist, which are distinguished by morphological, behavioral, and genetic characteristics (*8*, *9*). *Ae. aegypti formosus* is a forest-dwelling, generalist that evolved in Africa. *Ae. aegypti aegypti*, which is characterized by an affinity for human hosts and dwellings, evolved later from *Ae. aegypti formosus*, and was introduced to the Americas during the trans-Atlantic slave trade (*10*). The globally invasive *Ae. aegypti* is of the human-adapted subspecies, but the location of its evolution is disputed. The presence of *Ae. aegypti aegypti* ancestry among some African populations and *Ae. aegypti formosus* ancestry in the Americas (*11*, *12*) raises the question of where the globally invasive human-adapted *Ae. aegypti aegypti* evolved, in Africa or the Americas?

Crawford *et al*. conducted a comprehensive genomic investigation of the evolutionary origin of the invasive form of *Ae. aegypti*. To resolve the major challenge of distinguishing signals of ancient and contemporary migration events, the authors compiled *Ae. aegypti* genomes from 73 geographically distinct populations from around the world. The results confirmed previous findings that the two *Ae. aegypti* subspecies are genetically distinct but that mixed populations exist in both Africa and the Americas. As a critical step to determine the origin of the invasive form, Crawford *et al*. combined coalescent and phylogenetics analyses to determine the timing of the split between the oldest *Ae. aegypti aegypti* lineages (i.e., proto *Ae. aegypti aegypti*) in the Americas and those in Africa and revealed a split coinciding with the trans-Atlantic slave trade. They also estimated the timing of the split between proto *Ae. aegypti aegypti* and invasive *Ae. aegypti aegypti* and revealed a broad temporal range of possible splits between populations.

Putting these puzzle pieces together, Crawford *et al*. tested two demographic models to find the one that best fit the data from four representative populations. The "one-emigration" model involves a "stepping-stone" progression with a single introduction of proto *Ae. aegypti aegypti* (i.e., the Americas as the origin of invasive *Ae. aegypti aegypti*). The "two-emigration" model involves both proto and invasive *Ae. aegypti aegypti* emigration to the Americas (i.e., an African origin of invasive *Ae. aegypti aegypti*). The model with the best fit supported a single emigration out of West Africa into the Americas during the trans-Atlantic slave trade, which means that invasive *Ae. aegypti aegypti* originated in the Americas. These findings are important because they provide a historical framework for identifying the genomic basis of the adaptations that helped the invasive mosquito spread across the globe. Genome scans for signatures of positive selection revealed that during its expansion in the Americas, invasive *Ae. aegypti* adapted to new viruses and food sources. Additionally, Crawford *et al*.'s analysis revealed evidence of interbreeding between invasive *Ae. aegypti aegypti* and native *Ae. aegypti formosus* in Africa within the past several decades, which coincided with an uptick in dengue outbreaks, and a higher frequency of a specific type of mutation that confers resistance to insecticides (knockdown resistance mutations). The potential tie between invasive *Ae. aegypti aegypti* in Africa, dengue outbreaks, and insecticide resistance highlights the impact that invasive vectors can have on local transmission dynamics.

Both Boddé *et al*. and Crawford *et al*. provide important insights into the ancient and more recent evolution of mosquito vectors and the complex role that human activity, both passive and intentional, plays in their movement and adaptations. These processes have led to complex subspecies genomic diversity that likely translates to functional diversity that is yet to be fully elucidated. The next steps involve uncovering the evolutionary history of mosquito vectors in West Asia and the Horn of Africa, particularly in areas with highly active ground and maritime trade traffic and a history of invasive mosquito species such as *Anopheles stephensi* (*13*). With the plethora of vector genomes now available and evidence of adaptation to new microbial environments provided by Crawford *et al*., future work should home in on the impact of vector genomic variation on local pathogen transmission and evolution. This question becomes increasingly important in the context of on-going mosquito vector invasions (*14*). Building evidence of the functional relevance of candidate loci identified as being under selection could guide the development of vector control measures to combat the further spread of deadly mosquitoes. □

REFERENCES AND NOTES

1. World Health Organization (WHO), Updated WHO guidance for controlling vector-borne diseases through indoor residual spraying (2024); https://www.who.int/news/item/15-02-2024-updated-who-guidance-for-controlling-vector-borne-diseases-through-indoor-residual-spraying.
2. WHO, "World malaria report 2024: Addressing inequity in the global malaria response" (WHO, 2024).
3. WHO, Vector-borne diseases (2024); https://www.who.int/news-room/fact-sheets/detail/vector-borne-diseases.
4. M. Boddé *et al*., *Science* **389**, eadu3596 (2025).
5. J. E. Crawford *et al*., *Science* **389**, eadu8846 (2025).
6. J. O. Odero *et al*., *Mol. Ecol.* **33**, e17542 (2024).
7. D. Ayala *et al*., *Mol. Biol. Evol.* **28**, 745 (2011).
8. P. F. Mattingly, *Ann. Trop. Med. Parasitol.* **51**, 392 (1957).
9. J. E. Brown *et al*., *Proc. Biol. Sci.* **278**, 2446 (2011).
10. J. R. Powell, A. Gloria-Soria, P. Kotsakiozi, *Bioscience* **68**, 854 (2018).
11. J. Soghigian *et al*., *Mol. Ecol.* **29**, 3593 (2020).
12. J. E. Crawford *et al*., *BMC Biol.* **15**, 16 (2017).
13. Y. A. Baheshm *et al*., *Parasit. Vectors* **17**, 507 (2024).
14. I. Gunarathna, J. D. Spear, T. E. Carter, *Parasit. Vectors* **17**, 530 (2024).

ACKNOWLEDGMENTS

The author thank C. Mulligan, E. Waymire, I. Gunarathna, and B. Oriyomi for their feedback and M. Chembars for facilitating photography.

10.1126/science.aea9024

[1]Department of Biology, Baylor University, Waco, TX, USA. Email: tamar_carter@baylor.edu

SEISMOLOGY

Deep down in the fault zone

Distant seismic waves provide clues to the evolution of crustal structure after a large earthquake

Alba M. Rodriguez Padilla

Tectonic stresses are transmitted to a fault through the surrounding fractured and altered rock, or fault zone. Measuring how seismic velocities (wavespeeds) behave in a fault zone offers a rare insight into the properties and deformation mechanisms operating within it. However, most wavespeed monitoring methods only resolve velocity changes at very shallow depths (<5 km below the surface). This constraint has obscured the deeper parts of fault zones where earthquakes initiate and grow. On page 1256 of this issue, Bryan *et al.* (*1*) report the evolution of seismic velocities from 0 to 20 km below Earth's surface around a fault zone by using teleseismic receiver functions. This approach could help scientists understand the processes that operate deep within a fault zone.

This approach could help scientists understand the processes that operate deep within a fault zone.

The speed at which seismic waves travel through Earth's crust depends on the properties of its constituent materials. Seismic waves travel more slowly through fractured rocks than intact ones. Consequently, a low-velocity zone around a fault is interpreted as the fractured and altered rocks in a fault zone. Wavespeed interferometry techniques often rely on local earthquakes or anthropogenic sources to image the shallow structure of a fault zone, losing resolution at depth. Alternatively, seismograms can record teleseismic waves from distant earthquakes (more than 1000 km away from a receiver). The fastest of these waves arrive from beneath Earth's surface and provide information about crustal structure from the bottom up.

Bryan *et al.* exploited seismic waves from distant earthquakes, which split apart and reverberate in the crust near the surface after crossing much of Earth's interior. This approach, called teleseismic receiver functions (*2*), was used to image the fault zones that produced the 2019 Ridgecrest earthquakes in California (*3*–*5*). Because the receiver functions are uniformly affected by depth-dependent seismic velocity changes, they can be used to track how wavespeeds evolve over a large depth range without losing resolution. Receiver functions resolved changes in seismic velocities from Earth's surface to depths of >20 km at Ridgecrest. The authors documented a rapid wavespeed decrease immediately after the earthquakes in the shallow crust, which returned to the pre-earthquake velocities. This was consistent with previous observations that showed a fast reduction in wavespeeds and subsequent recovery to velocities that were observed prior to the earthquake in the top 5-km section of the fault zone (*6, 7*). These results have been interpreted as rapid healing of fractured rock and fluid flow in the crust.

The lower parts of the crust (10 to 15 km below the surface) tell a different story. A gradual, months-long decrease in seismic velocities was observed. This drop persisted for more than 3 years after the earthquake. At 10 to 20 km below the surface, rocks transition from being cold and brittle to being hot enough to "flow" in response to deformation. The decrease in speed and subtle directional dependence of seismic waves (seismic anisotropy) suggest that fluid-mediated brittle deformation (*8*) could also occur in the lower crust after an earthquake. These observations may capture how the deformation processes inferred from the rock record of exhumed faults (*9*, *10*) evolve over time.

The study of Bryan *et al.* leaves open questions about the fate of deformation in the earthquake cycle, the cyclical accumulation of stress on a fault zone and release during earthquakes. The authors suggest two possible scenarios. Velocities may eventually recover as stress accumulates in the fault zone during the interseismic period (when strain is accumulating on the fault). Conversely, if these perturbations persist, they may represent permanent deformation of the fault zone at depth. The Ridgecrest fault zone is in its early stage of geological development (*11*). Immature faults generate unusually broad zones of deformation during earthquakes (*12*). If a large extent of this deformation is permanent, immature faults may substantially weaken even during a single earthquake.

For the Ridgecrest fault zones, only time will tell which one of the two scenarios occurs. However, other fault zones could serve as natural laboratories to probe these questions. The faults that hosted the Landers and Hector Mine earthquakes in California in the 1990s are in their later postseismic period. If seismic velocities in the lower crust are starting to recover along those faults, it could indicate that wavespeed evolution tracks stress during the earthquake cycle. Additionally, geophysical imaging shows the presence of low-velocity zones in many major faults. For example, the Calico fault in California's Mojave desert features a prominent low-velocity zone, which suggests that brittle deformation processes could persist for centuries after an earthquake (*13*). The more mature Garlock fault in California has a narrow low-velocity zone (*14*). Receiver functions require teleseismic earthquakes that are bigger than a magnitude of 5 (*2*). With more than 1500 such events annually around the world, the structure of other continental fault zones, subduction zones, and volcanoes awaits. □

REFERENCES AND NOTES

1. J. Bryan *et al.*, *Science* **389**, 1256 (2025).
2. J. Bryan, W. B. Frank, P. Audet, *Geophys. J. Int.* **234**, 1282 (2023).
3. Z. E. Ross *et al.*, *Science* **366**, 346 (2019).
4. D. J. Ponti *et al.*, *Seismol. Res. Lett.* **91**, 2942 (2020).
5. X. Xu *et al.*, *Science* **370**, 605 (2020).
6. H. Qiu *et al.*, *J. Geophys. Res. Solid Earth* **126**, e2021JB022043 (2021).
7. Y. Lu, Y. Ben-Zion, *Geophys. J. Int.* **228**, 620 (2022).
8. C. A. Trepmann, B. Stöckhert, *Solid Earth* **4**, 263 (2013).
9. J. A. Nüchter, B. Stöckhert, *J. Struct. Geol.* **29**, 1445 (2007).
10. R. H. Sibson, *Annu. Rev. Earth Planet. Sci.* **14**, 149 (1986).
11. D. E. Goldberg *et al.*, *Geophys. Res. Lett.* **47**, 3 (2020).
12. C. Milliner, J. P. Avouac, J. F. Dolan, J. Hollingsworth, *Nat. Geosci.* **18**, 793 (2025).
13. E. S. Cochran *et al.*, *Geology* **37**, 315 (2009).
14. J. Atterholt, Z. Zhan, Y. Yang, W. Zhu, *J. Geophys. Res. Solid Earth* **129**, e2024JB028900 (2024).

ACKNOWLEDGMENTS

The author thanks T. Lowry, A. Ault, K. Dascher-Cousineau, and A. Reid-McLaughlin for valuable discussions.

10.1126/science.aeb0721

Department of Geosciences, Utah State University, Logan, UT, USA.
Email: alba.rodriguez@usu.edu

The Turkana people live a nomadic, pastoral lifestyle in a water-limited environment.

PHOTO: SOPA IMAGES/GETTY IMAGES

EVOLUTION

Trade-offs and human adaptation at the extremes

Genomic analyses of Turkana pastoralists identify variants that increase water retention

Katherine McVay[1] and **Amy Goldberg**[2]

Despite being genetically homogeneous compared with other animals, humans are geographically diverse and have evolved to meet the demands of local environments, pathogens, and diets (*1*). In 1962, James Neel proposed that genes that predispose people to metabolic diseases may have been advantageous in the evolutionary past (*2*). Yet empirical support for his hypothesis remains limited. On page 1246 of this issue, Lea *et al.* (*3*) report genomic analyses of samples from the Turkana people in northwest Kenya that reveal a more nuanced narrative. The Turkana have practiced nomadic pastoralism (raising and herding of livestock) in extreme arid environments for ~5000 to 8000 years. The authors analyzed 367 genomes and discovered adaptations to ecological pressures, particularly chronic water scarcity. They identified physiological compromises in kidney function that improved water retention but mildly increased the amounts of urea in the blood. This context-specific trade-off may become pathological as Turkana populations urbanize.

Although phenotypic adaptation in humans has long been of interest, the increasing availability of genomic data from global populations over the past 20 years has allowed the identification of specific genes underlying these adaptations. For example, high-altitude tolerance in Tibetans is associated with variants in endothelial PAS domain protein 1 (*EPAS1*), whereas Andean populations adapted to

similar environments with variants in egl-9 family hypoxia inducible factor 1 (*EGLN1*) (*4*), and the ability of pastoralist populations to digest lactose into adulthood is associated with variants in the enhancer region of the lactase gene (*LCT*). These classic textbook examples are often presented as triumphs of natural selection, exemplifying how evolution crafts precise solutions to environmental challenges. However, as ongoing research expands the available genomic and environmental datasets, even these textbook cases are proving more complex than previously considered. When probed, the variants in *EPAS1* were found to come from interbreeding between human ancestors and Denisovans, another ancient hominin species (*5*); the variants in *EGLN1* were found to increase risk for carviovascular, metabolic, and pregnacy-related illnesses; and lactase persistence appeared long after Europeans were already exploiting dairy (*6*). These findings suggest that human adaptation rarely follows simple narratives of optimal solutions to environmental challenges at the expected times.

Lea *et al.* worked with Turkana communities to investigate their adaptation to extreme arid environments (*3*). The Turkana are a pastoral people who rely heavily on animal products to meet their daily nutritional needs, but the majority continue to meet the Western clinical definition of dehydration. The authors combined population genetic data from multiple East African populations with urine samples, interview data, and experiments in mouse models to investigate evidence of natural selection in individuals living in the arid, water-limited environment of the Turkana. Three methods of detecting positive selection identified a candidate region around the stanniocalcin 1 gene (*STC1*). Within this region, two variants were associated with an increase in the urea content of urine, which is a biomarker of kidney function. The authors also found that STC1 protein levels were higher in kidneys from mice with restricted water intake compared with controls. This suggests an association between *STC1* and kidney function under dehydration stress.

Previous genome-wide association studies (GWASs) implicated *STC1* in kidney function in humans, and overexpression of the gene in mouse models reduces acute kidney injury through activation of adenosine monophosphate–activated protein kinase (AMPK) (*7*, *8*). Lea *et al.* demonstrated that vasopressin (antidiuretic hormone released during dehydration to promote water reabsorption by the kidneys) induces an overexpression of *STC1* in human kidney cells exposed to water-restricted environments. Although the exact mechanism and variant under selection in the Turkana are not known, the role of overexpressed *STC1* in protecting against acute kidney injury in mice suggests that loci controlling expression of *STC1* may have a protective role in humans experiencing dehydration.

Notably, Lea *et al.* also identified *STC1* as under selection in another population from the Turkana region, the Daasanach. The Turkana and the Daasanach both inhabit an arid, water-limited environment, but they have their origins in separate migrations out of the Nile Valley around 5000 to 8000 years ago. Demographic inference to test the evolutionary history of the identified variants around the *STC1* gene (haplotype) showed that it was likely present in East Africa before the split of the Nilotic (Turkana) and Eastern Cushitic (Daasanach) lineages in these migrations out of the Nile Valley. This provides historical evidence that further strengthens the association of the haplotype with the arid ecology of the region.

Although large-effect genes underlying human adaptations comprise a tiny portion of the genome, they carry outsized research and public interest. It is rare to identify single genes with large effects on human phenotypes (*9*). Using data from the UK Biobank to identify which genetic variants affect metabolic traits in Europeans, Lea *et al.* then checked whether these same variants showed evidence of selection in the Turkana. Variants that affect the amount of cholesterol and triglycerides in the blood and biomarkers of kidney function in European populations were disproportionately under selection in the Turkana population compared with random genomic regions. This comparison revealed that the adaptation of the Turkana people to their environment involved metabolic compromises throughout the genome, with hundreds of small genetic changes collectively shifting metabolism to cope with chronic dehydration and dietary constraints.

...the adaptation of the Turkana people to their environment involved metabolic compromises throughout the genome...

Individuals from the Turkana people group are increasingly relocating to more urban environments. This transition is associated with a change in diet away from a high level of consumption of animal products (blood, milk, and red meat) and toward market-derived products. Previous studies have reported an increase in biomarkers associated with cardiovascular disease risk in the Turkana pastoralists who transition to urban environments (*10*). This aligns with observations in other populations—for example, the Daasanach, the Shuar of Ecuador, and the Tsimane of Bolivia—which shows that increased market integration is associated with an increase in the risk of cardiometabolic disease (*11*–*13*). Lea *et al.* performed a transcriptomic analysis to identify genes that differ in expression level between Turkana individuals living a pastoral lifestyle and those living in urban environments. The identified genes exhibited more evidence of selection than that of other genes, which suggests that these past adaptations could interact with the environmental changes experienced by migrating Turkana individuals to shape disease risk.

Rather than being blueprints for optimal health, human genomes encode a history of situational compromise. The findings of Lea *et al.* illustrate that deeper data and comparative approaches can reveal that genomic adaptations are more complex than early models considered; for example, there is a role for context specificity, and both monogenic and polygenic adaptation, perhaps from ancient variation. Most GWASs rely on European-centric genetic architecture, but population-specific adaptations, such as those of *STC1* observed by Lea *et al.*, create distinct disease risks (*14*). Understanding these evolutionary legacies could contribute to tailoring of clinical care in a rapidly changing world. □

REFERENCES AND NOTES

1. S. Fan, M. E. B. Hansen, Y. Lo, S. A. Tishkoff, *Science* **354**, 54 (2016).
2. J. V. Neel, *Am. J. Hum. Genet.* **14**, 353 (1962).
3. A. J. Lea *et al.*, *Science* **389**, 1246 (2025).
4. A. Bigham *et al.*. *PLOS Genet.* **6**, e1001116 (2010).
5. E. Huerta-Sánchez *et al.*, *Nature* **512**, 194 (2104).
6. R. P. Evershed *et al.*, *Nature* **608**, 336 (2022).
7. G. B. Loeb *et al.*, *Nat. Genet.* **56**, 2078 (2024).
8. J. S.-C. Pan *et al.*, *J. Am. Soc. Nephrol.* **26**, 364 (2015).
9. E. A. Boyle, Y. I. Li, J. K. Pritchard, *Cell* **169**, 1177 (2017).
10. A. J. Lea, D. Martins, J. Kamau, M. Gurven, J. F. Ayroles, *Sci. Adv.* **6**, eabb1430 (2020).
11. M. A. Liebert *et al.*, *Ann. Hum. Biol.* **40**, 228 (2013).
12. Z. S. Swanson *et al.*, *Evol. Med. Public Health* **11**, 318 (2023).
13. M. Gurven *et al.*, *Evol. Anthropol.* **26**, 54 (2017).
14. A. R. Martin *et al.*, *Nat. Genet.* **51**, 584 (2019).

10.1126/science.aeb2287

[1]Department of Evolutionary Anthropology, Duke University, Durhgam, NC, USA.
[2]Department of Human Genetics, University of California, Los Angeles, Los Angeles, CA, USA.
Email: amygoldberg@mednet.ucla.edu

LETTERS Edited by **Jennifer Sills**

A Sudanese cholera patient receives medical care in a United Nations–run makeshift clinic in Darfur, Sudan.

PHOTO: REUTERS/MOHAMMED JAMAL

Global implications of cholera in Sudan

After more than 2 years of conflict in Sudan, 10.5 million displaced people are stranded within Sudan's borders, and nearly 4 million are seeking refuge in surrounding countries and the European Union (*1*). The conflict has caused the collapse of Sudan's health infrastructure and increased malnutrition, especially among the elderly (*2*), exacerbating the risks of deadly disease outbreaks such as cholera. Cholera spreads mainly through ingestion of water or food contaminated with *Vibrio cholerae*. Although direct person-to-person transmission is rare, displaced persons who are infected can spread the disease to new locations, especially if they are living in overcrowded camps with poor water, sanitation, and hygiene (*3*). International organizations must work closely with Sudan and other countries affected by cholera to strengthen disease surveillance, improve access to clean water, and ensure timely outbreak response.

Between January and May, more than 92,000 cases of cholera were recorded in the six countries that comprise the Eastern Mediterranean, including about 16,500 cases in Sudan (*4*). Afghanistan, Haiti, and the Democratic Republic of Congo have also suffered from ongoing cholera outbreaks (*4*). In 2017, the Global Task Force on Cholera Control set an ambitious target of reducing cholera-related mortality by 90% by 2030 (*5*), using the 2015 global burden estimate as a baseline. In 2023, the World Health Organization (WHO) declared a Grade 3 emergency, its highest level, for cholera (*6*). Yet cholera barely registers on national political agendas or health priorities (*2*).

Global health institutions, including the WHO, can support displaced Sudanese populations by providing technical and financial assistance both within Sudan and in neighboring countries hosting refugees. To ensure that assistance reaches vulnerable populations and strengthens local capacity for disease prevention and health care delivery, funds and resources should be directed to local authorities, humanitarian agencies, and nongovernmental organizations operating in camps and communities. Efforts should also focus on community nutrition, educating the public by spreading health information through the media, and providing mental health services. Strengthening sentinel and hospital-based surveillance systems in the affected regions would improve data collection and interpretation, enabling a more effective response to outbreaks (*6*).

Partnerships abroad can help scale up DNA vaccines for cholera (*7*–*9*), which would be safer, longer lasting, more stable, and more cost efficient than the commonly used oral inactivated whole-cell vaccine (*10*, *11*). International partners could also boost vaccination programs. Sudan and its partners can learn from successful efforts to address and control cholera outbreaks in Haiti, Bangladesh, and other African countries (*12*), where integrated measures such as vaccination campaigns, improved water and sanitation, and rapid treatment centers have curbed transmission and reduced mortality, even in resource-limited settings.

Ahmed A. H. Abdellatif[1] and Emad M. Abdallah[2]

[1]Department of Pharmaceutics, College of Pharmacy, Qassim University, Buraydah, Saudi Arabia. [2]Department of Biology, College of Science, Qassim University, Buraydah, Saudi Arabia. Email: a.abdellatif@qu.edu.sa

REFERENCES AND NOTES

1. WHO Team, "Sudan conflict and refugee crisis: Multi-country External Situation Report #10, covering the reporting period March-April 2025," ed. 10 (WHO, 2025).
2. I. N. Hassan, *Lancet Healthy Longev.* **6**, 100692 (2025).
3. K. Shannon *et al.*, *PLOS Negl. Trop. Dis.* **13**, e0007347 (2019).
4. WHO Team, "Multi-country outbreak of cholera: External Situation Report #27 - 17 June 2025," ed. 27 (WHO, 2025).
5. *Lancet* **404**, 1493 (2024).
6. WHO, "Cholera – global situation," *Disease Outbreak News*, 26 January 2023.
7. J. Yu *et al.*, *Science* **369**, 806 (2020).
8. J. B. Kaper, H. Lockman, M. M. Baldini, M. M. Levine, *Nature* **308**, 655 (1984).
9. H. Cong *et al.*, *Parasit. Vectors* **6**, 63 (2013).
10. J. J. Mekalanos *et al.*, *Nature* **306**, 551 (1983).
11. S. N. Desai, A. Cravioto, D. Sur, S. Kanungo, *Hum. Vaccin. Immunother.* **10**, 1457 (2014).
12. WHO Team, "Multi-country outbreak of cholera: External Situation Report #6 – 6 September 2023," ed. 6 (WHO, 2023).

10.1126/science.adz3827

Protect academia in Sudan with global action

Sudan's civil war, which erupted in April 2023, has devastated the country's universities. More than 10 million Sudanese people have been displaced, including tens of thousands of university staff and students (*1*). Although the United Nations Educational, Scientific and Cultural Organization (UNESCO) has declared an education emergency in Sudan (*2*), the destruction of the country's intellectual capital has drawn scant global attention. Sudan's academic collapse is not just a regional tragedy—it is a global emergency that calls for urgent international action.

For decades, Sudan was a pillar of African science and scholarship. The University of Khartoum, for example, was established in 1902 and long regarded among Africa's top institutions (*3*). The

institution trained generations of doctors, engineers, and scientists. Today, the University of Khartoum is closed, along with more than 75% of Sudan's 128 higher-education institutes (*4*, *5*). Sudan is also home to about 66 medical schools, nearly 60% of which have been attacked or occupied by military forces (*4*, *6*). The country's national museums have been looted (*7*), and the only research center in the world devoted to the rare disease mycetoma has been destroyed (*8*).

To safeguard Sudan's academic future, universities around the world should provide fellowships, placements, and scholarships for displaced Sudanese faculty and students, even when transcripts or official records are unavailable. In conflicts such as those in Ukraine and Syria, similar programs have helped preserve scientific careers and national capacity (*9*, *10*). Governments should accelerate visa processing to allow Sudanese scholars to continue their work in safe environments. International organizations, academic institutions, and the global scientific community must work together to integrate Sudanese academics into research and training programs, support virtual learning platforms, and enable mentorship by Sudanese scientists in the diaspora.

Sudan's crisis management and postwar recovery must include higher education as a strategic priority. Models from Bosnia and Rwanda show that rebuilding universities contributes not only to national healing and sustainable development but also to restoring civic trust and institutional resilience (*11*). In Sudan, students and professors were central to the 2019 prodemocracy movement and continue to serve as vital voices for peace, reform, and accountability (*12*). To preserve their role, the world's universities, governments, donors, international nongovernmental organizations, and policy-makers must engage in coordinated and immediate action. Knowledge must not become a casualty of war.

Hisham Y. Hassan

Banoon ART & Cytogenetics Centre, Military Hospital, Royal Medical Services, West Riffa, Kingdom of Bahrain. Email: hisham.yousif@bdfmedical.org

REFERENCES AND NOTES

1. T. A. Mahdi, A. H. Fahal. *Sudan J. Med. Sci.* **19**, 356 (2024).
2. "Sudan: UNESCO is deeply concerned and is preparing to support the population," UNESCO, 12 May 2023.
3. M. H. Hassan, *Nature* **623**, 10 (2023).
4. E. A. A. Mahgoub *et al.*, *Confl. Health* **18**, 23 (2024).
5. M. M. Beshir *et al.*, *Afr. J. Rural Dev.* **5**, 115 (2020).
6. T. K. Mohamed *et al.*, *BMC Med. Educ.* **25**, 861 (2025).
7. "Sudan: UNESCO raises the alarm on reports of illicit trafficking of cultural heritage," UNESCO, 12 September 2023.
8. R. Badri, A. H. Fahal, *PLOS Negl. Trop. Dis.* **17**, e0011783 (2023).
9. B. Plackett, *Nature* **638**, 569 (2025).
10. A. Goodman, *Science* **354**, 1207 (2016).
11. S. Milton, S. Barakat, *Glob. Soc. Educ.* **14**, 403 (2016).
12. A. Roussi, *Nature* **570**, 16 (2019).

10.1126/science.aea1930

Wastewater surveillance requires ethical use

Wastewater-based surveillance (WBS) enables the early detection of infectious diseases (*1*, *2*) and monitoring of community health trends (*3*), making it a critical public health tool. This year, US policy-makers sought to politicize WBS by tracking compounds linked to reproductive behaviors and sexual health, threatening Americans' privacy under the banner of "environmental monitoring." WBS should be used exclusively to improve and protect public health, and communities and scientists must lobby local representatives to prevent its misuse as a tool of political or social coercion.

In March, the Texas legislature introduced Senate Bill 1976 (TX SB1976), mandating routine wastewater testing for specifically named pharmaceuticals, including mifepristone, ethinyl estradiol, pregnanediol, and testosterone (*4*). Many of these compounds and their metabolites are chemically stable and detectable at nanogram-per-liter levels in sewage (*5*), enabling government inferences about contraceptive use, abortion access, and gender-affirming care. Historically, WBS tracked pharmaceutical and illicit drugs in sewage, directing public health resources by revealing clusters of disease, including addiction (*6*, *7*). This proposed framework insidiously repurposes WBS to target safe, lawful personal actions (*8*).

The bill's framing, claiming to "regulate the quality of wastewater" and "ensur[e] public safety and environmental protection" (*4*) provides a template for governmental overreach. Such expansion of WBS would enable behavioral surveillance without consent, transparency, justification, or oversight, contradicting all previously established practices and protocols (*9*). Because WBS is regulated as environmental monitoring rather than health surveillance, it falls outside protections such as the Health Insurance Portability and Accountability Act (HIPAA), a US federal law that establishes standards for patient privacy. In states where reproductive autonomy is contested or criminalized, this infrastructure could enable targeted investigations or policy interventions.

TX SB1976 offered communities no clarity on why compounds were monitored or how results would be used. Although the bill died in committee (*10*), its sponsor previously advanced similar attacks on reproductive autonomy, including the Texas Heartbeat Bill of 2021 (TX SB8), which allows private citizens to sue anyone who aids or abets an abortion after the detection of a fetal heartbeat (*11*). TX SB1976 was clearly introduced in the spirit of Project 2025, which seeks to "use every available tool…to ensure that every state reports exactly how many abortions take place within its borders" (*12*) by weaponizing WBS, a tool meant to protect public health.

The integrity of WBS, and public trust in it, depends on action from citizen advocates and scientists to lobby policy-makers for clear ethical boundaries. Using WBS politically to track reproductive or gender-affirming health compounds is both wasteful of taxpayer dollars and a fundamental misuse of the technology. To prevent unethical WBS applications, legislators should require mandatory public notification requirements for all programs, specifying monitored compounds or targets and their public health justification. Oversight should also include independent ethics panels with community representation and explicitly prohibit the monitoring of reproductive health compounds without clear public health benefit.

Patrick M. D'Aoust

Department of Civil, Geological, and Mining Engineering, Polytechnique Montréal, Montréal, QC, Canada. Email: patrick-marcel.daoust@polymtl.ca

REFERENCES AND NOTES

1. P. Kilaru *et al.*, *Am. J. Epidemiol.* **192**, 305 (2023).
2. A. Keshaviah *et al.*, *Lancet Glob. Health* **11**, 976 (2023).
3. D. A. Bowes, *Curr. Epidemiol. Rep.* **11**, 131 (2024).
4. Senate Research Center, "Bill analysis – S.B. 1976" (89R11160 CMO-F, Texas Senate, 2025); https://capitol.texas.gov/tlodocs/89R/analysis/html/SB01976I.htm.
5. K. Zhang *et al.*, *Environ. Sci. Technol.* **51**, 6498 (2017).
6. T. B. Erickson *et al.*, *J. Med. Toxicol.* **17**, 397 (2021).
7. E. Zuccato *et al.*, *Environ. Health Perspect.* **116**, 1027 (2008).
8. S. Teal, A. Edelman, *JAMA* **326**, 2507 (2021).
9. D. Nainani *et al.*, *Water Res.* **258**, 121756 (2024).
10. Texas Senate Bill 1976 (TX SB1976), 89th Legislature (2025); https://legiscan.com/TX/bill/SB1976/2025.
11. Texas Senate Bill 8 (TX SB8) Supplement, Analysis (Introduced), 87th Legislature (2021); https://legiscan.com/TX/supplement/SB8/id/161280.
12. P. Dans *et al.*, *Mandate for Leadership: The Conservative Promise 2025* (The Heritage Foundation, 2023).

10.1126/science.adq6656

POLICY ARTICLE

SCIENCE FUNDING

Partisan disparities in the funding of science in the United States

Republican lawmakers consistently provided robust federal funding, often exceeding Democrats

Alexander C. Furnas,[1,2,3] Nic Fishman,[4] Leah Rosenstiel,[5] Dashun Wang[1,2,3,6]

The increasing complexity and extended timelines involved in scientific research and technological innovation highlight the importance of consistent, reliable support for science. The United States government—the largest research funder in the world—plays a pivotal role, mobilizing resources domestically while also serving as a global leader, shaping strategies of international funders and policy-makers (*1*, *2*). Despite this central importance of the US government in global science, the relationship between its political control and science funding remains poorly understood. This gap in understanding is particularly pressing in an era of growing political polarization. Here we leverage a comprehensive database of appropriations—the funding levels denoted in statute and directly set by policy-makers—to capture federal support for science from 1980 to 2020. Despite occasional public skepticism of science (*3*), Republican lawmakers consistently provided robust funding, often exceeding Democrats, underscoring the importance of bipartisan investments in science and research.

Partisan control of Congress and the presidency oscillates between Democrats and Republicans (*4*), creating short-term dynamics that can conflict with the long-term commitments that science demands. Divergence between the transient nature of political control and the enduring needs of scientific research raises critical questions: How do these political shifts influence the allocation of federal science funding? Does political volatility pose a threat to the steady investments essential for scientific progress? Understanding the interplay between political polarization, funding trends, and the lengthy timelines of scientific research is essential for safeguarding the future of long-term research.

The urgency of addressing these questions is heightened by recent proposed shifts by the administration in federal funding priorities. Recent decisions affecting indirect cost rates, federal grant disbursements, and agency funding priorities have introduced new challenges for research institutions and heightened uncertainty within the scientific community. Although some of these measures have faced legal and institutional pushback, the broader instability surrounding science funding underscores the need for a deeper understanding of how political control shapes long-term investments in research.

Since the US federal government began funding scientific research after World War II, this funding has primarily been guided by a vision of science, articulated by Vannevar Bush, in which scientists themselves hold substantial discretion over research methods and scope. This ideal of science highlights its philosophical and cultural independence and the need to shield research from short-term political or bureaucratic pressures.

Yet there are reasons to believe that science funding is not immune to political forces. Federal funding agencies are ultimately responsible to the political institutions that set their budgets, conduct oversight, and appoint their top officials. Congress and the president have a number of tools at their disposal to influence the bureaucracy. For example, all government funding requires an act of Congress, and members of Congress may attach strings and restrictions to this funding. Top jobs at federal agencies are usually held by presidential appointees, some of whom require Senate confirmation. The Executive Office of the President oversees many agency decisions, including promulgating regulations and requesting funds from Congress. A long line of political science research suggests that these factors allow for political control over the bureaucracy (see supplementary materials).

For example, between 2009 and 2012, there were three successive efforts by prominent Republicans in the House of Representatives to drastically cut or completely eliminate National Science Foundation (NSF) funding for political science research. Although congressional support for NSF is mostly bipartisan, Republicans are more likely to express concerns about accountability in NSF spending than Democrats (*3*) in the midst of long political battles over public funding for social sciences (*5*). In addition, the inclusion of the so-called "Dickey Amendments" in annual appropriation bills, sponsored and supported largely by Republican legislators for decades, limited the use of federal dollars in human embryonic stem cell research and gun violence research.

Key stages of the appropriations process

● Stages where account-level data were captured for study

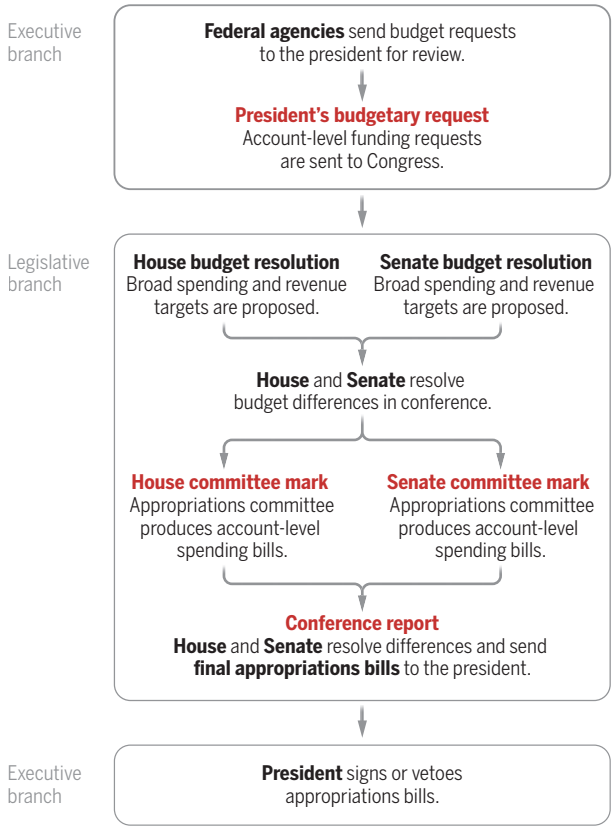

GRAPHIC: N. BURGESS/*SCIENCE*

The evolution of science– and research–related appropriations, and party control

Analysis of annual budget appropriations figures for 171 science and research accounts reflects how the proportion of the total budget that is allocated to research and development has changed over decades, as party control of different parts of the federal government has also changed. For each fiscal year, party control is shown as of the prior year, when the appropriations for that fiscal year were enacted.

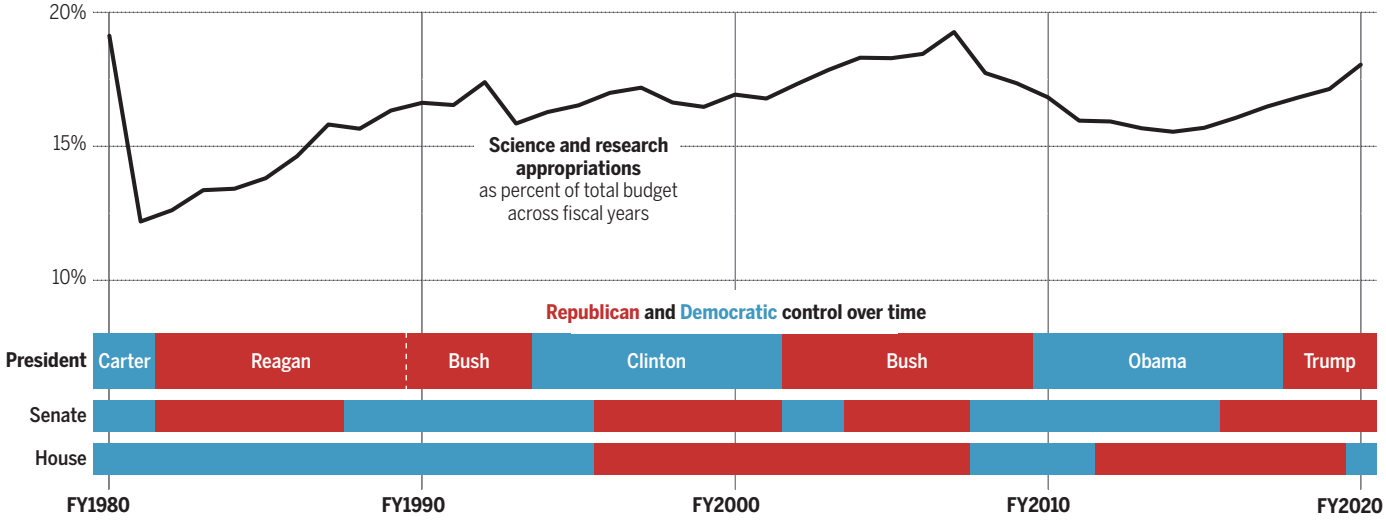

THE IMPORTANCE OF STUDYING APPROPRIATIONS

Despite such high-profile examples and reasons for concern about differential partisan support, we lack any systematic evidence about the full scope of federal science funding over time. Our understanding remains limited partly owing to the difficulties in systematically tracing the US government's science- and research-related expenditures. Here we leverage a database that categorizes discretionary base budget authority for federal science and research accounts from fiscal years 1980 to 2020 (beginning 1 October each year) (*6*). Base budget authority, as outlined in annual appropriations bills, serves as the primary mechanism for funding the recurring needs of the federal government for the normal operation of programs and agencies. It excludes emergency budget authority [e.g., 2009 "stimulus" American Recovery and Reinvestment Act (ARRA)], mandatory budget authority (e.g., entitlement spending like Medicaid, Veterans Benefits, or other one-off statutes like the Inflation Reduction Act), and tax expenditures (e.g., tax credits, or exclusions that are counted as foregone revenue instead of expenditures). Our analysis focuses exclusively on funding allocated through the regular appropriations process, which governs discretionary spending and excludes budget reconciliation and other forms of mandatory spending. Distinct from recent large-scale legislative packages that use one-time or mandatory funding mechanisms outside the annual appropriations process, our data capture the routine, institutionalized flow of federal support for science.

The data are derived from the Comparative Statements of Budget Authority (CSBAs) contained in the House and Senate committee reports, as well as the conference reports (or joint explanatory statements) accompanying public laws. CSBAs reflect the official scoring of appropriations language by the Congressional Budget Office (CBO), ensuring consistency in how budget authority is assessed.

We manually identify 171 specific federal appropriations accounts across 27 federal agencies associated with science or research activity. Appropriations accounts are the basic units that Congress uses to allocate funds. Each account typically corresponds to an unnumbered paragraph in an appropriations act (see supplementary materials). We define science and research broadly, focusing not only on research and development (R&D) funding but also on social science and policy research. These accounts include funding for the NSF, National Institutes of Health (NIH), Centers for Disease Control and Prevention (CDC), National Aeronautics and Space Administration (NASA), R&D programs within the Department of Defense (DoD), the National Agricultural Statistics Service, the Bureau of Labor Statistics, programs within the Census Bureau, policy evaluation by the CBO, and numerous other research, technology, and development programs across the federal government (see table S12 for a full list of programs). The accounts that we identify fund government programs related to science and research (e.g., NSF grants to external researchers), programs at agencies conducting their own scientific activities [e.g., NASA, US Geological Survey, or Department of Energy (DOE) National Laboratories like Fermi or Argonne], and contracts—legally binding agreements in which the government purchases goods or services, including research—from private entities.

All of these accounts are subject to the detailed budget and appropriations processes involving the president and both chambers of Congress (see the first figure). To measure proposed and enacted appropriation levels for every year and for each of these 171 science and research accounts, we use hand-collected comparative statements of new budget authority contained in documents produced at four key stages of the appropriations process: the president's budget request (the president sends account-level funding requests to Congress), reports from House and Senate committee marks (appropriations committees in each chamber produce separate bills containing account-level spending), and the conference report (House and Senate resolve differences in conference and send final appropriations to the president) of the appropriation that was ultimately enacted. We rely on the CBO score for each account, which reflects the spending within that account that would result from the appropriations bill. The inclusion of presidential budget requests and appropriations in House and Senate committee marks, in addition to enacted appropriations, allows us to explore differences in institutional priorities in the interbranch appropriation bargaining process (*6*).

The overall share of the federal budget allocated to science- and research-related appropriations accounts has evolved during our period of observation, as has party control of the Senate, House, and presidency (see the second figure). Prior studies of government science funding have tended to focus almost exclusively on grantmaking activity (see supplementary materials). However, our data reveal that the vast majority of federal funding for science comes in the form of government contracts rather than competitive grants. As of 2019—the last pre-COVID year for which data are available—the federal government had $370 billion in outstanding obligations related to grants (and

GRAPHIC: M. HERSHER/*SCIENCE* AND V. PENNEY/*SCIENCE*

other forms of assistance awards such as cooperative agreements and loan guarantees) for science and research accounts, but it had spending obligations of more than $1.5 trillion for hiring contractors from those same accounts (see fig. S2A.) These data document that although federal science grantmaking constitutes the majority of science funding allocated toward public and private higher learning institutions, it represents a relatively small proportion of total federal spending on science and research. Indeed, we find that during this period, total disbursements from publicly available grantmaking (*7*) totaled between 7 and 24% of total nonemergency science and research appropriations, with the exception of a short spike in grantmaking that aligns with ARRA. In addition, a substantial portion of the government's science and research activity is performed by private contractors.

Since 1980, total science appropriations have varied between $120 billion and $225 billion in 2021 constant dollars, with the largest share historically devoted to the DoD, followed by Health and Human Services, the DOE, and NASA (see fig. S2B) We observe a large initial outlay of funds for the Department of Energy in 1980, shortly following its establishment (see fig. S2C for the distribution of science and research appropriations across accounts in 2020.)

Together, these facts highlight the importance of studying appropriations—the funding levels denoted in statute and directly set by policymakers—to fully capture the government's role in funding science. Appropriations data have several key advantages over other measures of government funding and public policy. They reflect the budget authority that Congress provides to federal agencies to award grants, enter into contracts, or conduct research themselves, thereby encompassing all major spending categories. Because Congress enacts appropriations legislation annually, we can track yearly changes and fluctuations in partisan control. By examining appropriations legislation at key points throughout the policy-making process, we can see not only the president's request but also the funding levels proposed by the House and Senate, as well as those ultimately enacted into law, allowing us to directly examine the influence of partisan dynamics at each stage of the appropriations process. Focusing on bills enacted by Congress links funding decisions to legislative organization. By contrast, "downstream" measures of government funding (i.e., outlays) can take years to materialize, making it difficult to attribute funding choices to the party in control at the time of legislative action (*8*). Examining appropriation bills themselves sidesteps this problem.

More funding under Republican House or presidency

The chart shows estimated marginal effects, in millions of dollars appropriated to science and research accounts, of Republican control of the House, Senate, and presidency. Bars indicate 95% confidence intervals. See supplementary materials for full specifications of regression models.

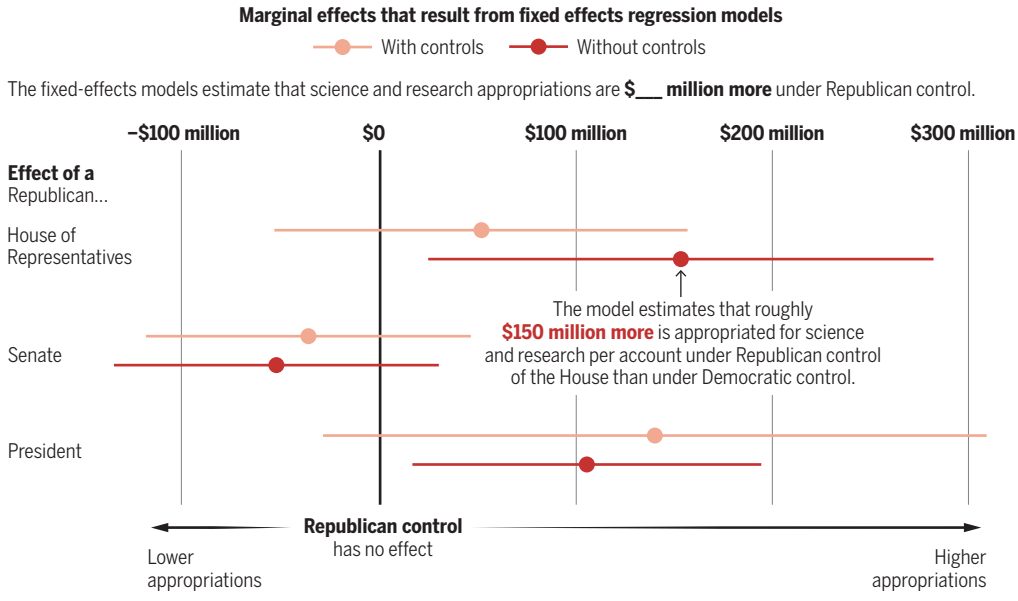

FEDERAL APPROPRIATIONS AND POLITICAL CONTROL

We find that, when the House of Representatives or the presidency has been controlled by Republicans, appropriations have been, on average, substantially higher for science- and research-related accounts than when they have been controlled by Democrats. These results occur in multiple important agencies and departments.

We assess the relationship between partisan institutional control on science funding, using a series of fixed effects regressions on the size of enacted appropriations to science and research accounts within a fiscal year, with indicator variables for Republican control of the House, Senate, and presidency on grant funding and science appropriations. Although we estimate all models on nominal dollars, we address secular and inflationary trends in spending as well as changes in the statutory discretionary spending caps by including a control for the topline size of the federal budget in all models, as inflation during this period fluctuated more sharply than the budget's overall size, and our descriptive focus is on the prioritization of spending in these accounts relative to the total budget. We choose these simple, parsimonious models with few controls as our main models, because they are most appropriate for drawing descriptive inferences about which party historically allocated more funding to science. Collinear controls may absorb relevant variance, and the descriptive meaning of a regression coefficient becomes increasingly opaque as more variables are included in the model (*9*). Nevertheless, for transparency and robustness, we also report results from expanded models with numerous additional controls in which we include indicators for whether it is a presidential election year, and whether the year's funding vehicle was a full-year continuing resolution, as well as the consumer price index, change in the unemployment rate, the size of the budget deficit (in real dollars), change in gross domestic product per capita, and account fixed effects. In the supplementary materials, we report a suite of alternative specifications—including models using real dollars without the topline budget; account allocations as a share of the topline, agency-level aggregations; stricter definitions of "science-related" accounts; and models that account for the margins of party control in the House and Senate.

Overall, we find that conditional on the size of the federal budget, federal science and research accounts receive more funding when Republicans control the House of Representatives or the presidency (see the third figure). Although these associations are consistent in direction and magnitude when we include the expanded suite of control variables, they are not statistically significant at conventional levels. Notably, these differences are substantial: According to the simple model, the science- and research-related appropriations accounts received, on average, roughly $150 million more per account in years when Republicans controlled appropriations in the House, and $100 million more per account when there was a Republican president. These results

GRAPHIC: M. HERSHER/*SCIENCE* AND V. PENNEY/*SCIENCE*

mirror the greater science funding under Republican principals that we observe in the grantmaking data, which we explore below.

Greater Republican funding of science extends beyond the DoD, which we might expect given the Republican issue ownership of national defense and their tendency to support higher defense spending than their Democratic counterparts (see supplementary materials). By reestimating our models of account-level enacted appropriations across agencies and departments, we find that Republican lawmakers in the House tend to appropriate more money for science in the DoD, CDC, NASA, NSF, and NIH, with statistically significant differences at the NIH ($P < 0.001$) and a marginal association at the NSF ($P = 0.06$). Conversely, appropriations to science and research in the DOE are lower when Republicans control the House ($P = 0.071$), possibly because renewable energy has been a priority area for many Democrats in recent years (*10*), and because of the large initial outlay when the department was established under a Democratic administration (see fig. S2B). Under Republican presidents, we observe higher appropriations to science and research accounts in the CDC ($P = 0.015$), DoD ($P = 0.012$), and NIH ($P < 0.001$). Notably, science and research accounts in the DoD received considerably greater appropriations under Republican presidents, averaging more than $1 billion additional dollars per account. By contrast, we observe lower appropriations to science and research accounts in the Department of Commerce ($P = 0.049$) when there is a Republican president. Under Republican control of the Senate, we observe lower appropriations to the CDC, NIH, and NSF, although these associations tend to be more modest in size and not statistically significant at conventional levels ($P > 0.05$). There are notable differences in average yearly appropriations at the department and agency level under Republican and Democratic control of the House of Representatives (see the fourth figure). The full regression results are reported in the supplementary materials (fig. S3 and table S3). Although individual agency- and department-level associations vary in strength and should not be overinterpreted in isolation, the overall pattern indicates that Republican support for science is spread across multiple agencies, rather than being concentrated solely in one department such as defense.

House funding patterns vary by department

The allocation of federal dollars to science and research appropriation accounts over time is shown by department.

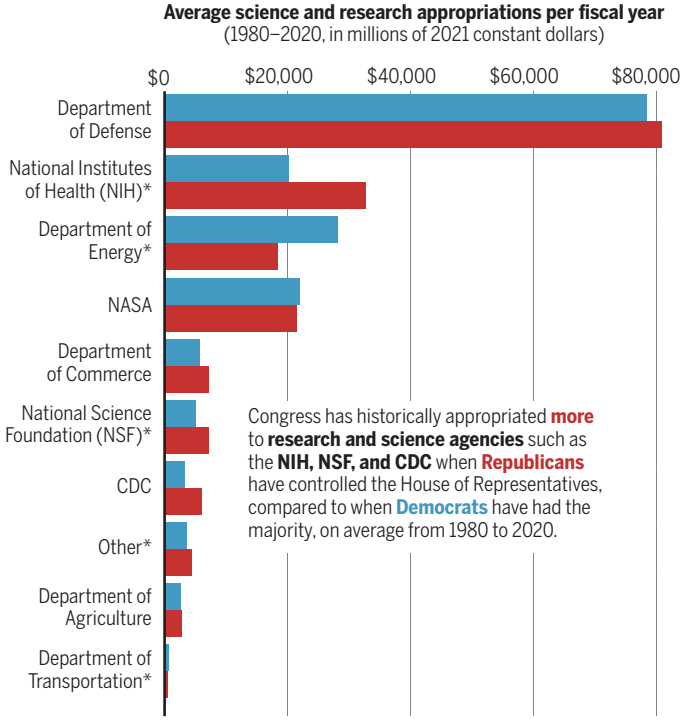

*Indicates significant difference in funding ($P < 0.05$) between Republican and Democratic control of the House of Representatives. See table S12 for a full list of programs; any of those programs that are not specified by name in this figure are included in the category "Other." NASA, National Aeronautics and Space Administration; CDC, Centers for Disease Control and Prevention.

Moreover, the relationships that we observe—where Republican control of the House or presidency is associated with greater science appropriations—are reinforced by the results from the House and Senate committee marks. Indeed, the particular nature of our appropriations data allows us not only to examine final enacted budgets but also to explore the influence of partisan institutional control throughout the budgeting and appropriations process. We estimate the relationship between partisan institutional control and each major stage of the budgeting process, beginning with the presidential budget request, followed by the committee marks drafted by the House and Senate Appropriations Committees (see fig. S4, A to C). We re-estimate the models underlying the third figure at each stage of the budgeting process to assess institutional priorities of each negotiating party separately. Consistent with the political science literature on legislative bargaining, we expect that policy-makers are strategic and likely anticipate what other actors will do (*6*). For example, senators would be expected to alter their appropriations bill depending on which party controls the House because the Senate is anticipating the House's changes to their proposal. In line with this logic, at all three stages of the budgeting process, we find a positive association between Republican control of the House of Representatives and higher appropriations to science and research accounts (see fig. S4, A to C). When looking at the House bill and the Senate bill, the effect for Republican control of the House is robust to the inclusion of our full set of controls (fig. S4, B and C). We also find a significant association between Republican control of both the presidency and the Senate and science funding in the House bill (fig. S4B). Overall, the observed effects of partisan control appear to be the most robust when we examine proposed appropriations in the House committee marks, with Republican control of all three institutions associated with more proposed spending on science and research accounts (see fig. S4, A to C).

Further breaking out our analysis for different time periods, we find that Republican control of the presidency is associated with higher science and research appropriations from 2001 to 2020 compared with 1980 to 2000 (see tables S9 and S10). This is consistent with scholarship showing that the capacity of Congress has declined since the 1990s, possibly making members of Congress more reliant on the expertise of presidents and their staff. Thus, we expect that the president's influence over federal appropriations is increasing over time. This would explain why Republican presidents are associated with higher science and research funding toward the end of our period of observation.

Taken together, our results highlight how partisan control of the presidency and the House of Representatives—but not the Senate—affects funding for science and research. The large influence of partisan control in the House is consistent with the majority party having more procedural control over the agenda in the House than in the Senate (*11*). This is partially due to the Senate cloture rule, which requires a three-fifths majority to end debate on nearly all proposals, including appropriations bills. As one party rarely has a three-fifths majority in the Senate, the cloture rule essentially requires appropriations bills to have bipartisan support in the Senate, limiting the influence of the majority party. Likewise, the president—as a unitary actor—does not need to negotiate with the other party before making their budget proposal. This may explain why partisanship has a greater influence on the budget proposed by the president and the House of Representatives than that proposed by the Senate.

Although appropriations data provide important insights into federal allocations for science and research, grantmaking data remain of intrinsic interest to the scientific community because federal grant-

GRAPHIC: M. HERSHER/*SCIENCE* AND V. PENNEY/*SCIENCE*

making bodies fund the majority of university-based sponsored R&D, and grant-funded science plays a central role in discovery and innovation. Further, unlike appropriations data, research grant data can be tied directly to research outputs, allowing us to explore the impact of partisan control of funding and oversight institutions on the allocation of funds by federal grantmaking bodies across different fields.

Using data from Dimensions (see supplementary materials), which capture $1.3 trillion (in 2020 constant dollars), we analyze grants from 103 US federal funders between 1952 and 2019 and find evidence that shifts in partisan control of the political institutions overseeing the agencies and departments that disperse federal grants are associated with changes in grant outlays. Here, we address the problem of temporally associating outlays to downstream outputs by looking at party control at the start date associated with a grant. This allows us to evaluate how grantmaking institutions perform differently when the principals responsible for their oversight are controlled by different parties at the time grants are made, not how they act depending on which party is in power when their budgets were set through the appropriations process. When Republicans control the House of Representatives, the average federal science funder disburses approximately $70 million more per year compared to when Democrats are in control. When the Senate is under Republican control, funders disburse $45 million less per year. (These results are from regression models of the same form as those that underlie the third figure, applied to grantmaking from 1952 to 2019, controlling for the size of the federal budget with funder fixed effects. See fig. S5A and table S2.)

Field-level funding consistency regardless of party control

The proportion of federal grants allocated to specific research fields remains roughly consistent, regardless of which party controls Congress.

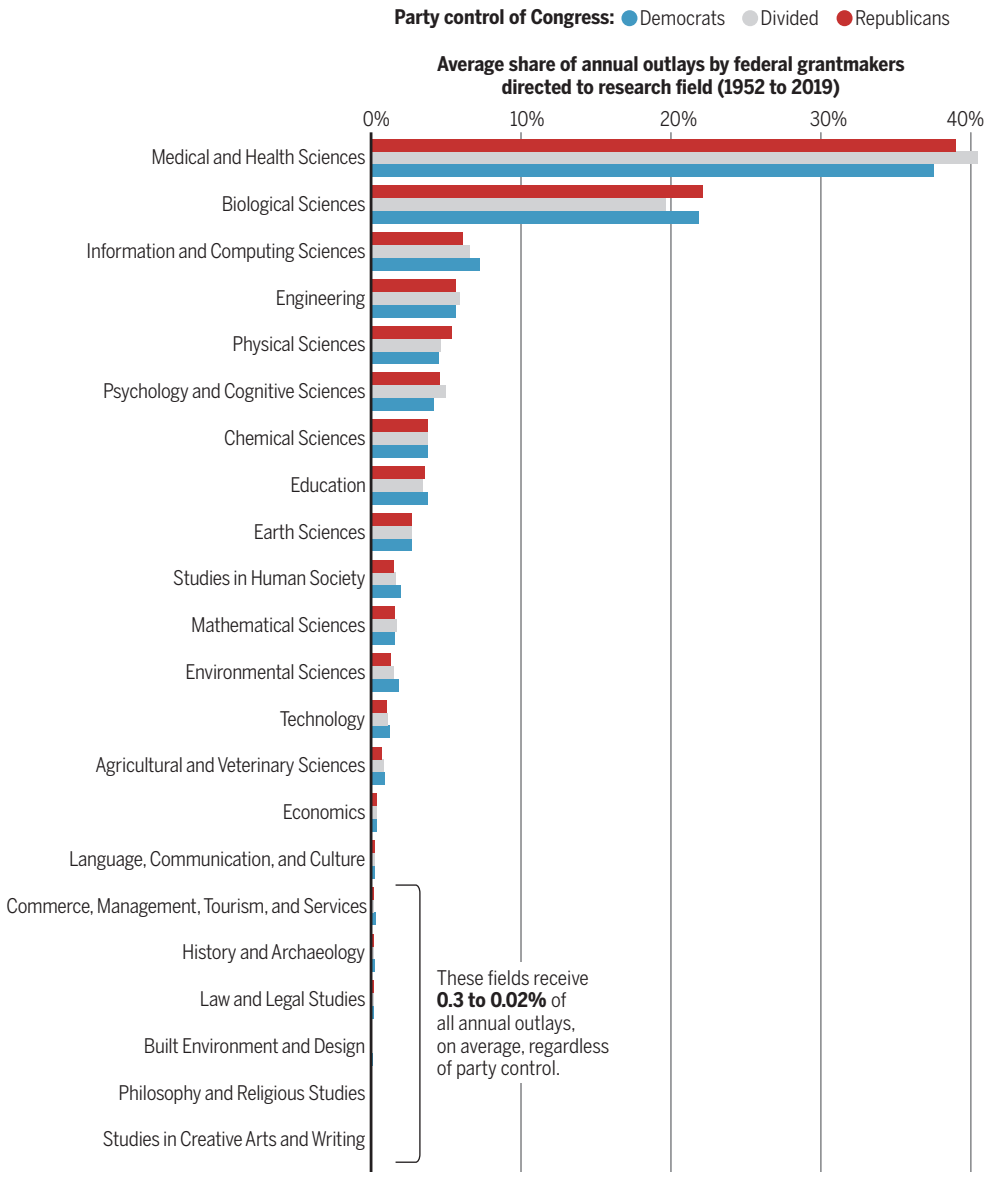

These variations in grant outlays do not appear to translate to notable differences in the prioritization of research fields at a broad level. With few exceptions, the proportion of federal grants allocated to specific research fields remains roughly consistent, regardless of whether Congress is controlled by Republicans or Democrats, or is divided among both parties (see the fifth figure). Overall, we find that funding across broad fields of research appears unassociated with changes in partisan control of Congress. Using market-share models, which apply a centered log ratio transformation of the compositional dependent variable (i.e., percent of funding to each field of research), we find no substantial differences in the share of funding allocated toward research fields based on party control of government at the time of disbursal, which holds both within individual funders and at the aggregate level across all funders (see fig. S5, B and C). This result suggests that whereas the overall level of funding for science by the federal government differs depending on which party controls the levers of power, how these funds are distributed across fields does not.

PATTERNS AND IMPLICATIONS

Our analysis of partisan dynamics in science funding reveals striking and previously unknown patterns, which may have important implications for scholars, science communicators, advocates, and policy-makers. First, our analysis of spending data highlights that grantmaking—long a central focus of the science of science research—represents only a fraction of total outlays made from US federal science- and research-related appropriations accounts. A sizable proportion of these expenditures is directed to private firms through contracts, while federal agencies also conduct substantial in-house research. Decisions about whether and when to enter into contracts, as well as to whom to offer them, are generally made by federal agencies. The Government Accountability Office estimates that in 2023, the federal government spent $478 billion on service contracts (*12*), including research. Thus, to fully understand federal spending, we need to capture government spending on contracts.

During the period 1980 to 2020, Republicans allocated more funding than their Democratic counterparts within the topline budgets, a finding that challenges prevailing narratives of Republicans as "anti-

GRAPHIC: M. HERSHER/*SCIENCE* AND V. PENNEY/*SCIENCE*

science" (*13*). This robust support, observed across multiple agencies and departments, underscores the historical importance of Republican investments in science and research. These findings suggest that current advocacy strategies for science funding aimed at Republican lawmakers could emphasize how investments in research have historically aligned with conservative values, such as economic growth, technological innovation, and national security. At the same time, they highlight that both parties have important roles to play in sustaining bipartisan commitment, and that long-term support for science depends on continued engagement across the political spectrum. Highlighting shared priorities that transcend party lines may help maintain bipartisan support for science funding, especially in polarized political environments.

Although these findings should not be interpreted as implying that Democrats do not value or support research and science funding, they do suggest that appropriations have historically been more generous under Republican control. One plausible explanation for our results is that Democrats may have more competing discretionary spending priorities such as health care, education, or social insurance, leaving less funding available for science and research. Given a relatively stable size of the overall federal budget, Democrats may be faced with more challenging trade-offs. Alternatively, it could be the case that Republicans prioritize science and research funding more than their Democratic peers because a substantial portion of this funding is outlaid to private firms. Overall, more research is needed to understand the mechanisms driving these partisan disparities in science and research funding.

Our analysis also underscores the pivotal role of the president and the House of Representatives in shaping appropriations for science and research. The president's budget request plays an important role in shaping the appropriations bill enacted by Congress. Likewise, House-led appropriations decisions appear to exert substantial influence on overall funding levels, suggesting that advocacy efforts targeting this chamber may be particularly impactful. To safeguard long-term research from the transient nature of political control, policy frameworks should emphasize continuity and bipartisan collaboration in science funding legislation. Mechanisms like multi-year appropriations or independent advisory boards could help insulate research funding from short-term political shifts, ensuring consistent support for critical scientific endeavors.

Our inability to detect differences in field-level grant allocations based on partisan control is a welcome result in today's politically charged climate. This contrast with appropriations results suggests that while partisan dynamics shape funding across agencies, the field-level distribution of grants appears comparatively stable, perhaps reflecting the influence of internal processes such as peer review. This consistency highlights the importance of maintaining mechanisms, such as peer-review processes and advisory panels, that help depoliticize individual grant-funding decisions. Strengthening these safeguards can further protect the independence of federally funded research, particularly as subtle differences in funding priorities may emerge under different partisan control.

Appropriations data, as presented in this study, provide a powerful tool for policy-makers, researchers, and advocates to monitor and evaluate the influence of political control on science funding. By identifying trends and patterns over time, such data can guide targeted advocacy efforts and ensure funding continuity for critical long-term research areas, such as climate science, public health, and basic research. The CHIPS and Science Act of 2022, which authorized $280 billion for science and technology research and manufacturing, illustrates that bipartisan collaboration is achievable, even in today's polarized climate. Although the full realization of these commitments depends on subsequent appropriations, the Act nonetheless aligns with our findings, showing that science funding can attract cross-party support when framed around shared priorities.

It is important to note, however, that although appropriations data provide a comprehensive view of federal science spending, they cannot be easily linked to specific scientific outcomes. Moreover, our ability to draw strong causal inferences is constrained by the limited variation in partisan control over the 40-year period of observation, and the endogeneity of party control. In some subperiods—particularly earlier decades—party control of the House and Senate is highly collinear, further limiting statistical leverage. As such, we caution against overinterpreting the magnitude of estimated effects. Our findings are best understood as descriptive patterns of association between partisan control and science funding—patterns that are robust across multiple specifications (see supplementary materials) and broadly consistent with institutional theories of agenda control (*11*). Finally, given the constraints of statistical power and the difficulty of isolating effects in more polarized recent periods (e.g., post-2010), these results should be viewed primarily as documenting historical relationships rather than fully capturing contemporary dynamics. Given recent signals of declining trust in science among Republican policy-makers (*14*), the past support that we observe is not a guarantee of future funding priorities. Indeed, recent executive budget proposals calling for substantial cuts to major scientific agencies illustrate how quickly shifts in political alignment can reshape the funding and scientific landscape. Policy-makers and science communicators should continue to emphasize the immense social, economic, and strategic value of bipartisan investments in science to sustain long-term support.

Overall, our findings highlight the complexity of the relationship between political control and federal science funding, challenging conventional narratives and providing a more nuanced understanding of the bipartisan dynamics at play. By illuminating these dynamics, this paper offers a foundation for more effective science advocacy and policy design. It underscores the importance of framing science funding as a bipartisan priority that advances shared societal goals, while also calling for vigilance to protect science from political interference. □

REFERENCES AND NOTES

1. D. Wang, A.-L. Barabási, *The Science of Science* (Cambridge Univ. Press, 2021).
2. P. Stephan, *How Economics Shapes Science* (Harvard Univ. Press, 2012).
3. A. Lupia, S. Soroka, A. Beatty, *Science* **6**, eaaz6300 (2020).
4. F. E. Lee, *Insecure Majorities: Congress and the Perpetual Campaign* (Univ. of Chicago Press, 2016).
5. M. Solovey, Social Science for What?: Battles over Public Funding for the "Other Sciences" at the National Science Foundation (MIT Press, 2020).
6. B. Hammond, *Essays on Budgetary Politics* (thesis, Princeton University, 2022).
7. C. Herzog, D. Hook, S. Konkiel, *Quant. Sci. Stud.* **1**, 387 (2020).
8. B. Hammond, L. Rosenstiel, *Am. Polit. Sci. Rev.* **114**, 603 (2020).
9. S. Ashworth, C. R. Berry, E. Bueno De Mesquita, *Theory and Credibility: Integrating Theoretical and Empirical Social Science* (Princeton Univ. Press, 2021).
10. Gustafson *et al.*, *Energy Policy* **141**, 111448 (2020).
11. G. W. Cox, M. D. McCubbins, Legislative Leviathan: Party Government in the House (Cambridge Univ. Press, 2007).
12. Government-Wide Contracting FY 2023 Update, US Government Accountability Office (May 2024).
13. N. Oreskes, E. M. Conway, *Daedalus* **151**, 98 (2022).
14. A. C. Furnas, T. M. LaPira, D. Wang, *Science* **388**, 362 (2025).
15. A. C. Furnas *et al.*, Data and code for "Partisan disparities in the funding of science in the United States," Harvard Dataverse (2025); https://doi.org/10.7910/DVN/UJ6RDU.

ACKNOWLEDGMENTS

The authors thank M. Reynolds, B. Hammond, and P. Hanson for their feedback and assistance, and A. Freilich for editing. We acknowledge grant suport from the National Science Foundation (award no. 2404035). All data and code necessary for replication can be found at (*15*).

SUPPLEMENTARY MATERIALS

science.org/doi/10.1126/science.adx5154

10.1126/science.adx5154

[1]Center for Science of Science and Innovation, Kellogg School of Management, Northwestern University, Evanston, IL, USA. [2]Ryan Institute on Complexity, Kellogg School of Management, Northwestern University, Evanston, IL, USA. [3]Northwestern Innovation Institute, Kellogg School of Management, Northwestern University, Evanston, IL, USA. [4]Department of Statistics, Harvard University, Cambridge, MA, USA. [5]Department of Political Science, Vanderbilt University, Nashville, TN, USA. [6]McCormick School of Engineering, Northwestern University, Evanston, IL, USA. Email: dashun.wang@northwestern.edu

REVIEW SUMMARY

BATTERIES

The contrast between monovalent and multivalent metal battery anodes

Yuanjian Li†, Sonal Kumar†, Gaoliang Yang†, Jun Lu*, Yan Yao*, Kisuk Kang*, Zhi Wei Seh*

Full article and list of author affiliations: https://doi.org/10.1126/science.adl5482

BACKGROUND: Batteries are an integral component of an electrified modern society, as they power consumer electronics and electric vehicles and help to integrate intermittent renewable energy into smart grids. With performance requirements constantly increasing, there is much demand for high–energy density and low-cost batteries, beyond the capabilities of widely commercialized lithium (Li)–ion batteries. For a battery anode, Li metal is considered to be one of the most attractive choices because of its high theoretical specific capacity and negative electrochemical potential. Other promising anode candidates include sodium (Na), potassium (K), magnesium (Mg), calcium (Ca), and aluminum (Al) metals, as their crustal abundance is higher than that of Li. Furthermore, all these monovalent (Li, Na, K) and multivalent (Mg, Ca, Al) metal anodes are indispensable for next-generation high-energy, low-cost metal-sulfur and metal-air batteries.

ADVANCES: After decades of research and development, the practical applications of the monovalent and multivalent metal anodes in nonaqueous rechargeable batteries are still plagued by common problems and specific challenges. (i) Irregular deposition is a common occurrence during electrochemical plating of Li, Na, K, Mg, Ca, and Al metals; however, the deposition morphologies are distinct for different metals. Specifically, monovalent metals easily grow into whisker-like, moss-like, and tree-like dendrites, whereas multivalent metals prefer deposition morphologies such as interconnected platelets and random fibers or spheres. There are also some reports of spherical dendrite growth for monovalent anodes and tree-like growth for multivalent anodes. (ii) Owing to their negative electrochemical potential, the considered metal anodes can readily react with electrolyte components such as solvents and salts to produce a heterogeneous interface layer, comprising both organics and inorganics. In monovalent batteries, Li^+, Na^+, and K^+ cations are mostly surrounded by solvent molecules, and the as-formed solvent-dominated solvation structure leads to the production of organic-rich solid-electrolyte interphases (SEIs) on Li, Na, and K anodes, which permit the facile conduction of their respective ions. Conversely, the multivalent nature of Mg^{2+}, Ca^{2+}, and Al^{3+} cations not only induces a strong tendency to form anion-participated solvation structure in conventional nonaqueous electrolytes but also tends to form inorganic-rich SEI layers. This makes it more difficult for multivalent cations with high charge density to diffuse across the nanointerface between the electrolyte and their corresponding metal anodes.

OUTLOOK: With a comprehensive understanding of the commonalities and differences between the electrochemical characteristics of monovalent and multivalent metal anodes, some general design principles and universal trends for these metal anodes emerge. (i) The desired deposition morphology for reversible metal cycling should comprise homogeneous and closely packed crystals with a specific crystallographic orientation, for example, (110) for Li, Na, and K; (002) for Mg; and (111) for Ca and Al. (ii) A favorable SEI usually requires similar homogeneous structures (e.g., multilayer and monolithic structures) yet different chemical compositions (e.g., a fluorinated inorganic-rich SEI for Li, Na, and K versus a hydrogenated organic-rich SEI for Mg and Ca) to achieve some universal merits of high ion conductivity, electronic insulation, (electro)chemical stability, and mechanically rigid-flexible synergy. (iii) Smart electrolyte design strategies are required to achieve desired deposition morphology and SEI chemistries, for example, (locally) high salt concentration and weakly solvating electrolytes for monovalent systems versus strongly solvating and weakly ion-paring electrolytes for multivalent systems. The successful commercialization of these metal anode-based battery technologies further demands leveraging intrinsic advantages for specific applications, for example, high-energy Li-metal batteries for long-range electric vehicles, cost-effective Na- and K-metal batteries for large-scale energy storage, and thermally resilient Mg-, Ca-, and Al-metal batteries for extreme-environment applications. □

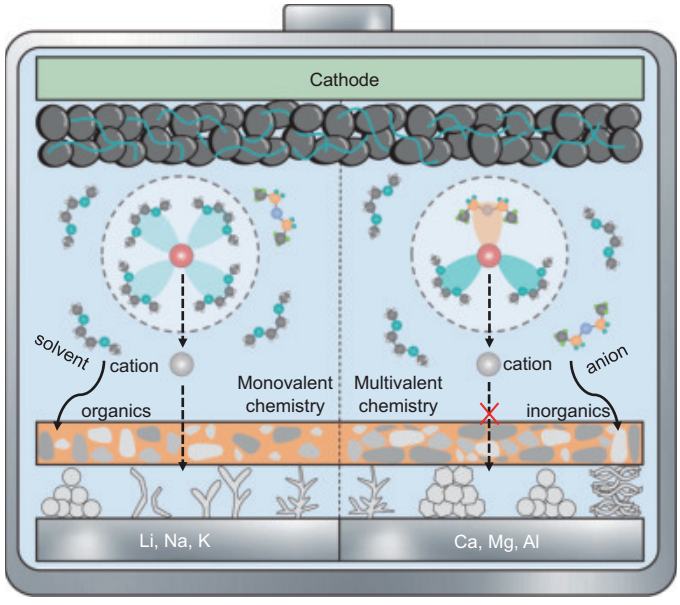

Electrochemical behavior of monovalent and multivalent metal anodes. In the monovalent battery (left), cations tend to coordinate with solvent molecules, forming a solvent-dominated electrolyte solvation structure that is easily reduced to form an organic-rich, ion-conducting interphase. In the multivalent battery (right), the stronger Coulombic force of multivalent cations toward anions leads to an anion-participated electrolyte solvation structure, the decomposition of which induces the formation of inorganic-rich, ion-insulating interphases. Furthermore, unlike monovalent metals, which easily grow into whisker-like, moss-like, and tree-like dendrites, multivalent metals prefer deposition morphologies such as interconnected platelets and random fibers or spheres.

*Corresponding author. Email: junzoelu@zju.edu.cn (J.L.); yyao4@uh.edu (Y.Y.); matlgen1@snu.ac.kr (K.K.); sehzw@imre.a-star.edu.sg (Z.W.S.) †These authors contributed equally to this work. Cite this article as Y. Li *et al.*, *Science* 390, eadl5482 (2025). DOI: 10.1126/science.adl5482

RESEARCH

IN *SCIENCE* JOURNALS

Edited by **Michael Funk**

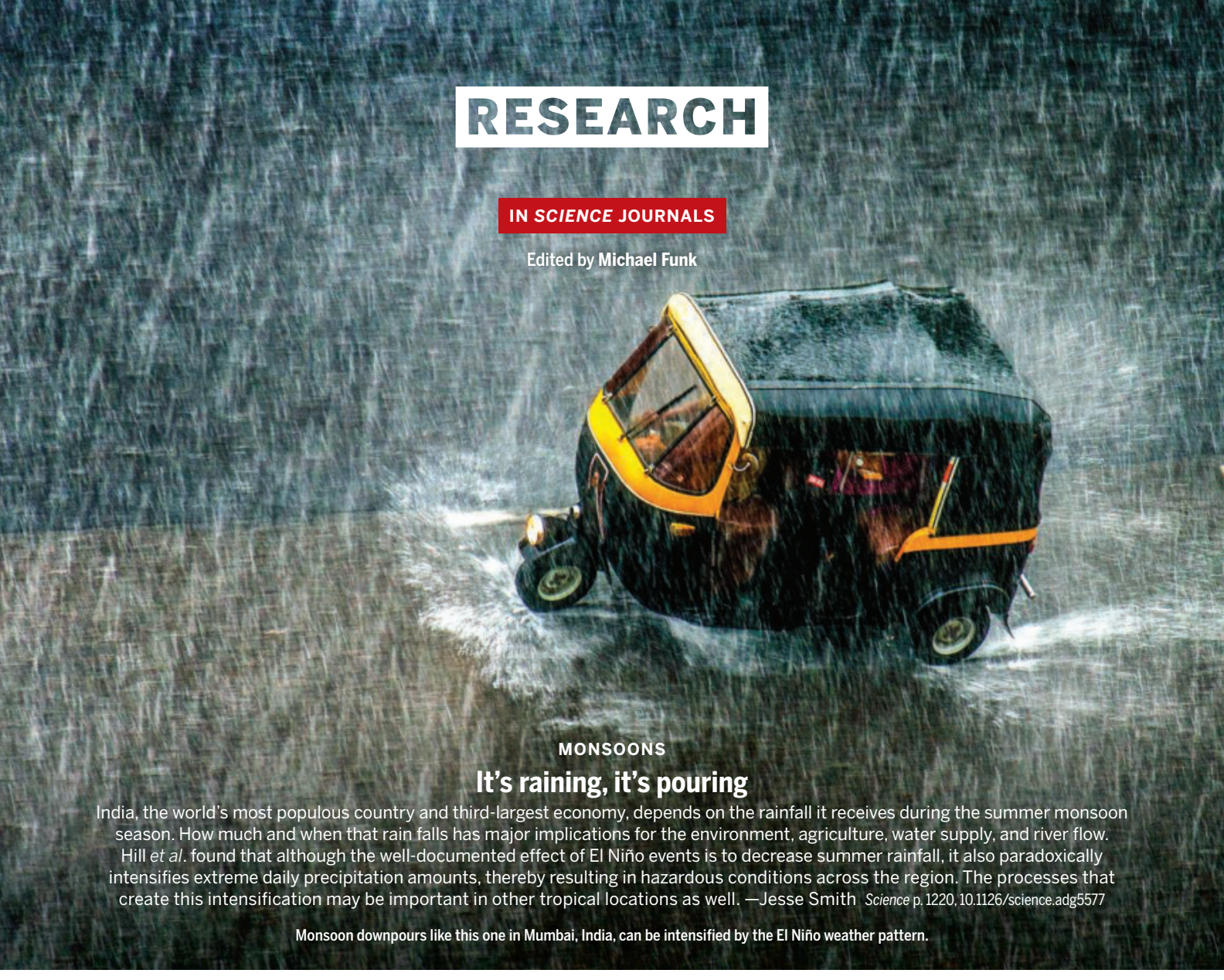

MONSOONS

It's raining, it's pouring

India, the world's most populous country and third-largest economy, depends on the rainfall it receives during the summer monsoon season. How much and when that rain falls has major implications for the environment, agriculture, water supply, and river flow. Hill *et al*. found that although the well-documented effect of El Niño events is to decrease summer rainfall, it also paradoxically intensifies extreme daily precipitation amounts, thereby resulting in hazardous conditions across the region. The processes that create this intensification may be important in other tropical locations as well. —Jesse Smith *Science* p. 1220, 10.1126/science.adg5577

Monsoon downpours like this one in Mumbai, India, can be intensified by the El Niño weather pattern.

PHOTO: PUNEET VIKRAM SINGH, NATURE AND CONCEPT PHOTOGRAPHER/GETTY IMAGES

ANIMAL COMMUNICATION

Confirming the intuitive

Humans naturally categorize sounds, whether they be from our own languages or those we perceive in other species. We can't directly ask those species, however, whether our categorization of their sounds matches their own interpretations of the meanings associated with them. Elie *et al*. conducted auditory discrimination tasks with zebra finches and found that the birds both discriminated and categorized the presumed meanings of their calls. Thus, the birds both understand the categories of their calls and create mental representations of their meaning, similar to what humans do. —Sacha Vignieri

Science p. 1210, 10.1126/science.ads8482

MARINE ECOLOGY

Stressed seas

Human activities are putting increased pressure on marine ecosystems. Halpern *et al*. mapped the intensity of 10 different types of human-caused pressure, including the effects of climate change, fishing, and pollution, across the global oceans. Overlapping these data with the distribution of marine habitats and their vulnerabilities to stressors provides estimates of total impacts on ecosystems. Cumulative impacts are expected to double by midcentury, including in countries and coastal areas where people depend heavily on marine resources. Ocean warming and fisheries are two of the largest impacts, suggesting that curbing climate change and sustainable fisheries management could relieve stress on marine ecosystems. —Bianca Lopez

Science p. 1216, 10.1126/science.adv2906

RANGELANDS

Drivers of degradation

Rangelands provide livelihoods for billions of people but are being increasingly degraded. Overgrazing is often cited as a cause of this degradation, but the relative effects of grazing and climate change are poorly understood. Purevjav *et al*. designed a quasiexperimental study to disentangle the effects of climate and herd size on rangeland primary productivity in Mongolia, where livelihoods depend on rangelands and more than half of these rangelands are considered degraded. Although herd size had a negative effect on productivity, weather effects were much larger, particularly at decadal scales over which herders can adapt to changing conditions. These results

suggest that policies limiting herd sizes may affect people without preventing rangeland degradation and support the need to curb climate change to protect ecosystems and livelihoods. —Bianca Lopez

Science p. 1229, 10.1126/science.adn0005

QUANTUM PROCESSING

Entangling nuclear spins

The maturity of experimental studies of nuclear magnetic resonance and the sophistication with which nuclear spins can be manipulated provided the first demonstration of a quantum computer platform. However, progress stalled early on when it was realized that scaling up was problematic. Stemp *et al*. now demonstrate direct entanglement between two nuclear spins that are separated by a relatively long distance. Two phosphorus atoms implanted in silicon formed a system comprising two ^{31}P nuclei and two bound electrons. Control of the exchange interaction between the two electrons resulted in quantum entanglement of the two nuclear spins. The results and scalability of the method are promising for the development of nuclear spin–based quantum computers. —Ian S. Osborne

Science p. 1234, 10.1126/science.ady3799

ORGANIC CHEMISTRY

Sulfur helps produce Z olefins

An enduring challenge in organic chemistry is the selective synthesis of Z olefins, carbon-carbon double bonds with the largest substituents on each carbon oriented on the same side of the bond axis. Verardi *et al*. report a method that electrochemically replaces carbon-hydrogen bonds on olefins with sulfonium groups. Surprisingly, one of the groups then underwent elimination in a Z-selective manner. The other group could then be replaced with a versatile range of substituents that preserve the Z geometry. —Jake S. Yeston

Science p. 1239, 10.1126/science.adv7630

INNATE IMMUNITY

Ramping up NK cells with mTORC1

Natural killer (NK) cells have antitumor activity that is primed by interleukin-15 (IL-15) and IL-18, components of a cytokine cocktail used in NK cell–based cancer immunotherapy. Fallone *et al.* found that IL-15 and IL-18 synergized to activate the signaling complex mTORC1, which resulted in increased proliferation and function of both mouse and human NK cells. IL-15 and IL-18 stimulated mTORC1 activity through distinct pathways not previously implicated in its regulation. The combination of IL-15 and IL-18 improved the survival of mice engrafted with tumor cells, suggesting a therapeutic strategy to enhance the efficacy of NK cell–based cancer immunotherapy. —Wei Wong

Sci. Signal. (2025) 10.1126/scisignal.adq8778

CLIMATE IMPACTS

A fiery blow to snow loss

As the climate has warmed, the mountainous regions of the western US have experienced earlier snow cover loss. This change threatens water resources and may result in greater wildfire extent and frequency, consequences that in turn pose a threat to ecosystems and communities. Koshkin *et al*. used remote sensing data to demonstrate that the increase in low-albedo burned and charred forests within snow-dominated watersheds is further exacerbating snow melt, particularly at lower elevations. This trend will likely continue with further warming. Identifying those areas where the timing of postfire snow decrease will be the greatest is critical for managing already vulnerable water resources. —Peter U. Clark

Sci. Adv. (2025) 10.1126/sciadv.adt9866

IN OTHER JOURNALS

Edited by **Corinne Simonti** and **Jesse Smith**

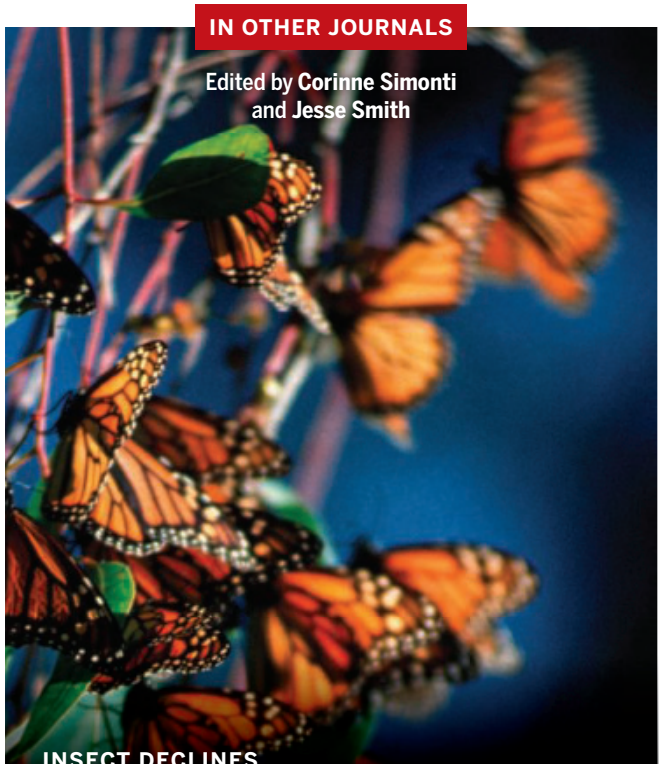

INSECT DECLINES

Mass monarch mortality

Monarch butterflies were once welcomed each year as they returned from their southern migrations to various mass roosting sites. However, since the 1980s, their North American populations have declined by 80 to 90%. Many drivers of this decline have been hypothesized, but the specifics remain unclear. Cibotti *et al.* tested butterflies collected from a mass mortality event that occurred at an overwintering site in California. They found evidence of 15 different pesticides within the bodies of the monarchs, with individuals containing several on average. Pyrethroid insecticides were present in nearly every animal and at or near the chemical's lethal dose. Although other factors may also be contributing to the decline of monarch butterflies, insecticides are clearly taking a heavy toll. —Sacha Vignieri

Environ. Toxicol. Chem. (2025) 10.1093/etojnl/vgaf163

Monarch butterflies collected near Pacific Grove, California, were found to contain high doses of insecticides, which is likely contributing to their declining populations.

IMMUNOMETABOLISM

Too tired to fight

$CD8^+$ T lymphocytes are specialized immune cells that kill tumors and foreign pathogens. As T cells lose the capacity to proliferate, they enter an exhausted-like state that reduces their ability to fight tumors and infected cells. Because T cell proliferation requires mitochondrial respiration, Steinert *et al.* investigated how mitochondrial functions affect distinct T cell states. Using genetically engineered T cells, the researchers studied the role of the mitochondrial electron transport chain and the effects of impaired complex III function. Mitochondrial metabolism was found to be

PHOTO: NORBERT WU/MINDEN PICTURES

FOOD CHEMISTRY

Chocolate's microbial flavor mixers

The appealing flavors of fermented foods are the result of microbial degradation and transformation of the raw food material. For complex foods such as cacao beans, this process can be heterogeneous and complex, with many species changing over time and according to local conditions. Gopaulchan *et al*. surveyed the microbial species involved in cacao bean fermentation at farms in Colombia and reconstructed a synthetic consortium containing five bacteria and four fungi capable of generating favorable flavors and chemical properties in fermentation experiments. These results provide a window of molecular and genetic insight into fermentation processes established by long tradition and experience.
—Michael A. Funk *Nat. Microbiol.* (2025) 10.1038/s41564-025-02077-6

Coffee bean fermentation using a synthetic mixture of particular bacteria and fungi can generate flavors and chemical properties similar to those produced by traditional fermentation methods.

required for T cell proliferation, whereas mitochondrial-derived reactive oxygen species were necessary for the formation of T cell memory responses.
—Priscilla N. Kelly
Nat. Immunol. (2025)
10.1038/s41590-025-02202-x

IMMUNOLOGY

Prior immunity changes pathology

After infection with *Mycobacterium tuberculosis* (Mtb), the bacteria that causes tuberculosis (TB), immune cells can aggregate in the lungs, forming structures known as granulomas. Gern *et al.* used mouse models to investigate the heterogeneity of these granulomas, particularly to understand how they differ depending on existing immunity to Mtb. In the absence of prior immunization, neutrophils prevented CD4 T cells from stimulating macrophages, and the mice developed granulomas with a core of dead cells, which had the potential to cause lung pathology. When mice were immunized in tandem with being infected, CD4 T cells and macrophage responses were more dominant, correlating with infected cells being contained within alveolar sacs.
—Sarah H. Ross
J. Exp. Med. (2025)
10.1084/jem.20250161

PHAGE WARFARE

Exclude and survive

Lytic bacteriophages infect bacteria, hijack their synthetic machinery to grow viral progeny, and then lyse the host cell, releasing new phages to infect new hosts. In a genetic screen for mutants of the bacterium *Bacillus subtilis*, Fiyaksel *et al*. identified the highly conserved protein YjbH as a key factor that restricts plaque expansion after infection by lytic phages. YjbH bound directly to the penetrating phage genome and accumulated beneath the phage injection site. Subsequently, YjbH confined the newly synthesized phage components to this specific subcellular position. The cell division machinery was then recruited to this site, forming an asymmetric septal barrier that encapsulated the phage components. This orchestrated "exclude and survive" mechanism effectively "cures" infected cells.
—Stella M. Hurtley
Cell Rep. (2025)
10.1016/j.celrep.2025.115994

FUEL CELLS

A gel makes contact

In traditional fuel cells, performance is often exchanged for flexibility. Tubular-shaped electrochemical cell configurations provide an expanded area for fuel generation, offering a portable energy supply. However, they require rigid support materials that decrease flexibility and interfacial contact. Yuan *et al.* incorporated woven cotton fibers encapsulated in a gel matrix in a direct methanol fuel cell. The cotton fibers provided support, and the cross-linked polymer gels underwent swelling in methanol that created external pressure in the radial direction. This produced sufficient interfacial contact between electrochemical cell components and suppressed unwanted methanol permeation into membrane electrode assemblies. This approach addresses key issues in flexible fuel cell design for practical applications. —Sumin Jin
Nat. Mater. (2025)
10.1038/s41563-025-02319-2

PHOTOPHYSICS

Double charged

Photoredox catalysis uses light to excite a chromophore that then activates reactants through electron transfer. In principle, the absorption of more than one photon could excite multiple electrons to spur complex reactions, but charge repulsion tends to hinder that option. Brändlin *et al.* now report the design of a special molecule that incorporates a ruthenium chromophore flanked by two electron acceptors on one side and two hole acceptors on the other. Sequential excitation produces two adjacent negative charges balanced by two adjacent positive charges in a high-energy state that persists for at least 100 nanoseconds, long enough for potential intermolecular reactivity.
—Jake S. Yeston
Nat. Chem. (2025)
10.1038/s41557-025-01912-x

PHOTO: CHUCHART DUANGDAW/GETTY IMAGES

RESEARCH ARTICLE SUMMARY

MOLECULAR BIOLOGY

Functional maps of a genomic locus reveal confinement of an enhancer by its target gene

Mathias Eder†, Christina J. I. Moene†, Lise Dauban, Mikhail Magnitov, Jamie Drayton, Marcel de Haas, Christ Leemans, Martijn Verkuilen, Elzo de Wit, Anders S. Hansen, Bas van Steensel*

Full article and list of author affiliations: https://doi.org/10.1126/science.ads6552

INTRODUCTION: Mammalian genes are regulated by promoters, in which transcription initiates, and enhancers that can activate them over long distances. However, exactly how the relative position of these elements within a genomic locus affects gene expression is still poorly understood.

RATIONALE: To study the logic underlying the relative positioning of genes and their enhancers, it is necessary to alter these arrangements systematically. We developed a high-throughput method based on the Sleeping Beauty transposon to randomly relocate ("hop") a fluorescent promoter reporter to thousands of positions within a single genomic locus. By sorting cells for different levels of reporter expression and mapping the location of integrations, we constructed detailed functional maps of reporter expression as a function of position throughout the locus. We applied this technology to map the functional landscape of the *Sox2* locus [about 1 megabase (Mb) in size] in mouse embryonic stem cells. This locus contains only one gene, *Sox2*, which is fully dependent on a large enhancer located ~100 kilobases (kb) downstream of the gene.

RESULTS: Hopping the reporter in the presence of the endogenous *Sox2* gene reveals that reporter activity is sharply confined to the region between the gene and the enhancer, with peaks of activity near the locations of the endogenous gene and enhancer. This functional map resembles the pattern of preexisting three-dimensional (3D) contacts of the enhancer, suggesting that these contacts are important for enhancer function. Upon deletion of the endogenous *Sox2* gene, reporter activity increases strongly throughout the locus and the enhancer can activate reporters across a larger region. This demonstrates that the endogenous *Sox2* gene confines the realm of influence of the enhancer. Because the reporter—driven by the *Sox2* promoter alone—had no such effect, we searched for a sequence in the gene that provides it with this competitive edge. Modified versions of the reporter revealed that the *Sox2* coding sequence, a single ~1-kb exon, boosts reporter activity and increases the ability to compete with the endogenous gene. Taken together with available epigenome and 3D interaction data, these results indicate that this coding sequence harbors an enhancer-like element that allows the gene to interact efficiently with the enhancer.

CONCLUSION: By inserting a promoter reporter into thousands of locations throughout the *Sox2* locus, we created high-resolution functional maps that reveal how the activity of a promoter depends on its precise genomic position. This revealed that the *Sox2* gene can confine the realm of influence of its own enhancer, limiting activation of a second promoter. This confining effect is at least partially encoded in the coding region of the *Sox2* gene. Our technology to locally relocate DNA elements in a highly scalable manner offers many opportunities to study fundamental aspects of genome biology. □

*Corresponding author. Email: b.v.steensel@nki.nl †These authors contributed equally to this work. Cite this article as M. Eder *et al.*, *Science* **389**, eads6552 (2025). DOI:10.1126/science.ads6552

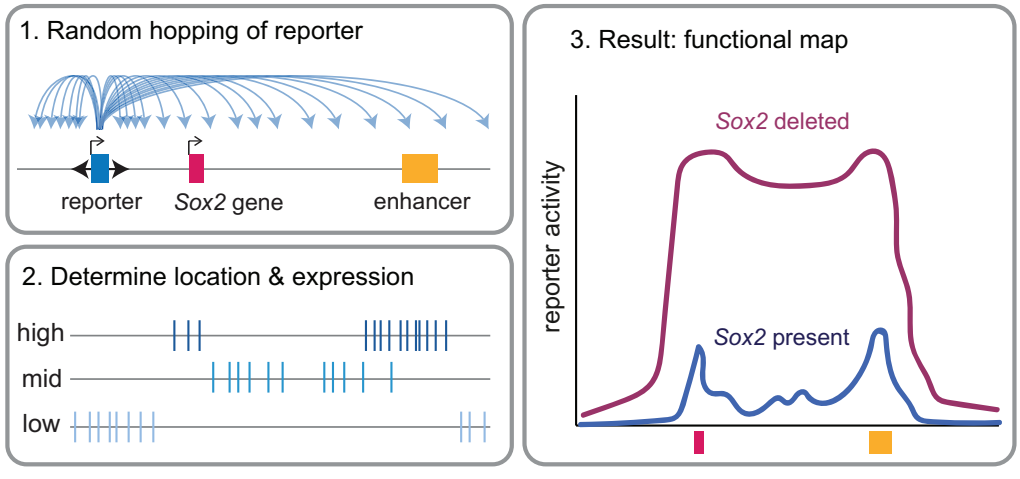

A high-throughput relocation tool to map the functional landscape of *Sox2* in mESCs. Relocation of *Sox2* reporters (1) to thousands of genomic locations in the endogenous *Sox2* locus (2) to map the location-dependent activity of the *Sox2* promoter. (3) The presence of the endogenous *Sox2* gene confines the realm of influence of the enhancer; upon *Sox2* deletion, the reporter activity increases and spreads across a wider region.

RESEARCH ARTICLE SUMMARY

MOLECULAR BIOLOGY

Kinetic organization of the genome revealed by ultraresolution multiscale live imaging

Joo Lee, Liang-Fu Chen, Simon Gaudin, Kavvya Gupta, Ana Novacic, Andrew Spakowitz, Alistair Nicol Boettiger*

Full article and list of author affiliations: https://doi.org/10.1126/science.adx2202

INTRODUCTION: Recent work revealed that genome folding is intricately organized, and this organization underlies critical genome functions, including how gene expression is regulated. A key player is cohesin, a motor protein complex hypothesized to extrude DNA loops and thus divide the genome into self-interacting structural domains. Yet individual genome folds are highly divergent and heterogeneous, where the domains only arise as a statistical average over many cells. Recent live imaging of genome motion highlights the dynamic nature of the genome, suggesting that motion, rather than structure, underlies genome function.

RATIONALE: To observe genome motion across multiple scales and chromatin states, we made improvements on current limitations of genome live imaging: resolution (in space and time) and coverage (both in number of observations and number of loci being observed). We optimized fluorescent DNA labels to be brighter, more photostable, and miniaturized. A pair of optimized fluorescent labels were inserted, and then one of the labels, designed to be self-tiling and self-mapping, was redistributed across the chromosome, rapidly generating cell lines with labels spanning various genomic separations. We imaged selected cell lines in ultraresolution—revealing previously unseen subsecond, nanometer-scale single-cell dynamics. Using automated microscopy and a computational framework to analyze high data volumes, we have collected unprecedentedly deep- and high-resolution live-cell genome motion data across genomic separations ranging from 5 kb to 73 Mb.

RESULTS: We find that genomic loci with submegabase separation, typical of regulatory elements and their target genes, can transition from their average distance (200 to 500 nm) to contact (<50 nm) in tens of seconds—much faster than previously anticipated. We find that these rapid search kinetics are confined within genomic domains, as crossing the domain boundary greatly impedes search speeds. Within these kinetic domains, search time is only weakly coupled to genomic separation—increasing from an average of 20 s for 20-kb separation to 60 s for 407-kb separation. Without cohesin, the kinetic differences between domains are lost. Intradomain searches take longer and depend more strongly on genomic separation, following the theoretical predictions of a "crumpled globule"—a densely packed, diffusing polymer. Moreover, we observed signatures of active loop extrusion in the form of previously unseen processive linear motion between loci pairs, unique to cohesin-positive cells and specific genomic separations predicted by polymer simulations with cohesin. These processive events provide an estimate of the in vivo speed of active loop extrusion of 2.7 kb per second.

CONCLUSION: Our results support the view of a highly dynamic, ever-refolding genome. We find that cohesin not only shapes the genome but also provides rapid motor activity, facilitating accelerated search between distant genomic elements. The domain boundaries function as a kinetic border, dividing the genome into kinetic domains of accelerated search—rather than stable, stereotyped structural domains as previously depicted. These findings, along with our improvements to live imaging of genome motion, help to elucidate how kinetic organization of the genome can shape genome function in individual cells. □

*Corresponding author. Email: boettiger@stanford.edu Cite this article as J. Lee *et al.*, *Science* **389**, eadx2202 (2025). DOI: 10.1126/science.adx2202

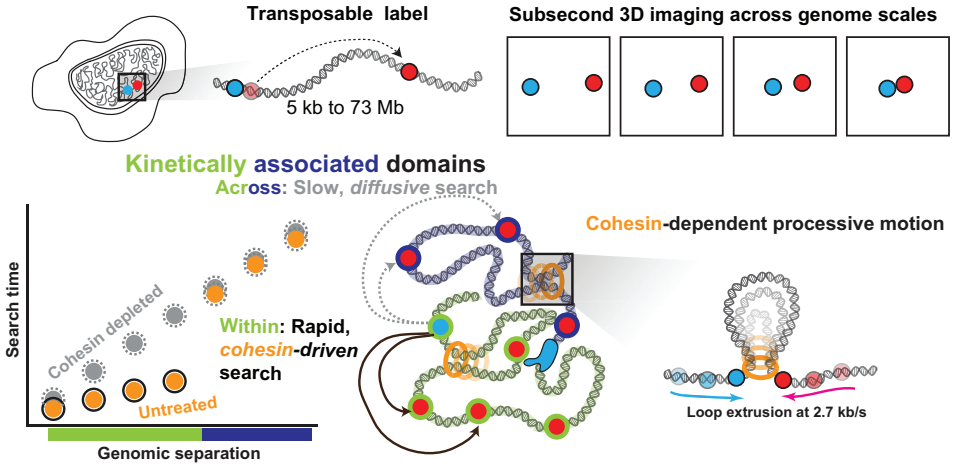

The genome is organized into kinetically associated domains. Pairs of DNA labels were distributed across the chromosome and imaged at subsecond resolution. Elements within the domains exhibit rapid, cohesin-driven search.

RESEARCH ARTICLE SUMMARY

POPULATION DYNAMICS

Genomic demography predicts community dynamics in a temperate montane forest

James P. O'Dwyer*, James A. Lutz, Tyler Schappe, Dana Alegre, Andrew N. Black, Niklaus J. Grünwald, F. Andrew Jones

Full article and list of author affiliations: https://doi.org/10.1126/science.adu6396

INTRODUCTION: Species population sizes inevitably fluctuate over time, with important consequences for ecological community composition and the maintenance of biodiversity. But developing and parameterizing predictive models for these population changes has been an outstanding challenge. Although abiotic variables such as rainfall can correlate with these fluctuations, a promising modeling approach for population dynamics is based on the effects of life history—i.e., the changes in vital rates over the life span of an individual organism. Life-history variation across species can serve to amplify or constrain population fluctuations, but quantifying these differences may require years or decades of observational data for mortality, growth, and reproductive rates.

RATIONALE: To address this challenge, we identify a connection between patterns of genomic variation within a single population, and the population dynamics within a community. Specifically, correlations among alleles across a set of genomes are related to the life history and recent size fluctuations of that population, particularly large demographic events such as population bottlenecks. Thus, population genomic assays across multiple co-occurring species in a community provide a window into their life-history differences and enable prediction of community dynamics. We test this connection in a temperate montane forest, the Wind River Forest Dynamics Plot in southern Washington state, where we characterize population genetic variation for eight dominant species and determine population size changes across three censuses.

RESULTS: Using a mean field model, we relate the observation of species population sizes at a single time point, alongside a single assay of genetic effective population size within each population, and use this combination to make predictions for the typical size of population fluctuations. In general, we expect that larger populations will exhibit larger fluctuations, but the precise relationship is nonlinear and has been challenging to predict from first principles. We show that our population genomic-derived predictions capture this scaling behavior, and that our predictions for population fluctuations are strongly correlated with demographic observations from traditional censuses. This accuracy is achieved without any tunable, free parameters.

CONCLUSION: Our study demonstrates that genomic demography can be used to make ecological predictions. Linkage disequilibrium correlations found within and among plant genomes record a history of past population dynamics, and this memory can then be used to make predictions for future dynamics. Notably, improvement in modeling accuracy was achieved with genetic information collected at a single time point. Given the expense of generating genetic data, only needing to collect such data once limits this potential burden. Our approach may also facilitate the incorporation of multiple other ecological processes, whenever those processes leave a detectable genomic signature. □

*Corresponding author. Email: jodwyer@illinois.edu Cite this article as J. P. O'Dwyer *et al.*, *Science* **389**, eadu6396 (2025). DOI: 10.1126/science.adu6396

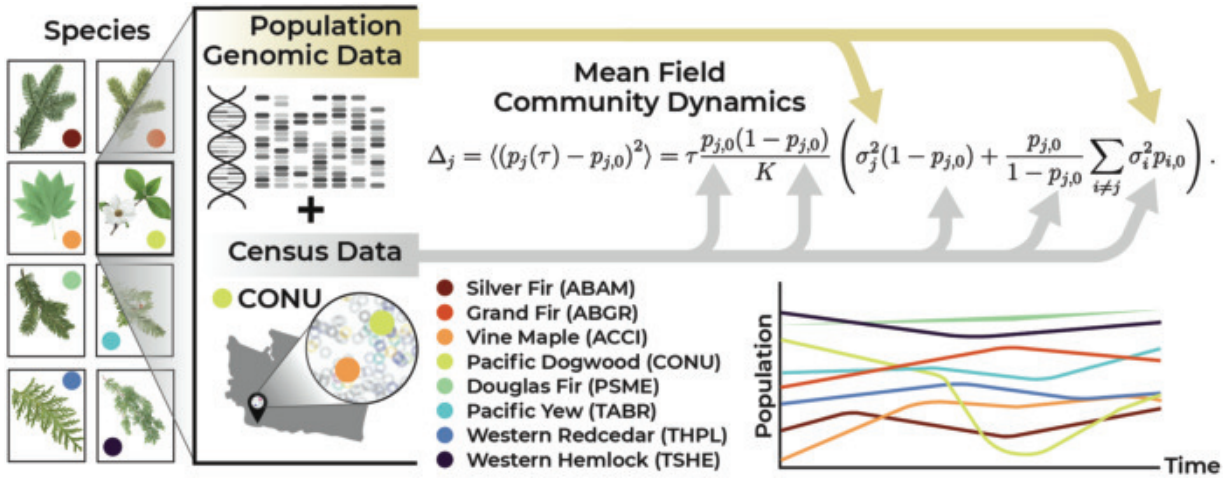

PHOTO CREDIT: DOROTHY LOUDERMILK

A pipeline for genomic demography. Population genomic data and census data can be combined to parameterize a mean field model of population dynamics and competition. The outcome of this model allows us to make predictions for population fluctuations over time. Species abbreviations are provided in table S1.

RESEARCH ARTICLE SUMMARY

MOSQUITO GENETICS

1206 genomes reveal origin and movement of *Aedes aegypti* driving increased dengue risk

Jacob E. Crawford* *et al.*

Full article and list of author affiliations: https://doi.org/10.1126/science.ads3732

INTRODUCTION: Approximately 4 billion people are at risk of contracting the mosquito-transmitted disease dengue each year in tropical and subtropical regions and increasingly in temperate regions. An effective vaccine for dengue is not widely available, so controlling the primary mosquito vector *Aedes aegypti* is key to limiting the impact of dengue and other viral diseases transmitted by this mosquito, including Zika, chikungunya, and yellow fever. The ancestral subspecies of *Ae. aegypti* is a forest-dwelling ecological generalist, *Ae. aegypti formosus* (*Aaf*), that feeds on a variety of hosts in Africa, but viral transmission is driven by a globally invasive, human-preferring subspecies, *Ae. aegypti aegypti* (*Aaa*), that emerged more recently. Historical disease records suggest that *Ae. aegypti* emigrated from Africa to the Americas on ships during the Atlantic slave trade (AST), but the role that the AST played in the origin of invasive *Aaa* is not clear. Previous global population genetic surveys revealed populations both inside and outside Africa distributed along an ancestry gradient between *Aaf* and *Aaa* that provided clues into the early stages of the domestication process leading to *Aaa*.

RATIONALE: Advances in whole-genome sequencing (WGS) and methods for inferring evolutionary patterns from WGS data have advanced the ability to resolve complex signals in population genetics data. However, WGS analysis of *Ae. aegypti* has been limited in large part by its genome that is both larger and more repetitive than most other insect pests. A WGS dataset including populations from both the ancestral subspecies *Aaf* and the invasive human-specialist *Aaa* would allow high-resolution inference of genetic signals that could produce a clearer understanding of historical shifts as well as contemporary movement and molecular changes that could impact public health.

RESULTS: In this work, we present the Aaeg1200 WGS dataset, including 1206 whole genomes from 73 locations throughout the distributions of *Aaf* and *Aaa*. We aligned sequencing reads to a chromosome-level genome reference sequence for analysis and identified sites of more than 141 million single-nucleotide polymorphisms (SNPs) , 53.3% of which are found exclusively in *Aaf*. To determine whether *Aaf*-like *Ae. aegypti* from Argentina is a recent introduction or relict from the AST, we fitted coalescent models to phased haplotypes and SNP frequency data and showed that Argentine *Ae. aegypti* split from African populations ~320 years ago around the time of the AST and that invasive *Aaa* split from Argentina ~100 years later. Representative invasive *Aaa* populations show signs of natural selection at several regions, suggesting a role for adaptation to new pathogens and feeding habits that may have enabled further expansion into new environments. On the basis of phased haplotype data, we show evidence for recent secondary contact among the subspecies that has, in some cases, resulted in extensive sharing of insecticide-resistance mutations and introduction of these mutations into Africa.

CONCLUSION: *Ae. aegypti* is a major threat to public health and also a useful model for the study of domestication, the evolution of human blood feeding, and neo-sex chromosome evolution, as well as additional basic and applied research questions. The Aaeg1200 WGS dataset was assembled to help address these and other questions to enable improved understanding of the molecular changes and evolutionary processes underlying this disease vector. Chemical insecticides are an essential tool in the fight against *Ae. aegypti*, and datasets such as Aaeg1200 will help understand and manage the spread of resistance and enable new tools to be developed in the fight to reduce the burden of dengue and other mosquito-borne viruses. □

*Corresponding author. Email: jacobcrawford@google.com Cite this article as J. E. Crawford *et al.*, *Science* **389**, eads3732 (2025). DOI: 10.1126/science.ads3732

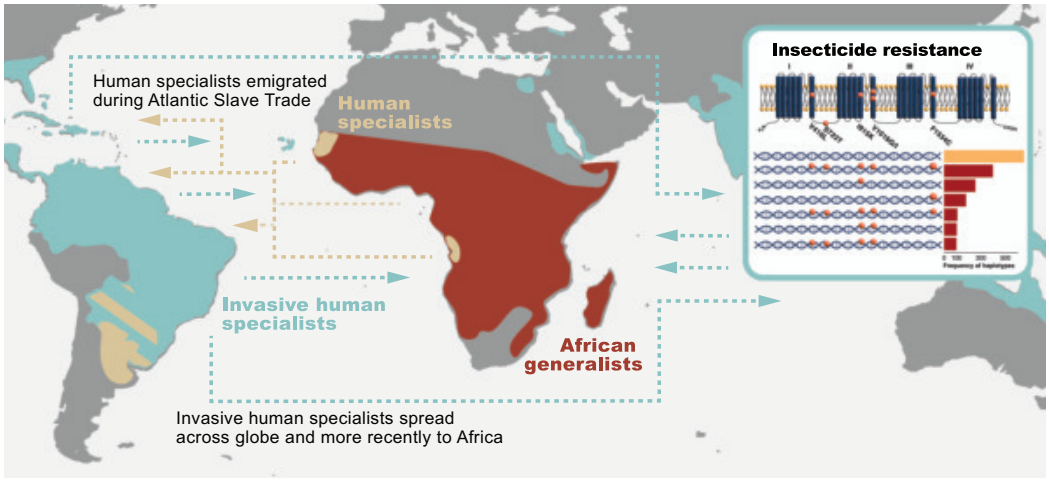

Invasive *Aedes aegypti* global migration spreads insecticide resistance and increases arboviral risk. DNA sequence analysis revealed that the origin of invasive *Ae. aegypti aegypti* occurred after emigration to the Americas and the Caribbean, where the subspecies adapted to new environments. Mutations conferring resistance to common insecticides have emerged independently in multiple locations and spread through recent transcontinental migration, increasing arboviral risk in Africa, among other locations.

RESEARCH ARTICLE SUMMARY

MOSQUITO GENETICS

Genomic diversity of the African malaria vector *Anopheles funestus*

Marilou Boddé†, Joachim Nwezeobi†, *et al.*

Full article and list of author affiliations: https://doi.org/10.1126/science.adu3596

INTRODUCTION: The mosquito species *Anopheles funestus* is a major contributor to human malaria transmission across its vast sub-Saharan African range. Vector control of the other three major malaria-transmitting species in the Gambiae Complex has benefited from a deep understanding of genetic diversity, population structure, and the emergence and spread of insecticide resistance through the whole-genome sequencing of hundreds of individuals from many African countries. We completed whole-genome sequencing of 656 modern samples collected since 2014 and 45 historic samples collected between 1927 and 1967 to create a foundational understanding of genomic diversity in *An. funestus* across the continent.

RATIONALE: Since large scale deployment of insecticides began in the 1950s, *An. funestus* has rapidly evolved resistance throughout much of its range. However, it is an open question whether resistance alleles have evolved independently in multiple locations, whether they are shared between different populations through gene flow, or whether resistant populations have entirely replaced historically susceptible populations. A clearer genomic view on continental population structure is crucial for implementing strategic use of insecticides, taking into account the potential emergence and spread of insecticide resistance alleles. Additionally, with the implementation of gene drive release for vector control likely in the coming years, we need to be able to predict the spread of gene drive under different release scenarios, which is only possible if detailed knowledge of population connectivity across the continent, and how it varies along the genome, is in place.

RESULTS: We found that the 17 geographic regions from which our samples originated form six population clusters with varying degrees of genome-wide differentiation. One of these populations, the Equatorial cohort, spans more than 4000 km and comprises individuals from seven countries. In close geographic proximity to this cohort, we found two genetically distinct ecotypes that appear to have a restricted range and distinct chromosomal karyotypes. Using a windowed principal components analysis (PCA) approach, we explored structure across the genome. We used this approach to identify segregating inversions and classify every individual into its specific inversion karyotype. We also identified genomic regions that have exceptional levels of divergence in comparison to other collinear parts of the genome. Some of these outlier regions are clearly driven by selection for insecticide resistance, as they contain loci with excessive haplotype sharing, often centered on genes known to play a role in insecticide resistance in many insect species. We show that the *Gste2* resistance allele has at least two independent origins and that, despite reports of DDT resistance emerging in the 1950s, none of the historic samples in this study carry DDT resistance alleles found in modern-day populations.

CONCLUSION: Variable structure—such as that observed in this work, with some populations readily sharing alleles across the continent, and others clearly geographically proximal but genetically distinct—is a challenge for vector control. Even if the Gambiae Complex disappeared today, malaria would still rage through Africa until *An. funestus* is also effectively targeted. The greater understanding of the high levels of genetic diversity and the complex population structure of *An. funestus* presented in this study will underpin smarter surveillance and targeted vector control. □

Corresponding author: Mara K. N. Lawniczak (mara@sanger.ac.uk) †These authors contributed equally to this work. Cite this article as M. Boddé *et al.*, *Science* **389**, eadu3596 (2025). DOI: 10.1126/science.adu3596

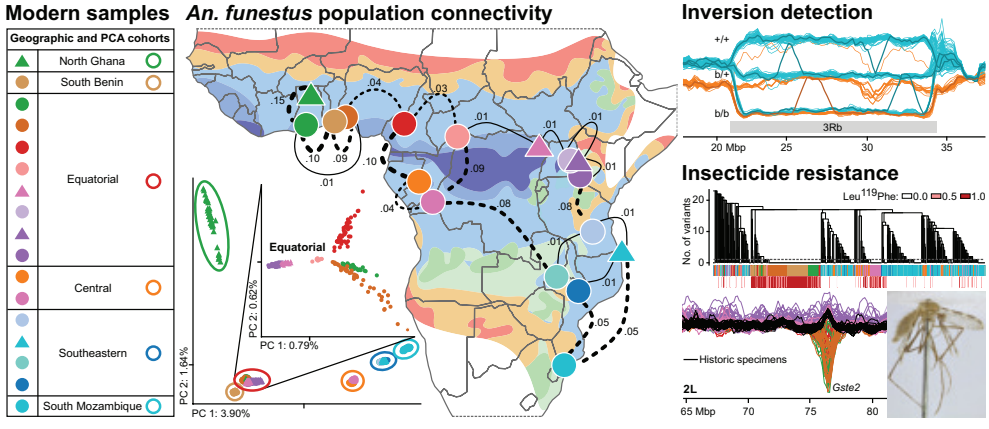

Continental population structure among 656 modern *An. funestus* specimens. PCA, fixation index (F_{ST}), and a windowed PCA approach reveal how population structure varies across the continent and along the genome. The windowed PCA shows distinct patterns for segregating inversions (including double recombinants) and loci under positive selection. Insecticide resistance mutations were found in selective sweeps on different haplotypic backgrounds, suggesting multiple independent origins, but most resistance mutations were not observed in 45 historic specimens. SNP, single-nucleotide polymorphism; L119F, Leu^{119}Phe mutation.

ANIMAL COMMUNICATION

Categorical and semantic perception of the meaning of call types in zebra finches

Julie E. Elie[1]*, Aude de Witasse-Thézy[2], Logan Thomas[3], Ben Malit[4], Frédéric E. Theunissen[1]*

Vocal communication in social animals involves the production and perception of various calls that ethologists categorize into call types based on their acoustical structure and behavioral context. Whether these categories indicate distinct meanings for the animals remains unknown. The zebra finch, a gregarious songbird, uses ~11 call types that are known to communicate hunger, danger, or social conflict and to establish social contact and bonding. Using auditory discrimination tasks, we show that the birds both discriminate and categorize all the call types in their vocal repertoire. In addition, systematic errors were more frequent between call types used in similar behavioral contexts than could be expected from their acoustic similarity. Thus, zebra finches organize their calls into categories and create a mental representation of the meaning of these sounds.

Social animals often possess a rich repertoire of distinct vocalizations used to communicate needs, internal states, and external events (*1*, *2*). To understand these vocal signals as a basic code for communication—the vocabulary of the species' "language" (*3*)—researchers have categorized the sounds into call types based on their acoustic properties, the context during which they are emitted, and the responses they elicit in receivers. However, the extent to which animals agree with human experts' categorizations remains an open question. Because such classification uses a multifaceted approach (*3*–*14*), we will refer to these call types as ethogram-based or Etho call types. Previous studies have shown that animals learn to categorize sounds along either natural or arbitrary acoustic dimensions (*15*) and generalize to new exemplars if the categories contain recognizable patterns (*16*). Here, we asked whether animals spontaneously distinguish all the Etho call types in their repertoire and whether their perception of these call types is categorical.

A second and more profound question is whether animals understand the meaning of Etho call types in a way that matches human interpretations. Without the ability to read animals' minds, answering this question is very difficult. The differences between the faculty of language in humans and that in other animals have often been argued to illustrate the gap in mental representations and cognitive abilities between them (*17*). It is a challenge to clearly demonstrate that animals' calls are not simply produced and responded to in a simple reflexive manner. The first demonstration of the potential referential property of animal calls came from studies in vervet monkeys, which adopt appropriate complex avoidance or escape behaviors in response to the playbacks of distinct alarm calls without the actual presence of the predator (*18*). This functional referential quality has now been demonstrated in multiple mammalian and avian species (*19*–*24*). However, it remains controversial whether animals that hear a specific alarm call have a mental representation of the predator or reflexively perform the appropriate escape or avoidance behavior that would be triggered upon hearing the specific alarm call (*25*). To address the nature of the mental or neural representation of the meaning of call types, ethologists must therefore rely on indirect measures where observed responses could not simply be explained as actions triggered by specific sound classes, but instead by their meaning.

To find out whether animals discriminate, categorize, and have a mental representation of the meaning of their Etho call types, we studied zebra finches. These gregarious songbirds have a vocal repertoire of 11 Etho call types used in distinct and well-characterized social behaviors [Fig. 1A, supplementary text, and fig. S1; (*7*, *8*)]. This vocal repertoire comprises a mixture of discrete signals (e.g., Begging call, Tet) and graded signals (e.g., Whine, Nest). Despite the differences in the degree of clustering, these 11 Etho call types are acoustically distinct and correctly classified by algorithms with ~60% accuracy; (average over diagonal terms in Fig. 1B) (*7*). Leveraging the ability of zebra finches to quickly learn to perform complex acoustical discrimination tasks (*26*, *27*), we quantified the birds' ability to discriminate all the Etho call types in their repertoire and assessed whether this discrimination shows properties of categorical perception. Next, we considered a hierarchical organization of their repertoire to cluster Etho call types into six semantic hypercategories (contact, agonistic, begging, courtship, pair-bonding, and alarm; Fig. 1A) and assessed whether discrimination is sensitive to the shared meaning of Etho call types beyond what could be expected from acoustic similarities.

Perceptual discrimination of Etho call types

To evaluate how adult zebra finches classify their species' vocalizations, we used an operant task (*26*, *27*) where birds (six males and six females) were asked to discriminate one Etho call type (rewarded) from all other 10 Etho call types (nonrewarded) (Fig. 2A). The bird self-initiated the playback of stimuli by pecking a key and demonstrated its classification of stimuli as rewarded or nonrewarded, respectively, by refraining from pecking the key for 6 s after the stimulus onset or by pecking the key within these 6 s and effectively interrupting the playback to fast-forward to the next trial (Fig. 2A). A reward was only dispensed after the full 6-s playback of a rewarded stimulus. Birds quickly learned to interrupt the nonrewarded stimuli. The probability of interruption quantified the classification performance. The set of stimuli used for each Etho call type consisted of a large ensemble of renditions ($n = 120$) produced by a dozen different unfamiliar birds (*7*). Because the same rendition from the same vocalizer was rarely heard twice, the birds had to rely on the acoustic features that are invariant and specific to each Etho call type. For each subject, all 11 Etho call types were successively used as the rewarded stimulus (Fig. 2, B and C). Despite the challenges of this task, all subjects successfully classified calls along Etho call types (Fig. 2D). The probability of correct classification across birds and Etho call types was highly significant with a large effect size [statistical significance established by conducting a likelihood ratio test (LRT) between two generalized linear mixed-effect (GLME) models that predicted the Probability of Interruption, with or without the Reward Contingency as the fixed effect, and with Subject as a random effect; LRT1 table S1, $n = 73{,}329$ trials, $p = 2.42 \times 10^{-8}$ (*28*)]. Male and female birds performed equally well (LRT2 table S1, $n = 73{,}329$, $p = 0.41$). Three of the least acoustically clustered Etho call types—the Nest, Aggressive, and Distress calls—were also the least well discriminated (Figs. 1 and 2D and table S2). Despite these small differences in performance (LRT3 table S1, $n = 73{,}329$, $p < 2.2 \times 10^{-16}$), all Etho call types were discriminated above chance level (Fig. 2D and table S2). Zebra finches excelled at discriminating all the Etho call types of their repertoire.

[1]Neuroscience Department, Helen Wills Neuroscience Institute, University of California, Berkeley, Berkeley, CA, USA. [2]Master de Biologie, École Normale Supérieure de Lyon, Université Claude Bernard Lyon 1, Université de Lyon, Lyon, France. [3]Department of Biophysics, University of California, Berkeley, Berkeley, CA, USA. [4]Rausser College of Natural Resources, University of California, Berkeley, Berkeley, CA, USA. *Corresponding author. Email: julie.elie@berkeley.edu (J.E.E.); theunissen@berkeley.edu (F.E.T.)

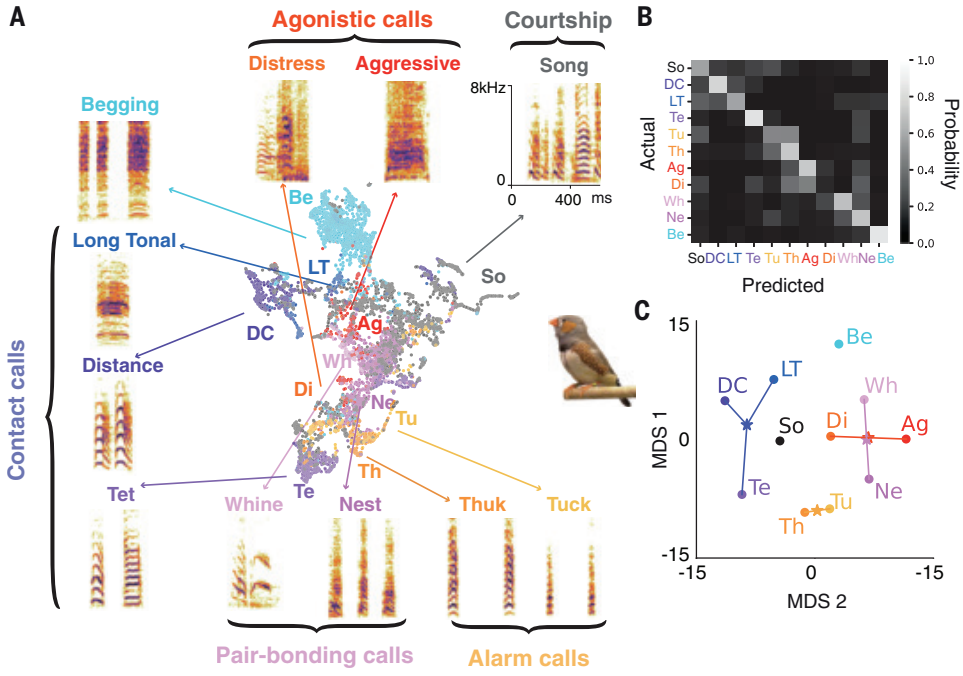

Fig. 1. The acoustic space of the zebra finch vocal repertoire. (**A**) The zebra finch vocal repertoire is divided into 11 Etho call types. All call renditions (>8000) in our database (*46*) collected from 45 male and female birds are projected in a 2D nonlinear embedding (UMAP) applied to predefined acoustic features and color-coded according to Etho call types [(*28*); fig. S1]. [Image credit: J.E.E.] (**B**) Confusion matrix quantifying the cross-validated performance of LDA at classifying calls into the Etho call types using spectrograms. Data are from (*7*). (**C**) The probability of correct (diagonal terms) and incorrect classification (off-diagonal terms) is used in an MDS analysis to obtain the acoustic "classification distances" between Etho call types (*28*). Distances between Etho call types depend on both the acoustic distances between the centroids of each cloud of points and the spread of these clouds as seen in (A). Etho call types belonging to the same semantic hypercategory are connected with edges to the centroid of the hypercategory (star). Ag, Aggressive call; Be, Begging call; DC, Distance call; Di, Distress call; LT, Long tonal call; Ne, Nest call; So, Song; Te, Tet; Th, Thuk; Tu, Tuck; Wh, Whine.

Etho call types are genuine perceptual categories

Given the very high number of exemplars used for each Etho call type in the discrimination task, it is highly improbable that birds memorized which stimuli were rewarded. Instead, they must have formed categories based on invariant features specific to each Etho call type and ignored the acoustic variability found across vocalizers (*26*) and renditions (*29*). But the formation of such a generalization rule (*16*) does not imply categorical perception. An individual demonstrates categorical perception when its perception is influenced by the sensory categories it possesses (*30*). One consequence of categorical perception is the formation of a sharp perceptual boundary in the binary classification of items (calls) belonging to two different categories (Etho call types) although these items are linearly dispersed along a physical similarity dimension (the acoustic similarity between calls). We evaluated this effect in zebra finches that were performing simple pairwise discriminations of three Etho call types (Distance call versus Tet, or Thuk versus Tet). All seven naïve birds successfully discriminated Etho call types between the multiple renditions from four different unfamiliar vocalizers (day 1 in Fig. 3, A and B; 7/7 Fisher's exact test with $p < 0.05$; LRT4 table S1, $n = 4822$ trials, $p = 2.77 \times 10^{-6}$). We then evaluated the shape of the empirical classification function. A theoretical model for categorical perception (*31*) predicts a sharp sigmoid for the classification function along the physical dimension that best discriminates between the two categories [red line in Fig. 3C and fig. S4 (*28*)], whereas in the absence of categorical perception, the theory predicts a linear function along the same dimension (blue line in Fig. 3C). The physical dimension that best differentiated rewarded from nonrewarded calls was obtained by applying linear discriminant analysis (LDA) on the spectrograms of calls (*28*). The empirical classification of each call rendition was then reported along that acoustic axis, the LDA dimension (Fig. 3C and fig. S4). As expected in the presence of categorical perception, the empirical classification values were similar for all calls belonging to the same Etho call type (horizontal solid lines in the bottom plots of Fig. 3C). We used GLMEs to predict the empirical classification function from the positions of the calls on the acoustic axis, the Etho call type, or both (full model). In the full model, the Etho call type was essential for predicting the empirical classification (LRT5 table S1, Distance call versus Tet: $n = 1079$ trials, four birds, $p = 0.036$; LRT6 table S1, Thuk versus Tet: $n = 285$ trials, three birds, $p = 1.02 \times 10^{-5}$). For Etho call types that formed distinct and nonoverlapping acoustic clusters, the positions of calls on the acoustic axis also contributed to the full model performance (LRT7 table S1, Distance call versus Tet: $n = 1079$, $p = 0.027$). By contrast, it had no additional effect for less acoustically clustered Etho call types (LRT8 table S1, Thuk versus Tet: $n = 285$, $p = 0.87$), and the GLME model using only the Etho call type as a predictive variable was the most parsimonious (Thuk versus Tet; dotted lines in Fig. 3C; Akaike information criterium shown in Fig. 3D). Irrespective of the pairwise discrimination, the empirical data and their statistical model using Etho call types as the unique predictor were close to the theoretical model of categorical perception and distinct from the theoretical model of linear perception [compare the dotted line with the red and blue lines in the top plots of Fig. 3C; fig. S4 (*28*)]. Thus, the discrimination of calls is influenced by the Etho call type categories and not solely driven by the calls' distinctive acoustic features. The classification behavior of the birds is also consistent with categorical perception.

Whether the categorical perception of Etho call types was innate or acquired during development rather than learned during the discrimination task also remained to be shown. We reasoned that deciphering the contingency rule (i.e., learning which Etho call type was rewarded for each test) would be enough to resolve the task if birds were relying on internal representations of Etho call types, and any reversal of the rule for the renditions of some specific vocalizers (incongruent calls; Fig. 3) would present an extra challenge to the birds, forcing them to learn a new categorization rule that does not follow their language. On days 2 and 3, we tested the capacity of zebra finches to generalize their classification to the calls of new unfamiliar vocalizers (New). On day 2, the reward contingency for the New calls followed that of day 1, whereas on day 3, the reward contingency of New calls was reversed. We found (*28*) that birds immediately and perfectly classified Etho call types from new vocalizers on day 2, but that on day 3, they continued to apply the discrimination rule that they had learned on prior days: They classified the new calls based on their Etho call types and not based on their reward contingency. Over the day, the birds slowly learned to flip the reward contingency for the new vocalizers' calls, indicating that they could learn to jointly recognize the call type and the signature of vocalizers (*26*, *27*) and apply the new arbitrary reward contingency rule. Taken together, these results show that zebra finches trained at Etho call type discrimination will spontaneously group new vocalizations using Etho call types.

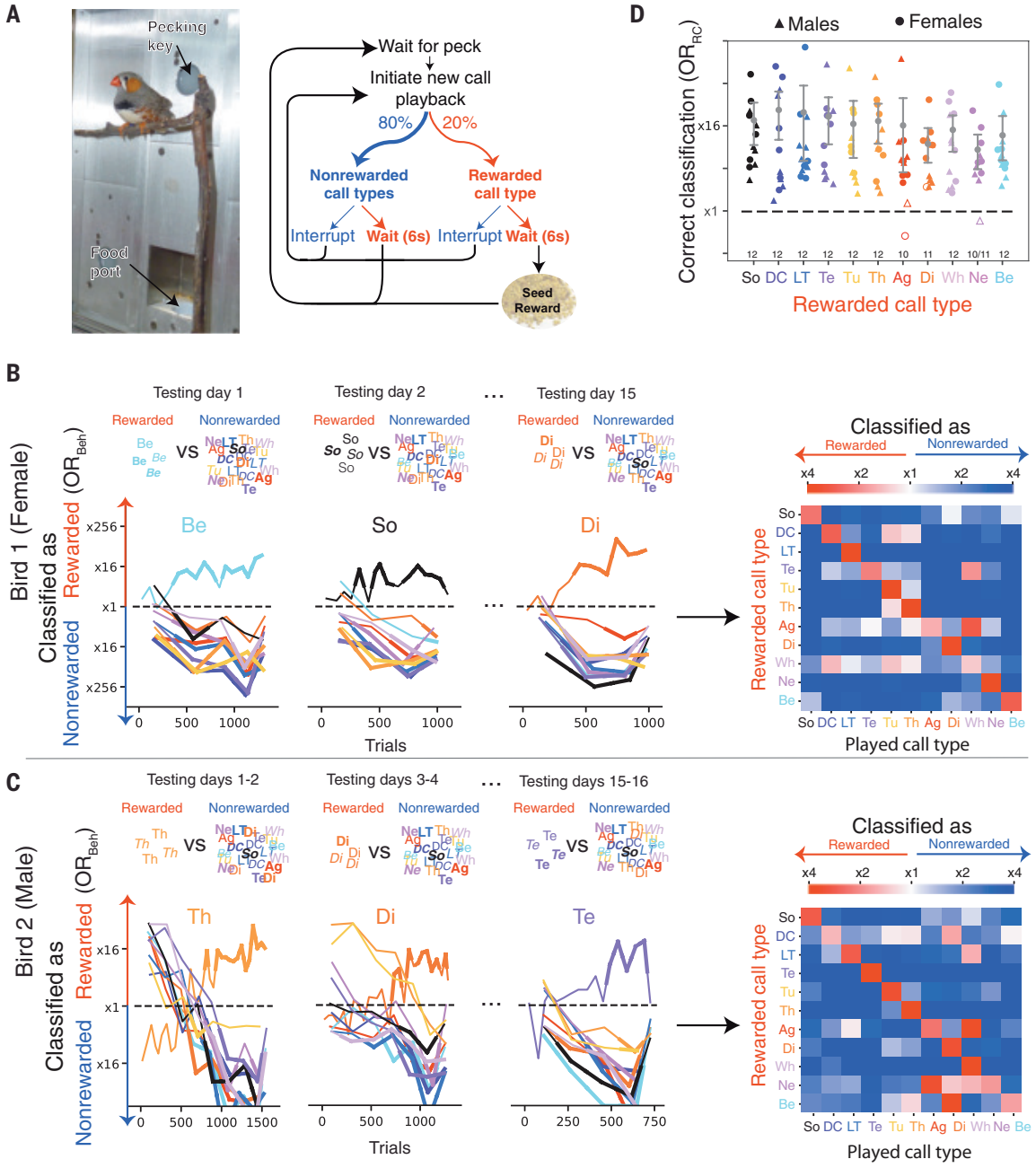

Fig. 2. Behavioral discrimination of Etho call types. (**A**) Zebra finches are trained in an operant conditioning task to interrupt nonrewarded stimuli and to refrain from interrupting rewarded stimuli (*26*,*27*). Stimuli are sampled across all renditions in our database (Fig. 1A). Rewarded stimuli are sampled from one Etho call type, and nonrewarded stimuli are sampled from all other Etho call types. (**B** and **C**) Performances of two birds [(B) female; (C) male)] in this Etho call type discrimination task for the first two tests and the last test. For a given call type test, birds have up to three consecutive days to identify the rewarded Etho call type and show their discrimination performance (results of all tests are provided in figs. S2 and S3). For each Etho call type (line color), the learning curves show the average bird performance at classifying calls as rewarded or nonrewarded stimuli. The performance is quantified by the odds ratio of correct behavioral classification, OR_{Beh} (*28*). Chance performance is $OR_{Beh} \approx \times 1$. Bold lines indicate a significant classification performance (Fisher's exact test, $p < 0.05$). The confusion matrices show the classification performance obtained on the last day of each call type test. (**D**) The performance at classifying the rewarded Etho call type on the last day of each call type test is quantified by the odds ratio of stimulus interruption following the reward contingency, OR_{RC} (*28*). Birds for which OR_{RC} is significantly greater than chance are indicated by filled symbols. The total number of significant tests is indicated at the bottom of the plot (127/131 Fisher's exact tests corrected for multiple comparisons, $p < 0.05$, $n = 12$ except for Ne, where $n = 11$; supplementary text). The gray circles and error bars are means and 95% confidence interval obtained by bootstrap across birds. Abbreviations are the same as in Fig. 1.

Hierarchical perception of call types based on their meaning

To test whether zebra finches have an internal model of Etho call types based on their meaning, we asked whether birds confused call types that were semantically related but acoustically distinct. We first established a linear measure of acoustic distance between Etho call types that we could compare with a measure of behavioral perceptual distance. The acoustic distances were obtained from the predictions of a supervised multiclass classifier (an LDA trained to classify calls into the 11 Etho call types) operating on sound spectrograms (*7*). The classifier predictions are gathered in a confusion matrix showing the

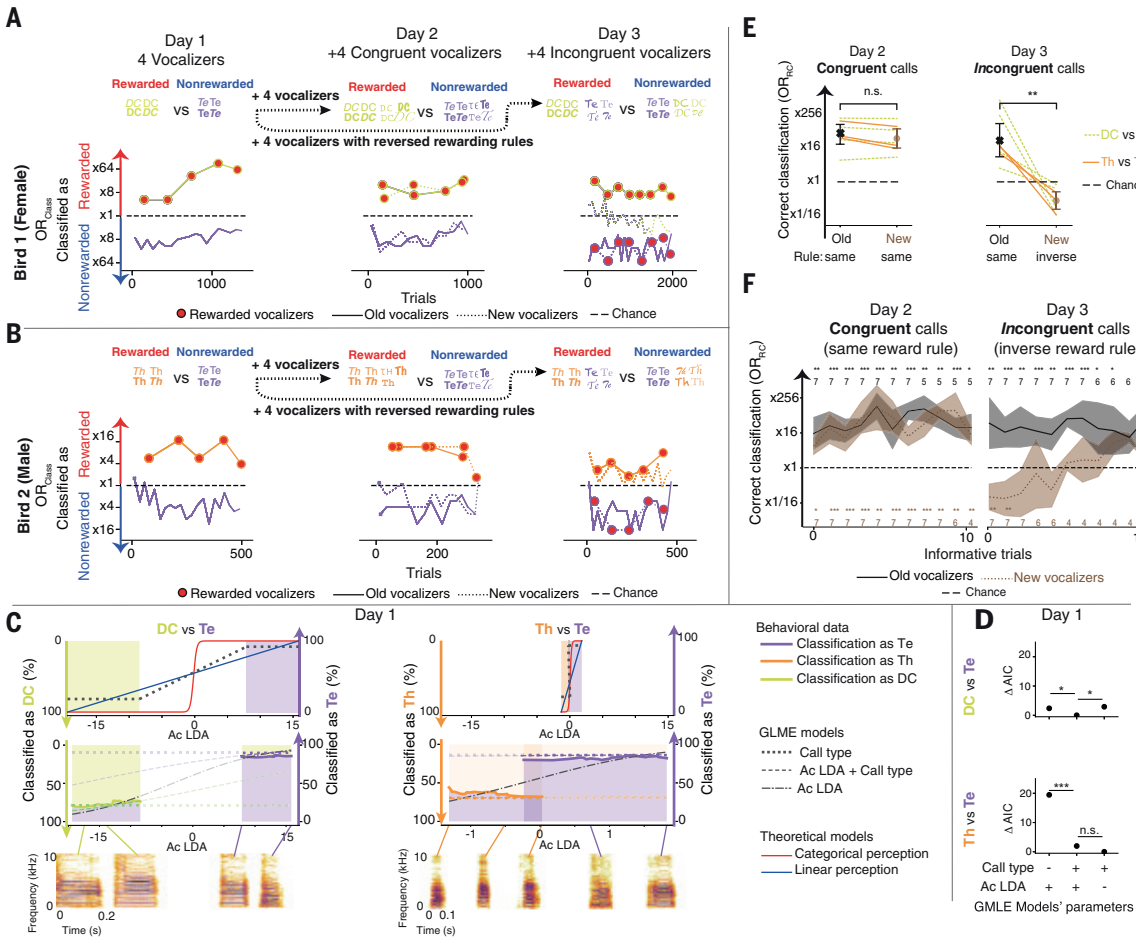

Fig. 3. Categorical perception of Etho call types. (**A** and **B**) Classification performances of two example subjects [(A) female; (B) male] in the pairwise call type discrimination task that tests the ability of zebra finches to generalize to new vocalizers (days 2 and 3) when the rewarding rule with respect to Etho call type is the same as day 1 (day 2, congruent calls) or reversed (day 3, incongruent calls). For each Etho call type (color) and each set of four vocalizers (Old and New), the learning curves show the average bird performance [odds ratio for classification (OR_{Class}) (*28*)] at classifying calls as rewarded or nonrewarded stimuli. (**C**) Day 1 behavioral performance dependence on the calls' acoustic structure and their Etho call type labels. The probability of correct classification of calls between DC and Te (left panel, $n = 4$ subjects) or Th and Te (right panel, $n = 3$) is plotted as a function of the acoustic dimension that best separates each call type pair (*Ac LDA*). Units on the *Ac LDA* axes are arbitrary but identically scaled for all plots. The same *x*-axis range is shown on the top plots, which compare the call type GLME model to theoretical models of perception (fig. S4). The bottom plots display the raw data along with their fit to three GLME models used to assess categorical perception. Spectrograms of example calls are shown below. (**D**) Akaike information criterium (AIC) of GLME models relative to the best model. LRTs were used to assess the significance of the difference of fit between models. (**E**) Birds' classification performances ($n = 7$) for Old versus New vocalizers on day 2 (LRT11 table S1, $n = 4601$, $p = 0.188$) and day 3 (LRT17 table S1, $n = 8027$, $p < 2.2 \times 10^{-16}$). The performance is quantified by the odds of correctly classifying calls according to reward contingency OR_{RC}. (**F**) Same as for (E) as a function of the number of informative trials (i.e., uninterrupted trials, which provide feedback on the reward contingency). The number of subjects for each data point is displayed at the top and bottom of the graph. (Statistical tests used were LRT; fixed effect, reward contingency; response variable, probability of interruption.) All data are means ± 2 SE. *$p < 0.05$; **$p < 0.01$; ***$p < 0.001$; n.s., not significant. Abbreviations are the same as in Fig. 1.

conditional probabilities of Etho call type prediction given the actual Etho call type (Fig. 1B). The diagonal of this matrix shows the average probability of correct classification for each Etho call type (56 ± 4%, bootstrap, mean ± 2 SE), and the off-diagonal terms quantify systematic errors. For example, the classifier often confuses calls belonging to the same hypercategory "alarm" (Tucks and Thuks). These misclassification probabilities were interpreted as acoustic distances between pairs of Etho call types (acoustic confusion matrix; Fig. 4A and see methods) and were compared to the measures of perceptual distance obtained from the behavioral discrimination performance of birds in the first series of experiments [Fig. 2, B and C; perceptual confusion matrix in Fig. 4A; (*28*)].

The comparison of distances between pairs of Etho call types was performed in two-dimensional (2D) spaces obtained by applying multidimensional scaling (MDS; Figs. 1C and 4, B and C). The variability in the calculations and robustness of both acoustic and perceptual maps were evaluated by bootstrap procedures across birds [(*28*); Fig. 4C]. Acoustic and perceptual maps were similar as quantified by a low value for the mean error of the match [Procrustes disparity = 0.042 ± 0.023, bootstrap; normalized effect size: coefficient of determination (R^2) = 0.703, $p = 0.0014$, permutation test]. Thus, behavioral performance in Etho call type categorization and their systematic misclassifications is in part due to calls' acoustic similarity. However, Etho call types belonging to the same semantic hypercategory, that is, that are closer in meaning, were closer in the perceptual map than they were in the acoustic map (Fig. 4B). This effect also appeared as shorter branches in the dendrogram obtained from an unsupervised hierarchical clustering of the perceptual distances as compared with the dendrogram obtained with acoustic distances (fig. S5). The merging and clustering of Etho call types in the perceptual space along the

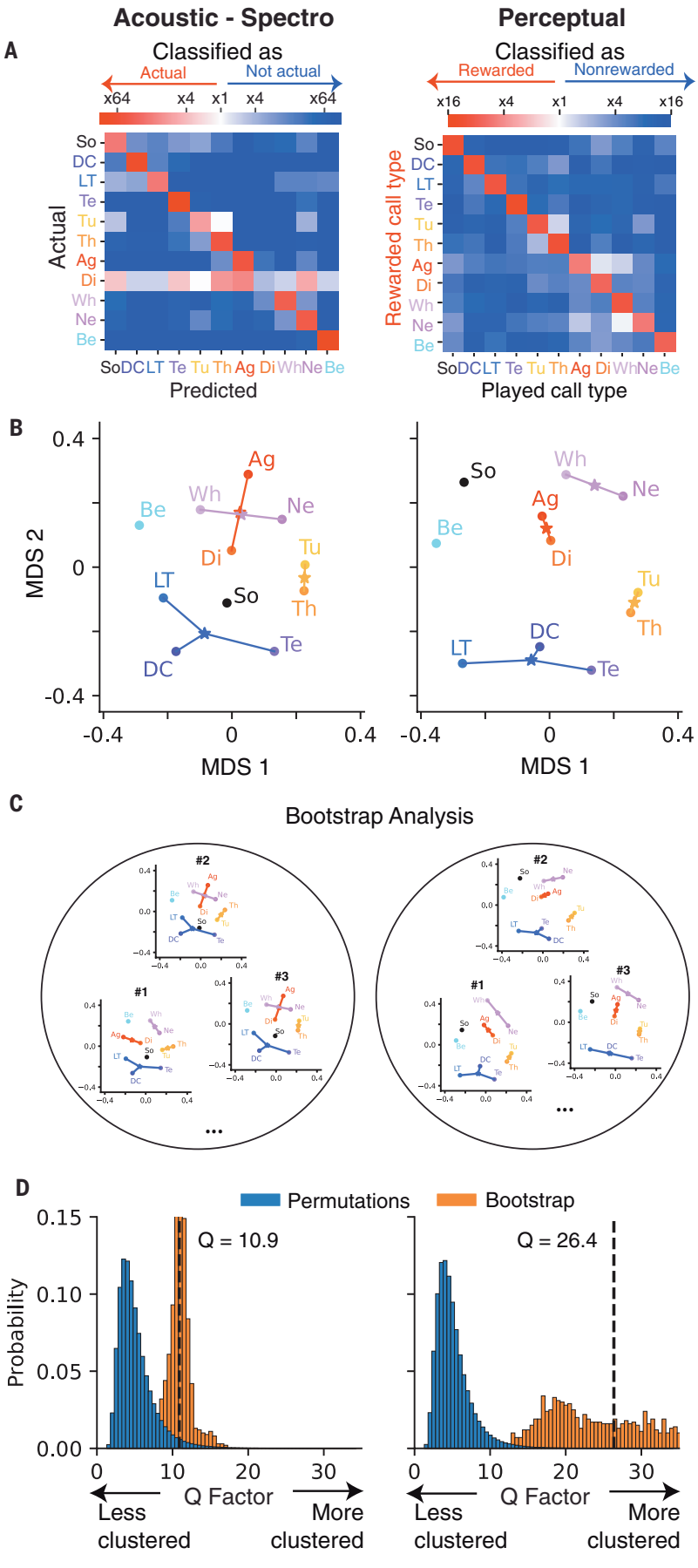

Fig. 4. Acoustic and perceptual space of Etho call types. (**A**) Comparison of the algorithmic and behavioral performance of classification of all Etho call types. In the acoustic space, the confusion matrix of classifier performance (OR_{AC}, left) is obtained from the matrix of classification probabilities [Fig. 1B; (*28*)]. In the perceptual space, the confusion matrix of behavioral performance (OR_{Beh}, right) is the average performance of all subject birds (n = 12) in the Etho call type discrimination experiment (Fig. 2). (**B**) Projection of the Etho call types in 2D MDS spaces build on the pairwise misclassification values obtained from the off-diagonals values of the confusion matrices shown in (A). To facilitate the visual comparison of the 2D acoustic and perceptual spaces of Etho call types, a Procrustes transformation (scaling and rotation) was applied to the acoustic space (original projection in Fig. 1C). Edges link the Etho call types to the centroid (star) of the semantic hypercategory they belong to and that are described in Fig. 1A. (**C**) Confidence estimates of the pairwise distances were obtained by a bootstrap procedure that randomly samples from the confusion matrices obtained for individual vocalizers in the call database (acoustic, n = 45) or individual subjects in the behavioral experiment (perceptual, n = 12). The results of three bootstrap samples out of 1000 are shown. (**D**) Histogram of Q factor [ratio of the between to within hypercategory Euclidian distance (*28*)] used to quantify the clustering of Etho call types into semantic hypercategories. To assess confidence levels on Q, we estimated Q on 1000 bootstrap samples of MDS spaces as illustrated in (C) (orange bars). To assess significance, a null distribution of Q based on sampling random hypercategories of the same size was generated by permutation (permutations, blue bars). The x axis is truncated at Q = 35. Abbreviations are the same as in Fig. 1.

hypercategories indicates that birds perceptually misclassified these calls more often than expected from their acoustic distances. To quantify the clustering effect along semantic hypercategories, we measured how close each Etho call type was on average to the semantic hypercategory it belongs to, as compared with other semantic hypercategories (distance ratio Q). A higher value of Q indicates a stronger clustering of Etho call types along the semantic hypercategories. In both the acoustic and perceptual spaces, values of Q were higher than expected for random hypercategories, demonstrating that although semantic hypercategories were based on human interpretations of the behavioral contexts of call type usage, independent measures of acoustic and perceptual distances between calls achieved a similar grouping of Etho call types (permutation test; perceptual map: $Q = 26.35 \pm 17.49$, $p = 0.0019$; acoustic map: $Q = 10.82 \pm 3.14$, $p = 0.0376$; fig. S5). Furthermore, the grouping of semantically related Etho call types was ~2.43 times greater in the perceptual space than in the acoustic space ($Q_{perceptual} > Q_{acoustic}$, $p = 0.004$, bootstrap). This result was robust to the choice of acoustic features used to calculate acoustic distances (fig. S7) and to the omission of Song in the dataset which, as a complex acoustic signal covering a large portion of the acoustic space (Fig. 1), could arguably be driving the effect (figs. S5 to S7). Thus, zebra finches make systematic errors of categorization between Etho call types of similar meanings at much higher rates than would be expected from their acoustic distances. We named this

local shrinkage of the perceptual space centered on semantic hypercategories of Etho call types the "semantic magnet effect" (*32*).

Conclusions

In multiple animal species, ethologists have described Etho call types without gathering evidence that animals would agree with their repertoire organization, with the exception of alarm calls (*18*–*20*, *33*, *34*), where the sophisticated usage and appropriate complex behavioral responses elicited in the receivers clearly demonstrated that these Etho call types are discriminated by animals. Drawing on previous characterization of the zebra finch vocal repertoire (*7*, *8*), we tested all combinations of Etho call types and demonstrated that this discrimination is not restricted to alarm calls but is performed by zebra finches for all the Etho call types. Furthermore, this discrimination shows generalization to new renditions, strong sigmoidal classification functions versus acoustics, and robustness to reward contingency changes, all of which are consistent with categorial perception. Just as humans discriminate isolated vowels (*35*) and marmosets categorize some of their call types (*36*), zebra finches not only categorize call types that are clearly distinct acoustically but also categorize those that are graded signals found along an acoustic continuum such as Tets and Thuks (Fig. 1). Thus, categorical processing of meaningful categories, such as species-specific call types, is not specific to primates.

Direct evidence for animals' mental states when hearing their conspecific calls is impossible, but indirect evidence can be gathered. Japanese tits that were primed with species-specific alarm calls for snakes scanned their visual space and performed investigative behaviors to wood sticks that were moved in snake-like motions (*37*). One interpretation is that the snake alarm call elicited a mental imagery of a snake, which yielded unexpected responses to moving sticks. Here, zebra finches confused Etho call types that have a similar meaning at a higher rate than would be expected given the acoustic similarity of these call types. Postulating that hearing calls elicits mental representations of call meaning could explain this semantic magnet effect. From a mechanistic perspective, higher-order auditory brain regions would perform a nonlinear mapping of acoustic information: Neural representations would be organized by the usage or "meaning" of Etho call types. Zebra finch Etho call types can be correctly decoded from the neural responses of avian neurons in cortical-like auditory pallium (*38*, *39*). However, whether these neural responses are shaped by semantic similarities remains to be seen. Neural selectivity to semantics over acoustics has been found in the macaque prefrontal cortex for a few call exemplars (*40*), but semantic cortical maps have so far only been described in humans who are listening to stories (*41*).

Although the extent of the semantic quality of animal vocal communication signals continues to be studied (*19*, *25*), common themes in the use of complex acoustic signals and their neural mechanisms are abundant, particularly in birds. Avian call types have been shown to be functionally referential (*20*), used in combinations to form rudimentary syntax (*42*), capable of eliciting visual imagery (*37*), under volitional control (*43*), deceitful (*44*), and, as demonstrated here, organized perceptually according to their meaning. Thus, avian communication offers distinctive opportunities to investigate the neural mechanisms in vertebrates that are essential for producing and interpreting communication calls (*45*).

REFERENCES AND NOTES

1. P. Marler, *Science* **157**, 769–774 (1967).
2. J. W. Bradbury, S. L. Vehrencamp, *Principles of Animal Communication* (Sinauer Associates, 1998).
3. P. Marler, *Ibis* **98**, 231–261 (1956).
4. N. E. Collias, *Condor* **89**, 510–524 (1987).
5. M. S. Ficken, R. W. Ficken, S. R. Witkin, *Auk* **95**, 34–48 (1978).
6. M. Dragonetti *et al.*, *Wilson J. Ornithol.* **125**, 34–49 (2013).
7. J. E. Elie, F. E. Theunissen, *Anim. Cogn.* **19**, 285–315 (2016).
8. R. Zann, *The Zebra Finch: A Synthesis of Field and Laboratory Studies* (Oxford Univ. Press, 1996).
9. L. R. Brand, *Anim. Behav.* **24**, 319–335 (1976).
10. J. J. Gros-Louis *et al.*, *Int. J. Primatol.* **29**, 641–670 (2008).
11. B. M. Bezerra, A. Souto, *Int. J. Primatol.* **29**, 671–701 (2008).
12. J. Soltis, *Zoo Biol.* **29**, 192–209 (2010).
13. É. C. Déaux, J. A. Clarke, *Behaviour* **150**, 75–101 (2013).
14. J. L. Fuller, *Am. J. Primatol.* **76**, 203–216 (2014).
15. P. A. Green, N. C. Brandley, S. Nowicki, *Behav. Ecol.* **31**, 859–867 (2020).
16. J. A. Comins, T. Q. Gentner, *Cognition* **128**, 113–118 (2013).
17. M. D. Hauser, N. Chomsky, W. T. Fitch, *Science* **298**, 1569–1579 (2002).
18. R. M. Seyfarth, D. L. Cheney, P. Marler, *Science* **210**, 801–803 (1980).
19. M. B. Manser, *Anim. Behav.* **86**, 491–496 (2013).
20. S. A. Gill, A. M. K. Bierema, *Ethology* **119**, 449–461 (2013).
21. M. C. Baker, A. M. Becker, *Wilson Bull.* **114**, 510–516 (2002).
22. M. Griesser, *Curr. Biol.* **18**, 69–73 (2008).
23. B. C. Wheeler, *Behav. Ecol. Sociobiol.* **64**, 989–1000 (2010).
24. I. M. Pepperberg, *Z. Tierpsychol.* **55**, 139–160 (1981).
25. J. Fischer, *Psychon. Bull. Rev.* **24**, 72–78 (2017).
26. J. E. Elie, F. E. Theunissen, *Nat. Commun.* **9**, 4026 (2018).
27. K. Yu, W. E. Wood, F. E. Theunissen, *Sci. Adv.* **6**, eabe0440 (2020).
28. Materials and methods are available as supplementary materials.
29. A. R. Fishbein, N. H. Prior, J. A. Brown, G. F. Ball, R. J. Dooling, *Sci. Rep.* **11**, 916 (2021).
30. R. L. Goldstone, A. T. Hendrickson, *Wiley Interdiscip. Rev. Cogn. Sci.* **1**, 69–78 (2010).
31. N. H. Feldman, T. L. Griffiths, J. L. Morgan, *Psychol. Rev.* **116**, 752–782 (2009).
32. P. K. Kuhl, *Percept. Psychophys.* **50**, 93–107 (1991).
33. T. N. Suzuki, K. Ueda, *Wilson J. Ornithol.* **125**, 412–415 (2013).
34. C. N. Templeton, E. Greene, K. Davis, *Science* **308**, 1934–1937 (2005).
35. P. Delattre, A. M. Liberman, F. S. Cooper, L. J. Gerstman, *Word* **8**, 195–210 (1952).
36. M. S. Osmanski, X. Wang, *Proc. Natl. Acad. Sci. U.S.A.* **120**, e2221756120 (2023).
37. T. N. Suzuki, *Proc. Natl. Acad. Sci. U.S.A.* **115**, 1541–1545 (2018).
38. J. E. Elie, F. E. Theunissen, *Eur. J. Neurosci.* **41**, 546–567 (2015).
39. H. Robotka *et al.*, *Cell Rep.* **42**, 112034 (2023).
40. G. W. Gifford III, K. A. MacLean, M. D. Hauser, Y. E. Cohen, *J. Cogn. Neurosci.* **17**, 1471–1482 (2005).
41. A. G. Huth, W. A. de Heer, T. L. Griffiths, F. E. Theunissen, J. L. Gallant, *Nature* **532**, 453–458 (2016).
42. T. N. Suzuki, D. Wheatcroft, M. Griesser, *PLOS Biol.* **16**, e2006532 (2018).
43. K. F. Brecht, S. R. Hage, N. Gavrilov, A. Nieder, *PLOS Biol.* **17**, e3000375 (2019).
44. T. P. Flower, M. Gribble, A. R. Ridley, *Science* **344**, 513–516 (2014).
45. J. E. Elie, F. Theunissen, *The Neuroethology of Birdsong*, vol. 71, J. T. Sakata, S. C. Woolley, R. R. Fay, A. N. Popper, Eds. (Springer, 2020), pp. 175–209.
46. J. E. Elie, F. Theunissen, Vocalization library of the Zebra finch. Figshare (2020); https://doi.org/10.6084/m9.figshare.11905533.v1.
47. F. Theunissen, J. E. Elie, A. de Witasse-Thézy, theunissenlab/zebra-finch-semantic-category: Resubmission July 2025. Zenodo (2025); https://doi.org/10.5281/zenodo.13623968.

ACKNOWLEDGMENTS

Funding: This work was funded by National Institutes of Health grant R01DC018321 (F.E.T.)
Author contributions: Conceptualization: J.E.E., F.E.T.; Formal analysis: J.E.E., F.E.T.; Methodology: J.E.E., L.T., F.E.T.; Investigation: J.E.E., A.d.W.-T., B.M., L.T.; Software: J.E.E., A.d.W.-T., L.T., F.E.T.; Resources: F.E.T.; Visualization: J.E.E., A.d.W.-T., L.T., F.E.T.; Funding acquisition: F.E.T.; Project administration: J.E.E., L.T., F.E.T.; Supervision: J.E.E., L.T., F.E.T.; Writing – original draft: F.E.T.; Writing – review & editing: J.E.E., A.d.W.-T., L.T., F.E.T. **Competing interests:** The authors declare that they have no competing interests. **Data and materials availability:** All behavioral data and the code used in the analysis is publicly available in Zenodo (*47*). The acoustical database of calls is publicly available in Figshare (*46*). **License information:** Copyright © 2025 the authors, some rights reserved; exclusive licensee American Association for the Advancement of Science. No claim to original US government works. https://www.science.org/about/science-licenses-journal-article-reuse

SUPPLEMENTARY MATERIALS

science.org/doi/10.1126/science.ads8482
Materials and Methods; Supplementary Text; Figs. S1 to S7; Tables S1 to S3; References (*48*–*50*); MDAR Reproducibility Checklist

Submitted 31 August 2024; resubmitted 5 March 2025; accepted 21 July 2025
10.1126/science.ads8482

MARINE ECOLOGY

Cumulative impacts to global marine ecosystems projected to more than double by mid-century

Benjamin S. Halpern[1,2]*†, Melanie Frazier[1]†, Casey C. O'Hara[1], O. Alejandra Vargas-Fonseca[3], Amanda T. Lombard[3]

Pressures from human activities are expected to increase substantially, affecting marine ecosystems globally. To plan for a sustainable future, we need to forecast the distributions of cumulative effects from multiple pressures. Here, we mapped (at 10-kilometer resolution) the future cumulative impacts of 10 climate, land-based, fishing, and other pressures on 20 marine habitats under two climate scenarios at mid-century (around 2050). We found that cumulative impacts are projected to increase 2.2 to 2.6 times globally, with coastal habitats facing higher impacts but offshore regions facing faster increases, especially in equatorial regions. Furthermore, many countries dependent on marine resources will have large increases in impacts. Incorporating these results into strategic policy and management will support more sustainable use and protection of marine ecosystems and the services they provide.

Marine ecosystems face many pressures from human demands for seafood (*1*–*3*), marine and coastal infrastructure (*4*, *5*), transportation (*6*), and resource extraction (*7*), as well as from nutrient and chemical runoff from various land-based agricultural, industrial, and urban activities, among others (*8*). Furthermore, climate change is markedly altering the temperature and other properties of marine waters (*9*). Individually and collectively, these anthropogenic pressures threaten the well-being of marine ecosystems (*10*, *11*) by affecting the physiology, morphology, life history, and existence of species and habitats (*12*, *13*), which ultimately threatens the benefits and services that we obtain from a healthy ocean.

Substantial progress has been made over the past two decades to identify, assess, and map the impacts of human pressures on marine ecosystems (*14*–*16*) and species (*12*, *17*–*21*). However, we are living in a rapidly changing world. Understanding how the magnitude and distribution of cumulative impacts are likely to change over time is necessary to plan for future uses of the ocean, prepare for emerging challenges, and sustainably protect marine ecosystems into the future (*22*, *23*). Recent work has begun addressing this need by mapping future impacts, but these studies focus on relatively small geographic areas (*24*) or on few, mainly climate, pressures (*25*). Missing from this work is a more complete understanding of expected future responses to a broader set of pressures in all regions of the ocean.

Here, we estimate how future human pressures will affect marine ecosystems with the most comprehensive datasets available of mapped current extent and future projections for 10 anthropogenic pressures (*26*). Pressure data cover five categories, including climate (water temperature, air-heat index, and sea level rise), ocean chemistry (ocean acidification and dissolved oxygen), land based (nutrient input, light pollution, and coastal human population density), net primary productivity (NPP), and fisheries (fisheries biomass loss). We mapped pressure data at 10-km resolution for both current (~2010 to 2020) and future (~2041 to 2060, or mid-century) pressure intensities, with focus on the Shared Socioeconomic Pathways SSP2-4.5 and SSP5-8.5 climate change scenarios. We estimate how these pressures will affect marine habitats based on their overlap with current distributions of 20 marine habitats and the unique vulnerability of each habitat to each pressure (*26*–*28*), averaging the cumulative impact per pixel. The SSP2-4.5, "middle-of-the-road" scenario approximates current climate policy, whereas the SSP5-8.5, "fossil-fueled development" is considered an "extreme counterfactual scenario" in which carbon dioxide emissions double by mid-century (*29*, *30*). We focus here on the mid-century because this period has the most complete data, and uncertainty increases further into the future. Impact scores ≥1 suggest that the habitats in that location are unlikely to survive in their current state (*26*).

With these forecasted cumulative impact maps, we address several key questions relevant to marine policy, conservation, and management. How much are cumulative impacts expected to increase in the near future? Which regions and habitats are projected to face the greatest future impacts from human activities? Which pressures will be key drivers of those changes and how does their importance change across regions? And how will these changes vary among countries with different levels of dependence on marine resources? Answers to these questions can inform efforts to design conservation and management plans that are more robust to change and thus help build a more sustainable future for both nature and people.

Global results

Projecting forward to mid-century, we found that the global cumulative impacts of human activities on marine habitats increase by 2.2× (SSP2-4.5) to 2.6× (SSP5-8.5). Future impacts will be felt unevenly across regions, with the tropics and the poles expected to experience the highest average future impacts (Fig. 1, B and C). In the tropics, impacts are predicted to approximately triple by 2041 to 2060 (2.7× under SSP2-4.5 and 3.2× under SSP5-8.5). At the poles, impacts are projected to increase more slowly but still enough for these regions to continue having the highest cumulative impacts of any latitude (1.7× in the North Pole and 2.1× in the South Pole under SSP2-4.5 and 2.0× to 2.5× for SSP5-8.5; table S1). Globally, these changes are in addition to already high current cumulative impacts (Fig. 1A, median global cumulative impact = 0.2; 99.99th quantile = 1.3). Currently, <0.1% of the world's oceans have an impact score of ≥1, but this is projected to increase to 2.7% by 2041 to 2060 under SSP2-4.5 (3.9% under SSP5-8.5); 1.4% of coastal areas have impact scores ≥1, but this is projected to rise to 12.3% under SSP 2-4.5 (20.6% under SSP5-8.5).

Coastal regions, waters within 20 km of the coastline, currently experience 1.7× greater average cumulative impacts than the rest of the ocean (Fig. 2A and table S2), which is not surprising given that several pressures (nutrient pollution, light pollution, coastal disturbance, sea level rise, and air-heat index) primarily or only affect coastal regions (Fig. 2B). Additionally, fishing pressures are largely concentrated within Exclusive Economic Zones (EEZs). Coastal regions are projected to continue experiencing higher impacts than offshore regions, but the rate of increase is projected to be somewhat slower than that of offshore areas (table S2).

The largest overall contributors to future cumulative impacts are from ocean warming (surface and benthic temperatures) and biomass loss due to fisheries (Fig. 2). These results are to be expected given the large global footprint of climate change and fisheries. Furthermore, the effects of fishing are likely underestimated because our model assumes that current rates of fisheries biomass loss will not accelerate. However, the model does allow biomass loss to decelerate and become biomass gains under good governance. In fact, fisheries pressures are probably accelerating in some regions (*31*). Rates of biomass loss are likely to accelerate when fishing fleets become larger, the technology

[1]National Center for Ecological Analysis and Synthesis, University of California, Santa Barbara, Santa Barbara, CA, USA. [2]Bren School of Environmental Science and Management, University of California, Santa Barbara, Santa Barbara, CA, USA. [3]Institute for Coastal and Marine Research, Nelson Mandela University, Gqeberha, South Africa. *Corresponding author. Email: halpern@nceas.ucsb.edu
†These authors contributed equally to this work.

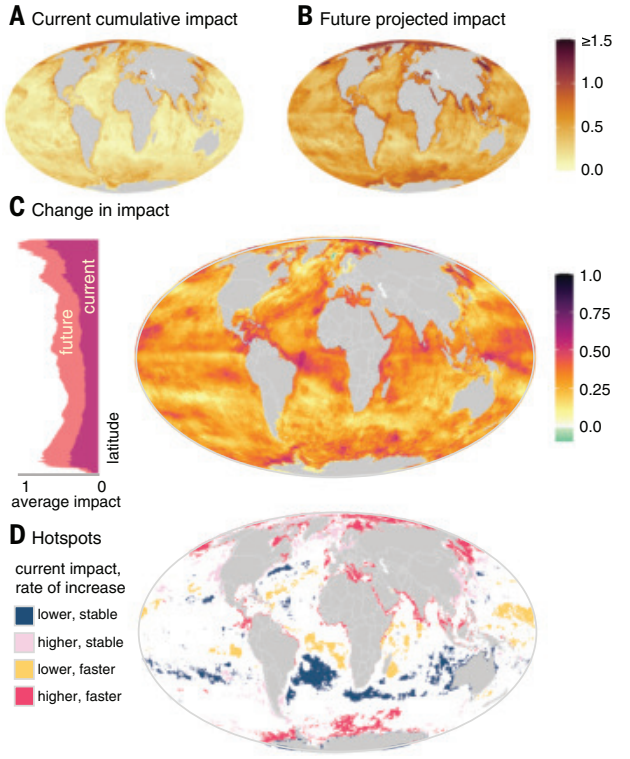

Fig. 1. Current and future cumulative impacts on marine habitats. (**A**) Current cumulative impacts (2010 to 2020) for 10 pressures on 20 marine habitats. (**B**) Future projected cumulative impacts (2040 to 2060) with values capped at 1.5. (**C**) Change in impacts (future minus current) with values capped between −0.1 and 1.0. (**D**) Hotspots of change were determined by identifying regions with current pressures and change in pressure for the <20th (lower and/or stable) and >80th (higher and/or faster) quantiles. Maps are at 10-km resolution. Figures represent scenario SSP2-4.5, with SSP5-8.5 results provided in fig. S3. Capping values mitigated the visual skew resulting from a few outliers that accounted for <0.01% of raster cells.

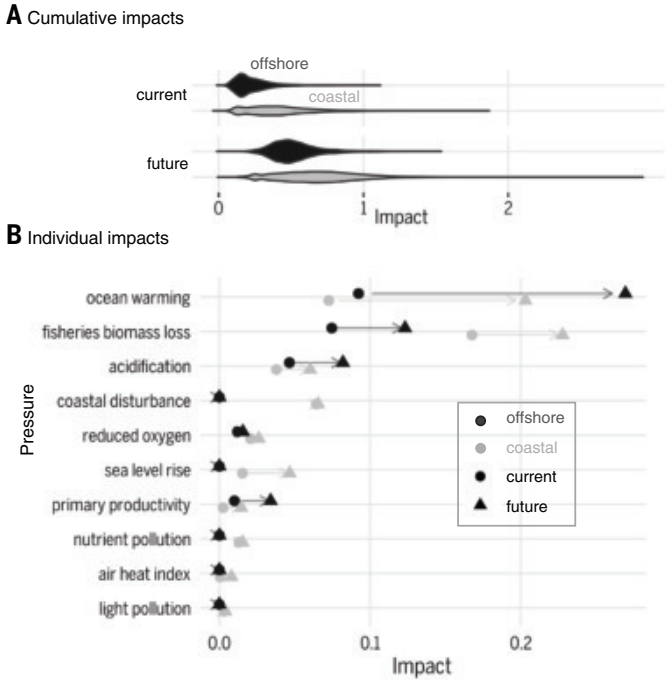

Fig. 2. Current and future cumulative and individual pressure impacts on coastal and offshore ecosystems. (**A**) Density plot of offshore and coastal raster cell estimates of cumulative impacts. Offshore raster cells were randomly sampled to have the same sample size as the coastal region (values are reported in table S2). (**B**) Average estimates of pressure impacts for offshore and coastal regions. Arrow depicts direction of change (values are reported in table S3). Coastal regions represent ocean waters within 20 km of the coastline. Results are for SSP2-4.5 in 2041 to 2060. Results for SSP5-8.5 are provided in fig. S4.

to locate and extract fish improves, or when regions are faced with increasing pressures to extract more fish due to expanding demand within the countries or through trade networks. To account for uncertainty in future fisheries pressures, we also explored a second model that allows for biomass loss to accelerate based on governance. Based on this additional model, the primary analysis may underestimate fisheries biomass loss in southern Africa, similar to results found by other analyses (*31*), and possibly in Southeast Asia and Oceania (fig. S2).

Nearly all regions are currently experiencing high fisheries impacts because substantial amounts of biomass have been removed (*1*). In general, we assume that declines in biomass will continue into the future; however, for countries with more effective fisheries management, we assume that biomass removal will not fall below a threshold that is sustainable, generally considered to be ~45% of historic biomass (*32*, *33*). For example, Europe and North America currently experience high impacts from fisheries, but these impacts are projected to increase very little in the future because of relatively good management in these regions (fig. S6). China is also expected to have little future increase, but this is because they are already fishing their EEZ at maximum levels, beyond what is considered sustainable. For countries with poorer projected governance, which is most countries (*34*), fisheries biomass is projected to continue to decrease below the sustainability threshold, resulting in increasing impacts.

Pressures with the smallest current impacts are light pollution and air-heat index, and the slowest increases are for coastal disturbance, nutrients, and light pollution (Fig. 2), although these results vary by habitat (Fig. 3) and geographic region (fig. S6). The rate of increase for these particular pressures is slowing in part because they are directly linked to human population size, which is expected to peak around mid-century, and in some places is even expected to decrease. For example, coastal disturbance is overall predicted to continue affecting habitats but is projected to remain fairly constant, and even to decrease slightly, in some areas (fig. S6 and data S2; e.g., countries in eastern and southern Europe and eastern and southeastern Asia).

We also found that habitats will experience different numbers of cumulative impacts driven by differences in exposure and vulnerability to pressures (Fig. 3). There is a nearly fourfold difference between future cumulative impacts on the most affected (salt marsh) and least affected (deep hard bottom) habitats. In general, coastal habitats are expected to experience some of the largest cumulative impacts, especially seagrass and salt marsh but also rocky intertidal, mangrove, and rocky reefs (Fig. 3). Habitats projected to experience the least future impacts are hard-bottom continental shelf, many of the deeper habitats (e.g., seamounts and the deep benthic and deep pelagic areas), kelp, and shallow soft-bottom habitats.

Regional patterns

Areas expected to experience the fastest increases and highest future impacts include portions of the Arctic and Antarctic oceans, seas around eastern Russia (Arctic, Bering Strait, and Sea of Okhotsk), the

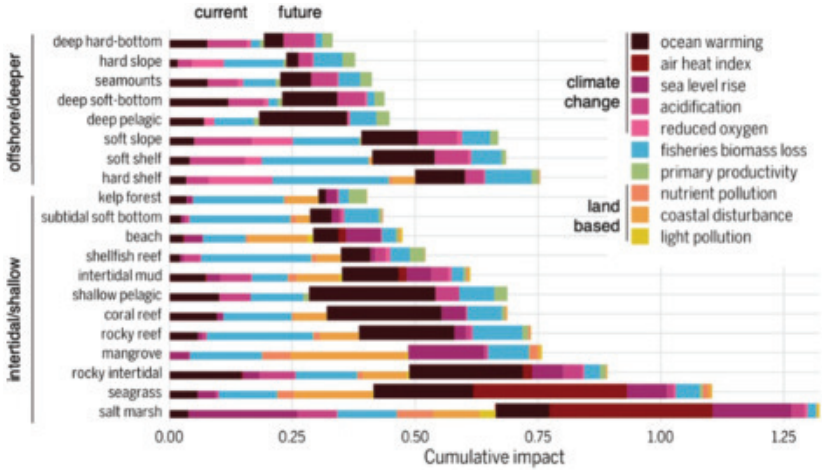

Fig. 3. Future impacts on marine habitats. Current (thinner bars) and projected additional future (thicker bars) cumulative impacts per habitat for SSP2-4.5 in 2041 to 2060. Results for SSP5-8.5 are provided in fig. S5 and data S1.

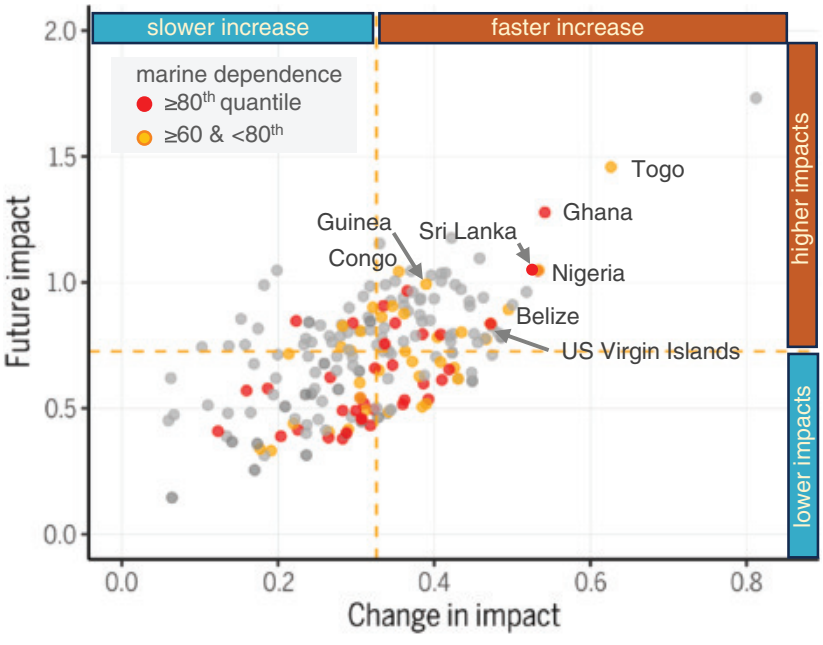

Fig. 4. Relationship between projected change and future cumulative impacts on marine habitats. Some countries with higher marine dependence (orange and red points) face large increases and high future cumulative impacts under SSP2-4.5. Example countries are labeled, with a focus on those at the edges in the upper right quadrant. Orange horizontal and vertical lines indicate median values. All data are based on coastal pressures. See also data S2 and S3.

Mediterranean Sea, Southeast Asia, and coastal regions spanning the Middle East and India (Fig. 1D, red areas). However, some regions with relatively low current impacts are projected to experience rapid increases (e.g., East Africa and Madagascar, some parts of Oceania, and scattered areas of the high seas in the Atlantic; Fig. 1D, yellow areas). These changes are driven by expected increases in climate change in the Arctic and fisheries and climate change in other regions. Conversely, impacts are fairly low, and expected to remain so through mid-century, around much of Australia and across a patchy band spanning the Southern Pacific, Southern Atlantic, and Indian oceans. A few areas (<0.01% of the global ocean), mostly in the Northern Hemisphere, are projected to experience small decreases in cumulative impacts, in particular areas near southern Greenland, between Iceland and Norway, and in parts of the Baltic Sea (fig. S1).

We identified countries projected to be most vulnerable based on their exposure to future impacts. Of most concern are countries facing large increases in pressure and high future pressures (Fig. 4, top right corner), especially regions with a high dependence on marine environments (e.g., Togo, Ghana, and Sri Lanka).

Discussion

Our results present a sobering picture of the future of ocean conditions globally, with cumulative impacts from multiple and increasing pressures expanding and intensifying. By mid-century, we project that cumulative impacts will more than double and potentially triple their current (already high) levels. Furthermore, essentially nowhere in the global ocean is going to improve with respect to cumulative impacts under the scenarios modeled here, even though individual pressures will likely improve in some places.

Many regions are projected to fare much worse. Both the poles and the tropics are predicted to experience substantial future impacts; the tropics because they face the fastest rates of increase and the poles because their current impacts are already high and projected to increase. Such high future impacts may exceed the capacity of ecosystems to cope with environmental change (*35*, *36*) and pose challenges for human societies and institutions adapted to historic conditions (*35*, *37*). Nearly all locations projected to change the most are near-coastal regions, an intuitive result given that most human uses, and thus impacts, on the ocean are near coasts, but this is a worrisome result nonetheless because these are the areas where people derive the most value from the ocean. In short, the places that we need the most to sustain our desired uses and benefits are the places that are the most at risk of increasing future impacts.

Because ocean warming and poorly managed fisheries are the two most impactful pressures across all regions and habitats, minimizing projected increases in cumulative impacts will require policy and management designed to reduce climate change effects and improve fisheries management in most countries. As has been noted by other assessments (*38*, *39*), these two actions, albeit enormously difficult ones, would substantially improve future ocean conditions globally.

The ability to determine which pressures contribute the most to cumulative impacts in different places on different habitats could help guide action toward where return on investment can be the greatest. For example, cumulative impacts are projected to be much higher for several coastal habitats, both because of diverse human uses and associated pressures in nearshore areas and because of the greater vulnerability of many coastal habitats to many different pressures. In particular, salt marshes and mangroves are sensitive to sea level rise, and this pressure is projected to play a dominant role in future impacts on these habitats. Salt marshes and seagrasses also appear to be sensitive to extreme air temperatures, making that pressure a likely key driver of future impacts for those habitats. Prioritizing management actions targeting these heavily affected habitats, and key drivers of those impacts, should improve ocean conditions the most in these coastal regions. Reduction in any pressure would still be valuable in helping to build resilience to the remaining pressures.

As with any forecast analysis, our results are based on models that require assumptions, inherently have some level of uncertainty, or are constrained by available data. A key limitation of our study is that we could not account for expected impacts from all human activities because of insufficient or missing data needed to model and project some pressures. Indeed, there are many gaps in our knowledge about the distribution and intensity of current and future pressures in marine environments (*40*–*42*). Most notably, we were not able to spatially project the future distribution and intensity of noise pollution, invasive species, habitat destruction from some fishing practices, marine plastics, coastal hardening, drought and salinity changes (for coastal habitats), and marine structures such as offshore wind and oil platforms. Most of these missing pressures arise from nearshore activities, such that our projected increase in cumulative impacts within EEZs is an underestimate of the future. Furthermore, we were only able to account for a small amount of known disturbance and habitat destruction connected to direct human presence, yet disturbance related to shipping, mariculture, and offshore energy, among others, will likely increase and may contribute substantially to future cumulative impacts. Finally, our models assume additive pressures, but many pressures likely interact synergistically and in ways that we are currently unable to predict (*43*, *44*).

Additionally, we expect that the results described here would differ if assessed instead by impacts to species (*18*). Increasing ocean warming and fishing pressure have been shown to have particularly large impacts on elasmobranchs and ray-finned fishes (*18*), but our analyses do not account for such species-level effects. Similarly, large projected increases in water temperature and ocean acidification are particularly concerning for corals and other invertebrate groups (i.e., mollusks, echinoderms, cephalopods, and crustaceans) given that these taxa are already experiencing very high impacts (*18*). Because species ranges will shift under future environmental change, projections of cumulative impacts to species would also require mapping the future locations of species. Such projections exist for many taxa (*17*, *45*) and, combined with process-based, spatialized ecosystem models (*46*), could be used to refine our results (*47*).

Projecting the future in a spatially explicit manner is inherently difficult and fraught with uncertainty, but efforts like ours here provide key baselines (or business-as-usual scenarios) against which scenarios can be compared, focusing on futures that account for more than just single-pressure impacts. These scenarios can guide the management of human activities and associated pressures and the conservation implications that follow. Ocean management is increasingly turning to marine spatial planning, with goals for sustainable multiuse economies and marine protection (*48*). Conducting these kinds of scenario analyses presents key opportunities for future research and application of our work.

Our results highlight the need to always assess and map cumulative impacts to allow for informed and strategic policy- and decision-making around improving overall ocean health and delivery of ecosystem services to people. A narrow focus on single issues or specific locations can miss the kelp forest for the trees.

REFERENCES AND NOTES

1. D. Bianchi, D. A. Carozza, E. D. Galbraith, J. Guiet, T. DeVries, *Sci. Adv.* **7**, eabd7554 (2021).
2. B. S. Halpern *et al.*, *Nature* **488**, 615–620 (2012).
3. D. A. Kroodsma *et al.*, *Science* **359**, 904–908 (2018).
4. A. B. Bugnot *et al.*, *Nat. Sustain.* **4**, 33–41 (2021).
5. F. S. Paolo *et al.*, *Nature* **625**, 85–91 (2024).
6. World Bank Group, "Data catalog: Global shipping traffic density" (World Bank Group, 2023); https://datacatalog.worldbank.org/search/dataset/0037580.
7. I. Micella, C. Kroeze, M. P. Bak, M. Strokal, *Mar. Pollut. Bull.* **198**, 115902 (2024).
8. A. H. W. Beusen *et al.*, *Glob. Environ. Change* **72**, 102426 (2022).
9. International Panel on Climate Change, "Climate change 2023: Synthesis report" (IPCC, 2023; https://www.ipcc.ch/report/ar6/syr/downloads/report/IPCC_AR6_SYR_FullVolume.pdf.
10. D. P. Tittensor *et al.*, *Nat. Clim. Chang.* **11**, 973–981 (2021).
11. R. H. Cowie, P. Bouchet, B. Fontaine, *Biol. Rev. Camb. Philos. Soc.* **97**, 640–663 (2022).
12. N. Butt *et al.*, *Ecosphere* **13**, e3919 (2022).
13. J. L. Penn, C. Deutsch, *Science* **376**, 524–526 (2022).
14. B. S. Halpern *et al.*, *Science* **319**, 948–952 (2008).
15. B. S. Halpern *et al.*, *Nat. Commun.* **6**, 7615 (2015).
16. D. Hodapp *et al.*, *Glob. Chang. Biol.* **29**, 3304–3317 (2023).
17. J. García Molinos *et al.*, *Nat. Clim. Chang.* **6**, 83–88 (2016).
18. C. C. O'Hara *et al.*, *PLOS ONE* **19**, e0309788 (2024).
19. D. G. Boyce *et al.*, *Nat. Clim. Chang.* **12**, 854–862 (2022).
20. R. R. Reisinger *et al.*, *Divers. Distrib.* **28**, 142–159 (2022).
21. C. C. O'Hara, M. Frazier, B. S. Halpern, *Science* **372**, 84–87 (2021).
22. C. Simeoni *et al.*, *Sci. Total Environ.* **861**, 160687 (2023).
23. A. Borja *et al.*, *Front. Ocean Sustain.* **1**, 1308125 (2024).
24. J. H. Andersen *et al.*, *Ambio* **52**, 1981–1991 (2023).
25. I. Wåhlström *et al.*, *Glob. Chang. Biol.* **28**, 5310–5319 (2022).
26. See the supplementary materials.
27. B. S. Halpern, K. A. Selkoe, F. Micheli, C. V. Kappel, *Conserv. Biol.* **21**, 1301–1315 (2007).
28. B. S. Halpern *et al.*, *Sci. Rep.* **9**, 11609 (2019).
29. M. G. Burgess, S. L. Becker, R. E. Langendorf, A. Fredston, C. M. Brooks, *ICES J. Mar. Sci.* **80**, 1163–1178 (2023).
30. D. S. Schoeman *et al.*, *Trends Ecol. Evol.* **38**, 843–858 (2023).
31. Y. Ye, J. S. Link, *Sci. Rep.* **13**, 10571 (2023).
32. J. T. Thorson, J. M. Cope, T. A. Branch, O. P. Jensen, *Can. J. Fish. Aquat. Sci.* **69**, 1556–1568 (2012).
33. M. C. Melnychuk, E. Peterson, M. Elliott, R. Hilborn, *Proc. Natl. Acad. Sci. U.S.A.* **114**, 178–183 (2017).
34. C. Costello, D. Ovando, *Annu. Rev. Environ. Resour.* **44**, 177–200 (2019).
35. L.-M. Chevin, R. Lande, G. M. Mace, *PLOS Biol.* **8**, e1000357 (2010).
36. C. J. Carlson *et al.*, *Nature* **607**, 555–562 (2022).
37. H.-O. Pörtner *et al.*, *Science* **380**, eabl4881 (2023).
38. R. Angelini *et al.*, *Mar. Environ. Res.* **204**, 106909 (2025).
39. F. Ramírez *et al.*, *Sci. Total Environ.* **756**, 144002 (2021).
40. O. A. Vargas-Fonseca, M. Frazier, A. T. Lombard, B. S. Halpern, *Earths Futur.* **12**, e2024EF004559 (2024).
41. C. C. O'Hara, B. S. Halpern, *Annu. Rev. Environ. Resour.* **47**, 291–315 (2022).
42. P. E. Posen, K. Hyder, M. Teixeira Alves, N. G. H. Taylor, C. P. Lynam, *Ocean Coast. Manage.* **192**, 105206 (2020).
43. C. Fu *et al.*, *Ecol. Modell.* **368**, 265–276 (2018).
44. C. M. Crain, K. Kroeker, B. S. Halpern, *Ecol. Lett.* **11**, 1304–1315 (2008).
45. W. W. L. Cheung *et al.*, *Glob. Chang. Biol.* **16**, 24–35 (2010).
46. T. D. Eddy *et al.*, *Earths Futur.* **13**, e2024EF005537 (2025).
47. Data for: B. S. Halpern, M. Frazier, C. C. O'Hara, O. A. Vargas-Fonseca, A. T. Lombard, Cumulative impacts to global marine ecosystems projected to more than double by mid-century, KNB (2025); https://doi.org/10.5063/F18K77KZ.
48. A. T. Lombard *et al.*, *Front. Mar. Sci.* **6**, 146 (2019).

ACKNOWLEDGMENTS

We thank the National Center for Ecological Analysis and Synthesis (NCEAS) for general support and D. Bianchi and J. Guiet for providing modeled fish biomass data. **Funding:** This work was supported by the MARISCO (Marine Research and Innovation for a Sustainable management of Coasts and Oceans) project, which is part of Ocean Sustainability Collaborative Research Action 2018 by Belmont Forum, with support from the National Science Foundation (NSF) for both US and South African researchers (federal award number FAIN 2019902 and subaward number NSF KK2153). **Author contributions:** Analyses: M.F.; Conceptualization: B.S.H., M.F.; Funding acquisition: B.S.H., A.T.L.; Methodology: M.F., B.S.H., C.C.O.; Project administration: B.S.H., M.F., A.T.L.; Visualization: M.F., B.S.H., C.C.O.; Writing – original draft: B.S.H., M.F.; Writing – review & editing: all authors. **Competing interests:** The authors declare no competing interests. **Data and materials availability:** All data are freely available at KNB (*47*) and all code at https://github.com/OHI-Science/stressors.

SUPPLEMENTARY MATERIALS

science.org/doi/10.1126/science.adv2906
Materials and Methods; Figs. S1 to S6; Tables S1 to S3; References (*49*–*124*); Data S1 to S3

Submitted 12 December 2024; accepted 24 July 2025; published online 4 September 2025
10.1126/science.adv2906

MONSOONS

More extreme Indian monsoon rainfall in El Niño summers

Spencer A. Hill[1]*, Destiny Zamir Meyers[2], Adam H. Sobel[3,4]
Michela Biasutti[3], Mark A. Cane[3], Michael K. Tippett[4], Fiaz Ahmed[5]

Extreme rainfall during the Indian summer monsoon can be destructive and deadly to the world's third-largest economy and most populous country. Although El Niño events in the equatorial Pacific are known to suppress total summer rainfall throughout India, we show using observational data spanning 1901 to 2020 that, counterintuitively, they simultaneously intensify extreme daily rainfall. This is partly driven by increases in extreme daily values of convective buoyancy, provided that both the undilute instability of near-surface air and the dilution by mixing with drier air above are considered. El Niño could plausibly drive similar changes in other tropical regions, and our framework could be further applied to changes in hourly extremes, to other internal variability modes, and to forced trends under climate change.

The influence of the El Niño–Southern Oscillation (ENSO) on total summer rainfall in India has been recognized since the early 20th century (*1*–*4*). Anomalously warm sea surface temperatures (SSTs) in the equatorial Pacific during El Niño summers generate anomalous season-mean ascent of tropospheric air locally but compensating descent over much of the rest of the tropics, including India.

One might expect summer-mean subsidence to inhibit moist convection of all intensities, extremes included, reducing both the mean and variance of daily rainfall. Indeed, recent studies (*5*, *6*) establish that El Niño reduces the average accumulation of precipitation on rainy days—the rainfall intensity—within southeastern India and in Rajasthan state in the northwest. These are the summer monsoon's climatologically dry areas, and within them during El Niño summers it tends to rain even less overall, less often, and less intensely when rain does fall (*5*, *6*).

But the opposite rainfall intensity signal emerges in the summer monsoon's climatologically rainy areas (*5*, *6*)—the broad Central Monsoon Zone in central India and the narrow southwestern band between the Arabian Sea and the Western Ghats mountains of peninsular India. Within them it tends to rain less overall and less often during El Niño summers but more intensely when the rain comes.

Whether these signals in rainfall intensity stem from destructive extreme daily rainfall events (*7*) or agriculturally beneficial moderate rainfall days (*8*), and what their mechanistic origins are, remain unanswered. Observational studies have investigated ENSO's influence on daily or hourly rainfall extremes in other tropical domains (*9*–*16*) but not in the Indian summer monsoon.

By comparison, the possibility of long-term positive trends in Indian summer monsoon extreme rainfall has received considerable attention (*17*, *18*), but the existence of such trends is contested (*19*), they can be sensitive to the particular metric used to characterize an extreme event (*19*), and they have largely flattened or reversed over the most recent years (*20*). Climatologically, daily rainfall in the Indian summer monsoon is strongly influenced by both intraseasonal modes as manifested in active and break periods (*21*) and by synoptic disturbances, particularly monsoon low-pressure systems (*22*, *23*). But ENSO's influence on intraseasonal modes is strongly contested (*21*, *24*), and its influence on low-pressure systems appears modest, at least on an India-wide basis (*22*). It is well established, however, no matter what the states of secular trends, intraseasonal modes, or synoptic systems are, that tropical rainfall is fueled by high values of local convective buoyancy, which depends on both the undilute buoyancy of near-surface air and on how moist is the air immediately above (*25*). These factors create a pressing need to understand how daily rainfall extremes in the Indian summer monsoon are affected by ENSO, using concomitant changes in local convective buoyancy to understand the underlying physical causes.

ENSO influences on extreme daily rainfall

Our primary metric of extreme daily rainfall is the cutoff accumulation (*26*, *27*), computed as the ratio of the variance to the mean of daily rainfall across summer days (*28*). This metric is motivated by the reliably γ-like distributions of daily rainfall (*29*): Probabilities follow a shallow power law below the cutoff before dropping off exponentially above it (Fig. 1A). Increasing the cutoff, which in the exact γ limit is identical to the scale parameter, therefore makes all extreme rain rates more likely. Our primary dataset is the India Meteorological Department (IMD) daily 0.25° by 0.25° gridded rainfall product spanning 1901 to 2020, derived from a dense, temporally varying in situ rain gauge network (*30*). We used all 122 days within each June-July-August-September (JJAS) summer season and all grid points within the "monsoonal India" domain (*31*) (Fig. 1, B and C), where the dataset is most reliable (fig. S1) (*28*). As shown below, key results are robust across alternative metrics of extremes and to another daily rainfall dataset.

Climatological summer-mean rainfall (Fig. 1B) spans from 0.4 mm to 39.4 mm day^{-1} across monsoonal India grid points and has a distinct spatial structure: high values within the southwestern coastal band, a sharp gradient moving east across the Western Ghats mountain range to much smaller values in the southeast, intermediate values in the north in most of the Central Monsoon Zone, and low values again in Rajasthan in the far northwest. This geographic pattern emerges in many properties of summer monsoon rainfall from daily to interannual timescales (*5*, *6*, *32*) (fig. S2) and includes measures of daily extremes, which additionally exhibit enhanced values in Gujarat (along the Arabian Sea coast within the Central Monsoon Zone), where most summers are quite dry but others receive synoptically driven extreme accumulations (*33*) (fig. S3).

According to lag-zero correlations of each grid point's JJAS cutoff with the standard NINO3.4 index of ENSO (*28*), extreme daily rainfall becomes more likely over much of the southwestern coastal band and central India as NINO3.4 increases but less likely over much of the southeast and far northwest (Fig. 1C). There is considerable noise, as expected for the extremes of an inherently sporadic quantity such as rainfall, but otherwise this pattern resembles the climatological summer-mean rainfall (Fig. 1B) and the established (*5*, *6*) ENSO-driven patterns in rainfall intensity.

For each of the four subregions of India outlined in Fig. 1, we computed an aggregate cutoff by combining all grid points within that region into a single daily rainfall distribution for each summer (*28*). Whereas the cutoff for Southeast India is negatively correlated with NINO3.4 and marginally statistically significant [correlation coefficient (r) = −0.16, P = 0.08], the corresponding correlations for All-Monsoonal India, the Central Monsoon Zone, and the Western Ghats regions are all significantly positive (r = +0.34, +0.34, +0.20 and P = 2×10^{-4}, 2×10^{-4}, 0.03, respectively) (*28*). Composites combining either all summers from 1901 to 2020, the 36 El Niño summers, or the 41 La Niña summers behave similarly: Except for Southeast India, the region-aggregated cutoffs are all significantly larger for the El Niño than for the La Niña composites (Fig. 2A) (*28*).

[1]Department of Earth and Atmospheric Sciences, City College of New York, New York, NY, USA. [2]Department of Civil Engineering & Engineering Mechanics, Columbia University, New York, NY, USA. [3]Department of Applied Physics and Applied Mathematics, Columbia University, New York, NY, USA. [4]Lamont-Doherty Earth Observatory, Columbia University, Palisades, NY, USA. [5]Department of Atmospheric and Oceanic Sciences, University of California, Los Angeles, Los Angeles, CA, USA.
*Corresponding author. Email: shill1@ccny.cuny.edu

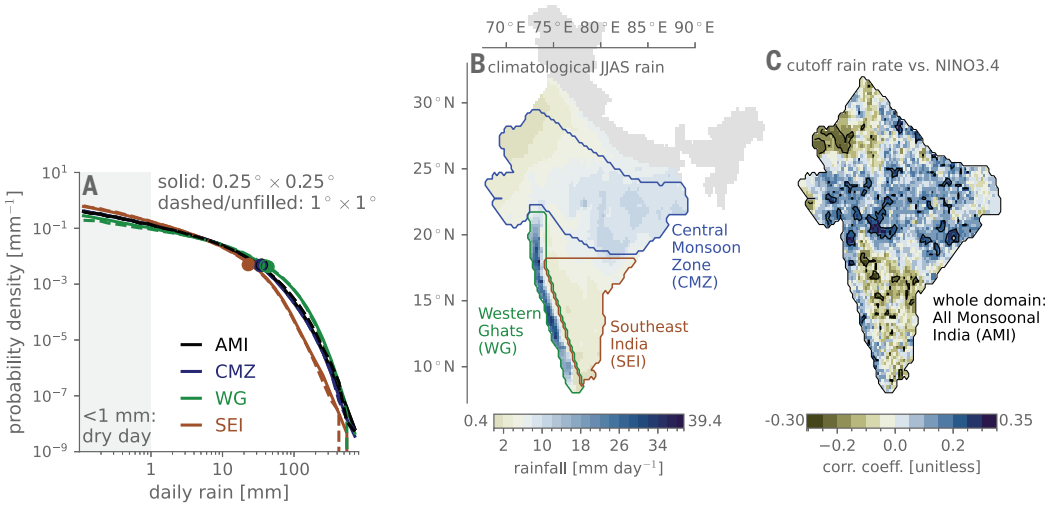

Fig. 1. Extreme daily rainfall over the Indian summer monsoon's rainiest areas becomes more likely the stronger that El Niño conditions are. (**A**) Daily rainfall empirical probability distributions, in log-log space, combining all June-July-August-September (JJAS) days from 1901 to 2020 and all grid points within all of monsoonal India (black), the Central Monsoon Zone (blue), the Western Ghats coastal band (green), or Southeast India [brown; subdomain outlines shown in (B) and (C)]. Overlaid circles indicate the climatological value of the cutoff rain rate, which is our primary metric of extreme daily rainfall. (**B**) Local climatological JJAS-mean rainfall (millimeters per day) according to the color bar. The portions of northern and northeast India shaded gray are excluded from all analyses. (**C**) Pearson correlation coefficient between detrended time series of the JJAS NINO3.4 value and each grid point's cutoff rain rate. Positive values indicate that extreme rainfall is enhanced for El Niño compared with La Niña conditions. The black contours enclose grid points with statistically significant correlations, using a false discovery rate of 0.3, which corresponds in this case to $P < 0.039$.

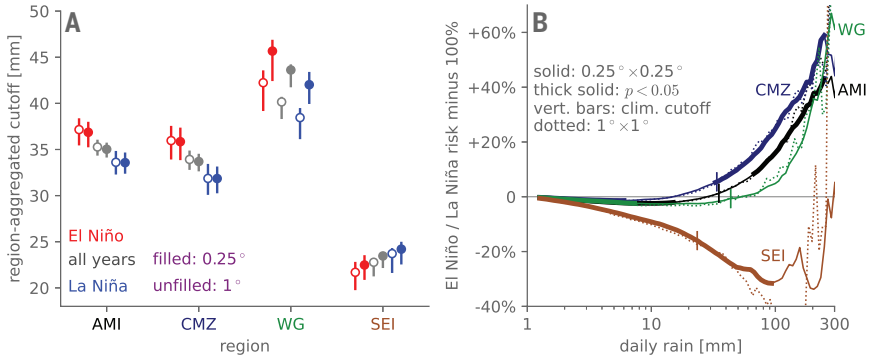

Fig. 2. Light to moderate accumulation likelihoods are suppressed everywhere, whereas heavy and extreme accumulation likelihoods are enhanced in the wet regions during El Niño summers. (**A**) Composite regional cutoffs (in millimeters) shown in filled circles. Bars indicate 95% confidence intervals based on yearly cutoff values. Open circles indicate the results computed from the IMD 1° by 1° dataset. (**B**) ENSO risk ratios: restricting to rainy days (>1 mm), the probability that rainfall exceeds a given rain rate in the El Niño composite divided by that in the La Niña composite, expressed as a percentage difference from unity. Thick lines denote where the risk ratio is significantly different from unity, according to a permutation test. Overlaid vertical lines show each region's climatological cutoff. Dotted curves are the risk ratios computed from the IMD 1° by 1° dataset.

These signals in extremes differ qualitatively from those in less-severe rain rates, which are suppressed throughout the domain by El Niño. This difference can be seen in ENSO risk ratios for each region (*26*, *27*, *29*), which are defined at each daily accumulation as the fraction of rainy days that accumulation value in El Niño summers divided by the corresponding fraction for La Niña summers (Fig. 2B) (*28*). Statistically significant reductions in the likelihoods of weak to moderate accumulations emerge in all four regions, and for Southeast India this reduction extends to the extremes as well (*28*). But for the other regions, the risk ratios minimize at moderate accumulations and then, near the climatological cutoff (overlaid vertical lines in Fig. 2B), they begin increasing quasi-exponentially with accumulation—the signature of an increased cutoff (*26*). For accumulations exceeding ~250 mm, for example, statistically significant increases in likelihoods are 43% for the whole domain and 59% for the Central Monsoon Zone; owing to greater interannual variability in this quantity for the southwestern coastal band, the 48% increase there is marginally statistically significant ($P = 0.07$). Presumably due to sampling uncertainty, behaviors for accumulations exceeding 300 mm are not statistically significant and are too erratic to be meaningfully physically interpreted. None of these key results are qualitatively sensitive to the specific methods or dataset chosen.

Correlations between NINO3.4 and pointwise exceedance counts—the number of days in a given summer exceeding a specified local-rainfall percentile or rain rate in millimeters—are predominantly negative for low through moderate values throughout the domain but become positive for sufficiently high values within the climatologically wet regions (fig. S4). Cutoffs and risk ratios estimated from γ fits to each composite distribution yield similar results (fig. S5) as do other metrics of extreme rainfall, including correlations of block maxima with

NINO3.4, pointwise Gumbel fits to the block maxima for El Niño versus La Niña composites, and quantile regressions of daily rainfall versus NINO3.4 (fig. S6) (*27*). Results are also similar in the IMD 1° by 1° gridded daily rainfall dataset (*34*), which, importantly for extremes (*35*), is generated from a fixed rather than temporally varying network of rain gauges (dashed curves and unfilled elements in Figs. 1, 2, and fig. S5) (*28*).

Lastly, whereas El Niño's propensity to generate summer-mean Indian drought weakened from the pre-satellite (1901–1978) to satellite (1979–2020) eras (*36*–*38*)—with the correlation between NINO3.4 and the all-Monsoonal India domain-mean, JJAS mean rainfall weakening by ~31%, from $P = -0.59$ to -0.41—the ENSO signals in extremes are more stationary (fig. S7) (*28*).

This finding holds in terms of the overall geographic patterns seen in pointwise cutoffs, linear regressions of the region-aggregated cutoffs on NINO3.4, and an index linearly combining the region-aggregated cutoffs of the Central Monsoon Zone, Western Ghats, and Southeast India regions (*28*). Nevertheless, within peninsular India, both the increase in extremes with NINO3.4 in the southwestern coastal band and the decrease in the southeast weaken nontrivially. As such, for the region-aggregate cutoffs, only the Central Monsoon Zone's regression against NINO3.4 is statistically significant within the satellite era. The extent to which these modest differences between epochs are physically forced versus merely sampling-driven (*37*) remains to be seen.

Mechanisms: ENSO-forced changes in convective buoyancy extremes

In general, one expects heavy rain where near-surface air is especially warm and moist and is sitting below air that is also nearly saturated. These conditions enable the near-surface air to easily begin rising, precipitating out copious amounts of water as it ascends, despite losing buoyancy to cooling through expansion and to dilution through mixing with the drier ambient air. These processes have been encapsulated into a scalar metric of convective buoyancy known as B_L (*25*, *39*), which we computed for each grid point and summer day of 1979 to 2020, using European Centre for Medium-Range Weather Forecasts Reanalysis Fifth Generation (ERA5) reanalysis data (*28*, *40*).

Daily rainfall depends strongly on local convective buoyancy, with nonlinear Spearman correlation coefficient positive at every grid point (Fig. 3A), up to +0.71, and the expected quasi-threshold relationship (*25*, *39*) in region-aggregated conditional averages (Fig. 3B) and quantiles (Fig. 3C) of rainfall as a function of local buoyancy (*28*). Rainfall is typically absent or weak until buoyancy reaches a threshold value slightly less than zero, above which rainfall increases sharply, rapidly consuming buoyancy with it (Fig. 3B). These conditional curves rise to higher rainfall values in the rainy southwestern coastal band and Central Monsoon Zone compared with those for drier southeast India, but for a given region to first approximation they are insensitive to the state of ENSO (Fig. 3C).

This consistency of the rainfall-buoyancy relationships across ENSO states, combined with the responses of the convective buoyancy distributions themselves to ENSO, help explain the responses of rainfall to ENSO. At the summer-mean timescale, pointwise correlations of convective buoyancy against NINO3.4 are negative at every grid point (fig. S8). But for extremes, such as 99th-percentile rainy-day values, they are significantly positive over much of central-eastern India but significantly negative over much of the southeast and northwest (Fig. 4A). These signals are shared by the individual buoyancy components (Fig. 4, B and C): Both nearly saturated and very gravitationally unstable days are predominantly enhanced over eastern-central India versus suppressed over the northwest and southeast.

What, then, accounts for these convective buoyancy signals? Preliminary results point toward synoptic low-pressure systems (*41*), which generate heavy rainfall within their cores (*42*) and track predominantly over Central India, although occasionally traveling farther

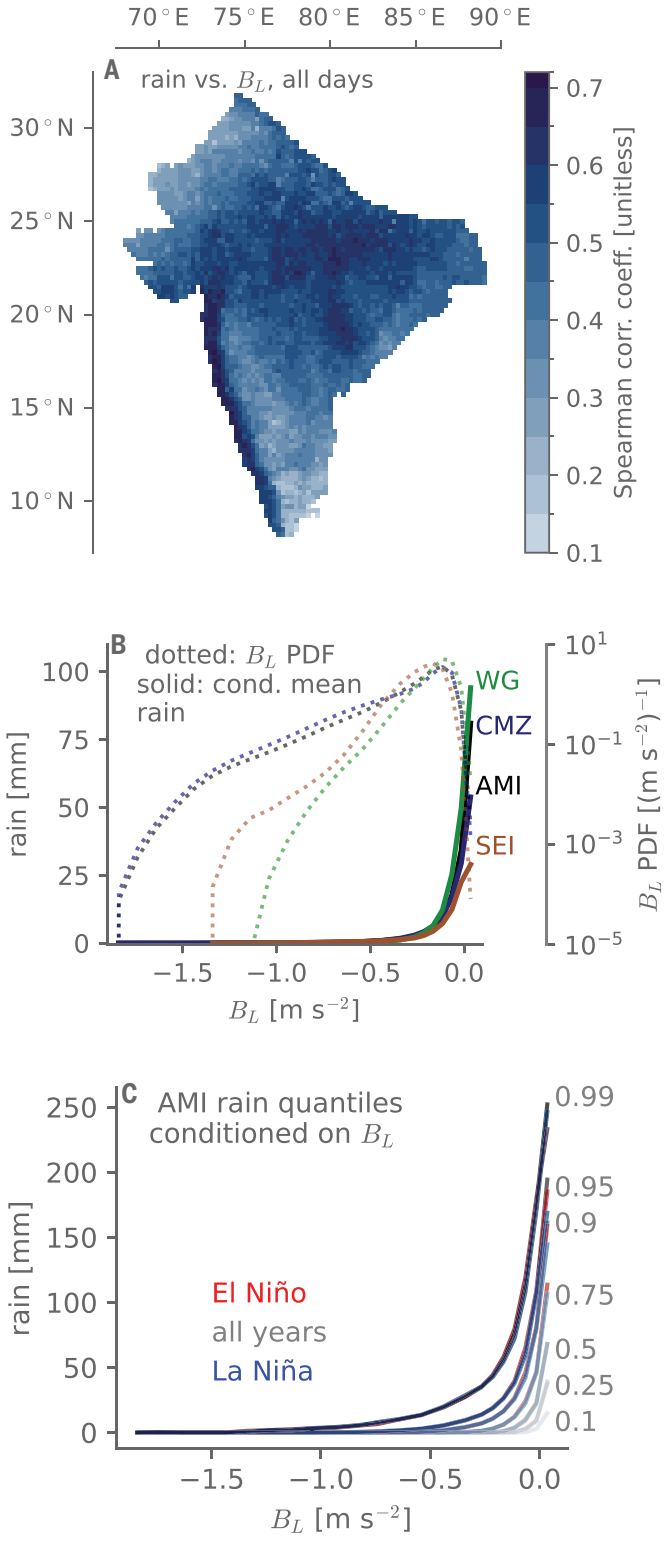

Fig. 3. Local convective buoyancy strongly controls daily rainfall. (**A**) Spearman correlation coefficient across all JJAS days from 1979 to 2020 at each grid point between daily rainfall and a metric of convective buoyancy (B_L) computed from ERA5 reanalysis data. (**B**) In dotted curves, probability density functions of B_L for each region, according to the right axis. In solid curves, daily rainfall is conditionally averaged on the buoyancy metric, according to the right axis. (**C**) For the entire monsoonal India domain, composite quantiles of rainfall are conditioned on B_L as labeled. For each quantile, red curves for El Niño are almost entirely obscured by others because of weak ENSO dependence in the relationships.

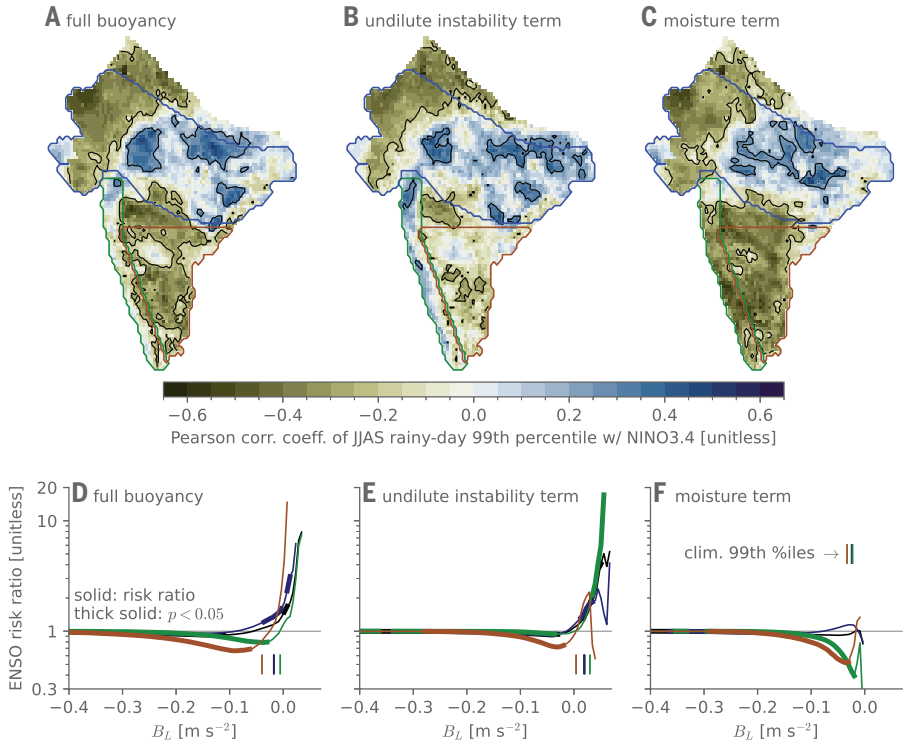

Fig. 4. Right-tail daily convective buoyancy occurrence under ENSO largely tracks with the extreme rainfall. (**A** to **C**) Pearson correlation coefficient of NINO3.4 versus 99th-percentile daily values of (A) the full buoyancy metric, (B) just the undilute instability term, and (C) just the moisture term, for each JJAS. The black contours enclose areas deemed statistically significant on the basis of a false discovery rate of 0.3. (**D** to **F**) Regional ENSO risk ratios of rainy-day buoyancy, for (D) the full metric, (E) just the undilute instability term, or (F) just the moisture term. Thick lines denote where the risk ratio is significantly different from unity, on the basis of a permutation test. Overlaid vertical lines denote the climatological 99th-percentile values for each region of the given buoyancy component.

south or extending to Rajasthan in the northwest (*33*). A prior study indicates that the cores of monsoon low-pressure systems are very humid and that during El Niño summers, the rainfall within those cores is enhanced (*43*). One possibility is that those low-pressure system tracks over and ending in central India are favored by El Niño at the expense of those over peninsular India and any long tracks that might reach northwestern India. This would promote very humid, buoyant days—and with them extreme rainfall likelihoods—in central-eastern India and suppress them in the southeast and northwest.

For the southwestern coastal band—which is less directly influenced by these synoptic systems—whereas nearly saturated days above the boundary layer are strongly suppressed in El Niño summers, highly gravitationally unstable days are strongly enhanced. This is particularly evident in risk ratios of the convective buoyancy terms on rainy days (Fig. 4, D to F) (*28*): Gravitationally unstable days are as much as 17 times more likely in El Niño than La Niña summers. Moreover, according to differences in the ENSO composites of rainfall conditioned on the buoyancy terms (fig. S9), tropospheric dryness inhibits heavy rainfall somewhat less during El Niño summers. We therefore speculate that the anomalous time-mean free-tropospheric subsidence and dryness under El Niño (fig. S10) suppress moderate rain events, enabling higher undilute instability values to occasionally build up, fueling extreme convection once a passing wave or advective event remoistens the lower free troposphere just enough. This mechanism would be broadly consistent with observational and modeling evidence for less frequent but more intense rain events in drier ambient conditions (*44*), such as in the pre-monsoon season (*45*)

Outlook: Seasonal forecasts, climate change, and other extensions

Despite ENSO's known "spring predictability barrier" (*46*), existing seasonal forecasts of ENSO during boreal summer are skillful (*47*); for example, the multimodel-mean forecasted JJAS value of NINO3.4 from the North American Multi-Model Ensemble (NMME) (*48*) seasonal forecast integrations initialized annually on 1 May are correlated with the actual value at $r = 0.86$ over 1981–2020 (*28*). We have recomputed the correlations between the JJAS cutoff rain rate and NINO3.4 using this forecasted value, and the overall signals remain (fig. S11). This raises the prospect of skillful ENSO-based seasonal forecasts of extreme rainfall probabilities within monsoonal India. However, the statistical significance weakens nontrivially, and risk ratios that use NMME 1-May forecasted JJAS NINO3.4 show considerably weaker separation between El Niño and La Niña summers. Providing societally actionable information may therefore require even more-skillful forecasts of the state of ENSO.

The observed long-term trend toward more extreme daily rainfall events in central India into the early 2000s has been argued to stem from mean moistening of the troposphere due to global warming (*17*, *18*) as have future projections of increased extreme rainfall events globally (*27*). Notwithstanding that more recent trends in the Indian summer monsoon have been flat or negative (*20*), underlying this argument are the assumptions that right-tail daily moisture events (i) track with the season-mean value and (ii) predominate over changes in undilute instability. On the basis of our results, however, for ENSO, (i) is violated within central India, and (ii) is violated within the southwestern coastal band—precisely the regions where daily extreme rainfall is projected to increase most in model simulations under future global warming (*49*). This finding argues for revisiting both observed trends and model projections of extreme rainfall, incorporating the full daily distributions of rainfall and of the convective buoyancy terms. This evaluation must be done in tandem with careful analysis of secular changes in monsoon low-pressure systems—both weaker lows and stronger depressions—because projected increases in rainfall intensity within these systems likely play a major factor in the overall expected increase in Indian summer extreme rainfall (*50*). Only then can we meaningfully evaluate whether these observed, interannual, internally generated ENSO signals constitute a meaningful emergent constraint on model-projected, secular, externally forced trends (*51*).

Our approach could also be applied to climate variability modes in the Indian (*52*, *53*) and Atlantic Oceans (*54*) thought to influence the summer monsoon, as well as to hourly rainfall. Many Indian summer monsoon rain events are considerably shorter than 24 hours in

duration (*55*), and a study (*15*) using hourly rainfall suggests that the average rain rate during rainy hours increases with El Niño over much of the Tropics. Perhaps, as for daily rain in the Indian summer monsoon, these signals reflect buoyancy-driven increased extremes.

REFERENCES AND NOTES

1. G. T. Walker, "On the Meteorological Evidence for Supposed Changes of Climate in India" (Tech. Rep., India Meteorological Department, 1910).
2. G. B. Pant, S. B. Parthasarathy, *Arch. Meteorol. Geophys. Bioklimatol. [B]* **29**, 245–252 (1981).
3. E. M. Rasmusson, T. H. Carpenter, *Mon. Weather Rev.* **111**, 517–528 (1983).
4. S. Gadgil, *Annu. Rev. Earth Planet. Sci.* **31**, 429–467 (2003).
5. V. Moron, A. W. Robertson, D. S. Pai, *Clim. Dyn.* **49**, 3403–3423 (2017).
6. S. A. Hill, A. H. Sobel, M. Biasutti, M. A. Cane, *Geophys. Res. Lett.* **49**, e2021GL096541 (2022).
7. D. L. Suhas, N. Ramesh, R. M. Kripa, W. R. Boos, *NPJ Clim. Atmos. Sci.* **6**, 48 (2023).
8. S. Gadgil, S. Gadgil, *Econ. Polit. Wkly.* **41**, 4887–4895 (2006).
9. S. Curtis *et al.*, *J. Hydrometeorol.* **8**, 678–689 (2007).
10. R. P. Allan, B. J. Soden, *Science* **321**, 1481–1484 (2008).
11. J. V. Revadekar, A. Kulkarni, *Int. J. Climatol.* **28**, 1445–1452 (2008).
12. A. M. Grimm, R. G. Tedeschi, *J. Clim.* **22**, 1589–1609 (2009).
13. X. Sun, B. Renard, M. Thyer, S. Westra, M. Lang, *J. Hydrol. (Amst.)* **530**, 51–65 (2015).
14. K. Saunders, A. G. Stephenson, P. G. Taylor, D. Karoly, *Weather Clim. Extrem.* **18**, 17–28 (2017).
15. X.-F. Li *et al.*, *Clim. Dyn.* **54**, 4823–4839 (2020).
16. A. Vashisht, B. Zaitchik, *J. Clim.* **35**, 2019–2034 (2021).
17. B. N. Goswami, V. Venugopal, D. Sengupta, M. S. Madhusoodanan, P. K. Xavier, *Science* **314**, 1442–1445 (2006).
18. M. Rajeevan, J. Bhate, A. K. Jaswal, *Geophys. Res. Lett.* **35**, 2008GL035143 (2008).
19. S. Ghosh, D. Das, S.-C. Kao, A. R. Ganguly, *Nat. Clim. Chang.* **2**, 86–91 (2012).
20. C. Bajrang, R. Attada, B. N. Goswami, *NPJ Clim. Atmos. Sci.* **6**, 120 (2023).
21. V. Krishnamurthy, J. Shukla, *J. Clim.* **37**, 4867–4884 (2024).
22. S. Vishnu, W. R. Boos, P. A. Ullrich, T. A. O'Brien, *J. Geophys. Res. Atmos.* **125**, e2020JD032977 (2020).
23. S. Vishnu, M. D. Risser, T. A. O'Brien, P. A. Ullrich, W. R. Boos, *NPJ Clim. Atmos. Sci.* **6**, 111 (2023).
24. S. Dwivedi, B. N. Goswami, F. Kucharski, *Geophys. Res. Lett.* **42**, 8201–8207 (2015).
25. F. Ahmed, Á. F. Adames, J. D. Neelin, *J. Atmos. Sci.* **77**, 2163–2186 (2020).
26. J. D. Neelin, S. Sahany, S. N. Stechmann, D. N. Bernstein, *Proc. Natl. Acad. Sci. U.S.A.* **114**, 1258–1263 (2017).
27. J. D. Neelin *et al.*, *Curr. Clim. Change Rep.* **8**, 17–33 (2022).
28. Materials and methods are available as supplementary material.
29. C. Martinez-Villalobos, J. D. Neelin, *J. Atmos. Sci.* **76**, 3611–3631 (2019).
30. D. S. Pai *et al*., *Mausam* **65**, 18 (2014).
31. S. Gadgil, K. Rajendran, D. S. Pai, *Mausam* **70**, 485–500 (2019).
32. V. Krishnamurthy, J. Shukla, *J. Clim.* **13**, 4366–4377 (2000).
33. K. M. R. Hunt, J. K. Fletcher, *Clim. Dyn.* **53**, 1859–1871 (2019).
34. M. Rajeevan, J. Bhate, J. D. Kale, B. Lai, "Development of a high resolution daily gridded rainll data for the Indian region" (India Meteorological Department, Met. Monograph Climatology No. 22/2005, 2005); https://apdrc.soest.hawaii.edu/doc/india_rain_ref_report.pdf.
35. M. Lin, P. Huybers, *Geophys. Res. Lett.* **46**, 1681–1689 (2019).
36. K. K. Kumar, B. Rajagopalan, M. A. Cane, *Science* **284**, 2156–2159 (1999).
37. A. Gershunov, N. Schneider, T. Barnett, *J. Clim.* **14**, 2486–2492 (2001).
38. K. K. Kumar, B. Rajagopalan, M. Hoerling, G. Bates, M. Cane, *Science* **314**, 115–119 (2006).
39. F. Ahmed, J. D. Neelin, *J. Atmos. Sci.* **75**, 1587–1608 (2018).
40. H. Hersbach *et al.*, *Q. J. R. Meteorol. Soc.* **146**, 1999–2049 (2020).
41. D. A. Mooley, *Mon. Weather Rev.* **101**, 271–280 (1973).
42. A. C. Nikumbh, A. Chakraborty, G. S. Bhat, *Sci. Rep.* **9**, 10321 (2019).
43. K. M. R. Hunt, A. G. Turner, P. M. Inness, D. E. Parker, R. C. Levine, *Mon. Weather Rev.* **144**, 3391–3416 (2016).
44. D. J. Raymond, Z. Stone, S. Sentic, *J. Adv. Model. Earth Syst.* **16**, e2023MS003980 (2024).
45. M. Biasutti, S. E. Yuter, *J. Geophys. Res. Atmos.* **118**, 9534–9551 (2013).
46. M. K. Tippett, M. L. L'Heureux, E. J. Becker, A. Kumar, *Geophys. Res. Lett.* **47**, e2020GL087008 (2020).
47. M. K. Tippett, M. Ranganathan, M. L'Heureux, A. G. Barnston, T. DelSole, *Clim. Dyn.* **53**, 7497–7518 (2019).
48. B. P. Kirtman *et al.*, *Bull. Am. Meteorol. Soc.* **95**, 585–601 (2014).
49. A. Katzenberger, J. Schewe, J. Pongratz, A. Levermann, *Earth Syst. Dyn.* **12**, 367–386 (2021).
50. S. Vishnu, W. R. Boos, W. D. Collins, *NPJ Clim. Atmos. Sci.* **6**, 182 (2023).
51. S. A. Klein, A. Hall, *Curr. Clim. Change Rep.* **1**, 276–287 (2015).
52. R. S. Ajayamohan, S. A. Rao, T. Yamagata, *J. Clim.* **21**, 5437–5454 (2008).
53. R. S. Ajayamohan, S. A. Rao, *J. Meteorol. Soc. Jpn.* **86**, 245–252 (2008).
54. P. J. Borah, V. Venugopal, J. Sukhatme, P. Muddebihal, B. N. Goswami, *Science* **370**, 1335–1338 (2020).
55. V. Moron, R. Barbero, H. J. Fowler, V. Mishra, *Philos. Trans. R. Soc. London Ser. A* **379**, 20200137 (2021).

ACKNOWLEDGMENTS

Funding: S.A.H. acknowledges funding from NSF award AGS-2123327. S.A.H., M.B., M.A.C., and A.H.S. acknowledge support from the Monsoon Mission Project under India's Ministry of Earth Sciences. **Author contributions:** S.A.H. designed the study, oversaw preliminary analyses performed by D.M.Z., performed most analyses, and led writing the manuscript; D.M.Z. performed the initial analyses establishing the ENSO-extreme rainfall signals; A.H.S., M.B., and M.A.C. provided scientific feedback throughout the project; M.K.T. provided guidance on statistical procedures; and F.A. provided guidance on convective buoyancy. All authors contributed to revising the manuscript. **Competing interests:** The authors declare that they have no competing interests. **Data and materials availability:** India Meteorological Department rainfall data used is available at https://www.imdpune.gov.in/cmpg/Griddata/Rainfall_25_NetCDF.html and https://www.imdpune.gov.in/cmpg/Griddata/Rainfall_1_NetCDF.html. ERSST data are available at https://www.ncei.noaa.gov/pub/data/cmb/ersst/v5/netcdf/. ERA5 data are available at https://www.ecmwf.int/en/forecasts/dataset/ecmwf-reanalysis-v5. NMME data are available at https://iridl.ldeo.columbia.edu/SOURCES/.Models/.NMME/.

SUPPLEMENTARY MATERIALS

science.org/doi/10.1126/science.adg5577
Materials and Methods; Figs. S1 to S11; References (*56*–*66*)

Submitted 3 December 2024; accepted 16 July 2025

10.1126/science.adg5577

QUANTUM MECHANICS

Quantum squeezing of a levitated nanomechanical oscillator

Mitsuyoshi Kamba, Naoki Hara, Kiyotaka Aikawa*

Manipulating the motion of macroscopic objects near their quantum mechanical uncertainties has been desired in diverse fields, including fundamental physics, sensing, and transducers. Despite progress in ground-state cooling of a levitated solid particle, realizing its nonclassical states has been elusive. Here, we demonstrate quantum squeezing of the motion of a single nanoparticle by rapidly varying its oscillation frequency. We reveal appreciable narrowing of the velocity variance to −4.9 ± 0.1 decibels of that of the ground state using free-expansion measurements. Our work shows that a levitated nanoparticle offers an ideal platform for studying nonclassical states of its motion and provides a route to developing applications in quantum sensing and exploring quantum mechanics at a macroscopic scale.

Oscillators have played a crucial role in diverse areas of modern quantum technologies, ranging from clocks (*1*) and sensors (*2*) to superconducting devices (*3*), where the accurate and precise measurement of the oscillation has been a crucial issue. Extensive studies with microscopic particles, most of which behave as harmonic oscillators, have revealed that the fundamental limit of observing the oscillation is imposed by quantum mechanics as $\Delta z \cdot \Delta p \geq \hbar/2$, where $\hbar$, Δz, and Δp are the reduced Planck's constant and the uncertainties in the position and momentum, respectively. This uncertainty principle dictated by Heisenberg suggests that even though both quadrature components cannot be observed with infinite precision at the same time, either of them can be measured more precisely than that of the quantum ground state. Because of the absence of its classical analog, such a process is called quantum squeezing and has been the subject of intensive research aiming at enhancing the sensitivity of observing the oscillators (*4*, *5*). Quantum squeezing also constitutes an important building block for quantum information processing (*6*). Bringing the knowledge achieved with microscopic particles to larger, more classical objects is an important task for extending the understanding and applications of quantum physics (*7*).

A levitated nanomechanical oscillator, a solid particle confined in an optical or electrical harmonic potential, provides an ideal opportunity for testing quantum mechanics at the meso- and macroscopic scales (*8*–*10*). Being isolated from other objects, levitated particles are expected to be ideal for sustaining fragile quantum states, and the wide tunability of their trapping potential has enabled various quantum protocols to be developed with microscopic particles, including a wavefunction expansion through a free fall. In recent years, technical developments have realized cooling the motions of levitated nanoparticles to their quantum ground state (*11*–*15*). However, observing quantum mechanical behavior of their motions remains challenging. An unexplored issue, unique to levitated quantum systems, is whether the the minute quantum effect in one motional degree of freedom can be revealed without being affected by other degrees of freedom.

Here, we demonstrate quantum squeezing of the center-of-mass (CoM) motion of a levitated, neutral, fast-spinning nanoparticle by rapid modulation of the laser intensity. We reveal a substantial reduction of the velocity uncertainty directly through time-of-flight (TOF) free-expansion measurements. The observed velocity variance is narrower than that of the ground state by 4.9 dB, which is comparable to the largest mechanical quantum squeezing obtained thus far (*16*). To quantitatively support our claim about the degree of squeezing, we propose and demonstrate a method to determine the displacement of the nanoparticle using an optical standing wave as a reference. This approach is in agreement with the conventional approach for calibrating displacement and provides a quantitative confirmation of the measured level of squeezing.

Features of a levitated system

Our experimental platform is a single charge-neutral nanoparticle levitated in the standing wave of a single-frequency laser—that is, an optical lattice (*17*) (Fig. 1A). Exploring a neutral nanoparticle has the advantage that its velocity can be measured through free expansion without the impact of residual electric field noises (*18*), similar to the case with ultracold atoms. The optical lattice provides a high oscillation frequency and facilitates cooling to the ground state, and the strong feedback force required to reach the ground state is exerted by manipulating the lattice with laser phase modulation (*14*). The strong photon scattering through the nanoparticle is a key aspect enabling continuous position measurement and feedback cooling, and it also imposes a relatively short motional coherence time with ~20 oscillations (*11*). This short coherence time makes it challenging to realize squeezing through the parametric modulation of the potential, which has been successfully applied to achieve squeezing of up to −3 dB in various quantum systems (*19*–*21*). Getting past the −3 dB limit has been intensively explored both theoretically (*22*, *23*) and experimentally (*16*).

To overcome the difficulty of short coherence time, we used a scheme based on rapid variations of the oscillation frequency (*24*–*27*). In this scheme, a sudden decrease in the oscillation frequency is followed by the recovery of the frequency to the original value (Fig. 1B). Similar schemes have been useful for exploring thermal squeezed states (*28*) and the delocalization of the nanoparticle's position (*29*, *30*). We consider a phase space with the coordinates of the position normalized by $\sqrt{\hbar/2m\omega_0}$ and the momentum normalized by $\sqrt{\hbar m\omega_0/2}$, where m and ω_0 are the mass of the nanoparticle and the oscillation frequency, respectively. When the oscillation frequency is abruptly varied from ω_0 to ω_1, the uncertainty on the phase space is modified by a factor of $\exp(-r)$, where $r = \ln(\omega_0/\omega_1)/2 = \ln(I_0/I_1)/4$ is a squeezing parameter (*24*), with I_0 and I_1 being the initial intensity and the decreased intensity, respectively. The elliptical uncertainty rotates on the phase space at the frequency of oscillation (Fig. 1C). Here, both the intensity reduction at $t = 0$ and the intensity increase at $t = t_1$ modify the uncertainty on the phase space. When the time duration for each process is carefully chosen to be $\omega_1 t_1 = \pi/2$ and $\omega_0(t_2 - t_1) = N\pi$, with N being an integer, the momentum uncertainty at t_2 can be minimized to e^{-2r} of that of the initial state.

Experimental procedure

We investigated the CoM motion of a neutral silica nanoparticle with a radius of 137 ± 3 nm in an optical lattice (*14*, *31*). The position of the nanoparticle was measured continuously by monitoring the photons scattered by it. The position signal was used for both feedback cooling of the CoM motions and the free-expansion measurement of the velocity distribution. We focused on the motion along the optical lattice (z direction), which has an oscillation frequency of $\omega_0 = 2\pi \times 252$ kHz. The initial state before the squeezing protocol had an occupation number of $n_z = 0.98 \pm 0.17$. The impact of librational motions on the CoM motion is a great concern (*18*). To stabilize the angular motions through a gyroscopic effect, we let the nanoparticle spin around the z axis at a frequency of ~5.6 ± 0.2 GHz by introducing a circularly polarized light into the trapping laser (*32*, *33*). During the entire

Department of Physics, The University of Tokyo, Tokyo, Japan. *Corresponding author. Email: aikawa@phys.s.u-tokyo.ac.jp

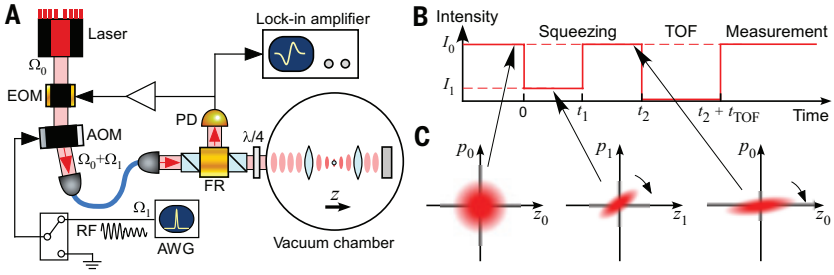

Fig. 1. Experimental system. (**A**) A single-frequency laser at a wavelength of 1551.38 nm forms an optical lattice in the vacuum chamber. The light scattered by the nanoparticle is collected through a Faraday rotator (FR) and is incident on a photodetector (PD). The signal from the PD is used for feedback cooling through modulating the laser phase with an electro-optic modulator (EOM). The intensity of the laser is controlled by an acousto-optic modulator (AOM) driven by an radiofrequency (RF) signal from an arbitrary waveform generator (AWG). The light is turned off by switching off the RF with a switch. A beam for cooling motions perpendicular to the *z* direction is incident from the right side. (**B**) Time sequence for the squeezing protocol. (**C**) Variation of the uncertainty on the normalized phase space during the squeezing protocol. z_i, p_i indicates the position normalized by $\sqrt{\hbar / 2m\omega_i}$ and the momentum normalized by $\sqrt{\hbar m\omega_i / 2}$, respectively, with $i = 0,1$.

measurement time, the background pressure was kept at ~1.0×10^{-6} Pa such that the decoherence rate through background gas collisions $\Gamma_{BG} = 2\pi \times (0.1 \pm 0.01)$ kHz was negligibly smaller than the decoherence rate caused by photon scattering $\Gamma_{qba} = 2\pi \times (2.1 \pm 0.1)$ kHz.

After the initial state preparation, we turned off feedback cooling and applied the squeezing protocol by modulating the laser intensity (Fig. 1B). Hereafter, we focus on the velocity instead of the momentum, because the velocity was directly obtained from the experiments. To measure the velocity v_z through a free-expansion measurement, we turned off the laser for the TOF of $t_{TOF} = 51$ μs. The displacement during the TOF, *z*, was measured by recording the oscillation amplitude after recapturing the nanoparticle. We obtained the distribution of the velocity $v_z = z/t_{TOF}$ by repeating the same procedure ~300 times. Given that the velocity distribution follows the Maxwell-Boltzmann distribution, we extracted the velocity width Δv_z by fitting the distribution with a Gaussian function:

$$f(v_z) = \exp\left[-(v_z - v_0)^2 / 2(\Delta v_z)^2\right] \quad (1)$$

The center of the velocity distribution v_0 reflects the displacement during the TOF caused by various forces such as the projection of gravity along the optical lattice and radiation pressure from a weak leakage light.

Results of squeezing experiments

When we varied $t_2 - t_1$, we observed a substantial time evolution of the velocity variance $(\Delta v_z)^2$. A plot of the time evolution of $\tilde{V}(t) = (\Delta v_z)^2 / V_0$, where $V_0 = \hbar\omega_0 / 2m$ is the variance of the ground state, for the squeezing parameter of $r = 0.85$ is shown in Fig. 2. In this measurement, t_1 was chosen so that the velocity width was minimized at $t = t_1$. We observed a variation of $\tilde{V}(t)$ over two orders of magnitude with a period of π/ω_0, implying that the elliptical uncertainty was rotating on the phase space. At $t_2 - t_1 = N\pi/\omega_0$, we observed significant reductions in $\tilde{V}(t)$ (Fig. 2, B and C).

We achieved a comprehensive understanding of the observed time evolution profile by fitting the following expression to the measured data (see the supplementary text) (*29*):

$$\tilde{V}(t) = \tilde{V}_1 \cos^2\left[\omega_0 (t_2 - t_1)\right] + \tilde{V}_2 \sin^2\left[\omega_0 (t_2 - t_1)\right] \quad (2)$$

where $\tilde{V}_1$ and $\tilde{V}_2$ characterize the uncertainty on the phase space. The increase in the variance due to photon scattering Γ_{qba} was negligible in the presented measurement duration. We found that our measurements were in good agreement with Eq. 2. From the fit, we determined the values of $\tilde{V}_1$ and $\tilde{V}_2$ to be 0.32 ± 0.01 and 104 ± 4, respectively. The value of $\tilde{V}_1$ determined with this fit corresponds to −4.9 dB of quantum squeezing. Our results overcome the well-known limit of −3 dB obtainable through a standard parametric modulation technique (*34*) and are comparable to the value achieved with quantum reservoir engineering in a membrane oscillator (*16*).

The choice of t_{TOF} requires careful consideration of the uncertainties of both the position and the velocity. For a nonsqueezed state, which is typical with cold atom experiments, the contribution of the position uncertainty before free expansion is smaller than that of the velocity uncertainty by $\omega_0 t_{TOF}$. Thus, $t_{TOF} \gg 1/\omega_0$ is sufficient to ensure that the measured distribution is mostly due to the velocity uncertainty. By contrast, the squeezed state explored in this study had a broader position uncertainty and a narrower velocity uncertainty. The requirement for dominantly observing the velocity uncertainty was therefore more stringent as $t_{TOF} \gg e^{4r}/\omega_0$. In the present study, the contribution of the velocity uncertainty was expected to be 87% even at the largest squeezing parameter.

The limit of the squeezing at larger values of *r* in our protocol is an intriguing issue. By repeating the measurements described above for various values of *r*, we revealed the dependence on *r*. The entire time evolutions of $\tilde{V}(t)$ for various values of *r* are provided in fig. S1. In Fig. 3, we show $\tilde{V}_1$ and $\tilde{V}_2$ extracted from the time evolutions as a function of *r*. In addition to the values obtained with the squeezing protocol, the variance before the squeezing protocol, obtained by performing TOF measurements for the initial state, is also shown at $r = 0$. We found that the observed variance was in good agreement with the following expression (see the supplementary text) (*24*, *29*):

$$\tilde{V}_1 = \tilde{V}_n + \tilde{V}_{ini} \exp(-4r) \quad (3)$$

$$\tilde{V}_2 = \tilde{V}_n + \tilde{V}_{ini} \exp(4r) \quad (4)$$

where $\tilde{V}_{ini}$ denotes the normalized velocity variance of the initial state. $\tilde{V}_n$ originates from various sources of uncertainties. In particular, we experimentally recognize that the vibration of the system due to a scroll pump and a turbomolecular pump significantly broadens the width with $\tilde{V}_n \simeq 0.25$. These pumps can potentially shake the optical setup for trapping and the resonator for stabilizing the laser phase noise. Therefore, the measurements presented in this work were performed with these pumps turned off. From the fit on $\tilde{V}_1$, we obtain $\tilde{V}_n = 0.21 \pm 0.01$. The agreement with a simple model for our squeezing protocol suggests that our protocol was working properly and the level of squeezing was ultimately limited to $\tilde{V}_n$.

To gain insight into the ultimate limit of squeezing in our protocol, we analyzed the possible sources of $\tilde{V}_n$ in our system and estimated their contributions (table S1). The details of our calculations are explained in the materials and methods (*31*). The important contributions were the position uncertainty before free expansion, timing jitter, photon recoil heating through the trapping laser, motions perpendicular to the *z* direction, and residual vibrations. We calculated the estimated values for the first three mechanisms and derived the upper bounds on the other effects from the experimentally measured values caused by complexities in calculating these effects. The sum of the estimated values gives $\tilde{V}_n < 0.24$ and is consistent with the value $\tilde{V}_n = 0.21 \pm 0.01$ obtained from the squeezing measurements. Reducing the residual vibration of the system and the timing jitter is expected to be technically feasible. The initial position uncertainty can be further reduced by taking a longer TOF. The effect of the motions perpendicular to the *z* direction can be decreased by optimizing the beam alignment and feedback cooling for them. Thus, we envision that improving the technical issues will allow us to significantly enhance the squeezing

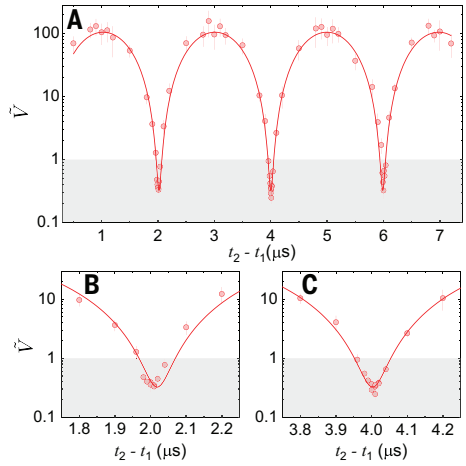

Fig. 2. Time evolution of the normalized velocity variance for $r = 0.85$. (**A**) Plot for the entire time range. When $t_2 - t_1$ is varied, we observed a variation of the velocity variance for more than two orders of magnitude, implying the rotation of the elliptical uncertainty on the phase space with a period of ~4 μs. The error bars indicate the error in determining the width with a fit to the measured velocity distribution. The shaded area indicates quantum squeezing. The observed minimum velocity variance obtained from a fit on the entire profile corresponds to the squeezing level of −4.9 ± 0.1 dB with respect to that of the ground state. (**B** and **C**) Expanded views of (A) around the minima of $\tilde{V}$.

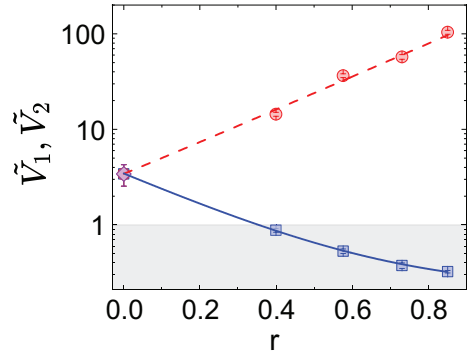

Fig. 3. Measured variance with respect to the squeezing parameter. For each r, we plotted $\tilde{V}_1$ (squares) and $\tilde{V}_2$ (circles) extracted by fitting Eq. 2 to the measured time evolution. The variance of the initial state before the squeezing protocol is shown by a diamond at $r = 0$. The error bars indicate the error in determining the parameters with a fit. The shaded area indicates quantum squeezing. For the fit on $\tilde{V}_1$ shown by the solid line, we found $\tilde{V}_n = 0.21 \pm 0.01$. For the fit on $\tilde{V}_2$ shown by the dashed line, we set $\tilde{V}_n$ to 0.21.

level. As discussed in a recent theoretical investigation for a similar setup (*25*), the fundamental mechanism that limited squeezing in our protocol was photon recoil heating at $t_1 < t < t_2$, resulting in the maximum squeezing of −13 dB (*31*).

$\tilde{V}_n$ can in principle include an effect of quantum mechanical origin. When the measurements were performed simultaneously for both the position and the momentum, as realized with short t_{TOF} in our scheme, the quantum mechanical uncertainty of the detector can also come into play (*35*, *36*). A recent study suggested that an optically levitated nanoparticle in the weak measurement regime, where the particle oscillatates nearly coherently and its position is continuously measured through scattering of the trapping laser, undergoes the simultaneous position and momentum measurements with enhanced uncertainties (*29*). In the present work, we anticipate that the additional uncertainty due to the simultaneous measurements was negligibly small because we monitored predominantly the velocity through free expansion measurements with a long TOF. However, a quantitative understanding of such an uncertainty in the present setup requires further theoretical considerations, which will be an interesting area for future study.

Accurate measurement of the displacement with an optical lattice

Our claim of quantum squeezing relies on a correctly calibrated position signal, because the level of squeezing was determined by taking the ratio of the measured velocity variance to V_0. All of the plots presented in the present work relied on the following calibration procedure. We first performed TOF measurements of Δv_z for various values of n_z prepared by varying the feedback gain. By fitting the measured relation between Δv_z and n_z with the Maxwell-Boltzmann distribution, we found Δv_z as expected for $n_z = 0$, which provides a calibration of the position signal (fig. S2) (*31*). This approach is based on the value of n_z obtained with the integration of power spectral density (PSD) under an assumption that the PSD without cooling thermalizes to room temperature (*37*, *38*). However, it has been argued that thermal fluctuations at room temperature can be a source of large errors (*39*). The flatness of the noise floor of the PSD is also an important prerequisite because the subtraction of the noise floor is required for an optimum estimation of the area of the PSD. This requirement is also important for the quantum mechanical approach based on Raman side-band asymmetry (*40*).

To quantitatively confirm that our calibration was correct, we introduced an independent approach for calibrating the position signal that uses the nature of an optical lattice and does not rely on the integration of the PSD. Because the nanoparticle is trapped in an optical lattice, the effective distance between the nanoparticle and the retroreflecting mirror L is proportional to the wavelength of the laser $2\pi c/(\Omega_0 + \Omega_1)$, with $\Omega_0 + \Omega_1$ being the laser frequency. This fact indicates that shifting the laser frequency to $\Omega_0 + \Omega_2$ should induce an oscillation with an amplitude proportional to the frequency difference $\Omega_2 - \Omega_1$ (Fig. 4A). The induced displacement of the optical potential is given by

$$\delta = L(\Omega_2 - \Omega_1) / (\Omega_0 + \Omega_2) \quad (5)$$

In our measurements, after the initial state preparation, we turned off feedback cooling and shifted the optical potential for a short time τ, during which we let the particle oscillate, and then we recovered the original potential for position measurements (Fig. 4B). When we varied τ, we observed a clear oscillation with an amplitude of 2δ (Fig. 4C). The measured amplitudes calibrated with the temperature measurements are in excellent agreement with Eq. 5 within 2% (Fig. 4D), indicating that both calibration procedures are reliable. Because of its simplicity, the proposed approach for calibrating the position signal can also be a useful alternative means for future sensing applications.

Concluding remarks

We have demonstrated quantum squeezing of the CoM motion of a levitated nanoparticle by manipulating the velocity uncertainty with rapid frequency variations, revealing the reduction of this uncertainty by directly observing the narrowing of the velocity distributions with TOF free-expansion measurements. The velocity variance was reduced to −4.9 dB that of the quantum ground state. The observed level of squeezing is comparable to the mechanical squeezing realized with quantum reservoir engineering in a micromechanical oscillator (*16*). Our study clearly shows that quantum squeezing of a levitated nanoparticle was realized without being masked by its multiple motional degrees of freedom and that the generated squeezed state was very sensitive to various ways of fluctuating the system. Our work demonstrates the validity of the free expansion of the wavefunction, which has been required in various theoretical proposals to elucidate the quantum mechanical nature of the motional state of levitated particles (*41*–*44*).

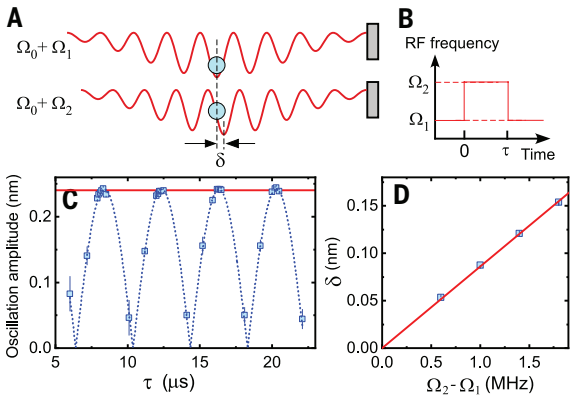

Fig. 4. Calibration of the position signal through shifting the laser frequency. (**A**) Schematic showing the mechanism of inducing the oscillation of the trapped nanoparticle by shifting the laser frequency. (**B**) Time sequence of the measurement. (**C**) Oscillation amplitude with respect to τ. The error bars indicate the SD of the oscillation amplitude. The dashed lines is a fit of Eq. 2 (*31*) to the measured amplitude, and the solid line is a calculated value with Eq. 5 and is not a fit. (**D**) Extracted amplitude with respect to the frequency difference. The error bars indicate the error in determining the amplitude with a fit to the oscillation signal. The solid line shows calculated values with Eq. 5 and is not a fit.

From a practical point of view, levitated particles are expected to be a promising system for realizing sensing devices beyond current technologies (*45*), and as demonstrated thus far with various quantum systems, quantum squeezing is a powerful technique to enhance their sensitivity (*4*, *5*, *7*). Our scheme is expected to be useful for future applications in acceleration sensing. In fact, our measurements were substantially influenced by the vibration of the vacuum pumps. Extending the limit of squeezing may allow us to reveal an otherwise undetectable effect, including the quantum mechanical uncertainty through the simultaneous position and momentum measurements (*35*, *36*). Furthermore, our system provides exciting possibilities for exploring thermodynamics under continuous quantum measurements and feedback (*46*, *47*).

REFERENCES AND NOTES

1. M. Takamoto, F.-L. Hong, R. Higashi, H. Katori, *Nature* **435**, 321–324 (2005).
2. C. L. Degen, F. Reinhard, P. Cappellaro, *Rev. Mod. Phys.* **89**, 035002 (2017).
3. J. Clarke, F. K. Wilhelm, *Nature* **453**, 1031–1042 (2008).
4. J. Ma, X. Wang, C.-P. Sun, F. Nori, *Phys. Rep.* **509**, 89–165 (2011).
5. G. Tóth, I. Apellaniz, *J. Phys. A Math. Theor.* **47**, 424006 (2014).
6. S. L. Braunstein, P. Van Loock, *Rev. Mod. Phys.* **77**, 513–577 (2005).
7. S. Barzanjeh *et al.*, *Nat. Phys.* **18**, 15–24 (2022).
8. J. Millen, B. A. Stickler, *Contemp. Phys.* **61**, 155–168 (2020).
9. J. Millen, T. S. Monteiro, R. Pettit, A. N. Vamivakas, *Rep. Prog. Phys.* **83**, 026401 (2020).
10. C. Gonzalez-Ballestero, M. Aspelmeyer, L. Novotny, R. Quidant, O. Romero-Isart, *Science* **374**, eabg3027 (2021).
11. U. Delić *et al.*, *Science* **367**, 892–895 (2020).
12. L. Magrini *et al.*, *Nature* **595**, 373–377 (2021).
13. F. Tebbenjohanns, M. L. Mattana, M. Rossi, M. Frimmer, L. Novotny, *Nature* **595**, 378–382 (2021).
14. M. Kamba, R. Shimizu, K. Aikawa, *Opt. Express* **30**, 26716–26727 (2022).
15. A. Ranfagni, K. Børkje, F. Marino, F. Marin, *Phys. Rev. Res.* **4**, 033051 (2022).
16. C. U. Lei *et al.*, *Phys. Rev. Lett.* **117**, 100801 (2016).
17. M. Kamba, R. Shimizu, K. Aikawa, *Nat. Commun.* **14**, 7943 (2023).
18. M. Kamba, K. Aikawa, *Phys. Rev. Lett.* **131**, 183602 (2023).
19. D. Rugar, P. Grütter, *Phys. Rev. Lett.* **67**, 699–702 (1991).
20. M. Zalalutdinov *et al.*, *Appl. Phys. Lett.* **78**, 3142–3144 (2001).
21. J. Suh, M. D. LaHaye, P. M. Echternach, K. C. Schwab, M. L. Roukes, *Nano Lett.* **10**, 3990–3994 (2010).
22. A. A. Clerk, F. Marquardt, K. Jacobs, *New J. Phys.* **10**, 095010 (2008).
23. X.-Y. Lü, J.-Q. Liao, L. Tian, F. Nori, *Phys. Rev. A* **91**, 013834 (2015).
24. M. Xin, W. S. Leong, Z. Chen, Y. Wang, S.-Y. Lan, *Phys. Rev. Lett.* **127**, 183602 (2021).
25. Q. Wu *et al.*, *Quantum Sci. Technol.* **9**, 045038 (2024).
26. M. G. Genoni, J. Zhang, J. Millen, P. F. Barker, A. Serafini, *New J. Phys.* **17**, 073019 (2015).
27. M. Duchaň, *et al.*, Experimental amplification and squeezing of a motional state of an optically levitated nanoparticle. arXiv:2403.04302 [quant-ph] (2024).
28. M. Rashid *et al.*, *Phys. Rev. Lett.* **117**, 273601 (2016).
29. M. Rossi *et al.*, *Phys. Rev. Lett.* **135**, 083601 (2025).
30. R. Muffato, T. Georgescu, M. Carlesso, M. Paternostro, H. Ulbricht, Coherent expansion of the motional state of a massive nanoparticle beyond its linear dimensions. arXiv:2408.09596 [quant-ph] (2024).
31. See the supplementary materials.
32. R. Reimann *et al.*, *Phys. Rev. Lett.* **121**, 033602 (2018).
33. J. Ahn *et al.*, *Phys. Rev. Lett.* **121**, 033603 (2018).
34. G. Milburn, D. Walls, *Opt. Commun.* **39**, 401–404 (1981).
35. E. Arthurs, J. L. Kelly Jr., *Bell Syst. Tech. J.* **44**, 725–729 (1965).
36. Y. Yamamoto, H. A. Haus, *Rev. Mod. Phys.* **58**, 1001–1020 (1986).
37. J. Gieseler, B. Deutsch, R. Quidant, L. Novotny, *Phys. Rev. Lett.* **109**, 103603 (2012).
38. J. Vovrosh *et al.*, *J. Opt. Soc. Am. B* **34**, 1421–1428 (2017).
39. E. Hebestreit *et al.*, *Rev. Sci. Instrum.* **89**, 033111 (2018).
40. F. Tebbenjohanns, M. Frimmer, V. Jain, D. Windey, L. Novotny, *Phys. Rev. Lett.* **124**, 013603 (2020).
41. O. Romero-Isart, *Phys. Rev. A* **84**, 052121 (2011).
42. A. Bassi, K. Lochan, S. Satin, T. P. Singh, H. Ulbricht, *Rev. Mod. Phys.* **85**, 471–527 (2013).
43. O. Romero-Isart *et al.*, *Phys. Rev. A* **83**, 013803 (2011).
44. B. A. Stickler *et al.*, *New J. Phys.* **20**, 122001 (2018).
45. F. Monteiro *et al.*, *Phys. Rev. A* **101**, 053835 (2020).
46. A. C. Doherty, A. Szorkovszky, G. I. Harris, W. P. Bowen, *Philos. Trans. A Math. Phys. Eng. Sci.* **370**, 5338–5353 (2012).
47. T. Yada, N. Yoshioka, T. Sagawa, *Phys. Rev. Lett.* **128**, 170601 (2022).

ACKNOWLEDGMENTS

We thank M. Aspelmeyer, M. Ueda, B. Stickler, M. Kozuma, M. Rossi, K. Funo, T. Sagawa, S. Sugiura, and T. Mukaiyama for fruitful discussions and S. Otabe for experimental assistance. **Funding:** This work was supported by the Murata Science Foundation, the Mitsubishi Foundation, the Challenging Research Award, the Planting Seeds for Research program, the Yoshinori Ohsumi Fund for Fundamental Research, a STAR Grant funded by the Tokyo Tech Fund, the Research Foundation for Opto-Science and Technology, the Japan Society for the Promotion of Science (JSPS KAKENHI grants JP16K13857, JP16H06016, JP19H01822, and JP22K18688), and the Japan Science and Technology Agency (JST PRESTO grant JPMJPR1661, JST ERATO grant JPMJER2302, JST CREST grant JPMJCR23I1, and JST COI-NEXT grant JPMJPF2015). M.K. is supported by JST (Establishment of University Fellowships Toward the Creation of Science and Technology Innovation grant JPMJFS2112) and JSPS (grant JP24KJ1058). N.H. is supported by JST (SPRING grant JPMJSP2108). **Author contributions:** K.A. and M.K. designed and built the experiments. N.H., M.K., and K.A. performed measurements and analyzed the data. N.H. performed the derivation of theoretical expressions. All authors discussed the results and contributed to writing the manuscript. **Competing interests:** The authors declare no competing interests. **Data and materials availability:** All data are available in the main manuscript or in the supplementary materials.

SUPPLEMENTARY MATERIALS

science.org/doi/10.1126/science.ady4652
Materials and Methods; Supplementary Text; Figs. S1 and S2; Table S1; References (*48*–*51*)
Submitted 23 April 2025; accepted 15 July 2025
10.1126/science.ady4652

RANGELANDS

Climate rather than overgrazing explains most rangeland primary productivity change in Mongolia

Avralt-Od Purevjav[1], Tumenkhusel Avirmed[2], Steven W. Wilcox[3], Christopher B. Barrett[4]*

Rangelands are Earth's dominant land type, supporting the livelihoods of more than 2 billion people. Concerns about rangeland degradation typically focus on overgrazing. But climate change may be a greater culprit. Using spatially disaggregated, nationwide data from Mongolia, from 1984 to 2024, we exploited seasonal variation in grazing locations to quasi-experimentally estimate the causal effects of livestock herd size, weather, and climate change on rangeland primary productivity. At interannual frequency, herd size modestly but significantly negatively affects primary productivity, with notable variation across ecological zones. The effects of weather fluctuations are, however, an order of magnitude larger. At the decadal scale, over which herders can adapt to climate change, herd size effects disappear, and temperature effects dominate. In Mongolia, climate change seems to drive most long-term change in rangeland primary productivity.

Rangeland conservation is important because rangelands are the dominant land type on Earth, supporting the livelihoods of more than 2 billion people (*1*, *2*). Effective conservation efforts require understanding the factors that cause variation in rangeland health (*3*). Extensive literature has studied how variation in rangeland conditions may result from herd size fluctuations on the basis of equilibrium carrying capacity or abiotic phenomena per nonequilibrium rangeland system theories, among other factors (*4*–*7*). If herd sizes and management drive degradation, policies such as livestock taxes or use restrictions can offer effective conservation tools. If abiotic phenomena are more to blame, the scope for effective local actions shrinks.

Identifying the causal contributions among multiple potential drivers is therefore crucial to effective rangeland management policy. Yet despite a broad observational literature describing the association of rangeland conditions with various explanatory variables, as well as small-scale experimental studies, scant strong causal evidence exists at scale about the causes of variation in rangeland conditions (*8*–*14*). The pervasive endogeneity of key explanatory variables in observational data—especially herd size, which is partly chosen by herders in response to rangeland and weather conditions—poses a formidable inferential challenge.

The inability to run large-scale experiments that control for herd stocking rates over an extended period prompts analysts' use of modeling or observational data. Modeling requires that one assume the causal relationship of interest and thus typically fails to resolve causal inference challenges. In observational data, correlations between livestock holdings and rangeland conditions can occur even when no underlying causal relationship exists. This may occur if, for example, (i) people managing large herds excel at locating quality rangeland (nonrandom "selection" bias), (ii) rangeland productivity contributes to herd growth (reverse causality), and/or (iii) extreme weather both reduces herd size and harms rangelands (a spurious correlation owing to unobserved factors). These and other statistical confounders cause the estimated correlation between herd size and rangeland conditions to deviate from the unobserved, true causal effect, potentially leading to poor policy guidance (*15*, *16*). Quasi-experimental methods can eliminate these statistical biases, enabling recovery of true causal effects with observational data.

These issues loom large in Mongolia, where rangelands comprise roughly 70% of the country's territory and underpin rural livelihoods. Herd sizes increased sharply after the country's 1990–1992 market economy transition (Fig. 1) (*17*–*19*), when 25 million livestock were privatized while grasslands remained open access across the country. By 2018, 57% of Mongolia's rangelands were considered degraded to some extent, with 10.3% fully degraded (*20*). Rangeland degradation threatens the country's ecosystems, the livelihoods of herders, and others who depend on the livestock industry. But alongside herd size growth, temperatures and wind speeds have increased, and precipitation has declined (fig. S8) (*21*–*23*), raising the prospect of climate change impacts.

Prior studies on Mongolia—which were limited by restricted spatial and time scales and the endogeneity of herd size—largely blame overgrazing from large herd sizes as a likely primary driver of rangeland degradation (*10*, *20*, *24*–*27*). Other work suggests synergistic relationships between grazing and weather (*4*, *28*–*37*), and small-scale experiments have emphasized the effect of exposure to grazing (*25*, *38*–*40*). Still other work conducted at scale has found evidence for positive effects from herd size on primary productivity and increasing trends in average greenness (*13*).

Mongolia's policy-makers have emphasized increasing herd sizes in addressing rangeland health. In 2021, Mongolia instituted a nationwide livestock head tax, aiming to induce lower stocking rates and address perceived adverse rangeland impacts (*41*). However, if increased stocking rates have not caused much decline in rangeland conditions, then livestock taxes and related policies may prove counterproductive. To date, evidence for negative effects of grazing rely mainly on correlational analyses and have not addressed the endogenous nature of herd size nor important potential confounding factors such as climate change effects.

In this work, we addressed these fundamental research challenges using nationwide data from Mongolia spatially disaggregated to soums (roughly equivalent to a US county, which vary in size from 14 to 27,930 km^2) (fig. S1) from 1984 to 2024. Our main contribution was to use quasi-experimental methods and unusually rich data to isolate the independent causal effects of herd size, short-run weather variation, and longer-term climate change on rangeland primary productivity—an important component of rangeland health (*3*). Our data and methods permit us to isolate exogenous components of herd size to enable causal inference as though the data were experimental over larger spatial and temporal domains than those in prior work. This approach directly addresses the question of whether herd size, short-term weather, or climate change has a larger effect on rangeland primary productivity.

Mongolian herders raise livestock—mainly camels, cattle, goats, horses, and sheep—with species composition varying by ecological zone and herders' income and husbandry skills (*42*). As the seasons change, herders move among distinct grazing ranges within their soum. In the winter and spring, they move to areas with consistent water sources and topography that provides protection from wind and snow (such as leeward sides of hills and ridgelines, and drainages), especially during extreme winter weather events known as dzud, which cause mass livestock mortality (Fig. 1 and figs. S6, S9, and S11) (*43*, *44*). In the summer and fall, livestock graze more open areas. The seasonal geography of grazing means that combinations of movement from leeward to windward sides of geographic features, from lower to higher elevation, or both creates spatial separation of seasonal grazing ranges (fig. S3). This movement provides livestock with year-round access to forage and water, protects herds from winter weather, and allows grasslands to recover (*42*, *45*–*47*).

[1]World Bank Group, Washington, DC, USA. [2]Center on Food Security of the Environment, Stanford University, Palo Alto, CA, USA. [3]Department of Applied Economics, Utah State University (USU), USU and Faculty Affiliate of USU Ecology Center, Logan, UT, USA. [4]Charles H. Dyson School of Applied Economics and Management, Jeb E. Brooks School of Public Policy and Cornell Atkinson Center for Sustainability, Cornell University, Ithaca, NY, USA.
*Corresponding author. Email: cbb2@cornell.edu

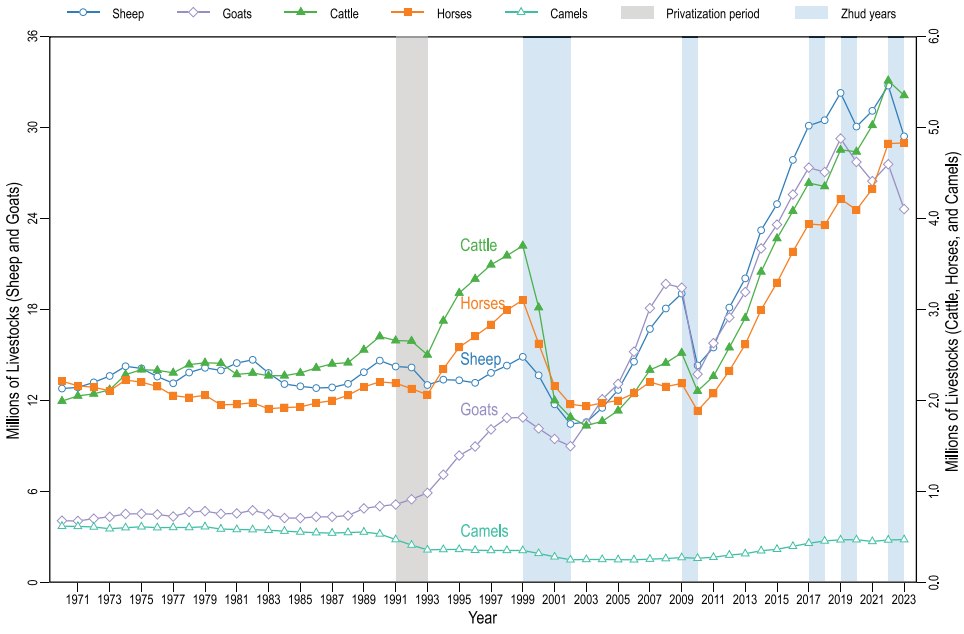

Fig. 1. Livestock population dynamics in Mongolia (1970–2024). Livestock population dynamics, 1970 to 2024, based on Mongolia's annual December livestock census (*55*, *76*). The left *y* axis indicates sheep and goats, and the right *y* axis indicates cattle, horses, and camels. The gray vertical line denotes the beginning of privatization after the country's democratic revolution. The light blue vertical lines indicate recorded instances of severe winter weather conditions (dzud), as documented by the government. Dzud events are clearly associated with significant reductions in herd size.

We exploited Mongolian herders' seasonal movement to disentangle the effects of herd size, short-run weather, and climate change on reflectance-based measures of primary productivity [for example, the normalized difference vegetation index (NDVI) (*48*–*51*)], which we validated with ground-based biomass data in analogous fashion to prior work (fig. S8 and table S2) (*52*, *53*). Specifically, we used a two-stage estimator that combines small area estimation (*54*) and instrumental variables (IV) methods (*15*, *16*). In the first stage, we used soum-level herd census data (*55*) and dzud events occurring on winter-spring grazing ranges (WGRs) to predict exogenous variation in June herd size (Fig. 2A) (*56*), which we then extrapolated over 1984–2024 using small area estimation. In the second stage (Fig. 2B), we used predicted June herd size from the first stage to generate causal estimates of the independent effects of herd size and weather or climate on summer rangeland primary productivity in soum-level summer-fall grazing ranges (SGRs). Using fitted values from the first stage eliminates variation in June herd size that could generate spurious correlation arising from spring and summer SGR weather, rangeland conditions, or unobserved factors that affect both SGR primary productivity and summer herd sizes. Both stages include statistical control variables for SGR-based seasonal precipitation, temperature (*57*, *58*), and SGR primary productivity from the previous year, as well as period and soum fixed effects—indicator variables for each year and for each soum, which control for unobserved heterogeneity. Given these controls, WGR winter weather and December herd size should have no effect on SGR primary productivity the following summer other than through their impact on June herd size. The geography of seasonal grazing and seasonality of soil moisture and rangeland plant growth phases justify this assumption. In addition to the physical separation between WGRs and SGRs, winter precipitation contributes little to soil moisture and plant growth compared with those from summer rains, which bring most of Mongolia's annual moisture (*59*–*61*). If a large portion of the soil moisture on which SGR plant growth relies came during winter and flowed from WGR to SGR through either surface or groundwater, our assumption would be questionable. But spatial separation, drainage, and precipitation seasonality allayed this concern.

To distinguish the effects of climate from short-run weather variation, we constructed multiyear averages of each variable and then differenced them over extended (10- or 20-year) periods (*62*). These differences were used in place of the annual levels regressand and regressors in the two-stage quasi-experimental estimation strategy. If herders, rangeland managers, government, or others adjust behaviors over multiyear periods in response to shifting weather patterns, then impact estimates derived from year-on-year responses to weather realizations might yield biased estimates of the impacts of climate change (*62*). For example, short-run estimates of annual weather fluctuations' impact on rangelands might be biased upward relative to the true impacts of (multiyear) climate change if sustainable adaptive mechanisms exist and mitigate the short-run effects of a sequence of unusually hot years. Conversely, regressions at annual frequency may face attenuation bias if unsustainable mitigation measures—such as groundwater extraction or distribution of supplemental feed during a drought—dampen impacts in the short run but are unsustainable.

To address heterogeneous effects, we also recovered ecological zone–specific causal estimates of herd size, short-run weather, and climate by interacting covariates of interest with indicator variables denoting which of the five primary ecological zones in Mongolia are dominant in a given soum (fig. S4) (*63*, *64*). Heterogeneous effects by livestock species are possible but not statistically identifiable with our methods because of the endogenous nature of herd composition; thus, we focused on total herd size in sheep equivalent units.

In quasi-experimental estimations, standard errors were clustered in the first stage and block-bootstrapped in the second stage to account for predicted herd size from the first stage (*65*–*69*). In comparison non–quasi-experimental estimations, standard errors were clustered at the soum level. We also addressed concerns over nonstationarity and serial correlation (*70*–*72*). Further details on all our methods, data, data acquisition, and summary statistics (figs. S1 to S11 and tables S1 to S14) are provided in the supplementary materials and replication files (*73*–*76*).

Results

Overall, larger herd sizes have a modest negative effect on rangeland primary productivity over short (interannual) time horizons (Fig. 3). Our quasi-experimental short-run elasticity estimates (Fig. 3, Short-run IV) indicate that on average, a doubling of herd size reduces reflectance-based greenness (our primary productivity indicator) by 4% ($P < 0.01$). These effects differ across the five main ecological zones in Mongolia. Herd size's largest impacts are in the mountain taiga (−0.112), forest steppe (−0.106), and steppe (−0.049) zones; point estimates for semidesert and desert zones are insignificant and near zero. Larger herds' short-run effects on primary productivity are concentrated in cooler, more productive, and preferred rangelands.

However, over longer, 10-year periods, allowing for potential adaptation to climate change (Fig. 3, Long-run IV) (*62*), herd size has no significant impact, either overall or in any ecological zone (Fig. 3). The sharp contrast with the short-run estimates based only on interannual weather variation carries powerful policy implications. Measures to reduce herd sizes can generate short-term rangeland productivity gains. But interventions meant to reduce herd sizes have no measurable impact over longer

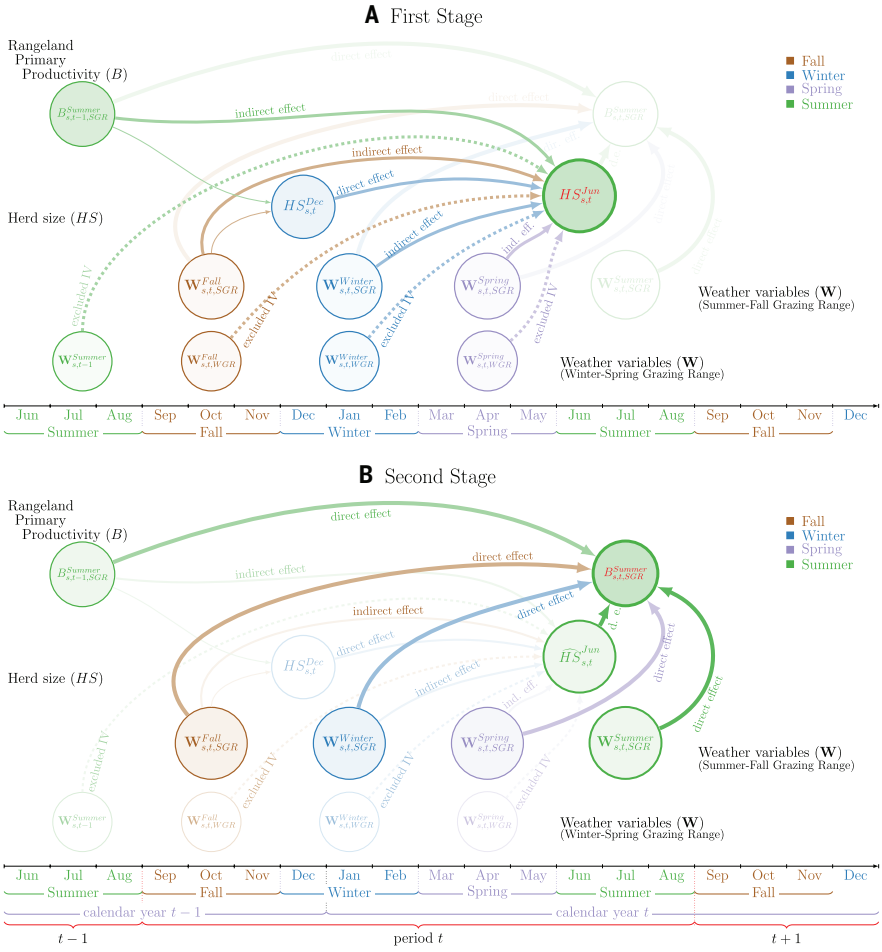

Fig. 2. Visualization of causal identification strategy. (**A**) The first stage. (**B**) The second stage. *HS*, herd size; *B*, rangeland primary productivity (proxied by the NDVI); W, weather variables, including growing degree days (GDD), freezing degree days (FDD), wind speed, total precipitation, snow coverage, and snow density; WGR, winter-spring grazing ranges; SGR, summer-fall grazing range; *s*, soum; and *t*, time period. Dashed lines indicate instrumental variables included in the first stage but excluded from the second stage.

periods, presumably because herders and land managers naturally adapt, rendering policy measures unnecessary, even costly.

Conventional, correlational approaches to estimating herd size effects can substantially misestimate the sign and magnitude of herd size effects (Fig. 3). This is evident in comparing our quasi-experimental estimates with conventional ordinary least squares (OLS) estimates akin to correlational results found in the literature. Including soum and time fixed effects (location-specific and year indicator variables) to control for time-invariant unobserved factors within a soum (such as altitude, distance to nearest city, or size) and unobserved period-specific factors common to all soums (such as livestock product prices) reduces the bias in OLS estimates. The OLS estimates without fixed effects (Fig. 3, OLS without FEs) are inconsistent in sign and greater than quasi-experimental estimates, revealing the positive bias to which correlational estimates are prone because of some combination of omitted variable, reverse causality, and selection bias. Incorporating fixed effects (Fig. 3, OLS with FEs) to partly control for such confounders generates estimates that are reasonably close to short-run IV estimates.

Tests for heterogeneous impacts by ecosystem type demonstrate even starker contrasts between quasi-experimental and conventional, correlational estimates. Conventional OLS point estimates of herd size effects on rangeland primary productivity are either inconsistent in sign and near zero (mountain taiga, forest steppe, or steppe) or positive and sometimes significant (semidesert and desert), depending on the sample size and geographic coverage (survey versus census). Although including fixed effects again improves conventional estimates, these still diverge substantially from quasi-experimental short-run IV estimates, particularly in more productive mountain taiga, forest steppe, and steppe zones. The generalizable methodological implication is that in settings where no quasi-experimental method equivalent to ours is feasible, control for fixed effects and weather covariates can improve estimates of herd size effects on rangeland primary productivity.

Turning to the impacts of weather and climate, our short-run IV estimates show that warmer weather statistically significantly adversely affects primary productivity; the marginal semi-elasticity of an additional growing degree day (GDD) > 20°C on rangeland NDVI is −0.012 ($P < 0.01$). An additional 3.5 GDD > 20°C per summer produces a comparable reduction in rangeland primary productivity to doubling herd size. Conventional (OLS) estimates are each negative, mostly smaller in magnitude than the quasi-experimental estimates, and inconsistently significant, although fixed effects estimates with census measures of herd size are comparable with short-run IV estimates. The largest heat effects occur in lower elevation or lower-productivity ecological zones (desert, semidesert, steppe, and forest steppe), not in the mountain taiga zone, which remains somewhat insulated from increased temperature exposure above 20°C. Conventional OLS point estimates are inconsistent in sign and significance across ecological zones. Fixed effects OLS estimates do not uniformly approach the preferred, short-run IV estimates, although this approach is more consistent with short-run IV estimates when census-based herd size measures are used.

Longer-run IV estimates of the impact of climate change point to even larger negative effects from increased exposure to higher temperatures. Comparing the estimated effects of climate and herd sizes, it becomes clear that climate change, not rising herd sizes, accounts for most of the variation in rangeland primary productivity in Mongolia over the past 40 years. The effects are especially large for desert, semidesert, steppe, and forest steppe ecological zones, with somewhat muted impacts on cooler, more productive ecological zones.

Further details on the estimation presented in Figs. 3 and 4, including first-stage results and robustness checks, are provided in the supplementary materials (figs. S12 and S13 and tables S15 to S47). Our qualitative results are robust to various alternative tests, including estimation with herd size in levels rather than in log, controlling for a lag of SGR NDVI, potential spillover effects from herder movement, use of 20-year-long rather than 10-year-long differences, accounting for (endogenous) herd composition, and interaction effects between herd size and weather or climate.

Because weather variables typically covary with one another significantly, it is difficult to interpret individual coefficient estimates independently of the others. We therefore calculated Shapley-Owen measures (*77*, *78*) of the joint impacts of different groups of variables. The Shapley-Owen decomposition captures estimated marginal effects, correlation among explanatory variables, and the magnitude of the within-sample variation in all variables, reflecting the percentage share of explained rangeland primary productivity variation attributable to variation in grouped explanatory variables. Even for year-on-year changes, weather variability is 10 times more impactful than herd size

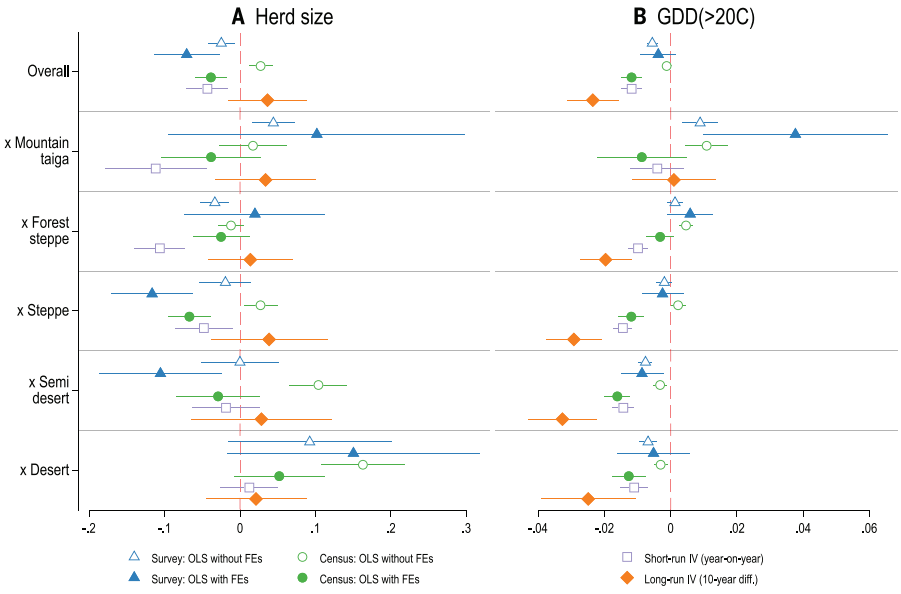

Fig. 3. Comparison of herd size and GDD (> 20°C) effect size estimates. (**A**) Estimated coefficients for herd size (in log). (**B**) Estimated coefficients for GDD > 20°C (in level). The top row shows results across rangelands overall, and the bottom five rows show results for the five main ecological zones. Within each row, six coefficient estimates are shown, with error bars indicating the 95% confidence intervals and a vertical dashed line indicating zero (the null hypothesis of no effect). Coefficient estimates in each row come from six different models: (i) Survey OLS without FEs: standard ordinary least squares (OLS), without soum and year fixed effects (FEs) estimated with 2016–2024 June herd size survey data only (sourced from table S15, column 2, for rangelands overall and table S25, column 2 for zone-specific results), which most directly replicate prior studies' methods; (ii) Survey OLS with FEs (where FEs are indicator variables for each soum and year that control for time-invariant unobserved features of soums and for unobserved year-specific factors common to all soums, respectively) estimated with 2016–2024 June herd size survey data only (sourced from table S15, column 6, for rangelands overall and table S25, column 6, for zone-specific results); (iii) Census: OLS without FEs estimated with December livestock stock census data 1984–2023 (sourced from table S16, column 2, for rangelands overall and table S26, column 2, for zone-specific results); (iv) Census: OLS with FEs estimated with December livestock census data 1984–2023 (sourced from table S16, column 6, for rangelands overall and table S26, column 6, for zone-specific results); (v) Short-run IV (year-on-year): quasi-experimental results estimated using interannual weather variation in our two-stage approach (sourced from table S19, column 6, for rangelands overall and table S29, column 6, for zone-specific results) (*15*, *16*, *54*); and (vi) Long-run IV (10-year diff.): quasi-experimental results estimated by using 10-year-long differences in our two-stage approach (sourced from table S37, column 6, for rangelands overall and table S41, column 6, for zone-specific results) (*15*, *16*, *54*, *62*). Because NDVI is in log, herd size coefficients have an elasticity interpretation, whereas weather coefficients (including GDD > 20°C) have a semi-elasticity interpretation.

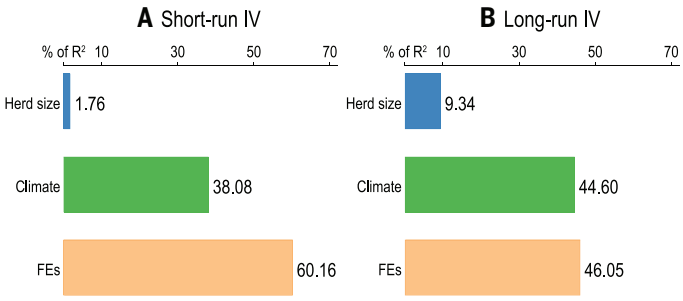

Fig. 4. Shapley-Owen decomposition. (**A** and **B**) The Shapley-Owen decomposition for herd size (in log), climate, and fixed effects in (A) Short-run IV and (B) Long-run IV models (10-year difference). Respective values come from tables S19 (column 6) and S37 (column 6), respectively. Each bar indicates the contribution of a factor to the total variation (100%) in coefficient of determination (R^2), with the text labels indicating the specific contribution value. The colors correspond to the difference factors: Fixed effects, light orange; climate, green; and herd size, blue.

on primary productivity (Fig. 4A). Changes in herd sizes explain <2% of the observed variation in primary productivity, whereas interannual changes in weather explain 38%. At longer (10-year) horizons, herd size variation explains <10% and climate change explains 45%. Time-invariant characteristics of soums and period-specific factors (fixed effects) account for much of the observed variation at both shorter- and longer-run horizons. Across Mongolia as a whole, both herd size and climate matter to rangeland primary productivity—but not at all equally.

Discussion

Our findings are intuitive. First, higher marginal herd size effects in upper elevation zones reflects that these cooler areas are herders' primary refuge owing to greater forage production in summer months. Herders will move livestock from less desirable rangelands as forage grows scarce but will remain in desirable mountain taiga grazing ranges as long as possible in hot years. Second, exposure to higher temperature has thus far had limited adverse impacts on primary productivity in the higher-elevation mountain taiga zone. Third, climate change's negative productivity impacts are greatest in the desert and semidesert zones, which experience no significant herd size impacts because these areas are infrequently used in summer. Fourth, if climate change causes more frequent or severe dzuds (*44*), then direct adverse climate effects on primary productivity may be partly attenuated in the short run by climate change's indirect effects through induced herd size reductions from dzud losses, but at great cost to livelihoods.

Our findings carry several implications for the scientific community and policy-makers. First, our findings suggest that policy levers focused on herd size alone—such as Mongolia's livestock taxes—may have a limited effect on desired rangeland outcomes, especially at multiyear time scales.

Second, efforts to mitigate rangeland productivity losses might be best targeted to where expected impact is greatest. For example, efforts to improve management in lower-elevation steppe and semidesert zones may reduce the need for higher use of mountain taiga and forest-steppe zones. Or livestock taxes might be levied solely, or at a higher rate, in the mountain taiga grazing ranges where short-run impacts of stocking rates are greatest.

Third, the growing availability of remotely sensed data over large spatial and temporal scales (*79*, *80*) opens new opportunities to apply quasi-experimental methods to study drivers of change in rangelands. However, although remotely sensed vegetation indices are well-established for measuring primary productivity, they have limitations. Future quasi-experimental work should study the independent effects of different hypothesized drivers on additional attributes of rangeland health when possible (*1*, *3*).

The key finding is that climate change is the main driver of longer-term rangeland primary productivity in Mongolia. Mongolian rangelands are affected more by the collective greenhouse gas–emitting behaviors around

the globe than by local herders. Policy-makers might therefore usefully focus attention on global mitigation and on international compensation for climate damages and less on taxing herders who already seem to adapt to climate change and appear responsible for little if any of the change in Mongolia's rangeland primary productivity over the past 40 years.

REFERENCES AND NOTES

1. D. D. Briske, in *Rangeland Systems: Processes, Management and Challenges*, D. D. Briske, Ed. (Springer, 2017), pp. 1–24.
2. International Livestock Research Institute (ILRI), International Union for Conservation of Nature (IUCN), Food and Agriculture Organization of the United Nations (FAO), World Wide Fund for Nature (WWF), United Nations Environment Programme (UNEP), International Land Coalition (ILC), *Rangelands Atlas. Nairobi Kenya* (ILRI, 2021).
3. M. Pellant *et al.*, *Interpreting Indicators of Rangeland Health, Version 5: Bureau of Land Management Technical Reference 1734-6* (BLM National Operations Center's Information and Publishing Services, 2020).
4. M. E. Fernandez-Gimenez, B. Allen-Diaz, *J. Appl. Ecol.* **36**, 871–885 (1999).
5. S. Vetter, *J. Arid Environ.* **62**, 321–341 (2005).
6. L. Gillson, M. T. Hoffman, *Science* **315**, 53–54 (2007).
7. D. D. Briske, Ed., *Rangeland Systems: Processes, Management and Challenges* (Springer, 2017).
8. M. Oesterheld, C. DiBella, H. Kerdiles, *Ecol. Appl.* **8**, 207–212 (1998).
9. P. Hiernaux, C. L. Bielders, C. Valentin, A. Bationo, S. Fernandez-Rivera, *J. Arid Environ.* **41**, 231–245 (1999).
10. T. Hilker, E. Natsagdorj, R. H. Waring, A. Lyapustin, Y. Wang, *Glob. Chang. Biol.* **20**, 418–428 (2014).
11. J. J. Gaitán *et al.*, *Land Degrad. Dev.* **29**, 210–218 (2018).
12. C. Li *et al.*, *Nat. Sustain.* **6**, 1363–1372 (2023).
13. L. Miao, Z. Sun, Y. Ren, F. Schierhorn, D. Müller, *Land Degrad. Dev.* **32**, 792–802 (2021).
14. F. T. Maestre *et al.*, *Science* **378**, 915–920 (2022).
15. J. D. Angrist, J. Pischke, *Mostly Harmless Econometrics: An Empiricist's Companion* (Princeton Univ. Press, 2009), pp. 113–220.
16. S. Cunningham, *Causal Inference: The Mixtape* (Yale Univ. Press, 2021), pp. 315–384.
17. Agency for Land Administration and Management, "2013 National Overview of Mongolia's Land Resources" (Geodesy and Cartography of Mongolia, 2013).
18. Agency for Land Administration and Management, "2019 National Overview of Mongolia's Land Resources" (Geodesy and Cartography of Mongolia, 2019).
19. Agency for Land Administration and Management, "2021 National Overview of Mongolia's Land Resources" (Geodesy and Cartography of Mongolia, 2021).
20. B. Densambuu, S. Sainnemekh, B. Bestelmeyer, U. Budbaatar, "National Report on the Rangeland Health of Mongolia: Second Assessment," Green Gold-Animal Health Project, SDC (2018).
21. N. B. Venable, S. R. Fassnacht, A. D. Hendricks, in *Proceedings of Building Resilience of Mongolian Rangelands: A Trans-disciplinary Research Conference on Spatial Changes in Climate across Mongolia* (2015), pp. 73–77.
22. J. Angerer, G. Han, I. Fujisaki, K. Havstad, *Rangelands* **30**, 46–51 (2008).
23. N. Davi *et al.*, *J. Geophys. Res.* **115**, 2010JD013907 (2010).
24. S. Sainnemekh, I. C. Barrio, B. Densambuu, B. Bestelmeyer, A. L. Aradottir, *J. Arid Environ.* **196**, 104654 (2022).
25. Y. Chen, G. Lee, P. Lee, T. Oikawa, *J. Hydrol.* **333**, 155–164 (2007).
26. A. Renchin, Tungalag, D. A. Miller, J. L. Sloan II, in *Proceedings of American Society for Photogrammetry and Remote Sensing Annual Conference on Land Use Change Analysis in Uvurkhnagai Province* (2009), pp. 679–686.
27. M. Hirobe *et al.*, *J. Soils Sediments* **13**, 1123–1132 (2013).
28. J. Addison, M. Friedel, C. Brown, J. Davies, S. Waldron, *Rangeland J.* **34**, 125–137 (2012).
29. D. Sheehy, D. Damiran, *Assessment of Mongolian Rangeland Condition and Trend (1997–2009)* (World Bank, Netherlands-Mongolia Trust Fund for Environmental Reform, 2012).
30. M. Nyamtseren *et al.*, *Desertification Atlas of Mongolia* (Institute of Geoecology, Mongolian Academy of Sciences and Environmental Information Centre, Ministry of Green Development, 2013).
31. Y. Y. Liu, J. P. Evans, M. F. McCabe, R. A. M. de Jeu, A. I. J. M. Dijk, *PLOS ONE* **8**, 1–6 (2013).
32. S. Bazha *et al.*, *Russ. J. Biol. Invasions* **6**, 223–237 (2015).
33. J. Khishigbayar *et al.*, *J. Arid Environ.* **115**, 100–112 (2015).
34. A. Narantsetseg, S. Kang, B.-E. Lkhamsuren, K. Jang, D. W. Ko, *Ecol. Inform.* **29**, 221–229 (2015).
35. S. R. Dangal *et al.*, *Ecosphere* **7**, e01274 (2016).
36. E. J. Lee *et al.*, *Forest Sci. Technol.* **15**, 210–220 (2019).
37. B. Lang *et al.*, *Ecol. Evol.* **10**, 678–691 (2019).
38. K. Wesche, K. Ronnenberg, V. Retzer, G. Miehe, *Acta Oecol.* **36**, 234–241 (2010).
39. T. Bat-Oyun, M. Shinoda, Y. Cheng, Y. Purevdorj, *J. Plant Ecol.* **9**, 508–519 (2016).
40. S. Takatsuki, M. Sato, Y. Morinaga, *Grassl. Sci.* **64**, 167–174 (2018).
41. Government of Mongolia, "Law on the Livestock Headcount Tax" (Integrated legal information system, 2020); https://legalinfo.mn/mn/detail/15729.
42. M. E. Fernández-Giménez, *Hum. Ecol. Interdiscip. J.* **30**, 49–78 (2002).
43. B. Nandintsetseg, M. Shinoda, C. Du, E. Munkhjargal, *Sci. Rep.* **8**, 14769 (2018).
44. M. E. Fernández-Giménez, B. Batkhishig, B. Batbuyan, *Glob. Environ. Change* **22**, 836–851 (2012).
45. M. E. Fernandez-Gimenez, in *Proceedings of the Conference on Transformations, Issues, and Future Challenges on Land use and land tenure in Mongolia: A brief history and current issues, in Rangelands of Central Asia* (USDA Forest Service Proceedings, 2006), pp. 30–36.
46. J. Addison, C. Brown, *J. Arid Environ.* **109**, 54–64 (2014).
47. N. Middleton, H. Rueff, T. Sternberg, B. Batbuyan, D. Thomas, *Landsc. Ecol.* **30**, 91–107 (2015).
48. United States Geological Survey (USGS), Landsat 8-9 Operational Land Imager / Thermal Infrared Sensor Level-2, Collection 2. *Earth Resources Observation and Science (EROS) Center* (2020); https://doi.org/10.5066/P9OGBGM6.
49. United States Geological Survey (USGS), Landsat 7 Enhanced Thematic Mapper Plus Level-2, Collection 2. *Earth Resources Observation and Science (EROS) Center* (2020); https://doi.org/10.5066/P9C7I13B.
50. United States Geological Survey (USGS), Landsat 8-9 Operational Land Imager / Thermal Infrared Sensor Level-2, Collection 2. *Earth Resources Observation and Science (EROS) Center* (2020); https://doi.org/10.5066/P9OGBGM6.
51. C. Schaaf, Z. Wang, MODIS/Terra+Aqua BRDF/Albedo Nadir BRDF-Adjusted Ref Daily L3 Global—500m V061. *EarthData* (2021); https://doi.org/10.5067/MODIS/MCD43A4.061.
52. A. Schucknecht, M. Meroni, F. Kayitakire, A. Boureima, *Remote Sens.* **9**, 463 (2017).
53. M. Chen *et al.*, *Ecosphere* **10**, e02889 (2019).
54. C. Elbers, J. O. Lanjouw, P. Lanjouw, *Econometrica* **71**, 355–364 (2003).
55. National Statistic Office of Mongolia, "The 2023 Census on Livestock and Domestic Animals, Fences, and Well" (Mongolian Statistical Information Center, 2023); https://www.1212.mn/en.
56. National Statistic Office of Mongolia, "Semi-annual livestock sampling survey 2023" (Mongolian Statistical Information Center, 2023); https://www.1212.mn/en.
57. J. Muñoz Sabater, ERA5-land hourly data from 1981 to present. *Copernicus Climate Change Service (C3S) Climate Data Store (CDS)* (2019); https://doi.org/10.24381/cds.e2161bac.
58. A. Ortiz-Bobea, in *Handbook of Agricultural Economics*, **vol. 5**, C. B. Barrett, D. R. Just, Eds. (Elsevier, 2021), pp. 3981–4073.
59. M. Shinoda, *J. Geophys. Res.* **106**, 33393–33403 (2001).
60. B. Nandintsetseg, M. Shinoda, *Int. J. Climatol.* **31**, 1143–1152 (2011).
61. M. Shinoda, B. Nandintsetseg, *Global Planet. Change* **79**, 110–117 (2011).
62. M. Burke, K. Emerick, *Am. Econ. J. Econ. Policy* **8**, 106–140 (2016).
63. National Agency for Meteorology and the Environmental Monitoring of Mongolia, Administrative Unit and Ecological Zone Map (Environmental Information Center of Mongolia, 2020); https://eic.mn/geodata.
64. S. Sainnemekh, B. Densambuu, B. Bestelmeyer, I. Barrio, A. Arado'ttir, Rangeland degradation in Mongolia—Using state and transition models to help understand rangeland dynamics. *IGC Proceedings (1985–2023)* **42**, 1 (2021); https://uknowledge.uky.edu/igc/24/1-2/42.
65. J. L. Horowitz, in *Handbook of Econometrics*, J. J. Heckman, E. Leamer, Eds. (Elsevier, 2001), pp. 3159–3228.
66. M. Dumont, G. Rayp, O. Thas, P. Willeme, *Oxf. Bull. Econ. Stat.* **67**, 421–433 (2005).
67. A. C. Cameron, D. L. Miller, *J. Hum. Resour.* **50**, 317–372 (2015).
68. J. Gardner, arXiv:2207.05943 [econ.EM] [Preprint] (2024).
69. L. Liu, Y. Wang, Y. Xu, *Am. J. Pol. Sci.* **68**, 160–176 (2024).
70. R. D. Harris, E. Tzavalis, *J. Econom.* **91**, 201–226 (1999).
71. A. Levin, C. F. Lin, C. S. J. Chu, *J. Econom.* **108**, 1–24 (2002).
72. A. Inoue, G. Solon, *Econom. Theory* **22**, 835–851 (2006).
73. D. P. Roy *et al.*, *Remote Sens. Environ.* **185**, 57–70 (2016).
74. N. Gorelick *et al.*, *Remote Sens. Environ.* **202**, 18–27 (2017).
75. Materials and methods are available as supplementary materials.
76. A. Purevjav, T. Avirmed, S. W. Wilcox, C. B. Barrett, Climate rather than overgrazing explains most rangeland primary productivity change in Mongolia. *Dryad* (2025); https://doi.org/10.5061/dryad.bg79cnpmz.
77. L. S. Shapley, *Proc. Natl. Acad. Sci. U.S.A.* **39**, 1095–1100 (1953).
78. G. Owen, in *Mathematical Economics and Game Theory: Essays in Honor of Oskar Morgenstern*, R. Henn, O. Moeschlin, Eds. (Springer, 1977), pp. 76–88.
79. A. Retallack, G. Finlayson, B. Ostendorf, K. Clarke, M. Lewis, *Environ. Sustain. Indic.* **19**, 100285 (2023).
80. G. E. Soto *et al.*, *Earth Syst. Sci. Data* **16**, 5375–5404 (2024).

ACKNOWLEDGMENTS

We thank the National Statistics Office of Mongolia for providing livestock data; S. Bayarsaikhan of the Institute of Geography-Geoecology at the Mongolian Academy of Sciences; and J. Alix-Garcia, G. Allington, P. Clark, F. Fava, R. Heilmayr, M. Jagnani, N. Jensen, C. Lundberg, I. Rudik, G. Soto, seminar audiences, and four anonymous reviewers for valuable feedback. **Funding:** No grant supported this research. **Author contributions:** Conceptualization, Methodology, Writing for original draft and review/editing: A.-O.P., T.A., S.W.W., C.B.B.; Data curation, investigation, visualization: A.-O.P., T.A.; Formal analysis, validation: A.-O.P., K.A., S.W.W.; Project administration, resources, supervision: C.B.B. **Competing interests:** There are no competing interests to declare. **Data and materials availability:** Data and code to reproduce all results are archived in an online repository (*76*).

SUPPLEMENTARY MATERIALS

science.org/doi/10.1126/science.adn0005
Materials and Methods; Figs. S1 to S13; Tables S1 to S47; References (*81*, *82*)

Submitted 16 November 2023; resubmitted 12 December 2024; accepted 14 July 2025

10.1126/science.adn0005

QUANTUM PROCESSING

Scalable entanglement of nuclear spins mediated by electron exchange

Holly G. Stemp[1,2]†, Mark R. van Blankenstein[1,2], Serwan Asaad[1,2]‡, Mateusz T. Mądzik[1,2]§, Benjamin Joecker[3], Hannes R. Firgau[1,2], Arne Laucht[1,2,4], Fay E. Hudson[1,4], Andrew S. Dzurak[1,4], Kohei M. Itoh[5], Alexander M. Jakob[2,6], Brett C. Johnson[7], David N. Jamieson[2,6], Andrea Morello[1,2]*

The use of nuclear spins for quantum computation is limited by the difficulty in creating genuine quantum entanglement between distant nuclei. Current demonstrations of nuclear entanglement in semiconductors rely on coupling the nuclei to a common electron, which is not a scalable strategy. In this work, we demonstrated a two-qubit controlled-Z logic operation between the nuclei of two phosphorus atoms in a silicon device, separated by up to 20 nanometers. Each atom binds separate electrons, whose exchange interaction mediates the nuclear two-qubit gate. We prepared and measured a nuclear Bell state with a fidelity of 76^{+5}_{-5}% and a concurrence of $0.67^{+0.05}_{-0.05}$. With this method, future progress in scaling up semiconductor spin qubits can be extended to the development of nuclear spin–based quantum computers.

Entanglement—the quintessential quantum mechanical property—is a vital ingredient for quantum computation and quantum communications and can provide a quantum advantage in sensing and metrology. However, the practical use of quantum entanglement quickly reveals a major challenge in quantum technologies: the conflict between isolation from the environment and coupling between different quantum systems. In the solid state, it is generally the case that the systems with the longest coherence, such as nuclear spins (*1*, *2*), are the most challenging ones to entangle.

Nuclear spins were the very first physical platform to demonstrate the execution of a quantum algorithm (*3*). Ensemble nuclear magnetic resonance (NMR) pioneered many of the sophisticated quantum control techniques that have subsequently been adopted by other platforms (*4*) but is no longer pursued for scalable quantum computing because of the lack of scalable methods to produce genuine quantum entanglement between multiple nuclei. We use the term "genuine" entanglement to highlight that although multiple quantum coherences between distant nuclei are routinely observed in ensemble NMR (*5*), such states can be described by mixtures of fully separable density matrices. A minimum spin polarization of 1/3, a sufficiently pure initial state, is required to satisfy the entanglement criterion of positive partial transpose (*6*, *7*). The development of methods to projectively measure single electron spins, and resolve nuclear spins that are coupled to them, has enabled the preparation of high-purity electron-nuclear states in, for example, diamond (*8*), silicon (*9*), silicon carbide (*10*), and rare-earth systems (*11*).

The remaining challenge is the extremely weak mutual coupling between nuclear spins. For example, the magnetic dipole coupling between two ^{31}P nuclei at 1 nm distance is on the order of 10 Hz. Therefore, most examples of nuclear entanglement rely on coupling the nuclei to a common electron (*12*, *13*), necessarily within distances of ~1 to 5 nm, dictated by the size of the electron wave function (*14*–*16*). These methods are inherently nonscalable, owing to exponential spectral crowding as more nuclei are included. The only way out of this gridlock is to involve multiple electrons (*17*, *18*), which themselves should be mutually coupled in a robust and scalable manner.

In this work, we demonstrated a scalable method to generate genuine entanglement between nuclear spins. We implemented a nuclear two-qubit geometric controlled-Z (CZ) gate between the nuclear spins of two ^{31}P donor atoms in a silicon metal-oxide-semiconductor (MOS) device. Each nucleus is bound to a different electron, and the two electrons are coupled by a Heisenberg exchange interaction. The exchange interaction strength of 12 MHz corresponds to an estimated interdonor distance of up to 20 nm (*19*) and enables fast (≈2 μs) entangling operations. The geometric two-qubit gate we report here relies solely on having an electron's spin resonance frequency depending on the state of two nuclei. This condition can be fulfilled in a wide range of donor locations, and with diverse methods for electron-electron interaction, which may also involve coupling to intermediary quantum dots. Therefore, our method underpins the exciting prospect of exploiting advances in the development and scaling of semiconductor quantum dots (*20*, *21*) and extending them to the operation of nuclear spin–based quantum processors.

Four-qubit, two-atom device

The system in which these experiments were performed consists of two ^{31}P donor nuclei, which we refer to as donor 1 (consisting of nucleus n1 and electron e1) and donor 2 (consisting of nucleus n2 and electron e2), introduced into an isotopically purified (*22*) ^{28}Si lattice by means of ion implantation (*23*). We use the symbols $|\downarrow\rangle$ and $|\uparrow\rangle$ for the electron spin states and $|\Downarrow\rangle$ and $|\Uparrow\rangle$ for the nuclear ones. Each donor nucleus was hyperfine coupled to a single bound electron, with a hyperfine coupling strength of $A_1 = 111$ MHz and $A_2 = 113$ MHz, respectively. The two electrons were coupled to one another with an exchange interaction strength of $J \approx 12$ MHz (*24*). Using a full configuration interaction method (*19*) to model the two donor atoms (Fig. 1, A and B), we estimate the largest interdonor distance for this value of exchange interaction strength to be 20 nm. The estimated interdonor distance for this value of exchange interaction strength depends on the exact axis over which the donors are separated. Averaging over all possible donor orientations, we obtained an average estimated interdonor distance of 16.13 nm. Details of this calculation are provided in the supplementary materials, Interdonor distance estimations. These calculations assume no electrical detuning between the donors, which would increase the interdonor distances possible for this exchange interaction strength.

The spin Hamiltonian of the two-donor electron-nuclear system, in frequency units, is

$$H = (\mu_B/h)B_0(g_1 S_{z1} + g_2 S_{z2}) + \gamma_n B_0(I_{z1} + I_{z2}) + A_1 \mathbf{S}_1 \cdot \mathbf{I}_1 + A_2 \mathbf{S}_2 \cdot \mathbf{I}_2 + J(\mathbf{S}_1 \cdot \mathbf{S}_2) \quad (1)$$

where μ_B is the Bohr magneton, h is Planck's constant, $g_{1,2} \approx 1.9985$ are the Landé g-factors of each electron spin, $g\mu_B/h \approx 27.97$ GHz/T, and $\gamma_n \approx 17.23$ MHz/T is the ^{31}P nuclear gyromagnetic ratio. Information on how the donor nuclei and electrons were initialized, controlled, and read out is provided in (*25*). Coherence time measurements of the ionized and neutral nucleus and the donor electron are provided in the supplementary materials, Nuclear and electron coherence times.

[1]School of Electrical Engineering and Telecommunications, UNSW Sydney, Sydney, NSW, Australia. [2]ARC Centre of Excellence for Quantum Computation and Communication Technology, Sydney NSW, Australia. [3]NNF Quantum Computing Programme, Niels Bohr Institute, University of Copenhagen, Copenhagen, Denmark. [4]Diraq Pty., Sydney, NSW, Australia. [5]School of Fundamental Science and Technology, Keio University, Kohoku-ku, Yokohama, Japan. [6]School of Physics, University of Melbourne, Melbourne, VIC, Australia. [7]School of Science, RMIT University, Melbourne, VIC, Australia. ***Corresponding author. Email: a.morello@unsw.edu.au** †Present address: Research Laboratory of Electronics, Massachusetts Institute of Technology, Cambridge, MA, USA. ‡Present address: Quantum Machines, Tel Aviv, Israel. §Present address: Intel Corporation, Hillsboro, OR, USA.

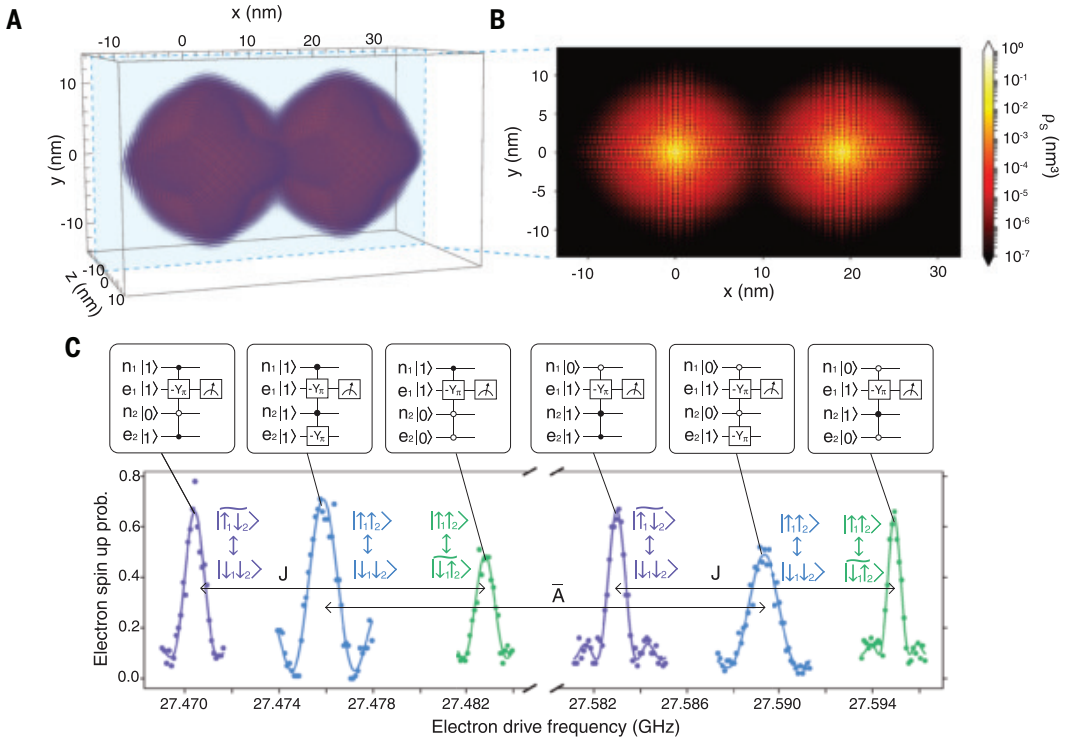

Fig. 1. Exchange-coupled, two-atom system. (**A**) Three-dimensional (3D) full configuration interaction simulation of the singlet wave function for two donor atoms exchange-coupled with a strength of 12 MHz. This exchange-coupling strength corresponds to a spacing of 19 nm along the [100] crystal axis, assuming no detuning between the two atoms. (**B**) 2D plane cut of the simulation in (A) for a value of $z = 0$ nm. (**C**) ESR frequency spectrum schematic for one of the electrons in an exchange-coupled, two-donor system for the case of $J > \bar{A}$, where J is the exchange interaction strength and $\bar{A} = (A_1 + A_2)/2$ is the average hyperfine value of the two donor atoms (*24*,*26*,*29*). Six resonance frequencies are present for electron 1, conditional on the state of both the other electron and the two donor nuclei. Four of these resonances represent the case for which the two donor nuclei are in an antiparallel spin configuration, for which $J < \Delta = \bar{A}$. The remaining two of these resonances represent the case for which the two donor nuclei are in a parallel spin orientation, for which $J > \Delta = |A_1 - A_2|$.

Within each donor, the hyperfine coupling results in two resonance frequencies being present for each spin, conditional on the other spin being in either the $\Downarrow$ ($\downarrow$) or $\Uparrow$ ($\uparrow$) state. Therefore, any operation on either the electron or nucleus represents a two-qubit conditional rotation (CROT) gate, which can be used to generate electron-nuclear entanglement (*9*).

This entanglement can be extended to multiple donor atoms by introducing an exchange coupling between the electrons of separate donor atoms. The electron spin resonance (ESR) frequency spectrum is shown in Fig. 1C for one of the electrons in the two-donor system in the presence of an exchange interaction between the electrons. The electron state transitions represented by each resonance frequency peak are shown in Fig. 1C, insets. The presence of the exchange interaction causes the electron eigenstates to hybridize, so that the two-qubit electron eigenstates become $|\downarrow_1\downarrow_2\rangle$, $|\downarrow_1\uparrow_2\rangle = \cos(\theta)|\downarrow_1\uparrow_2\rangle + \sin(\theta)|\uparrow_1\downarrow_2\rangle$, $|\uparrow_1\downarrow_2\rangle = \cos(\theta)|\uparrow_1\downarrow_2\rangle - \sin(\theta)|\downarrow_1\uparrow_2\rangle$, $|\uparrow_1\uparrow_2\rangle$, where $\tan(2\theta) = \frac{J}{\Delta}$, and Δ is the detuning between the two electrons dependent on the orientation of the nuclear spins. In this case, each electron resonance depends on the state of three spins: the two-donor nuclei and the second electron of the exchange-coupled pair. Each rotation therefore constitutes a four-qubit Toffoli gate. This gate has two main advantages. First, it allows us to generate entanglement between a donor electron and the nucleus of another donor atom. Second, this gate allows us to implement a two-qubit nuclear geometric CZ gate, thus enabling entanglement between neighboring donor nuclei.

The nuclear geometric CZ gate in a *J*-coupled system

The only requirement for being able to implement a nuclear geometric CZ gate is the presence of a resonance frequency of an electron, which depends on the state of two nuclei. This can be achieved in this system by using the four-qubit Toffoli gate, with the following steps.

First, both nuclei are initialized in the spin $|\Downarrow\rangle$ state by using the ENDOR scheme described in (*26*). Next, one of the two nuclei is placed in a superposition state by means of an NMR $-Y_{\frac{\pi}{2}}$ pulse, conditional on the electron bound to that nucleus being in the $|\downarrow\rangle$ state. For the example of n2 being placed in a superposition state, this therefore results in the following nuclear state (*15*)

$$|\Downarrow_1\rangle \otimes \frac{1}{\sqrt{2}}\left(|\Downarrow_2\rangle + |\Uparrow_2\rangle\right) = \frac{1}{\sqrt{2}}\left(|\Downarrow_1\Downarrow_2\rangle + |\Downarrow_1\Uparrow_2\rangle\right) \quad (2)$$

When a 2π rotation is then applied to one of the electrons, conditional on a given two-qubit nuclear state, this rotation imparts a geometric phase ϕ_G onto the two-qubit nuclear state on which the electron rotation was conditioned, with the magnitude of the geometric phase imparted given by

$$\phi_G = -\frac{1}{2}\Delta\Omega \quad (3)$$

where $\Delta\Omega$ represents the angle subtended on the sphere by the trajectory of the electron spin (*27*). For the case of $\Delta\Omega = 2\pi$, $\phi_G = -\pi$ and hence a phase of π is acquired by the two-qubit nuclear state on which the electron rotation was conditioned, relative to the other states in the nuclear superposition. For the case of the electron rotation being conditioned on the two-qubit nuclear state $|\Downarrow_1\Uparrow_2\rangle$, this would therefore result in the following

$$\frac{1}{\sqrt{2}}\left(|\Downarrow_1\Downarrow_2\rangle + |\Downarrow_1\Uparrow_2\rangle\right) \xrightarrow{\phi_G} \frac{1}{\sqrt{2}}\left(|\Downarrow_1\Downarrow_2\rangle - |\Downarrow_1\Uparrow_2\rangle\right) \quad (4)$$

If n1 was instead initialized in the $|\Uparrow_1\rangle$ state, then the 2π rotation of the electron would be far off resonance, and hence no geometric phase would be imparted. This gate therefore represents the implementation of a two-qubit nuclear CZ gate, where a phase of π is added to the target nucleus, conditional on the control nucleus being in the $|1\rangle = |\Downarrow\rangle$ state.

A controlled-rotation (CNOT) or zero-controlled-rotation (zCNOT) nuclear gate can be implemented by adding an extra $\frac{\pi}{2}$ pulse to the target nucleus after the CZ gate.

Entangling electrons and nuclei

By varying the frequency and duration of the drive applied to the electrons during the implementation of the nuclear geometric CZ gate, entanglement can be generated between one of the nuclei and both electrons in the exchange-coupled pair. In Fig. 2, we show the simulated (Fig. 2C) and experimental (Fig. 2D) results of the implementation of the pulse sequence shown in Fig. 2A. Before the beginning of the sequence, the two nuclei were initialized in the state $|\Downarrow_1\Downarrow_2\rangle$. A $-Y_{\frac{\pi}{2}}$ pulse was applied to n2 to prepare the nuclear superposition state $\frac{1}{\sqrt{2}}(|\Downarrow_1\Downarrow_2\rangle + |\Downarrow_1\Uparrow_2\rangle)$. A pulse of varying duration and frequency was then applied to the electrons. The frequency of this ESR pulse was swept across a range of 20 MHz, so that it crossed the resonance frequencies of e1 conditional on the $|\Downarrow_1\Uparrow_2\rangle$ nuclear state and of e1 and e2 conditional on the $|\Downarrow_1\Downarrow_2\rangle$ nuclear state, which together make up the nuclear superposition. Similarly, the duration of the ESR pulse was swept from 0 μs to ~20 μs, or ~20 π pulses of the electron when on resonance. A final $\frac{\pi}{2}$ pulse was then applied to n2. This acted to project the information along the *xy* plane of the Bloch sphere to the *z*-axis, so that it could be read out. For this measurement, we extracted the nuclear flipping probability, P_{flip}. The simulated trajectory on the Bloch sphere of n2 and e1 is shown in Fig. 2B, for the case of a 2π rotation of the electron performed on resonance.

In Fig. 2, E to G, we highlight three results shown in Fig. 2C. In Fig. 2E, we highlight a point at which e1 undergoes a 2π rotation at its resonance frequency (Fig. 2C, black star). This rotation is conditional on one of the states of the nuclear superposition: $|\Downarrow_1\Uparrow_2\rangle$. When the nuclei are in an antiparallel spin orientation, the detuning between e1 and e2 (given by $\Delta = \overline{A} = 112$ MHz, where $\overline{A}$ is the average hyperfine value of the donor atoms) ensures that only e1 is driven at this frequency. As indicated by the circuit diagram, this 2π electron rotation therefore corresponds to the implementation of the nuclear geometric CZ gate, as we have described. Because the operation is physically applied to the electron, it proceeds at the speed of electron rotations, much faster than nuclear rotations (*28*). In this case, with a moderate power of 15 dBm at the output of the microwave source, the nuclear CZ gate is completed in ≈2 μs. When followed by the final $\frac{\pi}{2}$ pulse on n2, this operation performs a zCNOT gate, flipping n2 if n1 is in the $|\Uparrow\rangle = |0\rangle$ state.

In Fig. 2F, we show the second point of note in Fig. 2C. This point represents the implementation of a π pulse on e1, once again at the ESR resonance frequency conditional on the nuclear state $|\Downarrow_1\Uparrow_2\rangle$ (Fig. 2C, blue circle). In this case, a π rotation of the electron will flip the state of e1, conditional on the state of n2, which is in a superposition state. This operation therefore acts to maximally entangle e1 with n2.

Last, in Fig. 2G we highlight the point for which both electrons undergo a π rotation, this time conditional on the nuclear state $|\Downarrow_1\Downarrow_2\rangle$ (Fig. 2C, pink triangle), which constitutes the other half of the prepared nuclear superposition state. For the case of the nuclei being in a parallel spin orientation, $J > \Delta$, where Δ is now given by the detuning

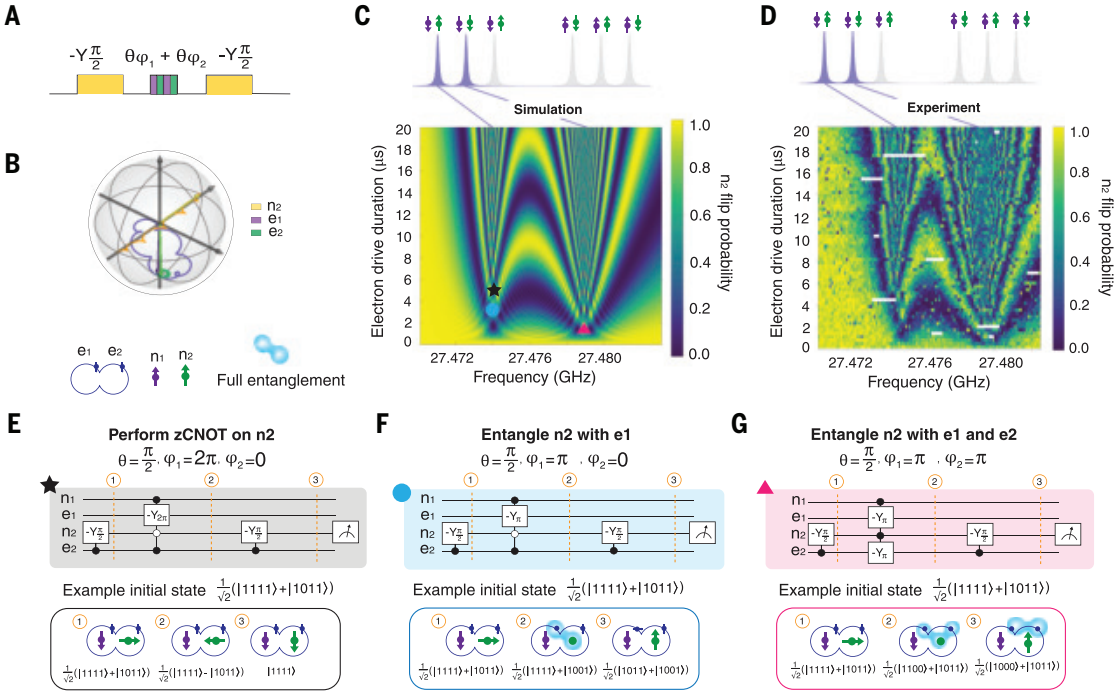

Fig. 2. Entangling electrons and nuclei. (**A**) Schematic of the pulse sequence used to generate the plots in (C) and (D). The yellow pulses indicate a $-Y_{\frac{\pi}{2}}$ performed on n2. The purple and green striped pulse indicates a pulse of varying duration and frequency performed on the electrons in the *J*-coupled system. (**B**) Simulation of the path of n2 (yellow), e1 (purple), and e2 (green) on the Bloch sphere for the case in which the electron drive is conditional on the nuclei being in the $|\Downarrow_1\Uparrow_2\rangle$ state. The arrows indicate the final state of the spins after the drive. For a drive duration of π, the arrows of n2 and e1 shrink to the center of the sphere as the two spins become entangled. (**C**) Simulation of the pulse sequence in (A). The axes correspond to the frequency and duration of the pulse applied to the electrons. (**D**) Experimental data from the implementation of the pulse sequence in (A). (**E** to **G**) Circuit diagrams and example input and output states representing the operations performed at the points in (C), with (E), the black star; (F), the blue circle, and (G), the pink triangle. Each state is written in the format $|n_1n_2e_1e_2\rangle$. Black dots in the circuit diagram indicate operations conditional on the $|1\rangle = |\downarrow\rangle$ state, and white dots indicate operations conditional on the state $|0\rangle = |\uparrow\rangle$.

between the two electrons $\Delta = |A_1 - A_2| = 2$ MHz. In this case, the eigenstates of the two electrons become strongly hybridized with one another (*24*, *26*, *29*); hence, driving at this frequency results in both e1 and e2 undergoing a rotation of π conditioned on n2. This results in both electrons becoming maximally entangled with n2, thus generating a three-qubit entangled state.

The phase imparted on n2 by the electrons depends on a combination of both the frequency detuning ($\Delta_f = f_0 - f_{MW}$, where f_0 is the resonance frequency and f_{MW} is the frequency of the driving field) and the duration of the electron drive. As Δ_f increases, the area of the cone enclosed by the path of the electron traversed on the Bloch sphere decreases. However, as the detuning from the resonance frequency increases, the spin precession frequency in the rotating frame increases, resulting in a greater number of rotations about this cone. There are therefore a number of regions shown in Fig. 2, C and D, away from the electron resonance frequencies, for which the electron imparts a phase of 2π on the nucleus or undergoes a rotation of π, resulting in either the implementation of a nuclear CZ gate or the generation of entanglement between the electrons and n2. A full simulation of this pulse sequence is shown in the supplementary materials, phase map simulations.

Long-range nuclear entanglement

Using the nuclear geometric CZ gate, we prepared an entangled state between the two distantly spaced donor nuclei. The pulse sequence used to prepare a Bell state between the two nuclei is shown in Fig. 3A. The nuclei were first initialized in the state $|\Downarrow_1 \Downarrow_2\rangle$. A $\frac{\pi}{2}$ NMR pulse was then applied to both of the nuclei sequentially, so that we prepared the nuclear superposition state $\frac{1}{2}(|\Downarrow_1 \Downarrow_2\rangle + |\Downarrow_1 \Uparrow_2\rangle + |\Uparrow_1 \Downarrow_2\rangle + |\Uparrow_1 \Uparrow_2\rangle)$. A 2π ESR pulse was then applied to e2 conditional on the nuclear state $|\Downarrow_1 \Uparrow_2\rangle = |10\rangle$, which imparted a phase of $-\pi$ to this component of the nuclear superposition, resulting in the state $\frac{1}{2}(|\Downarrow_1 \Downarrow_2\rangle - |\Downarrow_1 \Uparrow_2\rangle + |\Uparrow_1 \Downarrow_2\rangle + |\Uparrow_1 \Uparrow_2\rangle)$. A second $\frac{\pi}{2}$ pulse was then applied to n1, yielding the final state $\frac{1}{\sqrt{2}}(|\Uparrow_1 \Downarrow_2\rangle + |\Downarrow_1 \Uparrow_2\rangle) = \frac{1}{\sqrt{2}}(|01\rangle + |10\rangle)$, which represents the Ψ^+ Bell state between the two nuclei. The resulting nuclear state probability was then measured for both nuclei.

To quantify the degree of entanglement generated between the donor nuclei, we performed nuclear Bell state tomography. This involved first preparing the nuclear Bell state by using the pulse sequence detailed above, before projecting the Bell state information along different axes of the Bloch sphere to the z axis for read out (*30*). The pulse sequence used to prepare the nuclear Bell state is shown in Fig. 3A. This information was then used to reconstruct the density matrix of the prepared Bell state (Fig. 3B and supplementary materials, Bell state fidelity and concurrence). From this density matrix, we obtained a Bell state fidelity of $76^{+5}_{-5}\%$ and concurrence value of $0.67^{+0.05}_{-0.05}$, without removal of SPAM, indicating the clear presence of entanglement between the two nuclei. The error bars in Fig. 3C and throughout this work indicate 2σ. More information on how the error bars were calculated is provided in the supplementary materials, Error bar estimation.

The nuclear Bell state fidelity is primarily limited by the fidelity of electron initialization. The nucleus can be read out with high fidelity (>99%) (*31*) because of the ability to perform quantum nondemolition (QND) readout through the electron. Additionally, the operation fidelity of the nucleus, measured with single-qubit gate set tomography [supplementary materials, Nuclear one-qubit gate set tomography (GST)], also exceeds 99%. Consequently, the reduction in the amplitude of a Rabi oscillation performed on the neutral nucleus is primarily caused by electron initialization errors. By analyzing the amplitude of the neutral nucleus Rabi oscillations, we estimated an electron initialization fidelity of 86% (supplementary materials, Phase reversal tomography). This initialization error affects the performance of initializing and operating the neutral nuclei because each nuclear operation is conditional on the electron state.

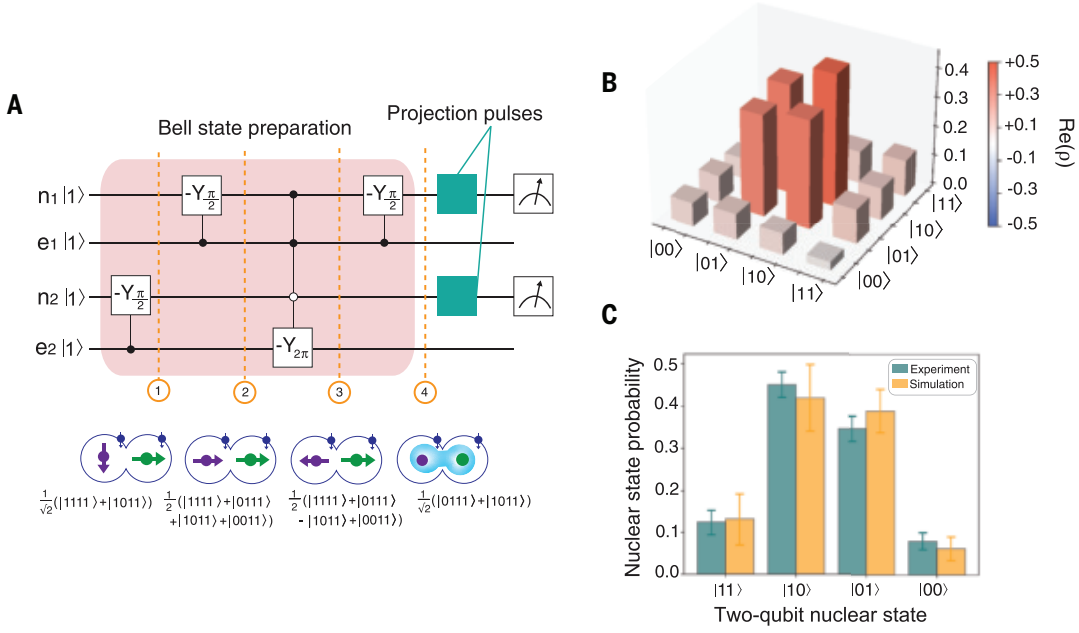

Fig. 3. Long-range entanglement between two nuclei. (**A**) Circuit diagram depicting the pulse sequence used to generate the Bell state $\frac{1}{\sqrt{2}}(|01\rangle + |10\rangle)$ between the two nuclei (red shaded region). A zCNOT was performed on n1 by sandwiching the nuclear geometric CZ gate between two $\frac{\pi}{2}$ pulses. The pulses depicted in the turquoise box above the circuit diagram indicate the projection pulses performed after the Bell state generation, so that the Bell state can be measured along all axes of the Bloch sphere, which is a requirement to perform Bell state tomography. (**B**) Reconstructed density matrix of the nuclear Bell state constructed by using Bell state tomography. This density matrix was reconstructed without removing state-preparation and measurement (SPAM) errors. (**C**) Experimental and simulated results of the two-qubit measurement of the Bell state along the z axis. The simulation assumed perfection in the gate operations and readout, with the only error introduced being the electron initialization error measured from experiments.

In Fig. 3C, we show the experimentally measured two-qubit state probabiliy of the prepared nuclear Bell state along the z axis of the Bloch sphere, without any projection pulses applied. This plot includes simulated two-qubit state probability, assuming perfect gates and readout, with the only introduced error being the experimentally informed electron initialization error. The overlap between the measured data and simulation results highlights the substantial role of electron initialization in limiting Bell state fidelity. The root cause of this problem is poor thermalization of the electron reservoir from which the $|\downarrow\rangle$ state is initialized (*32*). It is usually possible to solve this by using a Bayesian Maxwell's demon to beat the thermal limit of electron initialization (*32*). However, in this particular device, the method did not result in any improvements, owing to the short electron tunnelling times (supplementary materials, Electron initialization).

Previous implementations of Maxwell's demon on donor devices with longer electron tunneling times have demonstrated an electron initialization fidelity of 98.9%. With improvements to the amplifier chain to increase readout bandwidth, this fidelity could be realistically increased to 99.9% (*32*). Assuming this electron initialization fidelity, we obtained a simulated nuclear Bell state fidelity, using the same simulation as described above, of 99.7%. Use of deterministic single-ion implantation (*23*) to better control the distance between donor and single-electron transistor (SET) could further improve this value.

Conclusions

Entanglement is a vital resource for quantum computing. This work represents a key milestone, demonstrating the entanglement of nuclear spin qubits with a scalable method. Although different in the details of the operation, this result also represents the first realization of the original vision of Kane's silicon-based quantum computer (*33*), for which electron exchange was the key ingredient to provide universal quantum logic between nuclear spin qubits.

In the future, the distance between entangled nuclei could be further extended by adopting other methods of coupling the electron spins. This can be achieved, for example, by using a large jellybean quantum dot positioned between the donors to mediate the exchange interaction (*34*), or by using a superconducting resonator to mediate this coupling (*35*). These increased length scales could increase the viability of donor spins in silicon as a scalable quantum processor architecture. Promising experiments have already shown the ability to create large, deterministic donor arrays on a 300-nm pitch by means of ion implantation (*36*). Our results having been obtained by using a MOS-compatible silicon device, in which ion-implanted donors are integrated within the same device structure adopted in lithographic MOS dots (*37*), will allow us to link progress in nuclear spin–based quantum computing to the burgeoning field of semiconductor quantum dots (*20*).

REFERENCES AND NOTES

1. K. Saeedi *et al.*, *Science* **342**, 830–833 (2013).
2. M. Zhong *et al.*, *Nature* **517**, 177–180 (2015).
3. I. L. Chuang, L. M. Vandersypen, X. Zhou, D. W. Leung, S. Lloyd, *Nature* **393**, 143–146 (1998).
4. L. M. Vandersypen, I. L. Chuang, *Rev. Mod. Phys.* **76**, 1037–1069 (2004).
5. W. S. Warren, W. Richter, A. H. Andreotti, B. T. Farmer II, *Science* **262**, 2005–2009 (1993).
6. A. Peres, *Phys. Rev. Lett.* **77**, 1413–1415 (1996).
7. S. Simmons *et al.*, *Nature* **470**, 69–72 (2011).
8. S. Kolkowitz, Q. P. Unterreithmeier, S. D. Bennett, M. D. Lukin, *Phys. Rev. Lett.* **109**, 137601 (2012).
9. J. P. Dehollain *et al.*, *Nat. Nanotechnol.* **11**, 242–246 (2016).
10. A. Bourassa *et al.*, *Nat. Mater.* **19**, 1319–1325 (2020).
11. A. Ruskuc, C.-J. Wu, J. Rochman, J. Choi, A. Faraon, *Nature* **602**, 408–413 (2022).
12. P. Neumann *et al.*, *Science* **320**, 1326–1329 (2008).
13. W. Pfaff *et al.*, *Nat. Phys.* **9**, 29–33 (2013).
14. M. H. Abobeih *et al.*, *Nature* **576**, 411–415 (2019).
15. M. T. Mądzik *et al.*, *Nature* **601**, 348–353 (2022).
16. J. Reiner *et al.*, *Nat. Nanotechnol.* **19**, 605–611 (2024).
17. F. Dolde *et al.*, *Nat. Commun.* **5**, 3371 (2014).
18. N. Kalb *et al.*, *Science* **356**, 928–932 (2017).
19. B. Joecker *et al.*, *New J. Phys.* **23**, 073007 (2021).
20. G. Burkard, T. D. Ladd, A. Pan, J. M. Nichol, J. R. Petta, *Rev. Mod. Phys.* **95**, 025003 (2023).
21. S. Neyens *et al.*, *Nature* **629**, 80–85 (2024).
22. K. M. Itoh, H. Watanabe, *MRS Commun.* **4**, 143–157 (2014).
23. A. M. Jakob *et al.*, *Adv. Mater.* **34**, e2103235 (2022).
24. M. T. Mądzik *et al.*, *Nat. Commun.* **12**, 181 (2021).
25. Materials and methods are available as supplementary materials.
26. H. G. Stemp *et al.*, *Nat. Commun.* **15**, 8415 (2024).
27. D. J. Fernandez C., L. M. Nietot, M. A. Olmo, M. Santander, *J. Phys. Math. Gen.* **25**, 5151–5163 (1992).
28. J. J. Morton *et al.*, *Nat. Phys.* **2**, 40–43 (2006).
29. R. Kalra, A. Laucht, C. D. Hill, A. Morello, *Phys. Rev. X* **4**, 021044 (2014).
30. D. F. James, P. G. Kwiat, W. J. Munro, A. G. White, *Phys. Rev. A* **64**, 052312 (2001).
31. J. J. Pla *et al.*, *Nature* **496**, 334–338 (2013).
32. M. A. Johnson *et al.*, *Phys. Rev. X* **12**, 041008 (2022).
33. B. E. Kane, *Nature* **393**, 133–137 (1998).
34. Z. Wang *et al.*, *Adv. Mater.* **35**, e2208557 (2023).
35. Y.-Q. Xu *et al.*, *Sci. China Phys. Mech. Astron.* **66**, 237301 (2023).
36. A. M. Jakob *et al.*, *Adv. Mater.* **36**, e2405006 (2024).
37. M. Veldhorst *et al.*, *Nature* **526**, 410–414 (2015).
38. H. Stemp *et al*., Dataset for scalable entanglement of nuclear spins mediated by electron exchange. Dryad (2025); https://doi.org/10.5061/dryad.brv15dvm5.

ACKNOWLEDGMENTS

Funding: This research was funded by the Australian Research Council Centre of Excellence for Quantum Computation and Communication Technology (CE170100012) and the US Army Research Office (contracts W911NF-17-1-0200 and W911NF-23-1-0113). A.M. acknowledges an Australian Research Council Laureate Fellowship (FL240100181). We acknowledge the facilities and the scientific and technical assistance provided by the UNSW node of the Australian National Fabrication Facility (ANFF) and the Heavy Ion Accelerators (HIA) nodes at the University of Melbourne and the Australian National University. ANFF and HIA are supported by the Australian Government through the National Collaborative Research Infrastructure Strategy (NCRIS) program. H.G.S. and M.R.v.B. acknowledge support from the Sydney Quantum Academy. The views and conclusions contained in this document are those of the authors and should not be interpreted as representing the official policies, either expressed or implied, of the Army Research Office or the US government. The US government is authorized to reproduce and distribute reprints for government purposes notwithstanding any copyright notation herein. **Author contributions:** H.G.S., M.R.v.B., S.A., and A.M. conceived and designed the experiments. H.G.S., M.R.v.B., and H.R.F. performed and analyzed the measurements. M.T.M. and F.E.H. fabricated the device, with A.S.D.'s supervision, on materials supplied by K.M.I.. A.M.J., B.C.J., and D.N.J. designed and performed the ion implantation. B.J. performed full configuration interaction simulations. A.L. assisted with Floquet time evolution simulations. H.G.S., M.R.v.B., and A.M. wrote the manuscript, with input from all coauthors. A.M. supervised the project. **Competing interests:** A.S.D. is the CEO and a director of Diraq Pty. A.L., F.E.H., and A.S.D. declare equity interest in Diraq Pty. **Data and materials availability:** All data are available in the manuscript the supplementary material or are deposited at Dryad (*38*).

SUPPLEMENTARY MATERIALS

science.org/doi/10.1126/science.ady3799
Materials and Methods; Supplementary Text; Figs. S1 to S11; References (*39–57*)

Submitted 19 April 2025; accepted 15 July 2025

10.1126/science.ady3799

ORGANIC CHEMISTRY

Stereo-reversed E2 unlocks *Z*-selective C–H functionalization

Peter J. Verardi[1], Elizabeth A. Ryutov[1], Poulami Mukherjee[2], Remy Lalisse[2], Karina Targos[1], Tetsuya Inagaki[3], Megan Kelly[4], Ilia A. Guzei[1], Marcel Schreier[4]*, Osvaldo Gutierrez[2]*, Zachary K. Wickens[1]*

The stereoselective functionalization of C–H bonds represents a central challenge in modern organic synthesis. Despite decades of innovation in C–H activation chemistry, methods for *Z*-selective functionalization of alkenes have eluded synthetic practitioners. Terminal alkenes present the biggest challenge for *Z*-selectivity as they require selective cleavage of the more hindered of two otherwise virtually identical C–H bonds. Herein, we describe the transformation of alkenes into transient 1,2-*bis*-sulfonium intermediates found to undergo *Z*-selective elimination, overturning a textbook E2 stereoselectivity rule through stabilizing interactions. We identify paired electrolysis as an enabling strategy to both selectively generate the requisite *bis*-sulfonium intermediate and drive its rapid elimination in situ. The resultant *Z*-alkenyl sulfonium linchpins provide access to a wide array of *Z*-alkene targets from inexpensive feedstocks through robust cross-coupling reactions.

The transformation of C–H bonds is a longstanding goal of organic synthesis. Decades of research have delivered an array of mechanistically diverse approaches to replace these classically inert bonds with new C–C bonds (*1*, *2*). Within this broad arena, strategies to control stereoselectivity are of paramount importance. Although examples of atropo- (*3*) and enantioselective (*4*) aryl and alkyl C–H functionalization reactions have recently emerged, *Z*-selective alkenyl C–H functionalization reactions remain elusive (*5*, *6*). Such processes present a formidable challenge as a result of the inextricable introduction of unfavorable allylic-1,3 strain (Fig. 1A) (*7*, *8*). For example, a *Z*-selective variant of the Heck reaction has yet to arise despite over half a century of innovation on this Nobel Prize–winning reaction (*5*, *9*–*11*). Although other synthetic strategies to access *Z*-alkenes are known (*12*–*21*), all methods to selectively cleave the *pro-Z* C–H bond rely on directing groups to enforce stereoselectivity. This strategy intrinsically limits *Z*-selective C–H functionalization to a small pool of rigid alkenes bearing strongly coordinating auxiliaries (*22*). Overall, the realization of a complementary method for undirected, *Z*-selective C–H functionalization will require a new mechanistic strategy to overcome the inherent thermodynamic bias against *Z*-alkene formation.

We envisioned a fundamentally distinct approach to *Z*-selective C–H functionalization. Specifically, transformation of a terminal alkene into a transient 1,2-dinucleofuge followed by *Z*-selective elimination would deliver a *Z*-alkenyl linchpin (Fig. 1B) (*23*). This deceptively simple proposal requires stereoselective elimination to a *Z*-1,2-disubstituted alkene. Unfortunately, this seemingly elementary reaction requires violation of a basic rule taught in introductory organic chemistry: E2 stereoselectivity is predicted by the least sterically hindered Newman projection capable of *anti*-elimination (*24*). Indeed, while dinucleofuges, such as dihalides, can be readily prepared from terminal alkenes, they categorically eliminate to the predicted *E*-alkenyl halides alongside branched products (*25*–*27*). In fact, the *E*-selective elimination of dihalides served as the first case study when this teaching tool was presented by Newman in 1955 (*28*). Herein, we describe a strategy for *Z*-selective C–H functionalization that hinges on the discovery of a distinct *Z*-selective elimination. Our approach transforms an alkene into a transient 1,2-*bis*-sulfonium dinucleofuge that engages in stabilizing interactions to override steric hindrance in the *pro-Z* transition structure, overturning the 70-year-old E2 stereoselectivity model.

Discovery of a *Z*-selective E2 and translation to *Z*-selective thianthrenation

While studying the reactivity of **bis** and **mono**, electrogenerated adducts of thianthrene (TT) and an alkene (*29*), we observed an unambiguous correlation between the **bis**-to-**mono** ratio and the *Z*-to-*E* ratio of the resultant elimination products (Fig. 2A). This trend predicted that **bis** would eliminate selectively to *Z*-alkenyl thianthrenium product **1**. To validate this prediction, we isolated the small amount of **bis** formed through electrolysis and treated it with trifluoroacetate, a weak base found to not promote alkenyl thianthrenium isomerization. This experiment confirmed that **bis** eliminates with nearly perfect *Z*-selectivity. Given that alkenyl sulfonium salts can be engaged as cross-coupling electrophiles (*30*, *31*), this discovery sets the stage for a general approach to *Z*-selective C–H functionalization.

Having established that **bis** eliminates *Z*-selectively, we sought to translate this discovery into a useful *Z*-selective C–H functionalization protocol. Unfortunately, *bis*-thianthrenium adducts are exclusively minor products in established electrochemical processes (*27*, *32*, *33*) and are not observed under *S*-oxide–based thianthrenation (*31*). However, we reasoned that the divergent mechanisms of formation for **bis** and **mono** offer an untapped opportunity to develop a *bis*-selective protocol. Our current working mechanistic model for adduct formation posits that **bis** is formed by iterative addition of $TT^{\bullet+}$ across the alkene, whereas **mono** is formed through rapid cycloaddition of TT^{2+} with the alkene. Although chemical thianthrenation conditions are designed to access TT^{2+} and therefore exclusively form **mono**, electrochemical thianthrenation generates both $TT^{\bullet+}$ and TT^{2+} and thus provides access to **bis** as a minor product. Although $TT^{\bullet+}$ is formed at the anode throughout the reaction, formation of TT^{2+} requires an endergonic disproportionation of $TT^{\bullet+}$. Therefore, the rate of **mono** formation is highly sensitive to the concentrations of both $TT^{\bullet+}$ and TT. Consistent with this scenario, electrochemical thianthrenation is *bis*-selective at low conversion, when the concentration of TT is high. However, as TT is consumed anodically, disproportionation of $TT^{\bullet+}$ to generate TT^{2+} becomes increasingly feasible. As a consequence, **mono** formation accelerates as the reaction proceeds, furnishing **mono** as the major product by the end of electrolysis.

We hypothesized that increasing the concentration of TT should suppress **mono** by comproportionation with TT^{2+}. We found that increased TT loading considerably suppressed **mono** formation, although as expected, the absolute yield of **bis** was not affected (Fig. 2B, left). While on its own, this approach delivered low yield of **bis**, it suggested that simply extending the electrolysis time with a large excess of TT would deliver a high-yielding, *bis*-selective protocol. However, even with a large excess of TT (8 equiv.), allowing electrolysis to proceed to high conversion resulted in a substantial erosion in **bis** selectivity (10:1 decreased to 3:1). Given that high TT loading unambiguously suppresses the direct pathway to form **mono**, these data implicated an indirect pathway wherein **bis** converts to **mono** over time (*34*). Stirring isolated **bis** in reaction solvent revealed that **bis** is intrinsically unstable and converts to **mono** at a rate competitive with that of electrochemical adduct formation (Fig. 2B, right). In principle, this **bis**-to-**mono** conversion could be outpaced by rapid in situ elimination;

[1]Department of Chemistry, University of Wisconsin–Madison, 1101 University Avenue, Madison, WI, USA. [2]Department of Chemistry and Biochemistry, University of California, Los Angeles, Los Angeles, CA, USA. [3]Department of Applied Chemistry, Graduate School of Engineering, Osaka University, Suita, Osaka, Japan. [4]Department of Chemical and Biological Engineering, University of Wisconsin–Madison, Engineering Hall, 1415 Engineering Drive, Madison, WI, USA. ***Corresponding author. Email: mschreier2@wisc.edu (M.S.); o.gutierrez@ucla.edu (O.G.); wickens@wisc.edu (Z.K.W.)**

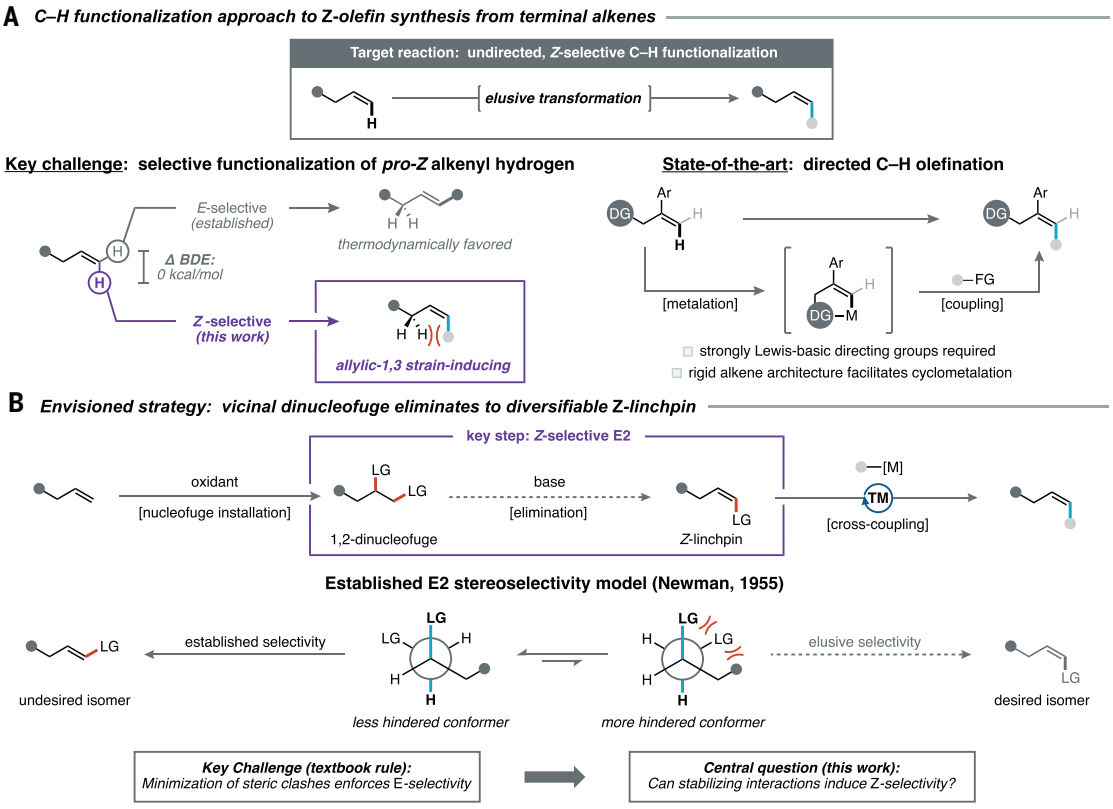

Fig. 1. Overview of this work. (**A**) C–H Functionalization approach to *Z*-olefin synthesis from terminal alkenes. (**B**) Envisioned strategy: vicinal dinucleofuge eliminates to diversifiable *Z*-linchpin.

however, we found that addition of a wide range of bases inhibited adduct formation altogether (table S3), presumably due to interactions with the electrophilic oxidized TT species.

We asked whether we could redesign the electrochemical system to both suppress **mono** and prevent **bis**-to-**mono** conversion. While divided cell electrolysis was initially used to maintain high faradaic efficiency, we envisioned that the use of an undivided cell—which introduces a cathode into the reaction chamber—could offer two strategic advantages (Fig. 2C) (*35*). First, the cathode would maintain an elevated steady-state concentration of TT through reduction of anodically generated $TT^{\bullet+}$. This would disfavor disproportionation and therefore suppress **mono** generation without requiring a large excess of TT. Second, cathodic hydrogen evolution reaction of trifluoroacetic acid would generate trifluoroacetate base at a rate intrinsically coupled to TT oxidation. This paired electrolysis manifold would ensure that base is only generated as adduct is formed, mitigating base-induced reaction inhibition. We found that undivided cell electrolysis inverted the typical stereoselectivity of thianthrenation, delivering model alkenyl thianthrenium salt **1** in both high yield and *Z*-selectivity with minimal additional optimization (Fig. 2D).

Scope and synthetic utility of *Z*-alkenyl thianthrenium salts

We next probed the scope of alkenes amenable to this *Z*-selective thianthrenation protocol (Fig. 3A). Throughout these studies, we found that the intrinsic *Z*-selectivity of the process was consistently high. Furthermore, the exceptional crystallinity of these *Z*-alkenyl thianthrenium salts enables recrystallization to afford nearly diastereopure products. This represents a practical advantage over traditional alkene syntheses, wherein separation of geometric isomers is notoriously challenging. Under these undivided cell conditions, *Z*-alkenyl thianthrenium salts are readily accessed from terminal alkenes bearing a diverse array of common functional groups (**3** to **25**). Notably, although amines are typically oxidized at lower potentials (*36*) than those required to oxidize TT (fig. S9), protonation under standard reaction conditions allows selective thianthrenation of alkenes bearing unprotected amines (**11** and **12**). While both alcohols and pyridines are known to attack oxidized TT species (*37*–*39*), *Z*-alkenyl thianthrenium salts can still be accessed from alkenes bearing both of these important functional groups (**13** and **14**). Pyridines are protonated in a manner similar to that of aliphatic amines, whereas alcohols are protected in situ with a labile trifluoroacetyl group by trifluoroacetic anhydride. Alkene substrates bearing other protic functional groups, such as amides (**15** and **16**), carboxylic acids (**17**), and sulfonamides (**18**) are each thianthrenated without in situ transformation. The oxidizing conditions do render some electron-rich groups, such as sulfides and enolizable ketones, incompatible. Nonetheless, ketone-containing *Z*-alkene products remain accessible since alkenes bearing Weinreb amides (**19**) undergo efficient *Z*-selective thianthrenation. Common electrophiles such as aryl and alkyl bromides are fully preserved in this *Z*-selective thianthrenation process (**20** and **21**). Notably, for substrates containing both terminal alkenes and acrylates, only the terminal alkene undergoes thianthrenation (**22**). This selectivity pattern complements transition metal–catalyzed alkenyl C–H activation reactions that commonly employ acrylate derivatives as substrates. Selective functionalization of a single alkene is also observed for substrates bearing two terminal alkenes (**23**). In this case, we posit that distal electronic communication from the electron-deficient alkenyl thianthrenium moiety in the product inhibits repeat thianthrenation. Our approach also successfully engages gaseous feedstocks using TT as the limiting reagent to access simple *Z*-alkene building blocks (**24**)

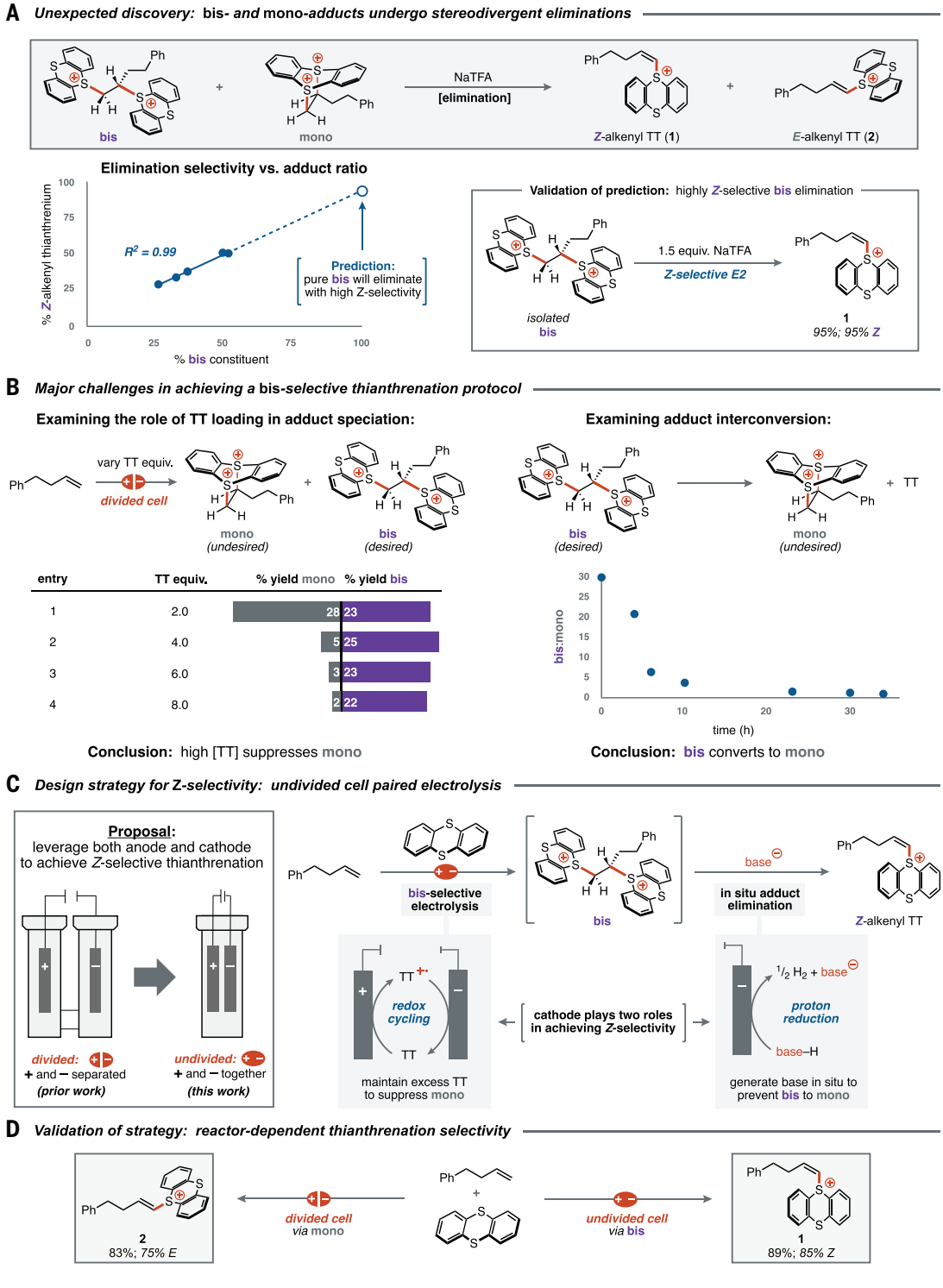

Fig. 2. Reaction design. (**A**) Unexpected discovery: *bis*- and *mono*-adducts undergo stereodivergent eliminations. Relationship between percent of **bis** constituent and percentage of *Z*-alkenyl thianthrenium is described with a linear fit ($R^2 = 0.99$). (**B**) Major challenges in achieving a *bis*-selective thianthrenation protocol. Reaction parameters: divided cell; constant current electrolysis; $i = 10.0$ mA; alkene (0.4 mmol); thianthrene (varying equiv.); TFA (5.0 equiv.); KPF_6 (4.0 equiv.); 1:1 MeCN:PhCN (0.05 M); 25°C; 2.6 hours. (**C**) Design strategy for *Z*-selectivity: undivided cell paired electrolysis. (**D**) Validation of strategy: reactor-dependent thianthrenation selectivity. For experimental details see SM, page S10. NaTFA, sodium trifluoroacetate; TFA, trifluoroacetic acid.

with high diastereoselectivity. Although monosubstituted alkenes are readily engaged, more substituted alkenes are not amenable to this electrochemical process: 1,1-disubstituted alkene substrates provide intractable mixtures of products, and internal alkenes fundamentally shift the stereodetermining step as they no longer possess both *pro-Z* and *pro-E* C–H bonds in the *bis*-thianthrenium intermediates. However, alkenes bearing allylic substituents still undergo *Z*-selective thianthrenation despite challenging the system with a substantial increase in 1,3-allylic strain (**25**). Finally, underscoring its practical synthetic utility, this undivided cell thianthrenation scales efficiently in batch using inexpensive graphite and stainless-steel electrodes to deliver multigram quantities of pure *Z*-alkenyl thianthrenium **1** after recrystallization (Fig. 3B).

In principle, *Z*-selective C–H thianthrenation provides an electrophilic linchpin for rapid diversification by means of stereospecific cross coupling. However, alkenyl thianthrenium salts can undergo isomerization under basic conditions (*40*, *41*). In all reported C–C coupling reactions of alkenyl thianthrenium salts derived from terminal alkenes, the more stable stereoisomer was used to generate an *E*-alkene. This has obscured whether stereochemistry is maintained through a stereospecific process or if different stereoisomers could converge to the same product (*31*). We found that the stereochemistry of *Z*-alkenyl thianthrenium **7** was translated to a variety of C–C bonds with minimal deviations from typical cross-coupling conditions (Fig. 4A) (*31*, *42*). Pd-catalyzed Sonogashira, Suzuki, and Negishi coupling protocols each afforded the corresponding C(sp), C(sp^2), and C(sp^3) cross-coupled products **26** to **28** with excellent retention of alkene geometry. A Heck reaction delivered *E*,*Z*-diene **29** with minimal erosion of diastereoselectivity despite proceeding through a Pd–H intermediate, which can promote *Z*- to *E*-alkene isomerization. Borylation transposed the polarity of the *Z*-alkenyl thianthrenium handle to furnish the nucleophilic *Z*-alkenyl building block **30** with an organoboron coupling handle (*43*). Finally, a Pd-catalyzed carbonylation

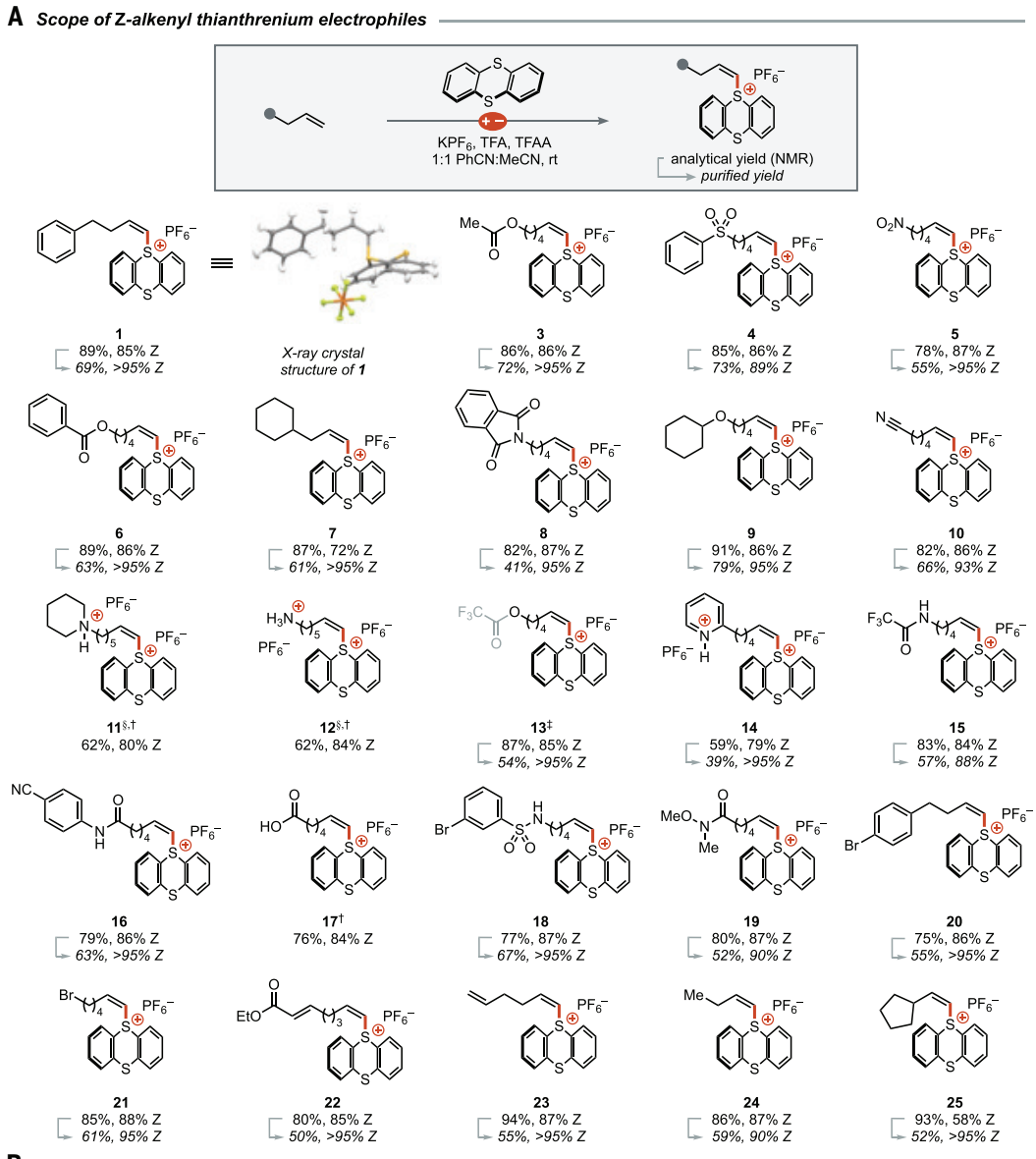

Fig. 3. *Z*-selective C–H thianthrenation. (**A**) Scope of *Z*-alkenyl thianthrenium electrophiles. Standard conditions: undivided cell; constant current electrolysis; $i = 93$ mA; alkene (3.1 mmol); thianthrene (2.0 equiv.); TFA (10.0 equiv.); TFAA (1.4 equiv.); KPF_6 (3.0 equiv.); 1:1 MeCN:PhCN (0.125 M); 25°C; 26.8 hours. Additional experimental details are available in the SM, page S16). §Reaction conducted with 11 equiv. of TFA. ‡Reaction conducted with 2.5 equiv. of TFAA. †Yield was determined by ^{1}H-NMR analysis using CH_2Br_2 as an internal standard. (**B**) Decagram-scale *Z*-selective C–H functionalization in batch. TFA, trifluoroacetic acid; TFAA, trifluoroacetic anhydride.

furnished *Z*-acrylate product **31**. Additionally, substrates bearing pendant nucleophiles known to react with alkenyl thianthrenium salts under basic conditions (*27*, *44*) did not impede productive coupling [see supplementary materials (SM), page S40]. Overall, successful implementation of these reactions suggests that *Z*-alkenyl thianthrenium salts will serve as *Z*-alkenyl pseudohalides across a wide range of stereospecific coupling reactions.

We envisioned that this *Z*-selective C–H functionalization protocol would enable approaches to a wide array of valuable synthetic targets from inexpensive petrochemical feedstocks through intuitive cross coupling disconnections (Fig. 4B). Through our C–H functionalization approach, 1-hexene underwent *Z*-selective thianthrenation (**32**) and cross-coupling with commercially available 10-undecyn-1-ol to provide key intermediate **33** on path to Clathculin B (*45*). Similarly, *Z*-selective thianthrenation of 1-pentene provided *Z*-linchpin **34**, setting the stage for a Suzuki coupling to furnish the Silk Moth sex pheromone Bombykol (**35**) in excellent yield in two steps (*46*). We next transformed 1-dodecene into the corresponding *Z*-thianthrenium salt **36**. Subsequent C(sp^2)–C(sp^3) Negishi coupling furnished **37**, a key intermediate in the synthesis of Spongy Moth sex pheromone (±)-cis-Disparlure (*47*). Finally, we synthesized pear fragrance ethyl decadienoate (**39**) in two steps through a *Z*-selective thianthrenation-Heck sequence from 1-heptene and ethyl acrylate (*48*). Beyond offering an efficient route to each of these compounds, our strategy presents several practical advantages. Recrystallization of each *Z*-alkenyl thianthrenium intermediate consistently provides stereopure material, contrasting traditional approaches to *Z*-alkene synthesis (e.g., Wittig olefination) that have variable stereoselectivity and lack any straightforward process to separate stereoisomers. Furthermore, the key *Z*-selective C–H functionalization step is robust, requiring no precautions to exclude air or moisture. This offers additional operational simplicity relative to emerging *Z*-selective metathesis strategies that rely on sensitive metal catalysts. Given the success of these proof-of-concept experiments, we anticipate the broad implementation of this synthetic tactic in the preparation of a wide range of *Z*-alkene targets.

Origins of *Z*-selectivity

Having demonstrated the synthetic value of this *Z*-selective C–H functionalization protocol, we sought to interrogate the mechanistic origins of the highly *Z*-selective elimination of *bis*-adducts. In

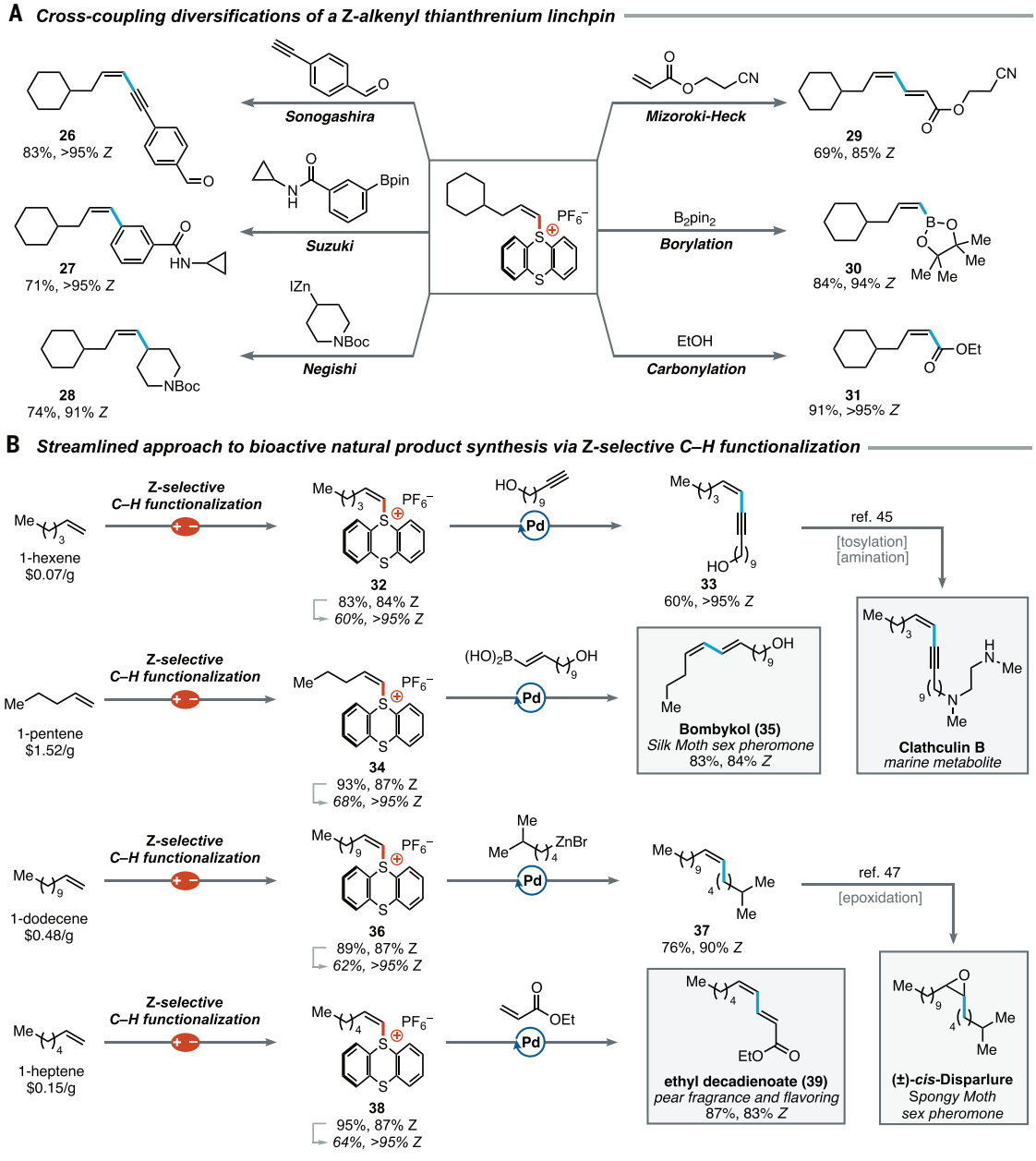

Fig. 4. Synthetic applications. (**A**) Cross-coupling diversifications of a *Z*-alkenyl thianthrenium linchpin. (**B**) Streamlined approach to bioactive natural product synthesis through *Z*-selective C–H functionalization.

introductory organic chemistry, students are taught to predict E2 stereoselectivity by identifying the least sterically encumbered Newman projection with an *anti*-periplanar arrangement of leaving group and hydrogen. Given that steric clashes from the ground state conformers reliably translate into the elimination transition structures, this approach has proven virtually infallible. In the present context, however, it incorrectly predicts *E*-selective elimination of **bis** because the *pro-E* conformer (**gauche-E**) has one fewer gauche interaction relative to its *pro-Z* counterpart (**gauche-Z**). To reconcile this disconnect, we computationally modeled these *gauche* conformers and their corresponding *anti*-elimination transition structures using 1-butene as a simple model substrate (Fig. 5A). These calculations establish that the relative stabilities of these conformers invert during elimination. While the rudimentary conformational analysis holds and **gauche-Z** is slightly higher in energy than **gauche-E** ($\Delta G^{\circ} = 0.7$ kcal/mol), the *Z*-forming *anti*-elimination transition structure (**TS-anti-Z**) is substantially lower in energy ($\Delta\Delta G^{\ddagger} = 3.2$ kcal/mol) than its *E*-forming analog (**TS-anti-E**). Further investigation using distortion-interaction analysis (*49*) indicated that distortion energies drive the energetic difference between these two *anti*-elimination transition states (fig. S17). To rationalize the difference in distortion energies, we analyzed the geometric changes that each gauche conformer undergoes to reach its elimination transition structure. This revealed that **gauche-E** requires extensive geometric reorganization to access **TS-anti-E**, whereas the geometry of **gauche-Z** is largely preserved in **TS-anti-Z**. This difference is clearly reflected in the change in dihedral angle between the two thianthrenium groups ($\Delta\angle$S–C–C–S), which is much larger for the *E*-forming pathway (contracts by 15.5°) than it is for the *Z*-forming pathway (expands by 1.0°).

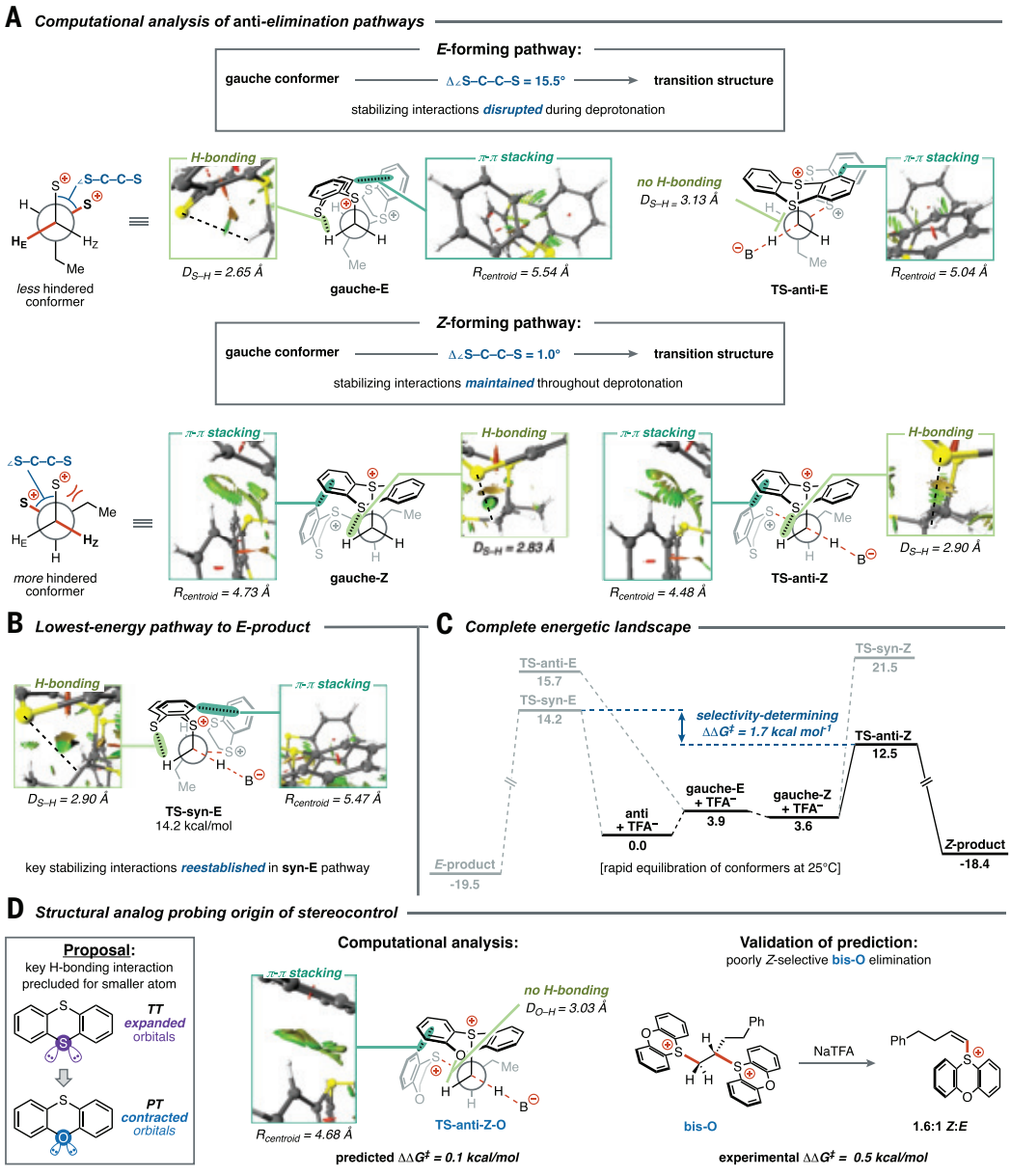

Fig. 5. Origins of *Z*-selectivity. (**A**) Computational analysis of *anti*-elimination pathways. (**B**) Lowest-energy pathway to *E*-product. (**C**) Complete energetic landscape. (**D**) Structural analog probing origin of stereocontrol. DFT calculations were performed at the UB3LYP-D3/def2TZVPP-CPCM(acetonitrile)//UB3LYP-D3/6-311G(d,p)-CPCM(acetonitrile) level of theory. NCI and Distortion Interaction Analysis calculated at the UB3LYP-D3/6-311G(d,p)-CPCM(acetonitrile) level of theory.

To elucidate the specific interactions underlying the pronounced difference in geometric distortion, we performed noncovalent interaction (NCI) (*50*) and natural bond orbital (NBO) (*51*) analysis on the two gauche conformers and their respective *anti*-elimination transition structures (figs. S18 to S21). We found that both conformers engage in a host of stabilizing interactions: (i) π-π contacts between the aromatic rings of the two thianthrenium units (*52*) and (ii) hydrogen bonding contacts between the neutral sulfur of each thianthrenium unit and its α-alkyl C–H bond (*53*). Each of these interactions was found to play a critical role in influencing *Z*-selectivity. First, the π-π contacts are stronger for **gauche-Z** than they are for **gauche-E**, offsetting the steric penalties of this more hindered conformer. Crucially, this differential carries into the corresponding elimination transition structures, in which **TS-anti-Z** engages in stronger π-π contacts than **TS-anti-E**. Second, the terminal thianthrenium unit hydrogen bonds to the *pro-E* C–H bond (H_E) in both gauche conformers. Since the *pro-E* C–H bond must be deprotonated in the *E*-forming pathway, **TS-anti-E** sacrifices this C–H···S hydrogen bonding interaction. Moreover, in **TS-anti-E**, the terminal thianthrenium unit must rotate away from the site of deprotonation, which forces the internal thianthrenium unit to rotate accordingly. This structural accommodation preserves π-π contacts and prevents destabilizing steric clashes but comes at the cost of the internal C–H···S hydrogen bonding interaction. By contrast, **TS-anti-Z** retains its entire network of stabilizing interactions, including both of its C–H···S hydrogen bonding contacts, rationalizing the minimal geometric reorganization required for the *Z*-forming pathway.

Although this comparative analysis of *anti*-elimination pathways clarifies the mechanistic origin of *Z*-selectivity, further scrutiny revealed an alternative pathway to the *E*-product that proceeds by means of a sterically congested *syn*-elimination. This *syn*-elimination (**TS-syn-E**) is lower in energy than **TS-anti-E** because it retains the key terminal C–H···S hydrogen bonding contact by inverting which C–H bond is deprotonated to form the *E*-product (Fig. 5B). This refinement of the model predicts an energy difference in excellent agreement with the experimentally observed *bis*-adduct elimination stereoselectivity ($\Delta\Delta G^{\ddagger}$ = 1.7 kcal/mol, both calculated and experimental). Taken together, these observations provide a complete mechanistic model for the reaction that explains the observed *Z*-selectivity: The least sterically hindered transition state that maintains key stabilizing interactions results in the *Z*-stereoisomer (Fig. 5C) (see SM, page S59 for additional commentary).

Finally, we designed an experiment to selectively probe the unusual hydrogen bonding interaction at the heart of our stereochemical model. We envisioned that swapping the neutral sulfur atom of TT with a smaller oxygen atom would disrupt this hydrogen bonding interaction (Fig. 5D). While oxygen is typically a better hydrogen bond acceptor than sulfur, the geometric constraints of the rigid *bis*-adduct system rely on sulfur's diffuse orbitals to engage in these long-range interactions (*54*). Indeed, NCI and NBO analyses predict that swapping the neutral sulfur atom with a smaller oxygen atom (**bis-O**) precludes the critical hydrogen bonding interactions while maintaining a similar steric profile and π-π interactions. As a result, **bis-O** is predicted to eliminate with poor stereoselectivity ($\Delta\Delta G^{\ddagger}$ =

0.1 kcal/mol). Experimentally, electrogenerated **bis-O** eliminates to a 1.6:1 *Z:E* mixture of alkenyl sulfonium products (figs. S24 and S25). This substantial decrease in selectivity upon such a seemingly distal structural modification supports the hypothesis that the hydrogen-bonding interaction plays a critical role in enforcing high *Z*-selectivity. Moreover, the fact that the **bis-O** system still does not revert to high *E*-selectivity underscores the contribution of π-π contacts that offset the steric penalties associated with the *Z*-forming pathway. Overall, these data establish that strategically positioned noncovalent interactions can override steric control in elimination reactions.

Conclusions

We have provided a solution to a longstanding challenge: *Z*-selective C–H functionalization of unactivated alkenes. This transformation was unlocked by an unexpected *Z*-selective elimination reaction of a transient *bis*-thianthrenium intermediate that overturns textbook E2 stereoselectivity predictions through stabilizing interactions. We illustrate how electrochemical cell design can be leveraged as a critical parameter to both selectively generate the requisite *bis*-thianthrenium dinucleofuge and drive its rapid elimination in situ to circumvent its inherent instability. Beyond providing a practical approach to *Z*-alkene synthesis, this work illustrates how noncovalent interactions can override intrinsic steric preferences in elimination reactions. We anticipate that both the synthetic methods and mechanistic principles uncovered herein will find broad application in accessing stereodefined alkenes.

REFERENCES AND NOTES

1. H. M. L. Davies, J. Du Bois, J. Q. Yu, *Chem. Soc. Rev.* **40**, 1855–1856 (2011).
2. J. F. Hartwig, *Acc. Chem. Res.* **50**, 549–555 (2017).
3. G. Liao, T. Zhou, Q.-J. Yao, B.-F. Shi, *Chem. Commun.* **55**, 8514–8523 (2019).
4. S.-L. You, *Asymmetric Functionalization of C–H Bonds* (The Royal Society of Chemistry, 2015).
5. I. P. Beletskaya, A. V. Cheprakov, *Chem. Rev.* **100**, 3009–3066 (2000).
6. S. Tang, K. Liu, C. Liu, A. Lei, *Chem. Soc. Rev.* **44**, 1070–1082 (2015).
7. R. W. Hoffman, *Chem. Rev.* **89**, 1841–1860 (1989).
8. M.-Z. Lu *et al.*, *Chem. Rev.* **122**, 17479–17646 (2022).
9. D. Schils *et al.*, *Org. Process Res. Dev.* **12**, 530–536 (2008).
10. K. Hirabayashi *et al.*, *Bull. Chem. Soc. Jpn.* **73**, 1409–1417 (2000).
11. X. Du *et al.*, *Org. Lett.* **3**, 3313–3316 (2001).
12. C. Z. Rubel *et al.*, *Angew. Chem. Int. Ed.* **63**, e202320081 (2024).
13. T. Neveselý, M. Wienhold, J. J. Molloy, R. Gilmour, *Chem. Rev.* **122**, 2650–2694 (2022).
14. M. J. Koh *et al.*, *Nature* **517**, 181–186 (2015).
15. M. J. Koh, T. T. Nguyen, H. Zhang, R. R. Schrock, A. H. Hoveyda, *Nature* **531**, 459–465 (2016).
16. S. J. Meek, R. V. O'Brien, J. Llaveria, R. R. Schrock, A. H. Hoveyda, *Nature* **471**, 461–466 (2011).
17. K. Endo, R. H. Grubbs, *J. Am. Chem. Soc.* **133**, 8525–8527 (2011).
18. G. Stork, K. Zhao, *Tetrahedron Lett.* **30**, 2173–2174 (1989).
19. C. Oger, L. Balas, T. Durand, J.-M. Galano, *Chem. Rev.* **113**, 1313–1350 (2013).
20. W. C. Still, C. Gennari, *Tetrahedron Lett.* **24**, 4405–4408 (1983).
21. W.-Y. Siau, Y. Zhang, Y. Zhao, in *Stereoselective Alkene Synthesis*, J. Wang, Ed. (Springer, 2012), pp. 33–58.
22. J. Zhang *et al.*, *Chem. Soc. Rev.* **50**, 3263–3314 (2021).
23. C. C. C. Johansson Seechurn, M. O. Kitching, T. J. Colacot, V. Snieckus, *Angew. Chem. Int. Ed.* **51**, 5062–5085 (2012).
24. M. Loudon, J. Parise, *Organic Chemistry* (Roberts and Company, ed. 6, 2015).
25. Q. Wang, N. A. Sasaki, C. Riche, P. Potier, *J. Org. Chem.* **64**, 8602–8607 (1999).
26. N. Kutsumura, K. Shibuya, H. Yamaguchi, T. Saito, *Tetrahedron Lett.* **58**, 4099–4102 (2017).
27. M. J. Kim *et al.*, *Angew. Chem. Int. Ed.* **62**, e202303032 (2023).
28. M. S. Newman, *J. Chem. Educ.* **32**, 344 (1955).
29. M. J. Kim, K. Targos, D. E. Holst, D. J. Wang, Z. K. Wickens, *Angew. Chem. Int. Ed.* **63**, e202314904 (2024).
30. M. H. Aukland *et al.*, *Angew. Chem. Int. Ed.* **57**, 9785–9789 (2018).
31. J. Chen, J. Li, M. B. Plutschack, F. Berger, T. Ritter, *Angew. Chem. Int. Ed.* **59**, 5616–5620 (2020).
32. D. E. Holst, D. J. Wang, M. J. Kim, I. A. Guzei, Z. K. Wickens, *Nature* **596**, 74–79 (2021).
33. D. Wang, K. Targos, Z. Wickens, *J. Am. Chem. Soc.* **143**, 21503–21510 (2021).
34. D.-Q. Qian, H. J. Shine, I. Y. Guzman-Jimenez, J. H. Thurston, K. H. Whitmire, *J. Org. Chem.* **67**, 4030–4039 (2002).
35. G.-Q. Sun *et al.*, *Nature* **615**, 67–72 (2023).
36. A. K. V. Mruthunjaya, A. A. J. Torriero, *Molecules* **28**, 471 (2023).
37. J. J. Silber, thesis, Texas Tech University (1972).
38. Y. Xiong, X. Zhang, H.-M. Guo, X. Wu, *Org. Chem. Front.* **9**, 3532–3539 (2022).
39. H. J. Shine, W. Yueh, *J. Org. Chem.* **59**, 3553–3559 (1994).
40. K. Targos *et al.*, *J. Am. Chem. Soc.* **146**, 13689–13696 (2024).
41. D. E. Holst, C. Dorval, C. K. Winter, I. A. Guzei, Z. K. Wickens, *J. Am. Chem. Soc.* **145**, 8299–8307 (2023).
42. F. Berger *et al.*, *Nature* **567**, 223–228 (2019).
43. R. Xie, J. Zhu, Y. Huang, *Org. Chem. Front.* **8**, 5699–5704 (2021).
44. M.-S. Liu, H.-W. Du, H. Meng, Y. Xie, W. Shu, *Nat. Commun.* **15**, 529 (2024).
45. R. C. Hoye, G. L. Anderson, S. G. Brown, E. E. Schultz, *J. Org. Chem.* **75**, 7400–7403 (2010).
46. N. Miyaura, H. Suginome, A. Suzuki, *Tetrahedron* **39**, 3271–3277 (1983).
47. M. B. Herbert, V. M. Marx, R. L. Pederson, R. H. Grubbs, *Angew. Chem. Int. Ed.* **52**, 310–314 (2013).
48. S. Tsuboi, T. Masuda, S. Mimura, A. Takeda, *Org. Synth.* **66**, 22 (1988).
49. F. M. Bickelhaupt, K. N. Houk, *Angew. Chem. Int. Ed.* **56**, 10070–10086 (2017).
50. J. Contreras-García *et al.*, *J. Chem. Theory Comput.* **7**, 625–632 (2011).
51. F. Weinhold, C. Landis, *Valency and Bonding: A Natural Bond Orbital Donor-Acceptor Perspective* (Cambridge Univ. Press, 2005).
52. S. E. Wheeler, *J. Am. Chem. Soc.* **133**, 10262–10274 (2011).
53. H. A. Fargher, T. J. Sherbow, M. M. Haley, D. W. Johnson, M. D. Pluth, *Chem. Soc. Rev.* **51**, 1454–1469 (2022).
54. J. S. Laursen, J. Engel-Andreasen, P. Fristrup, P. Harris, C. A. Olsen, *J. Am. Chem. Soc.* **135**, 2835–2844 (2013).

ACKNOWLEDGMENTS

We thank M. Levin for helpful suggestions during the manuscript drafting process, and the Weix, Stahl, Yoon, Schomaker, and Gellman groups for sharing their chemical inventories. We thank S. Yacoob (Stahl group) for sharing hood space during building power outages and K. Weber (Yoon group) for assistance with the carbonylation experiments. B. J. Thompson is acknowledged for his assistance with power supply design and fabrication. T. Drier is acknowledged for electrochemical glassware fabrication. K. Harper (Abbvie) is acknowledged for providing cell components for the decagram-scale synthesis. We also acknowledge support and suggestions from all Wickens group members throughout the investigation of this project. **Funding:** This work was financially supported by the NIH (R01 GM149674–01) and a Research Forward grant from the University of Wisconsin–Madison with support from the Wisconsin Alumni Research Foundation. This material is based upon work supported by the National Science Foundation Graduate Research Fellowship under grant DGE-2137424. Any opinions, findings, and conclusions or recommendations expressed in this material are those of the author(s) and do not necessarily reflect the views of the National Science Foundation. O.G. acknowledges NIH NIGMS (R35GM137797) for funding and Texas A&M University HPRC resources and the Hoffman2 Cluster at UCLA Office of Advanced Research Computing's Research Technology Group for providing computational resources (https://hprc.tamu.edu). T.I. acknowledges the JSPS Research Fellowship for Young Scientists (23KJ1498). M.S. acknowledges funding from the David and Lucille Packard Foundation through a Packard Fellowship for Science and Engineering. Spectroscopic instrumentation was supported by a generous gift from P. J. and M. M. Bender, NSF (CHE-1048642, CHE-1919350), and NIH (1S10OD020022-1, S10 OD012245). The Bruker Quazar APEX2 was purchased by the UW–Madison Department of Chemistry with a portion of a generous gift from P. J. and M. M. Bender. **Author contributions:** K.T., Z.K.W., and P.J.V. conceptualized the project. P.J.V., E.A.R., K.T., T.I., M.K., and M.S. designed and performed the experiments. P.M., R.L., and O.G. performed the theoretical modeling. P.J.V., E.A.R., O.G., and Z.K.W. wrote the manuscript. All authors edited and approved the manuscript. **Competing interests:** A US patent application has been filed on the technology described herein by P.J.V., Z.K.W., K.T., and E.A.R. under the following name: Reagents and Process for *Z*-selective Alkenyl C–H Functionalization. K.T. is currently employed by Corteva Agriscience. The authors declare no other competing interests. **Data and materials availability:** X-ray data are available free of charge from the Cambridge Crystallographic Data Centre under accession number CCDC 2379265. All other data and methodological details are in supplementary materials, including substrate preparation, cross-coupling procedures, product isolation and characterization, computational data, and NMR spectra.

SUPPLEMENTARY MATERIALS

science.org/doi/10.1126/science.adv7630
Materials and Methods; Supplementary Data; Figs. S1 to S26; Tables S1 to S18; References (*55–82*)

Submitted 6 January 2025; resubmitted 4 June 2025; accepted 25 July 2025

10.1126/science.adv7630

HUMAN GENETICS

Adaptations to water stress and pastoralism in the Turkana of northwest Kenya

A. J. Lea[1,2]*, I. V. Caldas[3], K. M. Garske[2,4,5], E. R. Gerlinger[4,5], J. P. Arroyo[6], J. Echwa[2], M. Gurven[7], C. Handley[8], J. C. Kahumbu[2,4,5], J. Kamau[9,10], P. Kinyua[2,11], F. Lotukoi[2], A. Lopurudoi[2], S. Lowasa[2], S. N. Njeru[11], R. Mallarino[12], D. J. Martins[2,13,14], P. W. Messer[3], C. Miano[2,5,11], B. Muhoya[2,4,5], J. Peng[4,5], T. Phung[7,8], J. D. Rabinowitz[5,15,16], A. Roichman[5,15], R. Siford[8], A. C. Stone[8,17,18], A. M. Taravella Oill[17,18], S. Mathew[8,17], M. A. Wilson[18,19], J. F. Ayroles[2,21]*

The Turkana pastoralists of Kenya inhabit arid, water-limited environments and rely largely on livestock for subsistence. Working with Turkana communities, we sequenced 367 whole genomes and identified eight regions with evidence for recent positive selection. One of these regions includes a putative regulatory element for *STC1*—a kidney-expressed gene involved in metabolism and the response to dehydration. We show that *STC1* is induced by antidiuretic hormone in human cells, is associated with urea levels in the Turkana themselves, and is under strong and recent selection in this population as well as a second East African population, the Daasanach. This work highlights how integrating anthropological and genomic approaches can lead to a new understanding of human physiology with biomedical relevance.

Humans inhabit an astounding variety of challenging habitats—from high-altitude plateaus to arctic tundras to scorching deserts. In many cases, natural selection has played a key role in sustaining human populations in extreme environments (*1*, *2*). For example, the hypoxic conditions experienced by Tibetans living at high altitudes have selected for changes in red blood cell production regulated by *EPAS1* (*3*), whereas the seafood-centered diets of Greenlandic Inuit have selected for changes in fatty acid metabolism regulated by the *FADS* gene cluster (*4*). Such examples highlight that, in addition to helping us understand our evolutionary history, studies of natural selection can uncover new genotype-phenotype links of biomedical importance. However, despite great interest in uncovering the genetic basis of adaptation, few studies have robustly linked ecological selection pressures, genetic variation, and human phenotypes (*2*).

To do so, we worked with the Turkana people of northwest Kenya, who live in environments that present several dietary and climatic challenges (Fig. 1, A and B). The Turkana are an Eastern Nilotic group, and like other members of their lineage, they originated in the Nile Valley region and began nomadic pastoralist practices ~5000 to ~8000 years ago (*5*, *6*). Oral histories suggest that the Turkana migrated from the Karamoja plateau highlands of Uganda to the more arid rift valley area of northwest Kenya 200 to 250 years ago. They managed the drier environment by further intensifying their reliance on livestock compared with other linguistically similar groups in the Karamojong cluster (*7*–*9*).

Although present-day Turkana pastoralists consume agricultural products obtained via trade and small-scale markets (e.g., maize, wheat flour, legumes, and sugar), the Turkana diet is overall rich in protein: previous studies have estimated that in certain areas and seasons, 70 to 80% of the diet is animal-derived (62% from milk and 8 to 18% from blood, marrow, and red meat) (*10*). Our dietary interviews with Turkana pastoralists revealed that 74% consumed blood several times per week, and 96.8% of individuals ate red meat at least once per week ($n = 346$; Fig. 1C and table S1).

The Turkana practice nomadic pastoralism because they inhabit extremely arid, water-limited (Fig. 1D) landscapes that cannot easily support agriculture, hunting and gathering, or other common subsistence strategies; instead, they effectively access transient rainfall and vegetation used by their livestock. To quantify the impact of water limitation, we interviewed Turkana pastoralists and found that water stress was a daily issue: 76% of Turkana spend more than a few hours a day collecting water, and 99% perceive this water to be insufficient in amount ($n = 311$; table S1). Using measures of urine-specific gravity, we also found that 89% of people meet the physiological criteria (*11*) for minimal (55%) or significant (34%) dehydration ($n = 175$; Fig. 1E and table S1), emphasizing the challenge of maintaining fluid balance in this environment.

Evidence of selection in Turkana genomes

We hypothesized that exposure to an animal product–rich diet and an arid ecology would select for genetic variants regulating metabolism and dehydration stress in the Turkana. To test this, we scanned for signatures of selection in 308 Turkana genomes sequenced at high (>20×, $n = 106$) and medium (~6×, $n = 202$) coverage. To understand population genetic parameters that could affect our analyses and interpretation, we also sequenced 59 genomes from nearby Kenyan and Ugandan groups, namely the El Molo, Ik, Karamojong, Masaai, Ngitepes (also known as Tepeth), Pokot, Rendille, and Samburu (fig. S1 and tables S2 and S3).

We genotyped 7,767,165 variants with a minor allele frequency >1% in our high-coverage Turkana dataset and then imputed missing data in the medium-coverage samples (Fig. 2A and fig. S2). We performed extensive quality control on our combined, imputed whole-genome sequencing (WGS) dataset (figs. S3 to S6), including corroborating our WGS-derived genotype calls using independent calls from the Infinium Global Screening Array (R^2 between WGS- and array-derived genotypes for 108 paired samples = 0.96 ± 0.03; table S4). Overall, population genetic analyses of the WGS dataset highlighted two key takeaways that were confirmed with the array dataset ($n = 783$ individuals total) and are consistent with the literature (*6*, *12*). First, there has been little European admixture in the East African groups we worked with (mean European ancestry proportion estimated by RFMix = 6.6 ± 4.4%; figs. S7 to S9 and table S5). Second, although they are culturally and linguistically distinct, the Turkana are similar at the genomic level to the Ik, Karamojong, Masaai, Ngitepes, and Pokot when examining common summary statistics (e.g., genotype PC loadings or F_{ST}; Fig. 2A; figs. S5, S8, and S10; and table S6).

[1]Department of Biological Sciences, Vanderbilt University, Nashville, TN, USA. [2]Turkana Health and Genomics Project, Turkana Basin Institute, Nairobi, Kenya. [3]Department of Computational Biology, Cornell University, Ithaca, NY, USA. [4]Department of Ecology and Evolutionary Biology, Princeton University, Princeton, NJ, USA. [5]Lewis Sigler Institute for Integrative Genomics, Princeton University, Princeton, NJ, USA. [6]Division of Nephrology and Hypertension, Department of Medicine, Vanderbilt University Medical Center, Nashville, TN, USA. [7]Department of Anthropology, University of California Santa Barbara, Santa Barbara, CA, USA. [8]School of Human Evolution and Social Change, Arizona State University, Tempe, AZ, USA. [9]Institute of Primate Research, National Museums of Kenya, Nairobi, Kenya. [10]Department of Biochemistry, School of Medicine, University of Nairobi, Nairobi, Kenya. [11]Center for Community Driven Research, Kenya Medical Research Institute, Kirinyaga, Kenya. [12]Department of Molecular Biology, Princeton University, Princeton, NJ, USA. [13]Turkana Basin Institute, Turkana, Kenya. [14]Department of Anthropology, Stony Brook University, Stony Brook, NY, USA. [15]Department of Chemistry, Princeton University, Princeton, NJ, USA. [16]Ludwig Institute for Cancer Research, Princeton University, Princeton, NJ, USA. [17]Institute of Human Origins, Arizona State University, Tempe, AZ, USA. [18]Center for Evolution and Medicine, Arizona State University, Tempe, AZ, USA. [19]School of Life Sciences, Arizona State University, Tempe, AZ, USA. [20]Comparative Genomics and Reproductive Health Section, Center for Genomics and Data Science Research, National Human Genome Research Institute, National Institutes of Health; Bethesda, MD, USA. [21]Department of Integrative Biology, University of California, Berkeley, Berkeley, CA, USA. ***Corresponding author. Email: amanda.j.lea@vanderbilt.edu (A.J.L.); ayroles@berkeley.edu (J.F.A.)**

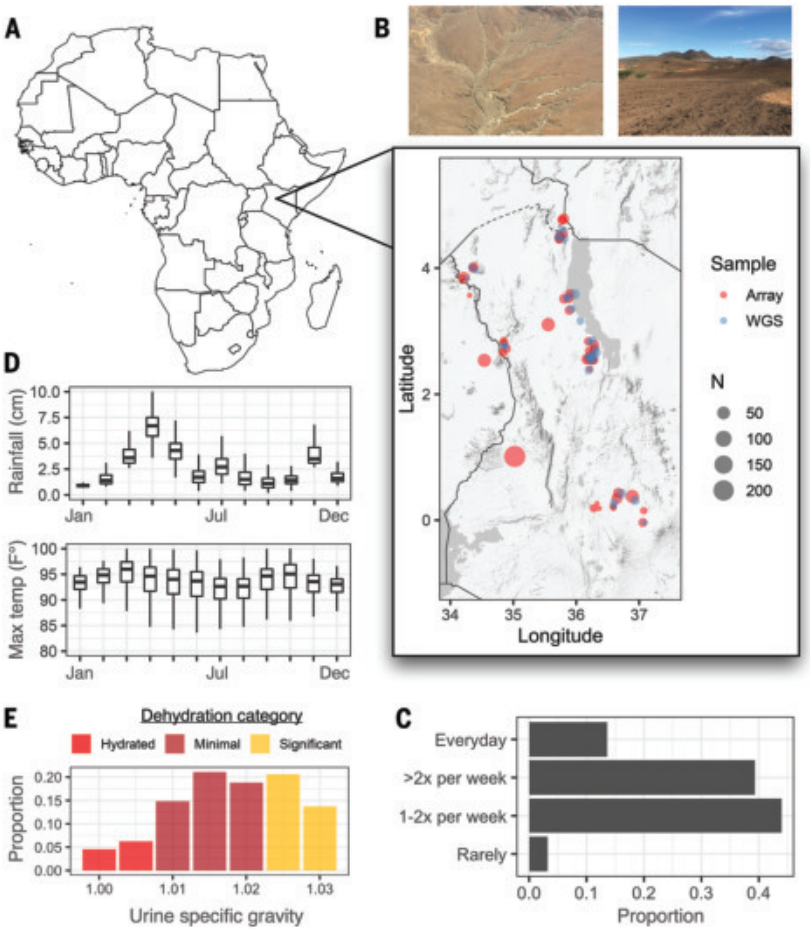

Fig. 1. Ecology and lifestyle of the Turkana people. (**A**) Map of Africa with an inset showing northwest Kenya (the present-day homelands of the Turkana people). Dots indicate where samples were collected for this study, for both WGS and array genotyping. (**B**) Representative photographs of the arid ecology of the Turkana region (photos taken by the authors). (**C**) Proportion of Turkana pastoralists in this study who consume meat at different self-reported frequencies ($N = 346$). (**D**) Average rainfall and maximum temperature for the Turkana country region by month. Data were sourced from WorldClim (*56*). (**E**) Proportion of Turkana pastoralists with different urine specific gravity values ($N = 175$), colored by whether each value meets the criteria for dehydration provided in (*11*).

To identify potential selective sweeps in the Turkana, we computed three statistics that rely on different assumptions and subsets of the data and that detect selection on the order of thousands to tens of thousands of years ago (*2*): (i) the integrated haplotype score (iHS) (*13*), computed on high-coverage Turkana genomes only; (ii) the population branch statistic (PBS) (*3*), computed on high- and medium-coverage Turkana genomes; and (iii) the XtX statistic (*14*), computed on all genomes. Additionally, our PBS and XtX analyses included the Luhya (East Africa) and Yoruba (West Africa) populations from the 1000 Genomes Project as outgroups ($n = 207$) (*15*). After computing all three statistics, we used a sliding-window approach to intersect the results and identified 13 50-kb outlier windows near eight genes (Fig. 2B and table S7). Two of these eight genes (*CCDC102B* and *SEMA6A*) were previously found to be under selection in the Maasai, a closely related Nilotic pastoralist group (*16*). To our knowledge, the rest have not been previously identified as targets of selection in humans.

When we investigated what phenotypes our candidate genes have been previously linked to by genome-wide association studies (GWASs), which have primarily focused on European ancestry cohorts, we found that they were enriched for a major predictor of cardiovascular disease—arterial stiffness [Fisher's exact test, odds ratio = 16.70, false discovery rate (FDR)–adjusted *P* value = 0.047]. Unexpectedly, they were also enriched for neurological biomarkers of Alzheimer's disease—namely, neurofibrillary tangles (odds ratio = 19.76, FDR-adjusted *P* value = 3.24×10^{-4}), PHF-tau (odds ratio = 5.68, FDR-adjusted *P* value = 0.079), and cortical surface area (odds ratio = 6.52, FDR-adjusted *P* value = 0.079; Fig. 2C and tables S8 and S9). In line with this observation, several of our candidate genes are most highly expressed in neurological cell types, such as inhibitory neurons, oligodendrocytes, and oligodendrocytes precursors (table S10).

Selection on *STC1*, a regulator of metabolic and renal system functions

Some of the strongest biological evidence from previous studies pointed to *STC1*, a gene that encodes a glycoprotein with autocrine and paracrine functions. Specifically, previous GWASs have linked *STC1* to (i) serum levels of urate, a waste product produced when the body breaks down purine-rich foods such as red meat; (ii) serum levels of urea and creatinine, two common biomarkers of kidney function; and (iii) estimated glomerular filtration rate, a measure of kidney health (*17*) (Fig. 2C and table S8). Beyond GWASs, *STC1* has been implicated in adaptation to challenging environments in multiple natural animal populations (*18*–*20*), and laboratory-based model organism studies have implicated *STC1* in the ability to suppress reactive oxygen species and reduce acute kidney injury (*21*, *22*), glucose homeostasis (*23*), and the response to dehydration. In particular, *STC1* transcription is induced up to eightfold in rodent kidneys after water deprivation (*24*), a response that is coordinated by antidiuretic hormone (ADH) (*25*) and involves *STC1*-based regulation of both rising hypertonicity and progressive hypovolemia (*26*). We replicated these results at the protein level, showing that *STC1* levels are higher in water-restricted versus control mouse kidneys (*t* test, *P* value = 6.74×10^{-3}; Fig. 2D and table S12). Given the clear involvement of *STC1* in metabolic and renal system traits of ecological relevance to the Turkana people, we prioritized this gene for follow-up analyses.

We identified two overlapping 50-kb candidate regions near *STC1*, with the collapsed 75-kb region located ~150 kb upstream of the transcription start site. This region was ranked first out of all tested regions by the iHS statistic and third by the PBS and XtX statistics (fig. S11 and table S7). Previously published high-throughput chromosome conformation capture (Hi-C) data from five tissues that express *STC1* (*27*) show that this regulatory region and the *STC1* gene body fall within the same topological domain (*28*) and are in consistent contact (*29*) (table S11, fig. S12). In our main tissue of interest, the kidney, *STC1* is highly specific to cell type and is expressed almost exclusively in the collecting duct (*30*, *31*). This structure is the final segment of the kidney to control fluid balance, accounting for ~5% of water reabsorption at baseline and up to ~25% during ADH surges induced by dehydration. When we analyzed ATAC-seq data previously generated from a mouse collecting duct cell line exposed versus unexposed to ADH (*32*), we found that our candidate region contained several differentially accessible, ADH-responsive regulatory elements (Fig. 2E). Although there is no human collecting duct cell line, we performed new experiments to show that *STC1* is induced by ADH in a human kidney (epithelial) cell line (linear model, *P* value for 10 and 25 nM = 0.033 and 0.0042, respectively; Fig. 2F and table S12).

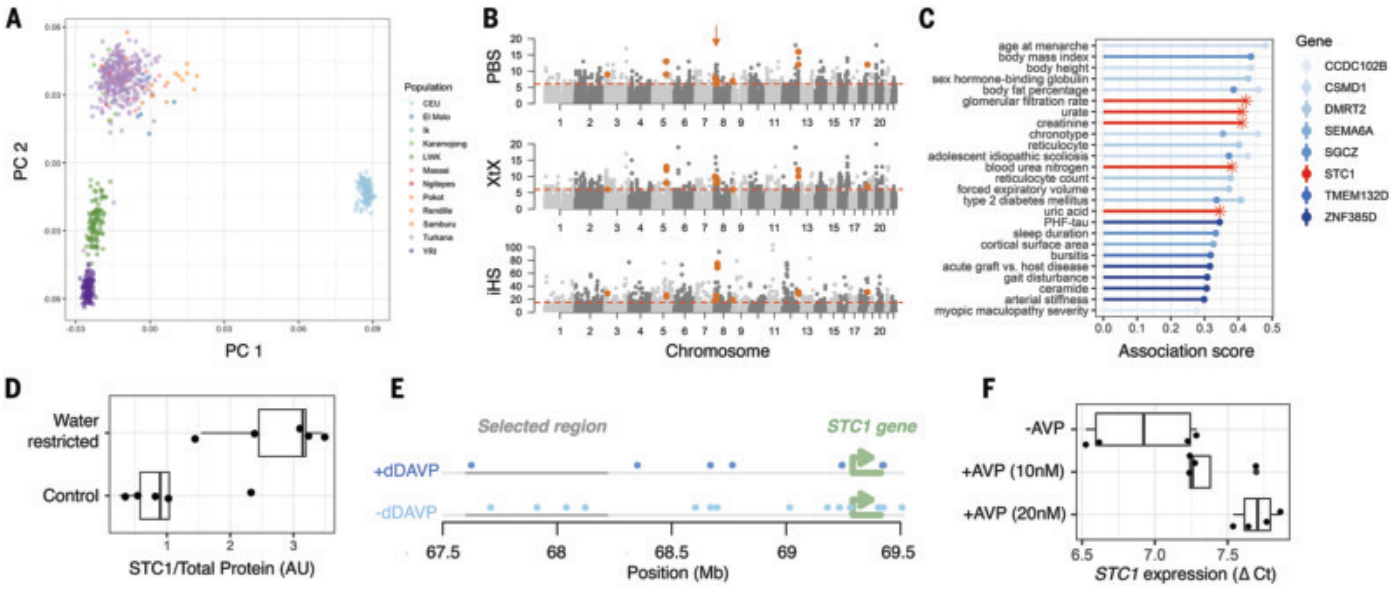

Fig. 2. Scans for selection and evidence for the *STC1* gene. (**A**) Principal components (PC) analysis comparing WGS data from the Turkana as well as other study communities to African populations included in the 1000 Genomes Study (*15*). CEU, Northern Europeans from Utah; LWK, Luhya in Kenya; YRI, Yoruba in Nigeria. (**B**) Number of PBS, XtX, and iHS outliers per 50-kb window. Red dotted lines represent the cutoff for the 99th percentile of each empirical distribution for each selection statistic. Windows that exceeded the 99th percentile for all three statistics are highlighted in red. The candidate region that falls near the *STC1* gene is highlighted with a red arrow. (**C**) Phenotypes associated with genes that fall in or near candidate regions. Phenotypic associations were sourced from the Open Targets Platform (*57*), and the association score (*y* axis) represents the aggregate evidence across all published studies for a gene-phenotype link. Only association scores >0.25 are plotted, and association scores involving the *STC1* gene are highlighted with an asterisk. (**D**) Normalized *STC1* protein concentrations in mouse kidneys after 24 hours of water restriction. (**E**) Open chromatin regions in mouse collecting duct cells exposed versus unexposed to desmopressin (dDAVP) (synthetic analog of vasopressin) (*32*). Coordinates are in mm10; open chromatin regions are highlighted in blue, and the *STC1* candidate region is highlighted in gray. (**F**) Quantitative polymerase chain reaction of *STC1* expression levels in human embryonic kidney 293 cells exposed versus unexposed to ADH (equivalent to AVP).

To further link our candidate region to kidney function, we measured serum creatinine and urea levels for 447 Turkana included in our genotyping array dataset. After subsetting to single-nucleotide polymorphisms (SNPs) within the *STC1* candidate region that passed our filters, we were able to test six SNPs typed on the array for associations with these outcomes; SNP density in the array dataset is sparse, and these six SNPs are thus expected to tag general haplotype structure (fig. S13). Using this approach, we found two SNPs that were significantly correlated with urea levels [linear mixed effects model, rs10107949 beta = 0.030 (FDR-adjusted *P* value = 0.059), rs75070347 beta = 0.040 (FDR-adjusted *P* value = 0.055); Fig. 3A and tables S13 and S14]. One of these SNPs falls on the same ~11.5-kb haplotype block as the top three derived SNPs with the strongest evidence for selection in the WGS dataset (rs6988698, rs7012892, and rs6994711; fig. S14). This haplotype block also contains several candidate regulatory elements in kidney [using ENCODE data and annotations (*33*); fig. S15]. Although further work is needed to identify the causal variant in the *STC1* region and the precise mechanism of action, we propose that these data, in aggregate, point toward selection on *STC1* regulation in the context of ADH induction, dehydration stress, and kidney function.

Evolutionary history of *STC1*

We next turned our attention toward understanding the evolutionary history of the *STC1* regulatory region, including the nature, strength, and timing of selection. We started by checking the worldwide allele frequencies of the top three derived SNPs with the strongest evidence for selection in the WGS dataset (derived allele frequency in Turkana for rs6988698 is 75%; rs7012892, 84%; and rs6994711, 84%). We found that these same SNPs are near invariant outside of Africa, with average minor allele frequencies of 2.66% (range = 0 to 8.65%; figs. S16 and S17 and table S15); for these three SNPs, the derived alleles are at high frequency outside of Africa, potentially resulting from genetic drift after the out-of-Africa bottleneck and highlighting the difficulty of interpreting selection signals in African populations with complex demographic histories. Within Africa, these three example variants have intermediate derived allele frequencies in non-Nilotic East African groups and at Turkana-like frequencies in the other East African groups we sampled (Fig. 3, C to E). The East African groups are almost all part of the same Nilotic lineage the Turkana belong to, which began pastoralist practices ~5000 to ~8000 years ago (*5*, *6*). Thus, we hypothesize that there was selection on standing variation within the Nilotic cluster starting sometime after pastoralist practices emerged.

To test this scenario, we estimated the site frequency spectrum for the Turkana and inferred their demographic history (figs. S18 and S19 and table S16). We then simulated genomic datasets under different evolutionary scenarios—varying the nature, strength, and timing of selection in the *STC1* region. We trained two separate convolutional neural networks (CNNs) with the same data: a regression model to infer sweep strength and a classification model to classify between three potential modes of selection (hard sweep, selection on recurrent new mutations, and selection on standing genetic variation) (*34*) (fig. S20). When applied to our real data, the CNNs inferred that selection on standing variation began ~348 generations ago (range, 187 to 571), with a selection coefficient of ~0.041 (range, 0.033 to 0.05; Fig. 3F and fig. S21). These estimates should be interpreted with caution, as they depend on assumptions about local demography and the unknown initial frequency of the selected alleles—parameters that remain poorly resolved. However, even under wide uncertainty, our

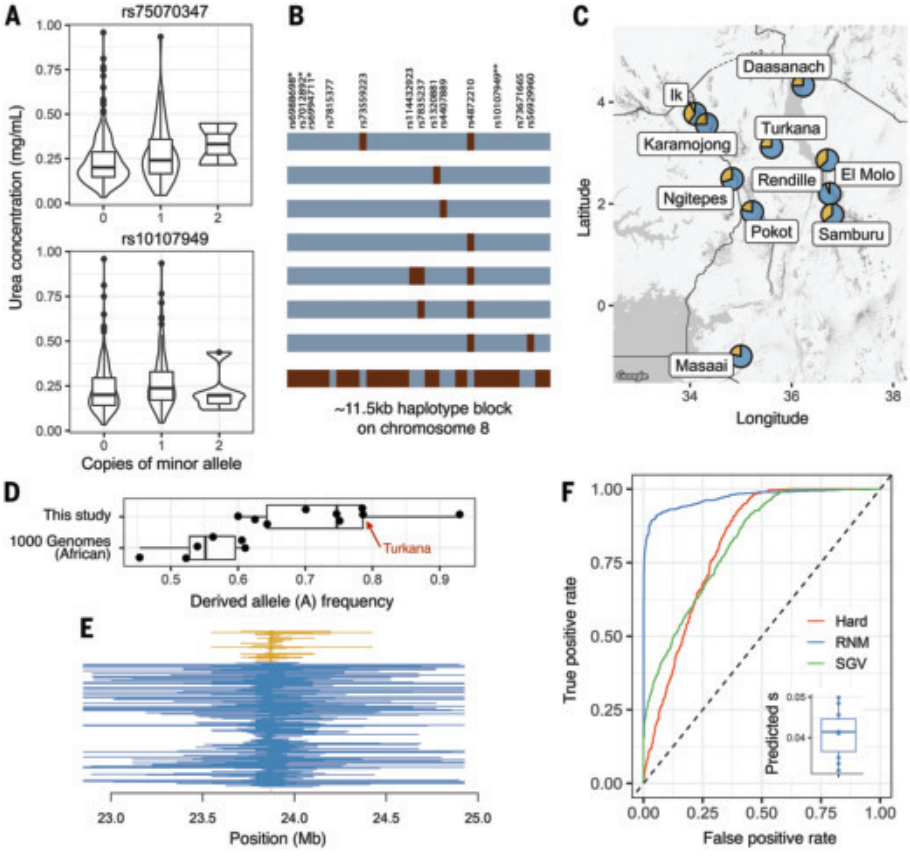

Fig. 3. Selection on genetic variation near the *STC1* gene. (**A**) Correlations between Turkana genotypes within the *STC1* region and serum urea levels (rs10107949: $R = 0.116$, FDR-adjusted P value = 0.059; rs75070347: $R = 0.130$, FDR-adjusted P value = 0.055). (**B**) Haplotype block 21, which is 11.5 kb (spanning chr8:23872028-23883577) and contains the three SNPs with the strongest evidence for selection (rs6988698, rs7012892, and rs6994711), as well as one SNP, rs10107949, which was found to be associated with urea levels in the Turkana. Dark colors indicate minor alleles, and light colors indicate major alleles. (**C**) Allele frequency for one of the strongest evidence SNPs (rs6988698) within data generated as part of this study. The map shows the frequency of the major or derived (blue) versus minor or ancestral (yellow) alleles. (**D**) Boxplot summarizing the frequency of rs6988698 in this study as well as African populations included in the 1000 Genomes Project (*15*). (**E**) Haplotype length at the rs6988698 SNP for individuals carrying the major or derived (blue) versus minor or ancestral (yellow) allele. Coordinates are in hg19. (**F**) Validation of the CNN used to infer sweep mode. Receiver operating characteristic (ROC) curves show the results of applying one CNN replicate on the simulated validation dataset. Each curve represents a one-versus-all comparison between the reference mode and all others combined; the area under each curve is given in parentheses. Hard, hard sweep [area under the ROC curve (AUC), 0.813; RNM, selection on recurrent new mutations (AUC, 0.971); SGV, selection on standing genetic variation (AUC, 0.819)]. Inset shows the results of applying 10 replicate CNNs to real data from the *STC1* locus, under the assumption that the selective sweep is codominant (see fig. S20 for results when the sweep is assumed to be dominant).

analyses suggest that selection was probably strong; for example, selection coefficient estimates for the malaria-protective Duffy (*35*) and lactase persistence (*36*, *37*) alleles range from 0.04 to 0.08 and 0.04 to 0.06, respectively. Our analyses also point toward an onset of selection sometime within the past ~7000 years. This timing overlaps with increasing aridification across East Africa (*38*) and the emergence of pastoralism in the region (*39*, *40*).

Selection on *STC1* in a Cushitic population, the Daasanach

Our CNN analyses indicated that the *STC1* haplotype of interest was likely segregating in East Africa before the Nilotic lineage split with the Eastern Cushitic lineage (speaking Afro-Asiatic rather than Nilo-Saharan languages). Both lineages are thought to have originated in the Nile Valley region but diverged during their distinct migrations to present-day Kenya and Ethiopia (*41*–*44*). Thus, we wondered whether there was also evidence for selection on *STC1* within this separate lineage, which has similarly inhabited arid regions around the horn of Africa and practiced a pastoralist lifestyle (*45*, *46*). To do so, we worked with Daasanach communities on the east side of Lake Turkana, where ongoing work suggests a complex, and potentially compensatory, relationship between water stress and hydration status (*47*–*49*). We generated WGS data from 95 Daasanach participants and tested for signatures of selection on chromosome 8 (which contains *STC1*). We found that the same region upstream of *STC1* identified in the Turkana is also an iHS outlier in the Daasanach (fig. S22 and table S17). This finding suggests that the regulatory region upstream of *STC1* has been under selection in both lineages.

Polygenic selection on metabolic and renal system biomarkers

Although selective sweeps—such as the one we have detected near *STC1*—are undoubtedly important in human evolution (*2*), complex traits are more commonly shaped by weak but simultaneous selection on numerous genetic variants (*50*). We were therefore motivated to also explore the contribution of polygenic adaptation to metabolic and renal system traits in the Turkana. To do so, we collapsed our three selection statistics into a Fisher's combined score (FCS) and assessed whether regions previously associated with 29 biomarkers (via multi-ancestry GWASs in the UK Biobank) exhibited higher mean FCS scores in the Turkana than expected by chance (*51*). These analyses revealed evidence of polygenic selection on metabolic biomarkers, such as triglycerides, cholesterol, and HbA1c, as well as renal system biomarkers, such as uric acid and cystatin C (all FDR < 5%; Fig. 4A and table S18). These results suggest that there has been diffuse, genome-wide selection on metabolism and kidney function in the Turkana, in addition to the localized signal we uncovered at *STC1*.

Lifestyle change and the fate of selected alleles

Although many Turkana still practice nomadic pastoralism in northwest Kenya and thus experience the ecological selection pressures we have highlighted here, subsets of the population are undergoing different types and degrees of market integration, urbanization, and acculturation. In recent decades, some Turkana have stopped practicing pastoralism but continue to live in rural environments in northwest Kenya, whereas others have migrated to urban areas in favor of wage labor jobs. Not surprisingly, moving to a city represents a major environmental shift: for example, whereas >90% of pastoralists regularly consume blood, milk, and red meat, these numbers drop to 0, 47, and 31%, in urban areas where large portions of the diet are instead market-derived (*52*, *53*) (Fig. 4B).

This ongoing lifestyle shift is relevant to our evolutionary genomic analyses because it sets the Turkana up for "evolutionary mismatch" (*54*). This occurs when previously advantageous variants, selected for in past ecologies, are placed in novel environments where they instead

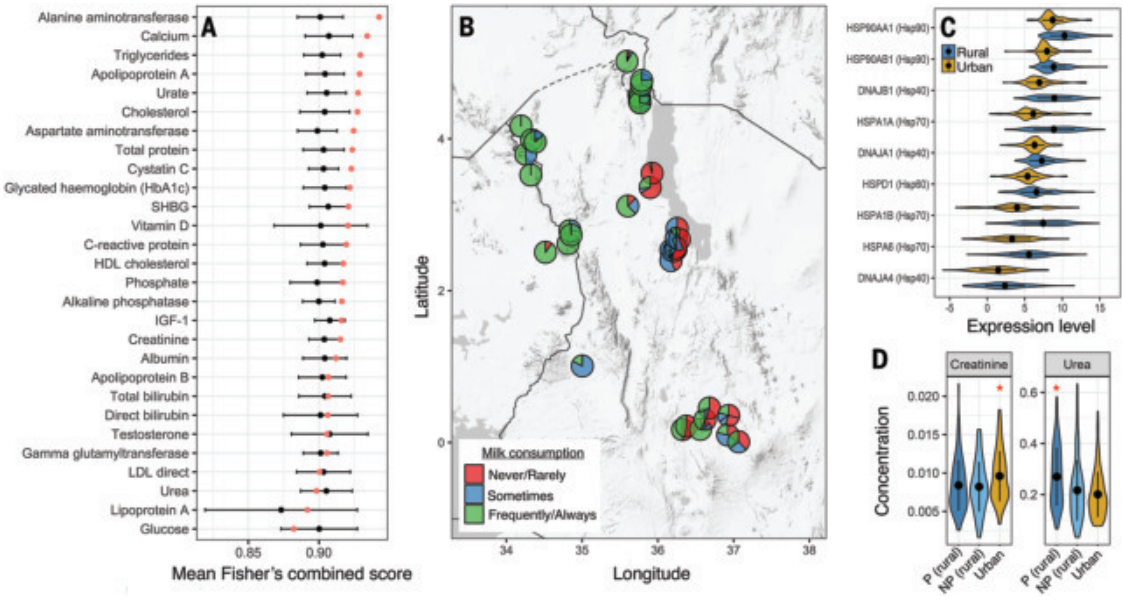

Fig. 4. Polygenic selection and lifestyle change. (**A**) Red dots represent the mean FCS (representing a composite of all three selection statistics) for each 50-kb window that contained a SNP associated with the focal trait (associations were sourced from multi-ancestry GWASs in the UK Biobank). Boxplots show the FCS distribution for 10,000 randomly sampled windows matched for SNP density, recombination rate, and background selection. HDL, high-density lipoprotein; LDL, low-density lipoprotein; SHBG, sex hormone–binding globulin. (**B**) Self-reported milk consumption summarized by location (for Turkana individuals only). (**C**) Normalized gene expression levels for samples collected from Turkana individuals in rural versus urban locations. Because of small sample sizes, the rural category includes pastoralist and nonpastoralist individuals (*52*); results are qualitatively similar when they are split (fig. S24). Plot includes all heat shock proteins in the "response to heat" gene ontology category that were significantly differentially expressed at a 5% FDR. (**D**) Serum concentrations of urea (mg/mL) and creatinine (mg/mL) for rural pastoralists (P), rural nonpastoralists (NP), and urban individuals. Red asterisks indicate groups that were significantly different from the other two (FDR < 5%).

have detrimental effects. In line with this idea, we have previously shown that transitions from pastoralist to urban lifestyles are associated with increases in biomarkers of cardiovascular disease risk (*52*). We generated new data on (i) serum urea and creatinine levels and found that both kidney function biomarkers also differ between urban and rural-pastoralist settings ($n = 447$, all FDR < 5%; Fig. 4D and table S14), as well as (ii) blood gene expression levels and found that genes involved in biological processes such as "response to heat," "protein folding," and "inflammatory response" are differentially regulated between urban and rural-pastoralist individuals ($n = 230$, all FDR < 5%; Fig. 4C, fig. S23, and tables S19 and S20). Furthermore, we found that SNPs that fall near genes differentially expressed by lifestyle exhibit more evidence for selection than SNPs near genes unaffected by lifestyle change (linear model P values: iHS < 2×10^{-16}, PBS = 0.007, and XtX = 0.0211; tables S21 and S22). This result suggests that past adaptations are poised to interact with the environmental and physiological shifts the Turkana are currently experiencing.

Conclusions

We integrated anthropological, biological, and genomic datasets to show that an arid ecology combined with pastoralist practices has likely led to selection on *STC1* in the Turkana; this signal appears to be shared across other groups in the region, as emphasized by our work with the Daasanach. Although we do not know the causal, selected allele at this time or the specifics of when and how the allele underwent selection, we show that the *STC1* gene is induced by ADH in human cells, that *STC1* variants are linked to urea levels in the Turkana themselves, and that selection likely occurred on standing variation near *STC1* on an ecologically plausible time scale. We also shed rare empirical light on the popular evolutionary mismatch hypothesis, which is commonly invoked to explain the high rates of noncommunicable, "lifestyle" diseases observed in Western countries (*55*). Our work highlights that partnerships with transitioning populations can lead to new models for understanding how present-day environments interact with past adaptations to influence disease risk.

REFERENCES AND NOTES

1. M. L. Benton *et al.*, *Nat. Rev. Genet.* **22**, 269–283 (2021).
2. S. Fan, M. E. B. Hansen, Y. Lo, S. A. Tishkoff, *Science* **354**, 54–59 (2016).
3. X. Yi *et al.*, *Science* **329**, 75–78 (2010).
4. M. Fumagalli *et al.*, *Science* **349**, 1343–1347 (2015).
5. O. Hanotte *et al.*, *Science* **296**, 336–339 (2002).
6. P. Triska *et al.*, *Genome Biol. Evol.* **7**, 3484–3495 (2015).
7. B. L. Korobe, *J. Afr. Interdiscip. Stud.* **7**, 29–67 (2023).
8. P. H. Gulliver, *The Family Herds: A Study of Two Pastoral Tribes in East Africa, The Jie and Turkana* (Routledge, 2013).
9. J. Lamphear, *J. Afr. Hist.* **29**, 27–39 (1988).
10. K. A. Galvin, *Am. J. Hum. Biol.* **4**, 209–221 (1992).
11. D. J. Casa *et al.*, *J. Athl. Train.* **35**, 212–224 (2000).
12. S. A. Tishkoff *et al.*, *Science* **324**, 1035–1044 (2009).
13. B. F. Voight, S. Kudaravalli, X. Wen, J. K. Pritchard, *PLOS Biol.* **4**, e72 (2006).
14. T. Günther, G. Coop, *Genetics* **195**, 205–220 (2013).
15. The 1000 Genomes Project Consortium, *Nature* **491,** 56 –65 (2012).
16. K. Wagh *et al.*, *PLOS ONE* **7**, e44751 (2012).
17. G. B. Loeb *et al.*, *Nat. Genet.* **56**, 2078–2092 (2024).
18. C.-L. Zhang *et al.*, *Sci. Rep.* **12**, 12264 (2022).
19. S. A. Rahmatalla *et al.*, *BMC Genet.* **18**, 92 (2017).
20. L. Kordonowy, M. MacManes, *BMC Genomics* **18**, 473 (2017).
21. L. Huang *et al.*, *Kidney Int.* **82**, 867–877 (2012).
22. J. S.-C. Pan *et al.*, *J. Am. Soc. Nephrol.* **26**, 364–378 (2015).
23. V. Schein *et al.*, *Mol. Cell. Endocrinol.* **414**, 1–8 (2015).
24. J. Turner, O. Sazonova, H. Wang, A. Pozzi, G. F. Wagner, *Mol. Cell. Endocrinol.* **328**, 8–15 (2010).
25. A. Y. Law *et al.*, *Mol. Cell. Endocrinol.* **348**, 183–188 (2012).
26. J. Turner, *Mol. Cell. Endocrinol.* **331**, 150–157 (2011).
27. A. Battle *et al.*, *Nature* **550**, 204–213 (2017).
28. J. R. Dixon *et al.*, *Nature* **485**, 376–380 (2012).
29. Y. Wang *et al.*, *Genome Biol.* **19**, 151 (2018).
30. J. Park *et al.*, *Science* **360**, 758–763 (2018).
31. Y. Muto *et al.*, *Nat. Commun.* **12**, 2190 (2021).

32. H. J. Jung, V. Raghuram, J. W. Lee, M. A. Knepper, *J. Am. Soc. Nephrol.* **29**, 1490–1500 (2018).
33. J. E. Moore *et al.*, *Nature* **583**, 699–710 (2020).
34. I. V. Caldas, A. G. Clark, P. W. Messer, bioRxiv 2022.07.19.500702 [Preprint] (2022). https://doi.org/10.1101/2022.07.19.500702
35. I. Hamid, K. L. Korunes, S. Beleza, A. Goldberg, *eLife* **10**, e63177 (2021).
36. J. Burger *et al.*, *Curr. Biol.* **30**, 4307–4315.e13 (2020).
37. L. Ségurel, C. Bon, *Annu. Rev. Genomics Hum. Genet.* **18**, 297–319 (2017).
38. J. E. Tierney, P. B. deMenocal, *Science* **342**, 843–846 (2013).
39. E. A. Hildebrand *et al.*, *Proc. Natl. Acad. Sci. U.S.A.* **115**, 8942–8947 (2018).
40. F. Marshall, E. Hildebrand, *J. World Prehist.* **16**, 99–143 (2002).
41. A. J. Ahmed, Ed., *The Invention of Somalia* (Red Sea Press, 1995).
42. C. Ehret, *Southern Nilotic History* (Northwestern Univ. Press, 2019).
43. B. M. Lynch, L. H. Robbins, *J. Afr. Hist.* **20**, 319–328 (1979).
44. W. S. Nasong'o, M. N. Amutabi, T. Falola, Eds., *The Palgrave Handbook of Kenyan History* (Springer International Publishing, ed. 1, 2024).
45. E. S. Poloni *et al.*, *Ann. Hum. Genet.* **73**, 582–600 (2009).
46. R. Blench, in *L'Homme et l'animal. Dans le bassin du lac Tchad*,C. Baroin, J. Boutrais, Eds. (Institut de recherche pour le développement, 1999), pp. 39–80.
47. L. Ford *et al.*, *Water Int.* **48**, 63–86 (2023).
48. A. Y. Rosinger *et al.*, *Am. J. Hum. Biol.* **34**, e23715 (2022).
49. H. J. Bethancourt *et al.*, *Am. J. Hum. Biol.* **33**, e23447 (2021).
50. E. A. Boyle, Y. I. Li, J. K. Pritchard, *Cell* **169**, 1177–1186 (2017).
51. M. Lopez *et al.*, *Curr. Biol.* **29**, 2926–2935.e4 (2019).
52. A. J. Lea, D. Martins, J. Kamau, M. Gurven, J. F. Ayroles, *Sci. Adv.* **6**, eabb1430 (2020).
53. A. J. Lea *et al.*, *Evol. Med. Public Health* **9**, 406–419 (2021).
54. D. E. Lieberman, *The Story of the Human Body: Evolution, Health, and Disease* (2013).
55. A. J. Lea *et al.*, *PLOS Biol.* **21**, e3002311 (2023).
56. S. E. Fick, R. J. Hijmans, *Int. J. Climatol.* **37**, 4302–4315 (2017).
57. D. Ochoa *et al.*, *Nucleic Acids Res.* **49**, D1302–D1310 (2021).
58. A. Lea, election_19May25_v2, Version v1.0.1, Zenodo (2025); https://doi.org/10.5281/zenodo.15468316.
59. A. Lea, Genotype calls from whole genome sequencing: Turkana high coverage samples, Zenodo (2025); https://doi.org/10.5281/zenodo.16588211.
60. A. Lea, Genotype calls from whole genome sequencing: Turkana high coverage samples, Zenodo (2025); https://doi.org/10.5281/zenodo.16556999.

ACKNOWLEDGMENTS

We thank previous members of the Turkana Health and Genomics Project for their contributions, especially S. Lowasa, D. Mukhongo, S. Ngatia, E. Loowoth, and M. Ndegwa. We are also grateful to the staff of the Turkana Basin Institute and the Mpala Research Centre for their support. We thank our research assistants affiliated with the Arizona State University team for aiding with data collection: E. Carlystus, A. Lotiira, C. Muya, G. Topos, and D. Lomelu. The authors acknowledge Research Computing at Arizona State University for providing high-performance computing resources that have contributed to the research results. The National Museums of Kenya provided institutional support to conduct the research in Kenya. We thank W. Tong and J. Grenier for scientific discussions. We thank I. Wallace for thoughtful comments on a previous version of the manuscript. Above all else, we thank our participants and host communities for their hospitality, feedback, and for their continued support in this work. **Funding:** This work was funded by internal awards from Princeton University to J.F.A., The John Templeton Foundation (grant 48952 to S.M.), The National Institute of General Medical Sciences of the National Institutes of Health (NIH) (R35GM124827 to M.A.W. and R35GM147267 to A.J.L.), and The National Institute of Environmental Health Sciences of the NIH (F32ES034668 to K.M.G.). It was also supported, in part, by the Intramural Research Program of the National Human Genome Research Institute, National Institutes of Health. A.M.T.O. was supported by The Graduate College at Arizona State University, The Achievement Rewards for College Scientists Foundation Phoenix Chapter as a Pierson Scholar, and Arizona State University Sigma Xi. A.J.L. was also supported by the Helen Hay Whitney Foundation, a Searle Scholars Award from the Kinship Foundation, and an Azrieli Global Scholars Award from the Canadian Institute for Advanced Research. **Author contributions:** Conceptualization: A.J.L. and J.F.A. Data curation: A.J.L., J.E., K.M.G., J.K., and B.M. Formal analysis: A.J.L., I.V.C., E.R.G., C.H., P.K., S.L., T.P., R.S., and J.F.A. Funding acquisition: A.J.L., A.C.S., S.M., M.A.W., and J.F.A. Investigation: Field – A.J.L., K.M.G., C.H., S.M., R.D., C.M., J.K., B.M., J.P., J.D.R., A.R., and J.F.A.; Lab – A.J.L., J.E., J.K., F.L., D.M., C.M., R.M., B.M., and J.F.A. Methodology: A.J.L., I.V.C., and P.W.M. Project administration: A.J.L., S.N.N., D.M., and J.F.A. Resources: A.C.S., S.M., and M.A.W. Visualization: A.J.L. and I.V.C. Writing – original draft: A.J.L. and J.F.A. Writing – review & editing: A.J.L., I.V.C., K.M.G., E.R.G., M.G., C.H., J.K., S.N.N., R.D., R.M., D.M., P.W.M., P.K., S.L., T.P., R.S., A.C.S., S.M., and M.A.W. **Diversity, equity, ethics, and inclusion:** This work is the result of several long-term collaborations with Turkana communities as well as other groups in the region, built on mutual respect and shared investment in the research process. Our research teams include Kenyan scientists and students, and our study was shaped by years of conversation with local leaders, health workers, and participants. **Competing interests:** The authors declare that they have no competing interests. **Data and materials availability:** The genomic data generated in this study have been submitted to (i) the NIH database of Genotypes and Phenotypes (dbGaP) under accession number phs002219.v1.p1 and (ii) Zenodo (*58*–*60*). Analysis code is available at https://github.com/AmandaJLea/Turkana_selection; https://github.com/SexChrLab/Kenya_Selection_and_Demography/tree/master/Population_History; and https://github.com/ayroles-lab/turkana-stc1. The analysis code has also been deposited at Zenodo (*58*). Raw immunoblotting images and communication materials used to return results to study participants are also available at https://github.com/AmandaJLea/Turkana_selection as well as Zenodo (*58*). **License information:** Copyright © 2025 the authors, some rights reserved; exclusive licensee American Association for the Advancement of Science. No claim to original US government works. https://www.science.org/about/science-licenses-journal-article-reuse

SUPPLEMENTARY MATERIALS

science.org/doi/10.1126/science.adv2467
Materials and Methods; Figs. S1 to S24; Tables S1 to S22; References (*61*–*126*)

Submitted 11 December 2024; accepted 30 July 2025

10.1126/science.adv2467

ELECTROCHEMISTRY

High-capacity, reversible hydrogen storage using H^--conducting solid electrolytes

Takashi Hirose[1,2], Naoki Matsui[2]*, Takashi Itoh[1], Yoyo Hinuma[2,3], Kazutaka Ikeda[4,5], Kazuma Gotoh[6], Guangzhong Jiang[2], Kota Suzuki[1,2], Masaaki Hirayama[1,2], Ryoji Kanno[2]*

Hydrogen absorption and desorption in solids are pivotal reactions involved in batteries and hydrogen storage devices. However, conventional thermodynamic and electrochemical hydrogen storage using high-capacity materials suffers from high hydrogen-desorption temperatures and instability of electrolytes. In this work, we explored electrochemical hydride ion (H^-)–driven hydrogen storage and developed a solid electrolyte, anti–α-AgI–type $Ba_{0.5}Ca_{0.35}Na_{0.15}H_{1.85}$, which exhibits excellent H^- conductivity and electrochemical stability. This electrolyte is compatible with several metal-hydrogen electrodes, such as titanim hydride and magnesium hydride (MgH_2), allowing for high-capacity, reversible hydrogen storage at low temperatures. Specifically, Mg–H_2 cells operating as hydrogen storage devices ($Mg + H_2 \rightleftarrows MgH_2$) achieved a reversible capacity of 2030 milliampere hours per gram at 90°C, offering safe and efficient hydrogen-electricity conversion and hydrogen storage devices.

Hydrogen is considered an ideal energy carrier owing to its high abundance and low molecular weight. However, hydrogen storage in high-pressure gas tanks as liquid hydrogen presents numerous challenges (*1*), with the main drawback being critical safety issues. Hydrogen storage alloys have been extensively explored to safely store hydrogen in the solid state using thermodynamic or electrochemical means. Among these, thermodynamic hydrogen storage is the most representative method, but it is limited by the availability of high-capacity materials that can effectively store or release hydrogen at reasonably low temperatures: $LaNi_5$ has a low hydrogen storage capacity (1.4 wt %) despite its ability to operate near room temperature (*2*). By contrast, light-element metal hydrides, such as MgH_2, LiH, and $LiBH_4$, although having high theoretical storage capacities, suffer from low effective capacities and high operation temperatures (>300°C) (*3*). On the other hand, electrochemical hydrogen storage relies on external voltages to store and release hydrogen through protons (H^+) or hydride ions (H^-, the anionic state of hydrogen). For proton-based electrochemical storage, either an alkaline or acidic aqueous solution serves as the electrolyte, facilitating the movement of protons in and out of the hydrogen storage material (*4*–*6*). This approach is used in the electrode reaction of Ni–metal hydride (MH) batteries; however, it exhibits several drawbacks, such as slow reaction kinetics and irreversible capacity loss in high-capacity materials (e.g., MgH_2) owing to electrode corrosion and dissolution in the electrolyte (*7*).

Electrochemical hydrogen storage based on hydride ions was proposed in 1985 by Huggins *et al*., who attempted to insert hydride ions into a metal using an ionic-liquid electrolyte containing dissolved H^- (*8*). However, this direction was not pursued further because of the high-temperature operating conditions (>300°C) (*9*). In recent years, H^--conducting solid electrolytes have been explored as an alternative media for electrochemical hydrogen storage (*10*, *11*). Hydride ions offer the advantage of high mobility because of their low charge density, moderate ionic radius ($r \approx 1.4$ Å) (*12*), and high polarizability ($\alpha \approx 1.8$ Å^3) (*13*). However, the performance of reported solid-state hydride-ion conductors is not satisfactory for use in H^--based electrochemical devices, such as hydride batteries. For example, the low ionic conductivity of the La_2LiHO_3 electrolyte necessitates high cell operating temperatures (300°C), which results in poor reversibility and low discharge capacities due to side reactions (*10*). More recently, LaH_3-based hydrides and oxyhydrides have been reported to exhibit high ionic conductivities of 10^{-4} to 10^{-2} S cm^{-1} at room temperature (*11*, *14*–*16*). However, the Ti–TiH_2 asymmetric cells using the LaH_x and $La_{0.8}Sr_{0.2}H_{2.8-2x}O_x$ as the electrolytes only delivered low and irreversible discharge capacities of 414 and 1120 mAh g^{-1}, respectively, presumably because of the electrolyte reduction during operation.

In this study, we developed a new hydride-ion conductor with high electrochemical stability and ionic conductivity by exploring the compositional space of the pseudoternary BaH_2–CaH_2–NaH system. The CaH_2 and BaH_2 end members are electrochemically stable with respect to their lower reaction potentials of −0.113 and −0.006 V versus Ti/TiH_2, respectively (table S1; see supporting note 1 for details), compared with other metal hydrides, such as LaH_3, whereas NaH was chosen as the third end member to allow the amount of hydrogen per metal to be varied. Although BaH_2 and CaH_2 have orthorhombic cotunnite–type structures (space group *Pnma*), the x-ray diffraction (XRD) patterns of the $Ba_{1-x-y}Ca_xNa_yH_{2-y}$ samples with $0.25 \le x \le 0.9$ and $0.05 \le y \le 0.375$ indicated that these compositions have a body-centered cubic (bcc) framework with space group *Im3m* (Fig. 1A and fig. S1, A and B). Figure 1B shows the formation range of this *Im3m* phase overlaid on the BaH_2–CaH_2–NaH ternary diagram, showing that three cations and $1.625 \le n < 2$, where n is the anion/cation ratio in MX_n, are necessary. The experimental ionic conductivity of these species was distinctly high ($\sigma \approx 10^{-5}$ S cm^{-1} at 50°C) and reached a maximum of 4.8×10^{-5} S cm^{-1} for $Ba_{0.5}Ca_{0.35}Na_{0.15}H_{1.85}$ (Fig. 1C). Transmission electron microscopy (TEM) (fig. S2A) revealed that the particle size of $Ba_{0.5}Ca_{0.35}Na_{0.15}H_{1.85}$ is approximately 400 nm. Energy-dispersive x-ray (EDX) spectroscopy (fig. S2, B to D) verified that the experimental composition agrees with the nominal ratio (Ba:Ca:Na = 0.51:0.37:0.12 and 0.5:0.35:0.15).

Neutron diffraction was used to determine hydrogen positions in the structure, and samples were deuterated to avoid the background noise arising from incoherent scattering of light hydrogen. Figure 1D shows the crystal structure of $Ba_{0.5}Ca_{0.35}Na_{0.15}D_{1.85}$ determined by Rietveld refinement of neutron diffraction data (see fig. S1, C and D, and table S2 for the Rietveld refinement results). In this structure, the Ba, Ca, and Na atoms randomly occupy the body-centered positions (2*a*), whereas D occupies the two distinct sites, 12*d* and 6*b*, corresponding to the centers of the DM_4 tetrahedra and DM_6 octahedra (M = $Ba_{0.5}Ca_{0.35}Na_{0.15}$), respectively (Fig. 1E). The experimental data were well fitted (weighted-profile R factor $R_{wp} = 1.6\%$) by a structural model with deuterium at both the 12*d* [occupancy = 0.1651(3)] and 6*b* [occupancy = 0.2865(6)] sites. Therefore, $Ba_{0.5}Ca_{0.35}Na_{0.15}H_{1.85}$ was concluded to have an anti–α-AgI–type structure, typical of superionic conductors (*17*). For a comprehensive discussion of diffusion pathways, molecular dynamics (MD) simulations were performed using a message-passing neural network (MPNN) potential (fig. S3, A and B). This approach allowed for long simulation time (1 ns) and a lower temperature range (300 to 700 K) (fig. S3, C and D), which is close to the range of experimental conductivity measurements. The hydrogen probability density obtained from the MD trajectories (Fig. 1, F and G) indicates that hydrogen atoms occupy not only tetrahedral sites (corresponding to silver positions in α-AgI) within the bcc framework but also octahedral sites, aligning with the neutron

[1]Department of Chemical Science and Engineering, School of Materials and Chemical Technology, Institute of Science Tokyo, 4259 Nagatsuta, Midori–ku, Yokohama, Japan. [2]Research Center for All–Solid–State Battery, Institute of Integrated Research, Institute of Science Tokyo, 4259 Nagatsuta, Midori–ku, Yokohama, Japan. [3]Department of Energy and Environment, National Institute of Advanced Industrial Science and Technology (AIST), 1–8–31, Midorigaoka, Ikeda, Japan. [4]Institute of Materials Structure Science (IMSS), High Energy Accelerator Research Organization, 203–1 Shirakata, Tokai, Ibaraki, Japan. [5]Neutron Industrial Application Promotion Center, Comprehensive Research Organization for Science and Society (CROSS), 162–1 Shirakata, Tokai, Ibaraki, Japan. [6]Center for Nano Materials and Technology (CNMT), Japan Advanced Institute of Science and Technology (JAIST), 1–1 Asahidai, Nomi, Ishikawa, Japan.
***Corresponding author. Email: matsui.n.ee49@m.isct.ac.jp (N.M.); kanno.r.ade9@m.isct.ac.jp (R.K.)**

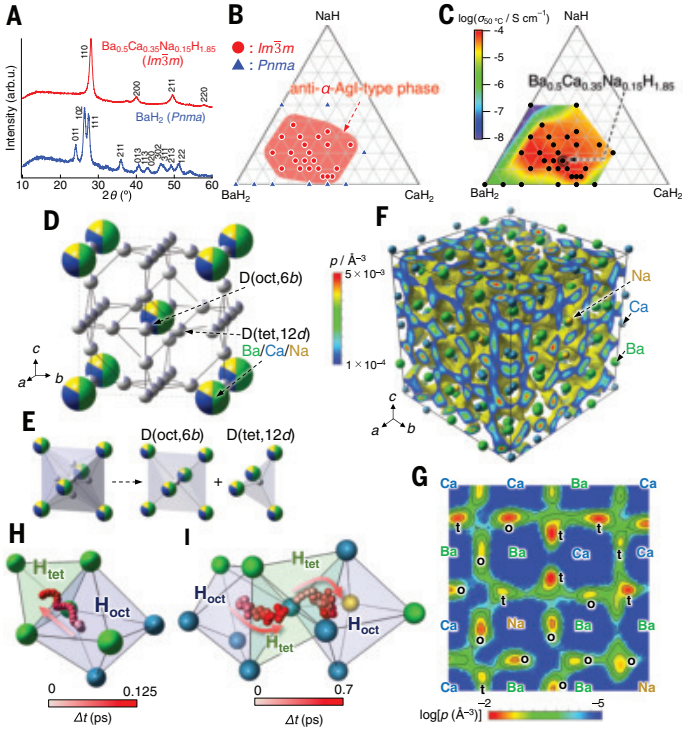

Fig. 1. Structural analysis of the BaH_2–CaH_2–NaH system. (**A**) XRD patterns of BaH_2 (blue) and $Ba_{0.5}Ca_{0.35}Na_{0.15}H_{1.85}$ (red). (**B**) Formation diagram of the cubic *Im*3*m* (red circles) and orthorhombic *Pnma* (blue triangles) phases in the BaH_2–CaH_2–NaH system. Arb. u., arbitrary units. (**C**) Heat map of the logarithm of ionic conductivity (σ) at 50°C in the BaH_2–CaH_2–NaH pseudoternary diagram. (**D**) Refined crystal structure of $Ba_{0.5}Ca_{0.35}Na_{0.15}D_{1.85}$. The green, blue, yellow, and gray spheres correspond to the Ba, Ca, Na, and D atoms, respectively. (**E**) Coordination of *M* ($Ba_{0.5}Ca_{0.35}Na_{0.15}$) toward D(6*b*) in DM_6 octahedra and D(12*d*) in DM_4 tetrahedra. (**F**) Three-dimensional isosurface plots of the probability density of hydrogen in the 4 × 4 × 4 supercell obtained through MPNN–MD simulations at 600 K. The isosurface of 1×10^{-4} Å^{-3} is depicted in yellow. The heat maps displayed on the lattice sections illustrate the probability densities ranging from 1×10^{-4} to 5×10^{-3} Å^{-3}. (**G**) Contour plots showing hydrogen probability density at $z = 0.75$ in the cross-section obtained through MPNN–MD simulations. The o and t symbols denote the octahedral (6*b*) and tetrahedral (12*d*) sites, respectively. The probability densities are presented on a log scale from 10^{-2} to 10^{-5} Å^{-3}, with contour plot intervals of 0.5 in logarithmic scale. (**H** and **I**) Hydrogen migration trajectories obtained through MPNN–MD simulations at 400 K. Hydrogen atoms were visualized using a white-red color gradient corresponding to elapsed simulation time (Δ*t*).

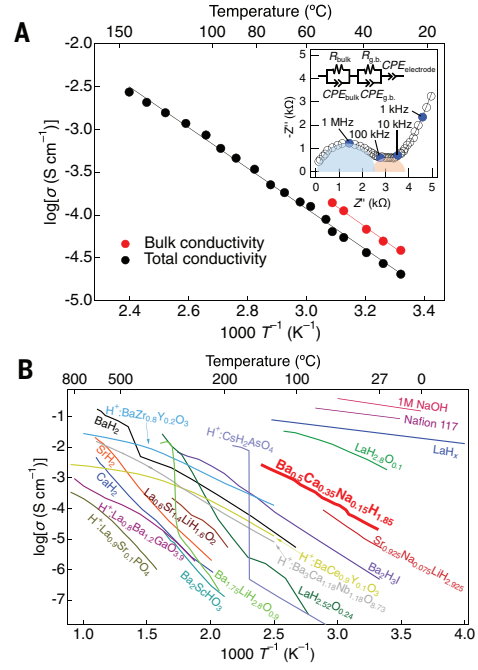

Fig. 2. Ionic conductivity of $Ba_{0.5}Ca_{0.35}Na_{0.15}H_{1.85}$. (**A**) Arrhenius plots of the ionic conductivity of cold-pressed $Ba_{0.5}Ca_{0.35}Na_{0.15}H_{1.85}$. The red and black circles indicate the bulk and total (bulk + grain boundary) conductivities, respectively. Nyquist plots obtained at 25°C and the equivalent circuit model used for fitting are shown in the inset. The experimental data and fitting curve are shown as black circles and a black curve, respectively. The blue and orange semicircles correspond to the R//CPE (R, resistance; CPE, constant-phase element) components of bulk and grain boundary (g.b.) resistances, respectively. (**B**) Arrhenius plots of the ionic conductivities of $Ba_{0.5}Ca_{0.35}Na_{0.15}H_{1.85}$ and reported proton and hydride ion conductors (*10*,*11*,*14*,*15*,*19*–*32*). T^{-1}, reciprocal temperature.

Rietveld analysis results. Analysis and visualization of hopping events from MD trajectories revealed that hydride ion conduction occurs between face-sharing tetrahedral and octahedral sites (Fig. 1, H and I), resulting in three-dimensional conduction. The simulated ionic conductivities at 298 and 400 K were determined to be 2.6×10^{-3} and 4.3×10^{-2} S cm^{-1}, respectively (fig. S3E), suggesting that the anti–α-AgI–type framework is suitable for hydride ion conduction.

Electrochemical properties of $Ba_{0.5}Ca_{0.35}Na_{0.15}H_{1.85}$

The Nyquist plot of $Ba_{0.5}Ca_{0.35}Na_{0.15}H_{1.85}$ obtained at 25°C (Fig. 2A, inset) exhibits two semicircles in the higher-frequency region, attributed to the resistance in the bulk and at the grain boundaries. The bulk and total ionic conductivities at 25°C were determined as 3.9×10^{-5} and 2.1×10^{-5} S cm^{-1}, respectively. Figure 2A shows the Arrhenius plots for the bulk and total ionic conductivities of $Ba_{0.5}Ca_{0.35}Na_{0.15}H_{1.85}$; the corresponding activation energies are 49(2) and 48.2(6) kJ mol^{-1}, respectively. The electronic conductivity, estimated from direct current (DC) polarization measurements, was 1.3×10^{-9} S cm^{-1} (fig. S4). This value is four orders of magnitude lower than the total conductivity determined by alternating current (AC) impedance measurements. In addition, the DC conductivity, measured by using a Mo|TiH_2+Ti+SE+AB|LaH_x|SE|LaH_x|TiH_2+Ti+SE+AB|Mo cell (SE, solid electrolyte of $Ba_{0.5}Ca_{0.35}Na_{0.15}H_{1.85}$; AB, acetylene black), was 2.2×10^{-5} S cm^{-1}, which closely aligns with the AC conductivity value (fig. S5). LaH_x functions as a mixed hydride ion and electronic conductor, exhibiting a H^- conductivity of 0.03 S cm^{-1} and an electronic conductivity of 2 S cm^{-1} at room temperature (*11*, *18*). These results indicate pure hydride ion conduction in $Ba_{0.5}Ca_{0.35}Na_{0.15}H_{1.85}$. Variable-temperature nuclear magnetic resonance (NMR) measurements were conducted (fig. S6), and pronounced line narrowing was observed at elevated temperature (343 K) in relation to that observed at room temperature (298 K), indicating enhanced hydrogen mobility within the material. The experimental bulk conductivity was one to two orders of magnitude lower than the simulated value (fig. S3E). Given the low crystallinity of the mechanochemically synthesized samples and relative density of 90%, advances in the synthesis and densification of $Ba_{0.5}Ca_{0.35}Na_{0.15}H_{1.85}$ could further increase its conductivity. Figure 2B compares the Arrhenius plot of $Ba_{0.5}Ca_{0.35}Na_{0.15}H_{1.85}$ with those of representative hydride ion and proton conductors (*10*, *11*, *14*, *15*, *19*–*32*), indicating that $Ba_{0.5}Ca_{0.35}Na_{0.15}H_{1.85}$ has a higher ionic conductivity than that of typical hydride ion conductors of cotunnite-type BaH_2 and perovskite-type $Sr_{0.925}Na_{0.075}LiH_{2.925}$ (*22*, *27*) as well as proton conductors based on oxides and inorganic solid acids [$BaCeO_3$ and CsH_2AsO_4 (*20*, *28*)]. The superior conductivity of $Ba_{0.5}Ca_{0.35}Na_{0.15}H_{1.85}$ is attributable to the bcc framework of highly polarizable cations. In fact, high anion conductivities have been reported for anti–α-AgI–type F^- and O^{2-} conductors. For example, the F^- conductivities of $Rb_{0.5}Pb_{0.5}F_{1.5}$ and $Pb_{2/3}K_{1/3}F_{5/3}$ are 1.4×10^{-5} S cm^{-1} at room

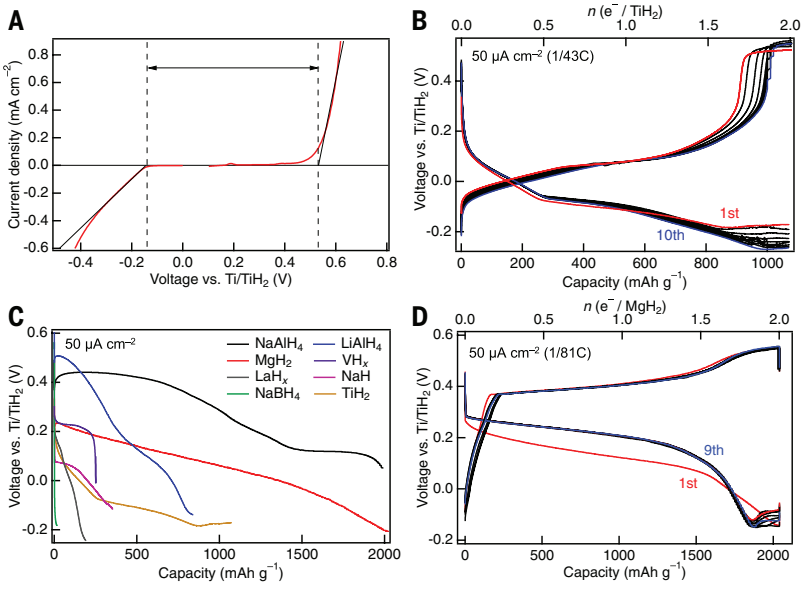

Fig. 3. Electrochemical stability of $Ba_{0.5}Ca_{0.35}Na_{0.15}H_{1.85}$ and the electrochemical hydrogen storage performance of metal hydrides in all-solid-state cells using $Ba_{0.5}Ca_{0.35}Na_{0.15}H_{1.85}$. (**A**) Linear sweep voltammogram of the (−) Mo|TiH_2+TiH+SE+AB|SE|Mo (+) cell recorded at 60°C. The red and black lines represent the experimental data and the fitting line, respectively. The potential window is indicated by vertical solid lines. (**B**) Charge-discharge curves of a (−) TiH_2+Ti+SE+AB|SE|TiH_2+SE+AB (+) cell recorded at 60°C. n, number of electrons transferred. (**C**) First discharge curves of the (−) TiH_2+Ti+SE+AB|SE|MH_x+SE+AB (+) (MH_x, metal hydride) all-solid-state cells recorded at 90°C for $NaAlH_4$, 100°C for LaH_x, and 60°C for other electrodes. (**D**) Charge-discharge curves of a (−) TiH_2+Ti+SE+AB|SE|MgH_2+SE+VGCF (+) (VGCF, vapor-grown carbon fiber) cell recorded at 90°C.

temperature and 4×10^{-1} S cm^{-1} at 247°C (*33*–*35*), respectively, whereas the O^{2-} conductivities of $Bi_{0.62}Pb_{0.38}O_{1.31}$ and $Bi_{0.75}Ba_{0.25}O_{1.375}$ are ~10^{-1} S cm^{-1} at 600°C and ~10^{-3} S cm^{-1} at 400°C (*36*, *37*), respectively.

The electrochemical stability window of the solid electrolyte was evaluated using the linear sweep voltammetry on a (−)Mo|TiH_2+Ti+SE+AB|SE|Mo (+) cell recorded at 60°C and was determined to range from −0.13 to 0.53 V versus Ti/TiH_2 (Fig. 3A). Such a low reduction potential of −0.13 V versus Ti/TiH_2 is presumably due to the dominant presence of reduction-resistant Ba and Ca in $Ba_{0.5}Ca_{0.35}Na_{0.15}H_{1.85}$, which is required for being compatible with the Ti electrode. Regarding the oxidation reaction, hydrogen gas evolution was detected at levels greater than 0.7 V versus Ti/TiH_2, as confirmed by the in situ monitoring of the mass-spectrometric H_2 signal (fig. S7). The positive correlation between the intensity of the H_2 signal and the applied current density indicated that hydrogen evolution was due to the oxidation of hydride ions ($H^- \rightarrow 1/2H_2 + e^-$). Subsequently, the electrochemical performance of $Ba_{0.5}Ca_{0.35}Na_{0.15}H_{1.85}$ as a solid electrolyte was explored using a (−) Mo|TiH_2+Ti+SE+AB|SE|TiH_2+SE+AB|Mo (+) asymmetric cell, a commonly used configuration in the field (*10*, *11*, *16*). The Ti–TiH_2 cell proceeded reversibly, delivering more than 84% of its theoretical capacity (1075 mAh g^{-1}) over 10 cycles at 60°C (Fig. 3B). Ex situ XRD measurements confirmed that TiH_2 underwent a two-step reaction that corresponds to a single-phase reaction of δ-TiH_{2-x} ($0 \leq x \leq 0.5$) with a face-centered-cubic metal lattice and a two-phase reaction between δ-$TiH_{1.5}$ and α-Ti with a hexagonal close-packed metal lattice (fig. S8, A to D). This is the first demonstration of an all-solid-state cell that exhibits both high capacity and reversibility. Notably, such a high-capacity, reversible performance for an all-solid-state cell had not been previously reported with LaH_3-based electrolytes (*11*, *16*).

Screening of hydrogen storage materials

We further examined the electrochemical hydrogenation and dehydrogenation reactions of various metal hydrides in all-solid-state cells. We first evaluated the reaction potential and theoretical capacity using density functional theory–based thermodynamic calculations (table S1). Then, we experimentally tested electrodes (TiH_2, MgH_2, $NaAlH_4$, $LiAlH_4$, $NaBH_4$, NaH, LaH_x, and VH_x) that are compatible with the stability window of the solid electrolyte ($-0.13 \leq E \leq 0.53$ V) (fig. S9). Figure 3C shows the discharge curves of the metal-hydride electrodes with the Ti–TiH_2 anode. Table S3 presents a summary of the discharge properties of the metal hydrides. The MgH_2–Ti and $NaAlH_4$–Ti (cathode-anode) cells achieved capacities approaching their theoretical values, with details on $NaAlH_4$–Ti presented in supporting note 2. The MgH_2 electrode exhibited a one-step reversible charge-discharge reaction with a high capacity of 1800 mAh g^{-1} (exceeding 88% of its theoretical capacity of 2037 mAh g^{-1}) at 90°C, corresponding to a two-electron reaction (Fig. 3D). MgH_2 was dehydrogenated to form Mg after discharging and was regenerated upon subsequent charging, indicating a two-phase reaction between MgH_2 and Mg (fig. S10). In addition, the charge-discharge reaction of MgH_2 proceeded at 25°C with a relatively high discharge capacity of 855 to 1220 mAh g^{-1} (fig. S11).

Electrochemical hydrogen storage of a Mg–H_2 cell

Given the reversibility and high capacity of the MgH_2 electrode (fig. S12), we demonstrated a H^--driven hydrogen-storage device using Mg–H_2 cells, where Mg and H_2 gas serve as active materials for the negative and positive electrodes, respectively. The cell configuration is (−) MgH_2+SE+AB|SE|LaH_x+SE+AB|SUS-mesh|H_2 (+) (SUS-mesh, stainless steel mesh current collector) (Fig. 4A) operating at 90°C. The choice of LaH_x as a cathodic electrocatalyst is based on its exceptional hydrogen exchange capability (*11*) and superior hydride ion and electronic conductivities. The open circuit voltage was 0.12 V, which is almost identical to the theoretical reaction potential of 0.186 V versus Mg/MgH_2 (refer to supporting note 1). The Mg–H_2 cell achieved the theoretical capacity of MgH_2 (~ 2030 mAh g^{-1}) over five cycles (Fig. 4B). The hydrogen desorption reaction of $MgH_2(s) \rightarrow Mg(s) + H_2(g)$ starts at a cell voltage of approximately 0.3 V. The discharge (H_2 absorption) proceeds with two steps at 0 V and −0.1 V. The subsequent discharge proceeds at −0.2 V plateau. Figure 4C shows the ex situ XRD patterns of the MgH_2 electrode during the first cycle. During charging, hydrogen was desorbed from MgH_2, resulting in the disappearance of the MgH_2 peaks and the appearance of Mg metal peaks. Subsequently, during discharging, hydrogen was absorbed into the Mg metal, leading to the disappearance of the Mg peaks and the reappearance of MgH_2 peaks. Notably, the hydrogen absorption reaction [$Mg(s) + H_2(g) \rightarrow MgH_2(s)$] is thermodynamically spontaneous at 90°C and hydrogen partial pressure $P_{H_2} = 0.2$ MPa. Control experiments demonstrated that H_2 crossover through the solid electrolyte contributes to the hydrogenation of Mg. When the charged (dehydrogenated) cell was placed in a H_2 atmosphere at 90°C, the formation of MgH_2 occurred through thermochemical hydrogenation (see supporting note S3 and fig. S13). Cross-sectional scanning electron microscopy images revealed voids within the solid electrolyte layer (fig. S14), causing hydrogen crossover. Given the current relative density of 85 to 90% for cold-pressed electrolytes, further densification optimization, e.g., hot-pressing, is necessary to minimize crossover effects (*22*, *26*, *38*). Electrochemical H^- insertion into Mg was verified in the all-solid-state cells operated under vacuum (Fig. 3 and fig. S10). However, once H_2 gas fills the cell, it can permeate through the solid electrolyte and react with Mg to form MgH_2 even under mild conditions (90°C and $P_{H_2} = 0.2$ MPa). Consequently, the discharge mechanism thus involves both direct H^- insertion and the electrochemical hydrogen pump. These findings demonstrate that hydrogen gas was electrochemically released from the MgH_2 electrode and electro- or thermochemically absorbed into the

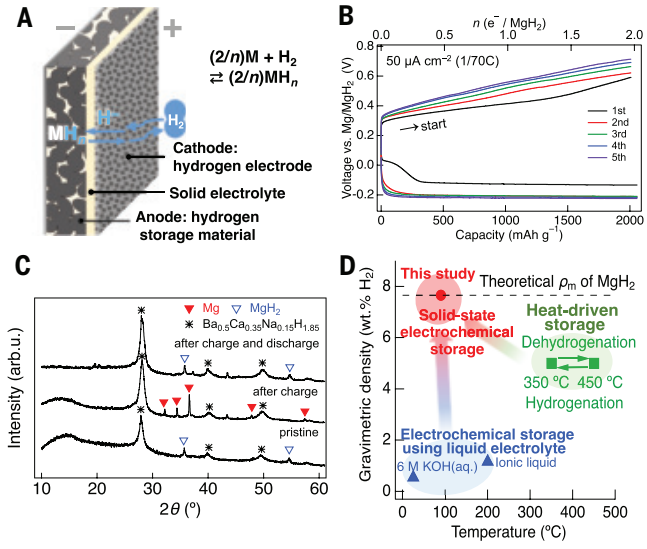

Fig. 4. Electrochemical hydrogen storage performance of a Mg metal electrode in metal–H_2 cells using $Ba_{0.5}Ca_{0.35}Na_{0.15}H_{1.85}$. (**A**) Schematic of a metal–H_2 cell. (**B**) Galvanometric hydrogen absorption or desorption using a (−) Mo|MgH_2+SE+AB|SE|LaH_x+SE+AB|SUS-mesh|H_2 (+) cell operated at 90°C. The red and blue curves correspond to the hydrogen desorption and absorption reactions, respectively. The charging process was performed under vacuum and the discharging process under a 0.2-MPa H_2 atmosphere. (**C**) Ex situ XRD patterns of the MgH_2 composite electrode before and after charging or discharging. The electrochemical measurements were performed at 90°C using a (−) Mo|MgH_2+SE+AB|SE|LaH_x+SE+AB|SUS-mesh|H_2 (+) cell. (**D**) Experimental gravimetric hydrogen storage density (ρ_m) of MgH_2 as a function of temperature compared with the corresponding heat-driven storage density (green squares). The theoretical density is indicated by a dashed line. The data pertaining to electrochemical storage using liquid and ionic-liquid electrolytes are shown as blue triangles (*7*). The capacity achieved by the Mg–H_2 cell at 90°C is plotted as red circles.

Mg electrode. Figure 4D summarizes the operating temperatures and hydrogen storage capacities of MgH_2 in H^--driven cells compared with those reported for heat- and proton-driven electrochemical hydrogen storage (*7*, *39*). Unlike thermodynamic and proton-driven storage, the MgH_2 electrode performs exceptionally well in H^--driven storage, offering low cost, good reversibility, and high storage capacity attainable at moderate temperatures (7.7 wt % at 90°C). In view of these distinct properties, H^--driven hydrogen storage devices hold great promise for the storage and utilization of hydrogen and electrical energy. For practical applications, it is essential to compare the total energy balance and gravimetric hydrogen storage density of actual device configurations between thermal and electrochemical hydrogen storage. Although a rigorous simulation under detailed assumptions is beyond the scope of this study, a simplified analysis indicates that electrochemical storage could outperform thermal methods through device-level improvements, such as reducing overpotentials, minimizing the thickness of the solid electrolyte, and increasing the proportion of active material in the composite electrode (see supporting note S4 for further discussion).

A new class of anti–α-AgI–type hydride-ion conductor, $Ba_{0.5}Ca_{0.35}Na_{0.15}H_{1.85}$, exhibited a high ionic conductivity and electrochemical stability. With this electrolyte, the charge-discharge operation of a MgH_2–Ti all-solid-state cell with a high reversible capacity was demonstrated. Furthermore, the solid electrolyte enabled the operation of Mg–H_2 hydrogen storage cells capable of high reversible capacity of 2030 mAh g^{-1} and a low operating temperature of 90°C. These properties were previously unattainable through conventional thermal methods or liquid electrolytes, offering a foundation for efficient hydrogen storage systems suitable for use as energy carriers.

REFERENCES AND NOTES

1. L. Schlapbach, A. Züttel, *Nature* **414**, 353–358 (2001).
2. L. Z. Ouyang, J. L. Huang, H. Wang, J. W. Liu, M. Zhu, *Mater. Chem. Phys.* **200**, 164–178 (2017).
3. Q. Lai *et al.*, *ChemSusChem* **8**, 2789–2825 (2015).
4. A. Eftekhari, B. Z. Fang, *Int. J. Hydrogen Energy* **42**, 25143–25165 (2017).
5. J. L. Yang *et al.*, *EnergyChem* **4**, 100092 (2022).
6. H. Guo, C. Zhao, *Small Methods* **8**, e2300699 (2024).
7. Y. L. Xu, F. M. Mulder, *Int. J. Hydrogen Energy* **46**, 19542–19553 (2021).
8. C. M. Luedecke, G. Deublein, R. A. Huggins, *J. Electrochem. Soc.* **132**, 52–56 (1985).
9. B. Y. Liaw, G. Deublein, R. A. Huggins, *J. Alloys Compd.* **189**, 175–186 (1992).
10. G. Kobayashi *et al.*, *Science* **351**, 1314–1317 (2016).
11. W. Zhang *et al.*, *Nature* **616**, 73–76 (2023).
12. R. D. Shannon, *Acta Crystallogr. A* **32**, 751–767 (1976).
13. P. W. Fowler, P. A. Madden, *Phys. Rev. B Condens. Matter* **29**, 1035–1042 (1984).
14. K. Fukui *et al.*, *Nat. Commun.* **10**, 2578 (2019).
15. K. Fukui, S. Iimura, A. Iskandarov, T. Tada, H. Hosono, *J. Am. Chem. Soc.* **144**, 1523–1527 (2022).
16. Y. Izumi *et al.*, *Adv. Energy Mater.* **13**, 2301993 (2023).
17. C. Tubandt, *Z. Anorg. Allg. Chem.* **115**, 105–126 (1921).
18. J. Shinar, B. Dehner, B. J. Beaudry, D. T. Peterson, *Phys. Rev. B Condens. Matter* **37**, 2066–2073 (1988).
19. K. D. Kreuer, *Annu. Rev. Mater. Res.* **33**, 333–359 (2003).
20. L. Malavasi, C. A. J. Fisher, M. S. Islam, *Chem. Soc. Rev.* **39**, 4370–4387 (2010).
21. M. C. Verbraeken, E. Suard, J. T. S. Irvine, *J. Mater. Chem.* **19**, 2766–2770 (2009).
22. M. C. Verbraeken, C. Cheung, E. Suard, J. T. S. Irvine, *Nat. Mater.* **14**, 95–100 (2015).
23. F. Takeiri *et al.*, *Inorg. Chem.* **58**, 4431–4436 (2019).
24. N. Matsui *et al.*, *J. Mater. Chem. A Mater.* **8**, 24685–24694 (2020).
25. H. Ubukata *et al.*, *Sci. Adv.* **7**, eabf7883 (2021).
26. F. Takeiri *et al.*, *Nat. Mater.* **21**, 325–330 (2022).
27. T. Hirose *et al.*, *ACS Appl. Energy Mater.* **5**, 2968–2974 (2022).
28. A. I. Baranov, V. P. Khiznichenko, L. A. Shuvalov, *Ferroelectrics* **100**, 135–141 (1989).
29. T. Norby, N. Christiansen, *Solid State Ion.* **77**, 240–243 (1995).
30. K. D. Kreuer, *Chem. Mater.* **8**, 610–641 (1996).
31. H. G. Bohn, T. Schober, T. Mono, W. Schilling, *Solid State Ion.* **117**, 219–228 (1999).
32. S. Li, F. Schönberger, P. Slater, *Chem. Commun.* **2003**, 2694–2695 (2003).
33. S. Hull, P. Berastegui, S. G. Eriksson, N. J. G. Gardner, *J. Phys. Condens. Matter* **10**, 8429–8446 (1998).
34. S. Hull, P. Berastegui, *J. Phys. Condens. Matter* **11**, 5257–5272 (1999).
35. Y. Yamane, K. Yamada, K. Inoue, *Solid State Ion.* **179**, 605–610 (2008).
36. F. Honnart, J. C. Boivin, D. Thomas, K. J. Devries, *Solid State Ion.* **9-10**, 921–924 (1983).
37. C. Michel *et al.*, *J. Solid State Chem.* **109**, 122–126 (1994).
38. N. Matsui *et al.*, *J. Am. Ceram. Soc.* **102**, 3228–3235 (2019).
39. B. Bogdanovic *et al.*, *J. Alloys Compd.* **292**, 57–71 (1999).

ACKNOWLEDGMENTS

The synchrotron XRD experiments were carried out as projects approved by the Japan Synchrotron Radiation Research Institute (JASRI) (proposal no. 2018B1724). The neutron diffraction experiment was approved by the Neutron Scattering Program Advisory Committee (proposal number 2019S06) of IMSS, KEK. The computing resources of the TSUBAME4.0 supercomputer at Institute of Science Tokyo were used. **Funding:** Japan Society for the Promotion of Science KAKENHI grant 17H06145; Japan Society for the Promotion of Science KAKENHI grant 19H05793; Japan Society for the Promotion of Science KAKENHI grant 22K14472; Japan Society for the Promotion of Science KAKENHI grant 23KJ0933; Japan Society for the Promotion of Science KAKENHI grant 24H00042; Japan Society for the Promotion of Science KAKENHI grant 25H01964. **Author contributions:** Conceptualization: N.M., M.H., R.K.; Methodology: T.H., N.M., I.T., G.J., K.I., K.G.; Investigation: T.H., N.M., Y.H.; Visualization: T.H., N.M.; Funding acquisition: T.H., N.M., M.H., R.K.; Project administration: N.M., M.H., R.K.; Supervision: N.M., M.H., R.K.; Writing – original draft: T.H., N.M., K.S., Y.H., R.K.; Writing – review & editing: T.H., N.M., T.I., Y.H., K.G., K.I., G.J., K.S., M.H., R.K. **Competing interests:** T.H., N.M., T.I., and R.K. hold a patent related to this work (Japanese unexamined patent application publication 2023-035854). T.H., N.M., and R.K. hold another patent related to this work (Japanese unexamined patent application 2023-035875). **Data and materials availability:** The data generated in this study are available from the corresponding authors upon reasonable request.

SUPPLEMENTARY MATERIALS

science.org/doi/10.1126/science.adw1996
Materials and Methods; Figs. S1 to S16; Tables S1 to S6; References (*40*–*61*)

Submitted 23 January 2025; accepted 4 August 2025

10.1126/science.adw1996

SEISMOLOGY

Crustal stresses and damage evolve throughout the seismic cycle of the Ridgecrest fault zone

Jared Bryan[1]*, William B. Frank[1], Pascal Audet[2]

Earthquakes abruptly release tectonic stress that builds slowly over time through the coupled evolution of faults and the surrounding crust. Seismic wavespeeds track crustal deformation and stress changes, but typical monitoring methods are most sensitive to shallow depths. Using receiver functions, we tracked rupture-zone wavespeed and anisotropy changes throughout the crust during the 2019 Ridgecrest earthquake sequence. Shallow coseismic wavespeed reductions recovered within months, whereas a deeper postseismic wavespeed drop persisted without measurable recovery over several years. The deep, persistent wavespeed drop likely reflects accumulating damage driven by postseismic deformation, suggesting two possible scenarios: (i) a slow interseismic recovery where wavespeed and anisotropy track long-term stress evolution; or (ii) permanent deformation of an immature fault zone. Both scenarios affect the dynamics and energy budget of the seismic cycle.

Earthquakes are fundamentally governed by how stress accumulates and is relaxed within fault zones, a process intrinsically linked to the coupled evolution of the fault zone and the surrounding crust (*1*). Earthquake ruptures deform the surrounding crust, as evidenced by fracturing at the surface (*2*) and transient decreases in seismic wavespeeds interpreted as damage in the shallow subsurface (*3*). Conversely, bulk crustal processes such as postseismic relaxation (*4*, *5*), healing of shallow rock damage (*3*), permeability changes (*6*), and long-term stress accumulation (*7*, *8*) directly affect the stress state of the fault. This interplay between dynamic ruptures on the fault and the physical evolution of the bulk is controlled by rheology, the material behavior that determines how Earth materials deform in response to applied stresses. Rheology dictates how the crust deforms and recovers over time, and it controls the seismic cycle. A better understanding of fault zone rheology is crucial for constraining how tectonic stresses are relaxed through deformation and for estimating the large-scale strength of the lithosphere.

The evolution of the crustal stress field at depth can be inferred from earthquake source analysis of microseismic data (*9*, *10*) or changes in seismic wavespeeds (*11*, *12*) and seismic anisotropy (*13*, *14*). However, these event-based measurements often require special repeating events whose spatial distribution is far from uniform and only sporadically provide information, often lacking resolution during episodic phases of the seismic cycle. Seismic noise–based measurements enable continuous monitoring of crustal seismic wavespeeds, but detecting velocity changes at depth requires long-period surface waves, whose broad sensitivity kernels and multiple scattering limit precise depth resolution (*15*, *16*), or specialized source distributions and array geometries to extract body waves from ambient noise (*17*, *18*). Deformation associated with the seismic cycle spans deeper portions of the crust with different rheological behaviors, which are poorly sampled in time and space by these seismological techniques. This observational gap challenges inferences of the evolving stress state of the entire crustal column throughout the seismic cycle.

We used teleseismic receiver functions to measure temporal variations in the seismic wavespeed structure during the 2019 Ridgecrest, California, earthquake sequence. The Ridgecrest sequence consisted of a moment magnitude (M_w) 6.4 event followed by a M_w 7.1 earthquake less than 2 days later (Fig. 1A) (*19*, *20*). Unlike mature fault systems such as the San Andreas, which have undergone extensive seismic slip over many earthquake cycles, resulting in well-developed damage zones (*21*) and highly localized fault cores (*22*), the Ridgecrest fault system has experienced fewer large earthquakes and distributes deformation over a broad damage zone (*2*, *23*). Previous seismic monitoring studies have shown a substantial coseismic wavespeed reduction and a short (<1 year) recovery in the vicinity of the fault using local seismicity (*24*) and noise-based interferometric techniques most sensitive to shallow (<2 km) wavespeed structure (*18*, *25*, *26*). To probe how the entire crustal column evolved through this major earthquake sequence, we leveraged advantageous features of receiver function data for seismic monitoring of the crust, including seismic anisotropy. The receiver function technique is a form of event-based seismic interferometry that uses the coda of near-vertically propagating *P* waves from large ($M_w > 5.0$) earthquakes at teleseismic (30° to 100°) distances to map crustal structure with uniform depth sensitivity (*27*) beneath a single seismograph station (*28*, *29*). With ~1500 $M_w > 5.0$ events annually, receiver functions quasi- continuously illuminate the seismic wavespeed structure of Earth's crust (*27*, *30*).

Deep crustal seismic wavespeed changes

We calculated receiver functions for 34 permanent three-component broadband seismic stations within ~120 km of the Ridgecrest fault zone (Fig. 1A). Of the 15,678 events with magnitudes of >5.0 between 2015 and 2023, we selected 5500 events that meet source location and quality control criteria for station CI.WRC2 (see materials and methods in the supplementary materials; fig. S1). Receiver function waveforms before and after the Ridgecrest earthquakes show clear changes in amplitude and time delays that increase with lag time (Fig. 2A).

Sample-to-sample variations in receiver function waveforms are due to a combination of seismic wavespeed changes, varying source-receiver paths of the teleseismic waves, and source- or receiver-side noise. Noise is assumed to be stochastic, but path effects, such as variations in the incidence angle and backazimuth of incoming rays due to the global distribution of teleseismic earthquake sources (fig. S2), result in nonlinear but predictable time-amplitude changes in receiver function waveforms (fig. S3). Changes in seismic wavespeeds and anisotropy also yield nonlinear waveform variations owing to time shifts accumulated through reverberations in the medium and modified impedance contrasts at layer boundaries (*30*–*34*). Capturing these nonlinear waveform changes is difficult with typical comparative metrics, such as the L2-norm that only quantifies the difference in amplitude, whereas noise-based monitoring tools such as trace stretching or moving-window cross-spectral analysis only quantify changes in time.

We overcome these challenges through a monitoring approach that leverages optimal transport (*27*) (see materials and methods). Optimal transport is a mathematical tool for measuring the distance between two distributions by finding a transformation (a "transport plan") that minimizes the "work" needed to transform a reference distribution into a perturbed observed distribution (*35*). We used the transport plan to capture and interpret the complex time-amplitude signal variations characteristic of receiver functions. We computed the optimal transport map and associated distance from each receiver function to a reference waveform (*27*), representative of the crustal structure prior to the Ridgecrest sequence. These optimal transport maps provide a structure to the space of waveform variations (*27*, *36*), allowing us to

[1]Department of Earth, Atmospheric and Planetary Sciences, Massachusetts Institute of Technology, Cambridge, MA, USA. [2]Department of Earth and Environmental Sciences, University of Ottawa, Ottawa, ON, Canada. *Corresponding author. Email: jtbryan@mit.edu

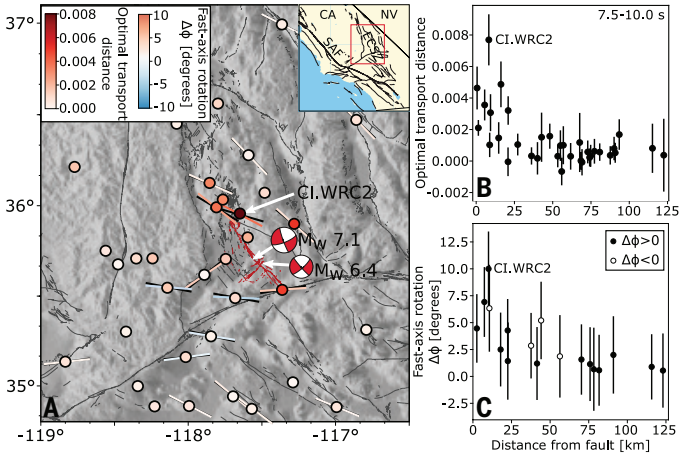

Fig. 1. Signatures of damage and stress change in the Ridgecrest fault zone. (**A**) Map of the Ridgecrest, California (CA), area with broadband seismographs shown as circles color coded by isotropic changes in seismic wavespeed measured at each station as well as the fast-axis direction of seismic anisotropy before (black) and after (color coded by their angular perturbation) the 2019 earthquake sequence. Station CI.WRC2 experienced the largest perturbation and is located near the northern tip of the mainshock rupture. The faults hosting the Ridgecrest doublet are in red (*62*) with other US Geological Survey (USGS) Quaternary faults in gray (*63*). The inset shows the study area in relation to the Eastern California Shear Zone (ECSZ), the main strand of the San Andreas Fault (SAF), and the state boundary with Nevada (NV). (**B**) Decay of the isotropic wavespeed change, captured by the optimal transport distance averaged over 90 days post-earthquakes, with distance from the faults of the M_w 6.4 and M_w 7.1 Ridgecrest doublet (whichever is closer). Error bars are the standard deviation in the optimal transport distance over all times before the earthquakes. (**C**) Absolute perturbation to the fast-axis direction with distance from the fault, for both positive (filled circle) and negative (open circle) angular perturbations, averaged over 1 year after the earthquakes.

construct empirical models for the independent modes of signal variations (e.g., wavespeed changes independent of backazimuth variations) in a linear framework and obtain receiver functions cleaned of nuisance source-side variability (Fig. 2B). We then calculated the lag time–dependent optimal transport distance (Fig. 3A) and mapped the waveform perturbations across the fault zone (Fig. 1, A and B). As a comparison, we also computed optimal transport distances for ambient seismic noise using the same workflow we used for the receiver functions. The optimal transport distances remain stable over time prior to the 2019 Ridgecrest earthquakes but show a clear coseismic change at the time of the earthquakes (Fig. 3A) that decays with distance from the fault zone (Fig. 1, A and B). Immediately after the events, receiver function waveform changes associated with early lag times (0.0 to 2.5 s), which capture direct converted phases and shallow reverberations, are more pronounced than those associated with later lag times (7.5 to 10.0 s), which are sensitive to deeper reverberations (Figs. 2B and 3A). We observed a similar evolution for seismic noise waveform changes, which likely lose sensitivity to wavespeed perturbations at depths of >10 km (*15*, *16*). Over several months after the earthquakes, the receiver function waveform changes at later lag times become larger than those at early lag times (Fig. 3A).

To estimate the depth at which these changes occur, we inverted the reference receiver function for a reference layered seismic wavespeed model (fig. S4) and examined the effect of a wavespeed perturbation in each layer on the synthetic waveforms. We applied a 1% decrease to *S* wavespeed V_S for each layer within the model and calculated the optimal transport distance as a function of lag time between the reference and perturbed synthetic receiver functions (*16*). Varying the depth of the perturbed layer produced waveform changes characterized by two distinct moveouts (Fig. 2C). The first moveout, associated with direct converted phases, is particularly prominent for crustal phase conversions above 25 km depth, affecting waveform perturbations up to 2.5 s. Perturbations in waveforms observed between 7.5 and 10.0 s cannot be explained by direct crustal conversions at <50 km depth. We surmise that seismic wavespeed perturbations at depths of >50 km are unlikely with the coseismic slip and aftershocks of the Ridgecrest earthquakes concentrated above 10 km depth (*19*, *20*, *37*). We observed that shallow wavespeed perturbations can generate waveform changes

Fig. 2. Waveform changes of observed and modeled receiver functions throughout the crust near the Ridgecrest fault zone. (**A**) Receiver functions through time for station CI.WRC2, located near the northern end of the fault rupture (Fig. 1A). Stacked receiver functions before (blue) and after (red) the 2019 Ridgecrest earthquakes show clear time delays that grow with lag time. (**B**) Receiver function waveforms corrected for source variability to isolate time-lapse waveform changes before (blue) and after (red) the earthquake sequence. (**C**) Optimal transport distances resolved in lag time of the receiver function due to buried wavespeed changes at a range of depths. Moveouts related to direct conversions and reverberated phases are highlighted.

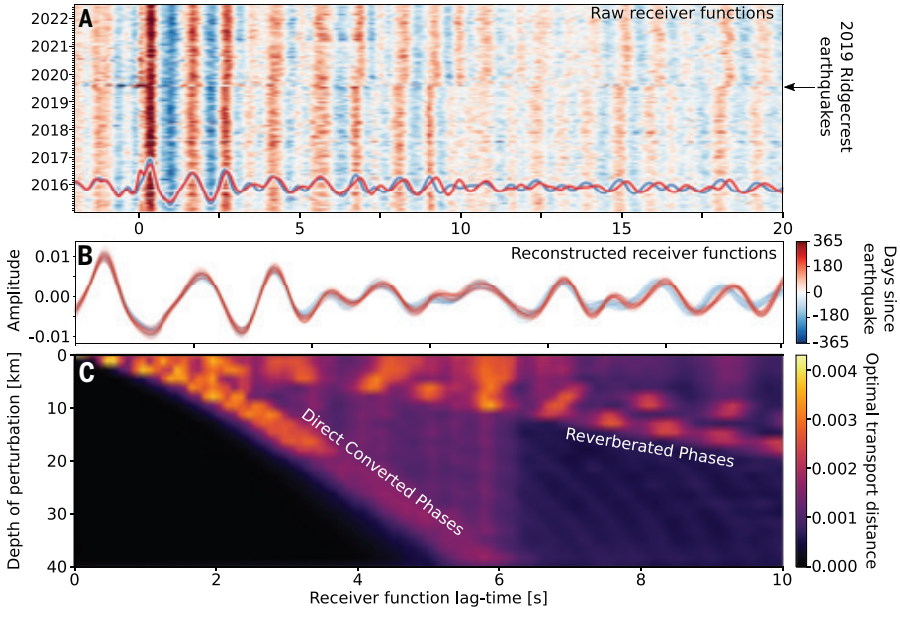

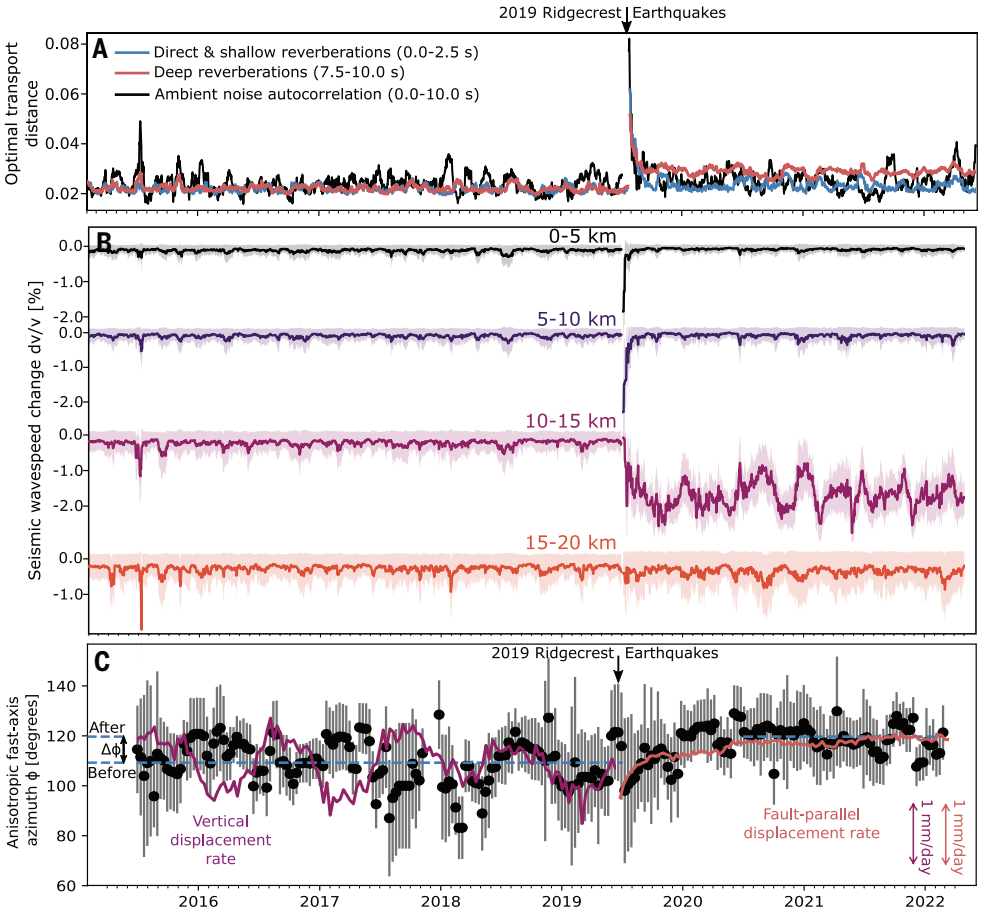

Fig. 3. Depth-dependent evolution of crustal seismic wavespeeds and anisotropy. (**A**) Time series of the optimal transport distance for station CI.WRC2. Early lag times (0.0 to 2.5 s) (blue) correspond to direct converted phases throughout the crust and reverberations in shallow layers. Late lag times (7.5 to 10.0 s) (red) correspond to deep reverberated phases. Optimal transport distance time series of seismic ambient noise from the pre-event time window (black) is estimated identically. Estimates of the optimal transport distances before and after the 2019 Ridgecrest earthquakes are made with no overlapping windows. (**B**) Time series of seismic wavespeed changes inverted for four depth ranges. The optimal wavespeed change is shown as a colored line, and the 95% confidence interval is shaded. (**C**) Time series of the azimuth of the fast axis of seismic anisotropy. Estimates of the fast-axis direction before and after the 2019 Ridgecrest earthquakes are made with no overlapping windows. The average fast-axis azimuth is shown for all times before and all times at least 1 year after the Ridgecrest earthquakes (dashed blue lines). The estimated rotation in fast-axis orientation $\Delta\phi$ plotted in Fig. 1C is shown. The GNSS vertical (purple line) and fault-parallel (red line) displacement rates for station P594 are averaged in the same way as the anisotropy and are respectively shown for the pre- and postseismic phases.

out to ~6.0 s through high-order reverberations, but they rapidly lose energy with increasing order. We measured waveform perturbations at many stations across the fault zone, and we see that these late perturbations are not an artifact of a spatially heterogeneous shallow change in wavespeed sampled by the lateral moveout of reverberated phases (Fig. 1, A and B, and fig. S5). We conclude that the observed perturbations in the waveforms between 7.5 and 10.0 s (Figs. 2B and 3A) cannot be explained by shallow wavespeed changes alone and likely result from reverberated phases originating at depths of 10 to 20 km (Fig. 2C).

The Ridgecrest fault zone exhibits considerable structural heterogeneity (*38*–*40*), but the observed waveform variations necessarily average the wavespeed perturbations over a large volume. The uneven distribution of global earthquake sources implies a nonuniform backazimuth sampling by the receiver functions (fig. S2), resulting in a heterogeneous distribution of ray-piercing points that broadens the spatial sensitivity of our measurements (fig. S5). Broad sensitivity kernels of scattered waves also inherently limit our ability to precisely constrain the lateral spatial scale of the observed seismic velocity changes (*41*). However, we can leverage this source variability to infer the depth and spatial localization of these changes. If the wavespeed reductions were shallow, then the waveform perturbations would be sampled by all receiver functions regardless of backazimuth. Conversely, wavespeed reductions confined to the Ridgecrest fault zone at greater depths would predominantly affect only waveforms whose raypaths intersect the fault region. We observe that the largest waveform perturbations occur in fault-crossing receiver functions, whereas fault-parallel receiver functions show smaller perturbations, and fault-outward receiver functions exhibit almost no change (fig. S6).

After establishing that the observed waveform changes likely originate at depth within the Ridgecrest fault zone, we quantified the depth and magnitude of wavespeed changes through time in four depth ranges down to 20 km (Fig. 3B; see materials and methods). Results were similar when repeating the inversion with eight thinner layers, indicating robustness to vertical discretization (fig. S7). We confirm a large coseismic wavespeed reduction (~2%) at depths corresponding to the distribution of coseismic slip (<10 km) (*19*, *42*), deeper than previous estimates of coseismic wavespeed changes inferred from ambient seismic noise and regional earthquake measurements (*24*–*26*). This shallow wavespeed reduction rapidly recovers within months back to pre-earthquake levels, in general agreement with previous studies (*18*, *24*–*26*). An additional deep (10 to 15 km) wavespeed change (~−2.0%) is needed to fit the observed perturbations, notably the phase shifts at later lag times (Figs. 2B and 3A). This deep wavespeed change accumulates postseismically and persists over the observational period; no wavespeed change at greater depths is required to explain the observations. These results imply a decoupling between persistent deformation at depth and the shallow recovery of a coseismic drop in wavespeed (*18*, *24*), suggestive of a depth-dependent response to the Ridgecrest ruptures.

Changes in crustal seismic anisotropy

We investigated how seismic anisotropy evolved as an additional constraint on the crustal response to the Ridgecrest earthquakes. We used the intrinsic backazimuth variability of receiver functions (fig. S2), which we previously removed to resolve isotropic wavespeed changes, to measure changes in the orientation of seismic anisotropy. For each station, we inverted for the set of harmonic coefficients that best reproduce the backazimuth variability in amplitude together with a fast axis of anisotropy ϕ (*43*, *44*) (fig. S8; see materials and methods). Estimating this in a 180-day moving window, we tracked the evolution of the fast-axis direction through time (Fig. 3C) and how it changes

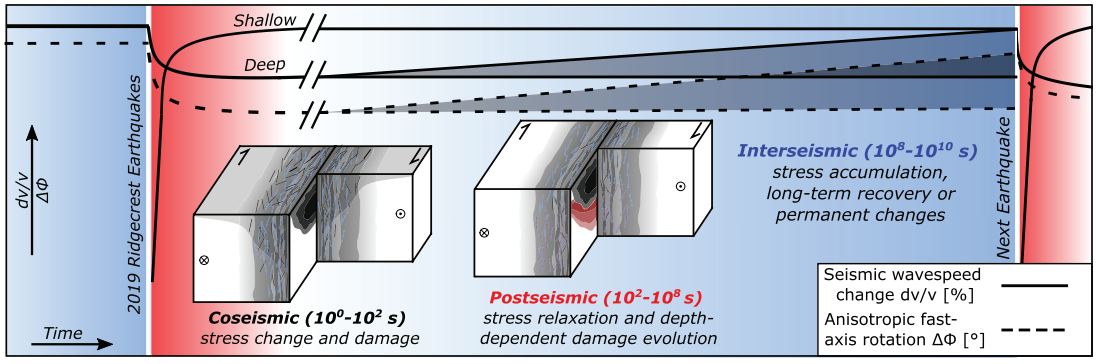

Fig. 4. Stress and damage evolution in the Ridgecrest fault zone throughout the seismic cycle. Deep seismic wavespeed changes and rotation in anisotropy in the fault zone serve as proxies for stress and damage throughout the seismic cycle. Inset schematic fault block models show coseismic damage localized near the surface and a fault core that recovers rapidly as well as deep damage accumulated along with anisotropy reorientation over the postseismic phase. There are two potential scenarios for the interseismic phase: Either (i) deep changes gradually recover, reflecting long-term stress-driven evolution; or (ii) deep changes persist indefinitely, indicating permanent structural changes in an immature fault zone. These two scenarios are represented by uncertainty in the interseismic evolution of seismic wavespeed and anisotropy.

in response to the Ridgecrest earthquakes. We observe that seismic anisotropy evolves over several months after the Ridgecrest sequence on a similar timescale to rapid postseismic deformation, as captured by the fault-parallel surface displacement rate at nearby Global Navigation Satellite System (GNSS) station P594 (*45*) (Fig. 3C). To examine whether these changes in fast axis are localized to the Ridgecrest fault zone, we averaged the fast-axis orientations for 1 year before and 1 year after (starting 1 year after the coseismic rupture to avoid the postseismic phase) the 2019 Ridgecrest earthquakes across the seismic network, mapping this reorientation across the fault zone (Fig. 1, A and C).

The background seismic anisotropy is spatially coherent and yields fast axes that reflect the dominant fault structures in the area (*46*), with a northwest–southeast trend along the Ridgecrest fault and a more east–west trend near the Garlock fault (Fig. 1A) (*47*). Stations that did not pass the stability criteria for a fast-axis estimate are spatially clustered, likely because of seasonal variations that dominate the recovered anisotropy prior to the Ridgecrest sequence (Fig. 3C). The observed post-Ridgecrest rotation is spatially coherent and decays with distance from the fault with a maximum of $|\Delta\phi| \approx 10°$ (Fig. 1C). The seasonal variability of anisotropy seen before the Ridgecrest sequence disappears afterward (Fig. 3C), suggesting that the evolution of anisotropy after Ridgecrest is dominated by the crustal response to the earthquakes. This rotation in anisotropy persists without recovery, similar to the isotropic wavespeed change at >10 km depth (Fig. 3, A and B). Our observations suggest that the post-Ridgecrest rotation of seismic anisotropy imaged here stems from changes at depths >10 km and is not related to postseismic healing of aligned brittle fractures in the upper crust (*48*).

Depth-dependent rheology shapes earthquake response

Our observations reveal a stark depth dependence of the crustal response to a major seismic sequence. Throughout the upper-crust portion of the rupture zone (<10 km depth), a rapid coseismic drop in wavespeed returned to pre-earthquake wavespeeds within months (*24*, *25*, *48*) (Fig. 3B). In contrast, the lower crust gradually accumulated a wavespeed perturbation over the postseismic phase that persisted without recovery during the 3-year observational period after the Ridgecrest sequence (Fig. 3B).

In the upper crust, coseismic stress changes (*23*, *40*) and strong shaking within the coseismic rupture zone (<10 km depth) (*19*, *49*) induced brittle failure, microcracking (*50*), and fluid flow in the fault zone (*51*), resulting in a rapid seismic wavespeed reduction (Fig. 3B). The uniform depth-sensitivity of receiver functions (*27*) demonstrates that brittle failure was not limited to the shallow subsurface and is present throughout the coseismic rupture zone (Fig. 3). This brittle damage began to heal almost immediately (*24*) through crack resealing, compaction, and fluid-assisted healing (*52*). In contrast, the lower crust beyond 10 km depth gradually accumulated a wavespeed perturbation over the postseismic phase that did not recover during our observational period (Fig. 3B). The slow accumulation of wavespeed changes at these depths suggests the coexistence of viscous deformation and localized brittle damage. High fluid pressure near Ridgecrest (*47*) may be an essential factor in accelerating deformation through semibrittle creep, where brittle damage driven by localized stress concentrations at fracture tips can be regulated by the slow rate of fluid flow into the new fracture (*53*, *54*). Such fluid-driven, semibrittle processes naturally account for both the timescale over which wavespeeds steadily decrease in the lower crust and the observed postseismic rotation in anisotropy (Fig. 3C). We suggest that such anisotropy could reflect a superposition of frozen crystallographic anisotropy (*44*) and stress-sensitive fracture- and fluid-based (*47*, *55*) anisotropy, both potentially responsive to reorientation of the stress field.

Observed earthquake-induced stress rotations require an upper crust that cannot support large differential stresses (*7*, *56*, *57*), whereas postseismic deformation in the lower crust requires differential stresses 10 to 1000 times larger than those supported within the fault zone in the upper crust (*58*). This strength contrast likely controlled the distribution of fault slip during the Ridgecrest earthquakes, with coseismic failure and subsequent aftershocks contained within the upper crust down to 10 km (*19*, *20*) and postseismic deformation governing stress relaxation at greater depths (*42*, *51*, *59*). The earthquakes, in turn, damaged the surrounding crust through brittle failure and microcracking in the upper crust and fluid-mediated semibrittle deformation in the lower crust. The observed depth-dependent damage and recovery throughout the Ridgecrest sequence reflect a coupled evolution of faults and their surrounding medium whose interaction is mediated by a complex crustal rheology.

Implications for the seismic cycle

Our inference of depth-dependent rheology highlights the time-dependent mechanisms that shape the overall strength of the lithosphere and its role in controlling deformation at tectonic plate boundaries. We show in Fig. 4 a schematic model for how this depth-dependent response to the Ridgecrest earthquakes evolves in the

crustal column throughout the seismic cycle. At shallow depths (<10 km), the crust is damaged by coseismic shaking (*60*) and static stress changes (*23*, *40*) over seconds to minutes (10^0 to 10^2 s); this damage is then rapidly recovered through crack resealing, compaction, and fluid-assisted healing (*50*), returning to pre-earthquake levels in days or months (10^5 to 10^7 s). Brittle damage also accumulates in the lower crust (10 to 15 km), but through different mechanisms, such as fluid-assisted fracture creep (*53*, *54*), and over the longer timescale of the postseismic phase that can last from days to years after the earthquake (10^5 to 10^8 s). This damage persists through the postseismic phase and beyond our observational timescale. The persistence of this deep, brittle damage and its associated anisotropy suggests two possible scenarios: (i) The perturbations to the medium do eventually recover but require years to centuries (10^8 to 10^{10} s) of tectonic loading, the timescale of the interseismic phase; or (ii) the perturbations to the medium do not recover, reflecting a permanent change in the structure of the fault zone at depth.

These scenarios have distinct implications for our understanding of fault zone evolution, crustal properties, and the energy budget of the seismic cycle. If the deep perturbations eventually recover, seismic wavespeeds and fault strength at depth must evolve continuously throughout the interseismic phase. This implies a dynamic interplay between fracture healing, fluid migration, and tectonic loading that controls the stress state of the fault zone throughout the seismic cycle. Conversely, permanent damage accumulation without substantial recovery implies that immature fault zones such as Ridgecrest progressively weaken or structurally evolve after major earthquakes (*61*). Distinguishing between these outcomes will be essential to improve our models of fault strength evolution and seismic energy partitioning.

Beyond the earthquake cycle on crustal faults, our results highlight that seismic wavespeed changes in the shallow subsurface are not generally reflective of the evolution of the fault zone at depth, highlighting a gap in our understanding of deep crustal processes. This has implications for continental fault zone mechanics, as we highlight here, but also for the dynamics of other major transcrustal geohazards, such as plate boundary deformation in subduction zones and volcanism.

REFERENCES AND NOTES

1. P. Thakur, Y. Huang, Y. Kaneko, *J. Geophys. Res. Solid Earth* **125**, e2020JB019587 (2020).
2. A. M. Rodriguez Padilla, M. E. Oskin, C. W. Milliner, A. Plesch, *Nat. Geosci.* **15**, 222–226 (2022).
3. F. Brenguier *et al.*, *Science* **321**, 1478–1481 (2008).
4. Q. Qiu, S. Barbot, T. Wang, S. Wei, *Bull. Seismol. Soc. Am.* **110**, 1701–1715 (2020).
5. A. M. Freed, R. Bürgmann, *Nature* **430**, 548–551 (2004).
6. L. Xue *et al.*, *Science* **340**, 1555–1559 (2013).
7. Y. Fialko, *J. Geophys. Res. Solid Earth* **126**, e2021JB022000 (2021).
8. K. Okubo, B. G. Delbridge, M. A. Denolle, *J. Geophys. Res. Solid Earth* **129**, e2023JB028084 (2024).
9. B. P. Allmann, P. M. Shearer, *J. Geophys. Res.* **112**, B04305 (2007).
10. S. Sheng, L. Meng, *Geophys. Res. Lett.* **47**, e2020GL087722 (2020).
11. J. E. Vidale, Y.-G. Li, *Nature* **421**, 524–526 (2003).
12. F. Niu, P. G. Silver, T. M. Daley, X. Cheng, E. L. Majer, *Nature* **454**, 204–208 (2008).
13. V. Miller, M. Savage, *Science* **293**, 2231–2233 (2001).
14. N. Nakata, R. Snieder, *Geophys. Res. Lett.* **39**, 2012GL051979 (2012).
15. C. Wu *et al.*, *Geophys. Res. Lett.* **43**, 6129–6136 (2016).
16. C. Yuan, J. Bryan, M. Denolle, *Geophys. J. Int.* **226**, 828–846 (2021).
17. Y. Sheng *et al.*, *Geophys. Res. Lett.* **49**, GL098509 (2022).
18. Y. Sheng *et al.*, *Seismol. Res. Lett.* **95**, 2452–2463 (2024).
19. Z. E. Ross *et al.*, *Science* **366**, 346–351 (2019).
20. D. R. Shelly, *Seismol. Res. Lett.* **91**, 1971–1978 (2020).
21. H. M. Savage, E. E. Brodsky, *J. Geophys. Res.* **116**, B03405 (2011).
22. J. F. Dolan, B. D. Haravitch, *Earth Planet. Sci. Lett.* **388**, 38–47 (2014).
23. X. Xu *et al.*, *Science* **370**, 605–608 (2020).
24. Y. Lu, Y. Ben-Zion, *Geophys. J. Int.* **228**, 620–630 (2022).
25. J. Boschelli, M. P. Moschetti, C. Sens-Schönfelder, *J. Geophys. Res. Solid Earth* **126**, e2020JB021465 (2021).
26. T. Clements, M. Denolle, *J. Geophys. Res. Solid Earth* **128**, e2022JB025553 (2023).
27. J. Bryan, W. B. Frank, P. Audet, *Geophys. J. Int.* **234**, 1282–1306 (2023).
28. L. Vinnik, *Phys. Earth Planet. Inter.* **15**, 39–45 (1977).
29. C. A. Langston, *J. Geophys. Res.* **84**, 4749–4762 (1979).
30. P. Herath, P. Audet, *Commun. Earth Environ.* **5**, 697 (2024).
31. P. Audet, *Bull. Seismol. Soc. Am.* **100**, 1356–1362 (2010).
32. D. Kim, V. Lekic, *Geophys. Res. Lett.* **46**, 13722–13729 (2019).
33. T. Richter, thesis, Freie Universität Berlin (2014).
34. J. M. Gosselin *et al.*, *Sci. Adv.* **6**, eaay5174 (2020).
35. L. V. Kantorovich, *Dokl. Akad. Nauk. SSSR* **37**, 199–201 (1942).
36. W. Wang, D. Slepčev, S. Basu, J. A. Ozolek, G. K. Rohde, *Int. J. Comput. Vis.* **101**, 254–269 (2013).
37. Q.-Y. Wang, H. Yao, *Earth Planet. Phys.* **4**, 532–542 (2020).
38. Z. Zhou, M. Bianco, P. Gerstoft, K. Olsen, *Geophys. Res. Lett.* **49**, e2021GL095024 (2022).
39. H. Qiu *et al.*, *J. Geophys. Res. Solid Earth* **126**, e2021JB022043 (2021).
40. X. Xu, D. Liu, L. Lavier, *Geophys. Res. Lett.* **50**, e2022GL101692 (2023).
41. S. Hansen, B. Schmandt, *Geochem. Geophys. Geosyst.* **18**, 4487–4502 (2017).
42. K. He, C. Xu, Y. Wen, *Geophys. J. Int.* **230**, 957–975 (2022).
43. I. Bianchi, J. Park, N. Piana Agostinetti, V. Levin, *J. Geophys. Res.* **115**, B12317 (2010).
44. P. Audet, *J. Geophys. Res. Solid Earth* **120**, 3527–3543 (2015).
45. Southern California Earthquake Center (SCEC), SCEC Community Geodetic Model (CGM) (2023); https://southern.scec.org/research/cgm.
46. J. Savage, W. Gan, J. Svarc, *J. Geophys. Res.* **106**, 21995–22007 (2001).
47. P. Tong *et al.*, *Geophys. Res. Lett.* **48**, e2020GL090853 (2021).
48. Y. Jia, S. S. Gao, K. H. Liu, *Earth Planet. Sci. Lett.* **644**, 118920 (2024).
49. K. Chen *et al.*, *Nat. Commun.* **11**, 22 (2020).
50. M. Gassenmeier, C. Sens-Schönfelder, M. Delatre, M. Korn, *Geophys. J. Int.* **200**, 524–533 (2014).
51. K. Wang, D. S. Dreger, E. Tinti, R. Bürgmann, T. Taira, *Bull. Seismol. Soc. Am.* **110**, 1603–1626 (2020).
52. J.-P. Gratier, P. Favreau, F. Renard, *J. Geophys. Res.* **108**, 2104 (2003).
53. C. A. Trepmann, L. Seybold, *Geoscience Frontiers* **10**, 43–54 (2019).
54. J.-A. Nüchter, B. Stöckhert, *J. Struct. Geol.* **29**, 1445–1462 (2007).
55. C. Seltzer, M. Peč, M. E. Zimmerman, D. L. Kohlstedt, *Geochem. Geophys. Geosyst.* **24**, e2023GC010927 (2023).
56. X. Wang, Z. Zhan, *J. Geophys. Res. Solid Earth* **125**, e2020JB019577 (2020).
57. C. Milliner, S. Aati, J.-P. Avouac, *J. Geophys. Res. Solid Earth* **127**, e2022JB024519 (2022).
58. W. M. Behr, J. P. Platt, *Geophys. Res. Lett.* **41**, 8067–8075 (2014).
59. Q.-Y. Wang *et al.*, *J. Geophys. Res. Solid Earth* **124**, 8924–8941 (2019).
60. C. Liu, T. Lay, E. E. Brodsky, K. Dascher-Cousineau, X. Xiong, *Geophys. Res. Lett.* **46**, 11820–11829 (2019).
61. P. Thakur, Y. Huang, *Geophys. Res. Lett.* **48**, e2021GL094679 (2021).
62. D. J. Ponti *et al.*, *Seismol. Res. Lett.* **91**, 2942–2959 (2020).
63. C. W Jennings, C. Gutierrez, W. Bryant, G. Saucedo, C. Wills, Geologic map of California, Geologic Data Map GDM-2.2010, National Geologic Map Database (California Geological Survey, 2010); https://ngmdb.usgs.gov/Prodesc/proddesc_96750.htm.
64. J. Bryan, W. Frank, P. Audet, Data and code for: Crustal stresses and damage evolve throughout the seismic cycle of the Ridgecrest fault zone, Zenodo (2025); https://doi.org/10.5281/zenodo.15985966.

ACKNOWLEDGMENTS

We thank M. Peč, B. Holtzman, B. Hager, M. Floyd, and R. Bürgmann for discussions about the observations and potential mechanisms of postseismic deformation at Ridgecrest. **Funding:** J.B. acknowledges the National Science Foundation (NSF) for supporting this work through the Graduate Research Fellowship Program under grant 1745302. J.B. and W.B.F. acknowledge the Statewide California Earthquake Center (SCEC) for supporting this work through grant 24190; this is SCEC Contribution No. 14258. SCEC is funded by NSF Cooperative Agreement EAR-2225216 and USGS Cooperative Agreement G24AC00072-00. P.A. acknowledges the Natural Sciences and Engineering Research Council for supporting this work through grant RGPIN-2024-03898. **Author contributions:** Conceptualization: J.B., W.B.F.; Methodology: all authors; Investigation: J.B.; Writing – original draft: J.B., W.B.F.; Writing – review & editing: all authors; Funding acquisition: all authors; Resources: W.B.F.; Supervision: W.B.F. **Competing interests:** There are no competing interests to declare. **Data and materials availability:** The facilities of EarthScope Consortium were used for access to waveforms, related metadata, and/or derived products used in this study. These services are funded through the National Science Foundation's Seismological Facility for the Advancement of Geoscience (SAGE) Award under Cooperative Agreement EAR-1724509. The data products, including receiver functions, time series of the optimal transport distances, wavespeed changes, and anisotropy, as well as the code used to process the data and generate the figures, are provided in a Zenodo repository (*64*).

SUPPLEMENTARY MATERIALS

science.org/doi/10.1126/science.adu9116
Materials and Methods; Figs. S1 to S9; References (*65*–*73*)

Submitted 26 November 2024; accepted 21 July 2025

10.1126/science.adu9116

Sloan Kettering Institute

Celebrating over 75 years of breakthroughs

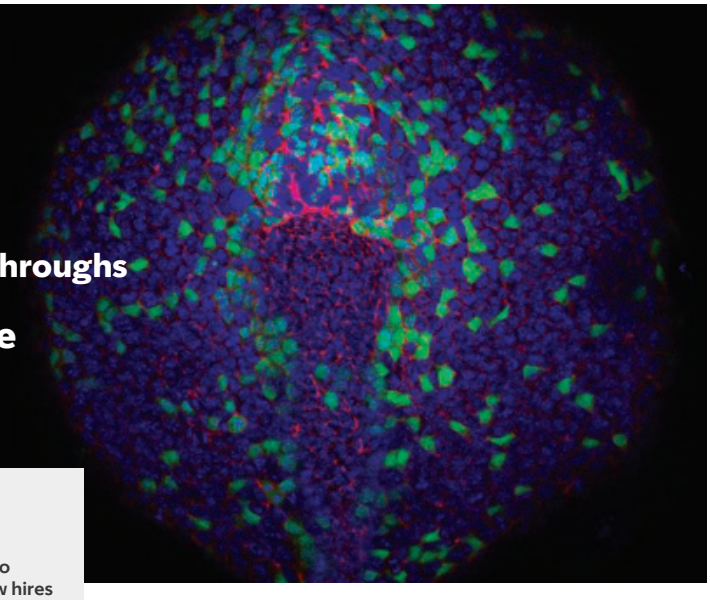

Join our faculty and help set the pace of biomedical science.

Join Us

Successful candidates will hold an appointment in one of SKI's research programs. Candidates may apply to up to two programs. Salary range is $195K-260K. Starting pay for new hires typically falls within the range shown above, based on candidate qualifications and experience, as well as other variables.This range represents annual salary only and does not include any one-time payments that eligible candidates may be offered at the time of hire.

Cancer Biology & Genetics
Chair: Scott Lowe, PhD

Cell Biology
Chair: Tobias Walther, PhD

Chemical Biology
Chair: Derek Tan, PhD

Computational & Systems Biology
Chair: Dana Pe'er, PhD

Developmental Biology
Chair: Anna-Katerina Hadjantonakis, PhD

Human Oncology and Pathogenesis Program
Chair: Charles Sawyers, MD

Immunology
Chair: Alexander Rudensky, PhD

Immuno-Oncology
Chair: Andy Minn, MD, PhD

Molecular Biology
Chair: John Petrini, PhD

Molecular Pharmacology
Chair: Omar Abdel-Wahab, MD

Structural Biology
Chair: Christopher Lima, PhD

Memorial Sloan Kettering Cancer Center

Areas of Basic and Translational Research

- Stem Cell Biology
- Developmental Oncology
- Regenerative Medicine
- Machine Learning
- 3D Single-Cell Analytics
- Biophysics & Imaging
- Organelle Biology
- Chromatin & Gene Regulation
- Genome Integrity and Functional Genomics
- Chemistry & Chemical Biology
- Metastasis & Tumor Microenvironment
- Immunity, Host-Microbial Interactions and Microbiomes
- Tumor Immunobiology
- Experimental Therapeutics, Imaging and Bioengineering
- Immuno-oncology

Research and Training

- 120 research laboratories housed in state-of-the-art buildings
- 26 Core facilities offering cutting-edge scientific services
- More than 900 pre- and postdoctoral trainees
- Appointments in the Gerstner Sloan Kettering Graduate School of Biomedical Sciences and the Weill Cornell Graduate School of Medical Sciences

Visit **www.ski.edu** to learn more.

MSK is an equal opportunity and affirmative action employer committed to diversity and inclusion in all aspects of recruiting and employment. All qualified individuals are encouraged to apply and will receive consideration without regard to race, color, gender, gender identity or expression, sexual orientation, national origin, age, religion, creed, disability, veteran status or any other factor which cannot lawfully be used as a basis for an employment decision.

Application deadline: **November 15, 2025** | Apply at: **https://facultysearch.ski.edu**

myIDP ScienceCareers
INDIVIDUAL DEVELOPMENT PLAN

Features in myIDP include:

- Exercises to help you examine your skills, interests, and values.
- 20 career paths with a prediction of which ones best fit your skills and interests.
- A tool for setting strategic goals with optional reminders to keep you on track.
- Articles and resources to guide you through the process.
- Options to save materials online and print them for further review and discussion.
- A certificate of completion for users that finish myIDP.

Start planning your future today!
myIDP.sciencecareers.org

In partnership with:

FASEB Federation of American Societies for Experimental Biology
UMASS University of Massachusetts Medical School
UCSF University of California San Francisco
UIC
BURROUGHS WELLCOME FUND

Research at UM6P

Dr. Jones Alami
Chief Research & Global Scientific Engagement Officer, UM6P

UM6P was created as a new kind of research university: experimental in spirit, impact-driven, and globally connected, while firmly rooted in Africa. This vision translates into a focus on strategic, future-facing fields such as agricultural sciences, advanced materials, energy storage and electric mobility, health sciences, artificial intelligence, biotechnology, ocean sciences, and climate resilience. What makes us distinctive is the way fundamental discovery and applied innovation are pursued together, ensuring that science contributes directly to both global understanding and local relevance.

From pioneering work on next-generation batteries for electric mobility to advances in sustainable agriculture for arid regions, UM6P is demonstrating how technologies developed locally can meet local needs while scaling globally. To cement our role as a hub where global science and African innovation converge, we are proud to host major scientific initiatives, including the International Meeting on Lithium Batteries (IMLB) in 2028.

Collaboration defines who we are. We are building interdisciplinary spaces where scientists and innovators co-create transformative ideas across fields, from AI-driven agriculture to marine sciences. Driving this vision is ouryoung, energetic, and ambitious community of researchers, students, and staff, who embrace the opportunity to contribute to a university that is shaping Africa's scientific future while strengthening its place in the global research community. For them, science at UM6P is not abstract, it is about impact: developing technologies in Morocco that matter to Morocco, Africa, and the world.

Looking ahead, UM6P aims to become a continental reference point for science and innovation: a place where the next generation of researchers is trained, where transformative technologies are born, and where Africa's voice in global science is both strong and distinctive.

BIOLOGY
TEXAS A&M UNIVERSITY

Five Tenure-Track Assistant Professor Positions in Microbiology, Evolution, and Biological Clocks

Position Description

The Department of Biology in the College of Arts and Sciences at Texas A&M University (TAMU) invites applications for **five full-time, tenure-track Assistant Professor positions** in the areas of **Microbiology (2), Evolution (2), and Biological Clocks (1)**. These are 9-month appointments with an anticipated start date of **Fall 2026**. As part of a major departmental expansion aligned with our 2020-29 Strategic Plan, these searches aim to build research excellence in the thematic areas of **Biological Resilience**, **Synthetic Biology**, **Evolution**, and **Biological Clocks**. We are especially interested in candidates who employ **interdisciplinary, collaborative, and innovative approaches** to address compelling questions in the biological sciences. Successful applicants are expected to develop and sustain an externally funded research program, contribute to undergraduate and graduate education, and engage in departmental and university service. We welcome applicants whose research spans disciplinary boundaries and support research programs that range from basic biological mechanisms to applied biomedical or environmental sciences.

Texas A&M's research enterprise is internationally recognized for excellence across the life sciences. The Department of Biology (www.bio.tamu.edu) provides a collegial, collaborative research environment that supports large undergraduate and graduate programs and promotes integration of students into active research. Faculty benefit from access to **world-class research and teaching infrastructure, competitive startup packages**, and participation in several **interdisciplinary doctoral programs**, including Ecology and Evolutionary Biology (eeb.tamu.edu), Genetics (genetics.tamu.edu), and Neuroscience (tamin.tamu.edu). The Department is home to the Center for Biological Clocks Research (CBCR) that supports research in circadian biology and sleep.

In support of growth in Biological Sciences, major remodeling of teaching space is presently underway, as is architectural design for a new Biology building that will add significant research space for our faculty.

Texas A&M University is located in Bryan-College Station. This vibrant and fast-growing community combines cultural diversity, arts and entertainment, and strong public schools with a high quality of life. Situated in the heart of the Houston-Dallas-Austin triangle, the region offers the amenities of a large metropolitan area while maintaining a welcoming, small-town feel.

Qualifications

Candidates must hold a Ph.D. in Biology or a related discipline and demonstrate a strong track record of impactful research in **microbiology**, **evolution**, or **biological clocks**, **emphasizing creativity, research excellence, and potential for interdisciplinary impact**.

Application Instructions

For full consideration, your application materials must include a short cover letter (one page), curriculum vitae, personal statement to include philosophy and plans for research (max three pages), teaching (max two pages), and service, and contact information for three references. These materials must be directly submitted online at apply.interfolio.com/171952. Please ensure all required documents are complete and accurate to facilitate a smooth application process. Review of applications will begin around October 1, but will continue to be accepted until the final deadline of November 15.

If you have questions about this search, please direct emails to Dr. Michael Benedik, Chair of the search committee, at benedik@tamu.edu.

What's Your Next Career Move?

From networking to mentoring to evaluating your skills, find answers to your career questions on *Science* Careers

To view the complete collection, visit **ScienceCcareers.org/booklets**

ScienceCareers
FROM THE JOURNAL SCIENCE AAAS

Caltech

DIVISION OF BIOLOGY AND BIOLOGICAL ENGINEERING
Tenure-Track Faculty Position in Neuroscience

The Division of Biology and Biological Engineering (BBE) at the California Institute of Technology invites applications for a tenure-track position in Neuroscience. We welcome applications from candidates working in any neuroscience subdiscipline, including molecular, cellular, developmental, comparative, behavioral, systems and computational neuroscience. Caltech especially values creative and innovative approaches to understanding neural function; candidates whose research program spans several of these subdisciplines and/or are working with non-traditional experimental systems are encouraged to apply.

Successful applicants are expected to develop innovative research programs and be committed to high quality teaching. Preference will be given to candidates at the Assistant Professor level; however, well-qualified applicants at the Associate or Full Professor level may also be considered.

Please submit an application at: https://applications.caltech.edu/jobs/bbe and include a brief cover letter; curriculum vitae; a list of published and submitted papers; a description of proposed research; and a statement of teaching interests. Applicants should also submit an education statement that addresses the applicant's thoughts on classroom and laboratory instruction, mentorship of students and postdoctoral scholars, and ways to foster an inclusive, equitable environment for the development of scholars who come to Caltech with many different backgrounds and experiences.

Applicants should arrange to have at least 3 reference letters uploaded.

Salaries for professorial faculty at Caltech fall in the range of $125,000-$400,000.

Applications will be reviewed in the order in which they are received and should be complete by October 15, 2025, for full consideration. Candidates must be available to interview on campus in Pasadena, CA, on January 12-13, 2026.

We are an equal opportunity employer and all qualified applicants will receive consideration for employment without regard to age, race, color, religion, sex, sexual orientation, gender identity, or national origin, disability status, protected veteran status, or any other characteristic protected by law.

Outstanding scientists from all research fields are invited to apply for a prestigious individual grant MUNI Award in Science and Humanities.

- An opportunity to conduct **independent research** at a **progressive university** in the Central European research and innovation hub
- 2 categories open: **MASH** with a budget of **$ 220 000 per year** for 5 years; **MASH StG/CoG** with a budget of **$ 130 000 per year** for 4 years
- Laboratory and office space, welcome service, administrative support
- Open to **all domains** of Social Sciences & Humanities, Physical Sciences & Engineering, Life Sciences

Call deadline: December 5, 2025

MASARYK UNIVERSITY

GAMU.MUNI.CZ/EN/MASH

utmb Health

Assistant Professor

A faculty position is available in the Department of Psychiatry and Behavioral Sciences, in conjunction with the Center for Addiction Sciences and Therapeutics at the University of Texas Medical Branch. Faculty are expected to be highly engaged in collaborative, translational research ventures and to provide mentorship to talented mentees. Successful candidates will have an M.D. or Ph.D. in Clinical Psychology or related clinical experience, a track record of scholarly research, publications, and history of, or evidence of potential for obtaining, extramural funding. A research focus in basic, translational and/or clinical sciences which directly contributes to the etiology, prevention, diagnosis and/or treatment of substance use disorders, neuropsychiatric and mental health disorders is appropriate.

A PDF application packet including (1) current curriculum vitae, (2) statement of research accomplishments, future directions, and teaching experience (≤ three pages), and (3) contact information for three potential references should be emailed to CAST@utmb.edu.

Institutional information can be found at http://www.utmb.edu, https://www.utmb.edu/cast/, and https://www.utmb.edu/psychiatry/.

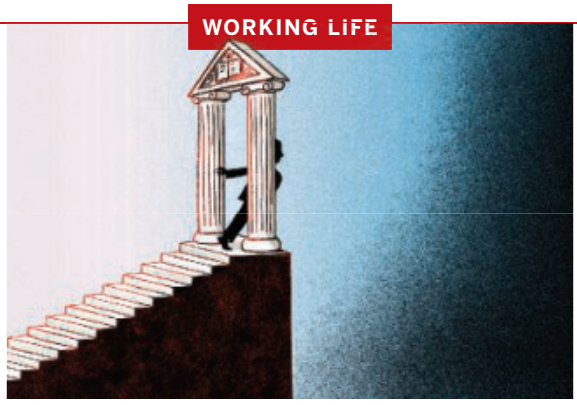

A gateway without guidance

Anonymous

The question caught me off-guard. The video call was supposed to be a simple wrap-up with a program evaluator—one last meeting to close my year in the postbaccalaureate program. I thought it would just be a chance to say thank you, talk about next steps, and get a bit of advice. Instead, I was asked a critical question: "How has this program shaped your sense of belonging in STEM, and in neuroscience specifically?" I stared at the screen for a moment, blinking. I wanted to be honest, but I didn't want to sound ungrateful. I knew how much the program had invested in my classmates and me. I also couldn't ignore the weight of what I had experienced.

The program's mission was to provide training to students from underrepresented backgrounds who had graduated from universities without many research opportunities. Coming from a small liberal arts college, I went into the program to gain the hands-on research experience I would need to be a competitive Ph.D. applicant.

It sounded like the gateway I was after. I wasn't exactly sure what I needed to learn to become a competent researcher. But, I reasoned, surely the program would know.

It didn't take long for those hopes to unravel. I soon learned that my cohort was the first. We were told we would be the "guinea pigs," and that there would be growing pains.

We had weekly group meetings with the program directors, mostly focused on research updates and goals. But no one seemed to grasp how new we were to all of this. We didn't just need feedback on our experiments. We needed someone to tell us what academia even was. How to navigate it. What questions to ask. We were hungry to learn, but the gaps were wide, and the silence around them made everything harder.

It's hard to say why those involved didn't understand what we needed. But it was clear that very few people on the medical campus where we were working looked like us. One day, as I was working on my laptop at a small coffee shop on campus, a woman in scrubs asked, "Do you have to be an employee, or can anyone just sit here?" My heart sank. I wasn't bothering anyone. I belonged. And yet, somehow, others didn't see it that way.

Meanwhile, I was struggling to get my experiments off the ground. Three months into the program, my mentor was put on administrative leave. I was unofficially placed under my mentor's supervisor, someone senior in the department. He was genuinely invested in the program. But he wasn't closely involved in my day to day. Without a direct mentor, I was left trying to piece things together on my own.

For months, I made almost no progress. When I asked questions of others in my lab, many of whom were stressed about their own future, they told me to "just look in the literature" and offered no further guidance. Once, a colleague said, almost casually, "Some people just aren't cut out for this."

Through my struggles, the program never checked in on me. It was a professor teaching one of my classes who ultimately filled that gap. After noticing I was obviously very unhappy, she invited me to switch to her lab.

I went on to work with her for the rest of the year. She gave me what I was missing: technical skills, insight into the unspoken norms of academia, and the red flags to watch out for. She helped me rebuild my confidence and gave me tools, language, and a way forward. "You're a star," she said once, so casually it felt like a fact.

In the end, I came out of the experience achieving what I set out to do. I applied to and was accepted into the graduate school of my choice. But it wasn't because I was guided or nurtured by the program. I decided to be honest and tell the program evaluator the truth. The program showed me I was capable of doing neuroscience research, but it didn't give me a feeling that I belonged.

Now as a first year Ph.D. student, I find myself fielding questions from students considering similar programs. I tell them to ask about the kind of support they'll receive in and outside of the lab and what programs mean when they say "mentorship." Who will be responsible for guiding you? What are their roles, and what are your options if things go off track? Talent and grit matter, but so do structure, transparency, and care. □

The author is a Ph.D. student in the United States.

ILLUSTRATION: ROBERT NEUBECKER

The Chen Institute and *Science* launched the "Chen Institute and *Science* Prize for AI Accelerated Research" in August 2024. This initiative aims to drive advancements in artificial intelligence that can expand scientific research. Young scientists from around the world are invited to submit AI-driven projects that demonstrate significant potential to improve research and lives.

The competition will award a Grand Prize of $30,000, with the winner's essay published in *Science* and an accompanying five-year AAAS membership. Additionally, up to two runners-up will receive $10,000 each, with their essays published on *Science* Online and the same membership benefits, promoting sustained engagement with scientific progress.

Apply at

cheninstitute.org/prize

Samsung Ho-Am Prize ignites the passion and innovative spirit for scientific discovery

We welcome your recommendations for the 2026 Ho-Am Prize candidates.

- Award Categories : **Physics & Mathematics, Chemistry & Life Sciences, Engineering, Medicine**
- Candidate Qualifications : Researchers of Korean heritage
- Nomination Deadline : Oct. 31, 2025

* Learn more about the prize and nomination : www.hoamfoundation.org

HOAM
THE HO-AM FOUNDATION